# Atmospheric $CO_2$ across the Plio-Pleistocene

## Climate Feedback Mechanisms during Late Pleistocene Climate Cycles and the Mid-Pleistocene Transition


**Sophie Nuber**

School of Earth and Ocean Sciences
Cardiff University

Submitted in partial fulfilment of the requirements for the degree of
*Doctor of Philosophy*

July 2020

# Abstract

The study of climate parameters and their feedback mechanisms have become exceedingly important in light of anthropogenic $CO_2$ release and its initiation of climate change. In this thesis, I investigate the interaction between different climate parameters during Late Pleistocene climate cycles and the Mid-Pleistocene transition (MPT). I use ocean sediment core-derived foraminiferal shells and geochemical analyses to reconstruct surface water temperature, salinity, and atmospheric $CO_2$ from a new site U1476 in the Mozambique Channel. I show for the first time that a peak in glacial Indian Ocean surface salinity creates a particularly salty Agulhas Leakage during Late Pleistocene deglaciations. This may influence changes in global climate by altering the surface salinity budgets at deep water convection sites, potentially driving a more vigorous overturning circulation. Late Pleistocene climate transitions established during the MPT "900kyr event", when glacial ice volume significantly increased forming a 100kyr cycle. I demonstrate that ice sheets during the early MPT sustained glacial ice volume, despite increases in summer duration insolation and temperature. The data combined with new $pCO_2$ reconstructions suggest that the early de-coupling of ice sheet dynamics caused a disruption in the forcing of earth's internal feedback mechanisms, leading to the global phenomenon of the "900kyr event". The $pCO_2$ data was reconstructed using multi-collector inductively coupled plasma mass spectrometry (MC-ICPMS) boron isotope analysis. I present accuracy and precision data of boron isotope standard measurements conducted on a new Nu plasma II instrument. Best results were achieved after adopting a PFA cyclonic spray chamber, $10^{11}\Omega$ resistors, and concentrated solutions. My additional laboratory test studies provide evidence that cleaning large samples, as used in boron isotope analyses, can be efficiently conducted without the necessity for scaling reagents. My research concludes that Late Pleistocene Indian Ocean circulation and early Pleistocene ice sheet dynamics are important internal climate drivers that have the potential for shaping Pleistocene climate when coupled with insolation- or atmospheric $CO_2$ change.

# Acknowledgements

First of all, I would like to thank all my supervisors Steve Barker, Morten Andersen, James Rae, and Ian Hall for their invaluable help and support. It was a tremendous group effort getting this project to the point where it is now. Without their knowledge and expertise, I would not be where I am today. Thank you also to Pallavi Anand, Marc Millet, and Jenny Pike for conducting the defense. I want to extend my thanks to all the fabulous assistance I received in the labs. A huge thank you to Bob Steele for being the best laboratory manager out there, to Heidi Block and Sandra Nederbragt for having prepared and measured so many of my samples, and to Eli Dennerly for having spent hours of her time helping me pick foraminiferal shells. Additionally, I am utterly grateful for the patience and encouragement received from Tom Chalk and Rosanna Greenop who answered all my emails on boron isotope analytics and kept telling me to persevere with the measurements. My gratefulness extends also to Lindsey Owen, Jenny Pike, Julie Ramage, and Emiliana Palk. You have stood by me in times of great distress and anxiety. I always remember the Lindsey-lunches who represented little moments that I could look forward to for days. You, and my karate group, huge thanks to Martyn, Emma and everyone else, kept me sane when sanity seemed far away. Karate friends, you gave me respect, happiness, support and made me feel worthy. You will always be in my heart. Thank you Emiliana and Mark Humblet for believing in my idea of a scientific internship for years! My two months in Japan were one of the best times I had. I am so proud that we managed to make it happen. I would also like to give a massive hug to all my colleagues Molly Trudgill, Eloise Littley, Jess Crumpton-Banks, Laura Crick and Helen Innes. You powerful women have taken me in with open arms and made my work in the lab and outside so much fun! Molly, I am so happy we are such a tight team and I look forward to many more hours of Ghibli films, tea, cake and batch :D. The greatest love and thanks I would like to give to my family and long-term friends. Mama, Papa, Claudio und Constantin. Ihr seit die beste Familie die ich mir wünschen würde und ich finde es toll wie ihr mich alle immer unterstützt. Ich freue mich dass wir so eng zusammen sind, und vorallem dass wir ein so tolles Geschwisterverhältnis haben. Mama du warst für mich immer ein Vorbild. Du hast mir gezeigt, dass ich

sein kann wer ich will; und dass mir im Leben alle Türen offen stehen! Danke Papa, dass du immer Zeit hattest für meine wissenschaftlichen Diskussionen und dass wir das Interesse für Mikroskope, welches ich erst lernen musste, teilen. Es macht so viel Spaß mit euch! Ich hab euch sehr lieb. Ganz dicke Umarmung und Küsse auch für Oma! Du bist immer für uns da und lachst und spielst mit uns. Wir haben die Beste Oma der Welt! Liebe Leonie, ich finde es toll, dass wir schon so lange befreundet sind. Unsere Treffen und Telefonate erheitern mich jedes mal. Unsere Kindheitsspiele finde ich bis heute super! Wer kann schon im Schlafzimmer den Mount Everest besteigenund gleichzeitig ins Schwimmbad gehen? Ich hoffe und freue mich auf eine lange Zukunft mit dir. Julianna, Sanna, Richard, Gabriel, and Jody thank you for always being there and lighting up my scientific excitement! You make me laugh and let me know that the world is more than excel spreadsheets on a screen. When I call you, I know I hang up with a smile on my face. Thank you for being my friends! Jody I absolutely agree that once in a while, I must make the boom harder! And most importantly last, I want to give my gratitude and affection to Lina and Huw. Without you, I would not have finished this PhD. Lina, you are my sunshine. Du gibst mir grundsätzlich das Gefühl genug zu sein und überaus intelligent noch dazu. Du bist immer für mich da, in guten wie in schlechten Zeiten. Du lachst und weinst mit mir, wir gehen durch dick und dünn. Ich freue mich immer wenn wir uns sehen, und doch bist du nie weit weg! Lass uns so weiter machen :D Huw, I have found my soul mate in you. You have supported me from the day we met, and have always believed in me no matter what. You have become my everyday companion, and without your help I wouldn't be where I am today. Thank you for being the most amazing person. I hope we share many years together.

Für Lina

*Wissenschaft ist Schönheit,*
*Wissenschaft ist Klarheit,*
*Wissenschaft ist Kleinlichkeit,*
*Nach jedem Ergebnis sehen wir die Welt*
*mit anderen Augen.*

# Table of contents

# List of figures

# List of tables

# Chapter 1

# MOTIVATION AND RATIONALE

## 1.1 Research Interest

In 2016, the EU together with 174 countries signed the Paris Agreement under the United Nations Framework Convention on Climate Change (COP21). The agreement states that each ratifying country will do everything possible to reduce its greenhouse gas emissions to limit the $21^{st}$ century global warming to an average global atmospheric temperature increase of 1.5°C. This shows how much impact the recent climatic changes have already had. Yet, no significant international political decisions have since underlined the Paris Agreement. Scientists emphasized the need for political action by publishing the IPCC 1.5 degrees special report (2018), but political advances at the Katowice Climate Summit in 2018 were minor. Yet, in many regions, local changes in extreme weather (Gillies, 2015), seasonality (Shepard, 2018), and sea level rise (The Washington Post, 2019; Weston, 2017) have not gone unnoticed. Despite slow process on international political levels, it is important that science provides the best knowledge possible on climate change processes, potential issues, and mitigation.

The climate system is a complex network of mechanisms that follow the laws of physics and interact on multiple spatial and temporal scales. Feedback loops and

stochastic behaviour make the prediction of causal relationships between different climate variables difficult. Yet, given the need for information on these relationships for local and regional governments, their research is of extreme importance. This doctorate thesis will extend the already existing pool of knowledge on how some of the climate variables act on longer timescales. In the following chapters, I will provide new scientific findings on the intercoupling between different climate system parameters, including Indian Ocean surface circulation and atmospheric carbon dioxide ($CO_2$) concentrations. This is done by sampling the past 1.5 million years (Ma) using ocean sediment cores. The past 1.5Ma present a unique opportunity to research the above questions as they were influenced by significantly varying atmospheric $CO_2$ levels in consistence with intense climatic changes. Ocean sediments enable us to reconstruct the different climatic factors, including atmospheric $CO_2$, and allow the investigation of their relationships via geochemical analyses. Within the last 1.5Ma, the Mid-Pleistocene Transition (MPT) has been chosen as a key period where changes in atmospheric $CO_2$ may have driven long-term multi-millennial climate shifts. This thesis will provide some of the first ever reconstructed atmospheric $pCO_2$ measurements for that time.

## 1.2 Research Impact Statement

Atmospheric $CO_2$ has been identified as an important climate feedback and potential driver of past, present and future climate (Denman et al., 2007). Modern greenhouse gas emission-induced global warming has set off significant climatic changes that have been recorded across the globe (IPCC, 2018). These include rising global air temperatures, sea surface and deep sea temperatures, decreases in ocean pH, reduction of mountain glaciers, ice shelf collapse, melting-induced sea level rise, deep thawing of permafrost soils and increases in extreme weather likelihoods (IPCC, 2018). Many of these processes show potential threshold behaviour and

are interlinked by feedback loops. Understanding these behaviours and feedback loops is of crucial importance to estimate the significance and duration of some changes observed in the climate system in relation to modern global warming. Past climate archives provide countless opportunities to reconstruct the different climate variables and study their interconnectivity. Ocean circulation has been identified as a major climate feedback mechanism, also directly linking with atmospheric $CO_2$ concentrations across the last 800,000 years. Throughout this time, Atlantic and Pacific surface circulation patterns are reasonably well understood. However, data from the Indian Ocean is sparse limiting our understanding of Indian Ocean surface processes and potentially of climate evolution during this time. I therefore propose the first research question:

**Research Question 1:** ***What role does the Indian Ocean play in shaping glacial-interglacial climate in the Late Pleistocene (0-1.2 million years)?***

Despite the importance of atmospheric $CO_2$ as a climate forcing greenhouse gas, our understanding beyond the last 800,000 years is significantly limited, due to analytical limitations. Recent advances in method and mass spectrometry development provide us with the new opportunity to collect first insights into the history of $CO_2$ beyond 800kyr. Here, I will use one of those methods, boron isotopes in planktonic foraminiferal calcite, to reconstruct atmospheric $CO_2$ from a glacial cycle ($\sim$1.1 million years) in the Mid-Pleistocene transition (MPT), a time characterised by significant global ice volume expansion. In later glacial-interglacial cycles, a tight coupling exists between global ice volume and $CO_2$. However, at the beginning of this thesis, no $CO_2$ data existed for the MPT. I hence propose the following second question:

**Research Question 2:** ***What happens to atmospheric $CO_2$ during the Mid-Pleistocene transition (0.8 - 1.2 million years)?***

This thesis was conducted in parallel to the set-up of a new analytical isotope facility and a multi-collector inductively-coupled mass spectrometer from Nu instruments at the School of Earth and Ocean Sciences, Cardiff University. As part of the laboratory set-up, the preparation methods and analytical procedures for trace element and boron isotope analyses from foraminiferal calcite were reviewed. During the review, the following inconsistencies were noted: (i) Cleaning methods for foraminiferal calcite were established on samples with 25 foraminiferal shells, while boron isotope analysis requires up to 200 shells. (ii) Published information on the contamination potential of ice-rafted debris and microscopic black particles diverged. (iii) All published analytical procedures for boron isotope analysis were established on mass spectrometers from Thermo Scientific. As such, I added the third question:

**Research Question 3:** ***Are established preparation methods and analytical procedures valid for different sized samples with varying initial contamination degrees, and different brands of mass spectrometers?***

## 1.3 Research Objective

To answer the above research questions, this doctoral thesis will use a multi-proxy approach to reconstruct a variety of new climate records using trace element, stable isotope, and boron isotope analyses across the Late Pleistocene and Mid-Pleistocene Transition. Combined with an estimate of alkalinity, the boron isotope measurements will be used to calculate atmospheric $CO_2$. The analyses will be conducted on planktonic and benthic foraminiferal calcite from a promising new IODP site U1476 cored in the western Indian Ocean in spring 2016 on IODP expedition 361 (Hall et al., 2017).

In chapter 7, I will present sea surface temperature, sea surface salinity, and global ice volume reconstructions from Indian Ocean sediment core U1476 to

answer research question 1. In chapter 8, I then provide the first atmospheric $CO_2$ reconstructions around 1.1 million years within the MPT to support research question 2. All findings concerning the methodological research question 3, including cleaning tests, and analytical set-up tests, are discussed in chapter 6. For the reader's interest, the thesis provides an extensive review of atmospheric $CO_2$ and its influence on modern and past climates that goes beyond the scope of the title in the Appendix.

# Chapter 2

# INTRODUCTION - PALAEOCLIMATE & OCEANOGRAPHY

## 2.1 The Icehouse world – Glacial-Interglacial climate cycles

Climate on earth has changed significantly throughout the geological past (Figure 2.1) (Zachos et al., 2001). Two overall climatic states have been identified in the earth's history: greenhouse and icehouse (e.g. Katz et al., 2008). The greenhouse world is characterised by the lack of global perennial ice, while the icehouse world describes geological times when the poles were ice covered (e.g. Katz et al., 2008). The last greenhouse world was active during the Mesozoic. It was characterised by higher atmospheric $CO_2$ concentrations between 500ppm and 1000ppm (Breecker et al., 2010; Quan et al., 2009; Royer et al., 2007), with high global mean temperatures (Littler et al., 2011; Skelton et al., 2003) and tropical climates up to the poles (Littler et al., 2011; Skelton et al., 2003; Tarduno et al., 1998). The shift from greenhouse to

icehouse world after the Cretaceous was most likely caused by a long-term decrease in atmospheric $CO_2$ (DeConto & Pollard, 2003; Pagani et al., 2005) in parallel with long-term deep-sea cooling (Zachos et al., 2001), and Antarctic thermal isolation (Kennett, 1977). Around 33.9 million years (Ma) ago, at the Eocene-Oligocene boundary, declining atmospheric $CO_2$ levels crossed a threshold allowing Antarctica to build up perennial ice (DeConto & Pollard, 2003; Galeotti et al., 2016). This was followed by further long-term $CO_2$ decline leading to northern hemisphere glaciation between 3.2Ma and 2.5Ma marking the onset of the Quaternary and the Pleistocene (Willeit et al., 2015). Parallels have been drawn to the closure of the Panama isthmus coinciding with the $CO_2$ decline which led to large reorganisations in ocean circulation and the formation of the Atlantic meridional overturning circulation (Bartoli et al., 2005; Driscoll & Haug, 1998; Haug & Tiedemann, 1998). The resulting northwards flowing Atlantic surface currents increased moisture transport to the Arctic supporting the development of larger ice sheets (Bartoli et al., 2005; Haug & Tiedemann, 1998).

The presence of ice on the planet leads to changes in the energy budget via alteration of the global albedo and promotes ice cap expansion through ice sheet height/mass-balance feedbacks (DeConto & Pollard, 2003). The insolation reaching earth surface changes on millennial timescales, due to the astronomical constellation of the sun and planets in our solar system (Laskar et al., 2004). In an icehouse world, the insolation oscillations can be amplified via the ice-albedo and other earth intrinsic climate feedbacks leading to insolation paced climate cycles alternating between glacial and interglacial states (Hays et al., 1976; Milankovic, 1930).

The energy received on earth is defined by the interference of three astronomical parameters known as eccentricity, obliquity and precession (Figure 2.2) (Laskar et al., 2004). Gravitational forces between the nearest planets (Jupiter, Mars and Venus) and the Earth lead to a deformation of the Earth's orbit around the sun (Laskar et al., 2004). As a result, the shape of the orbit varies between nearly circular to

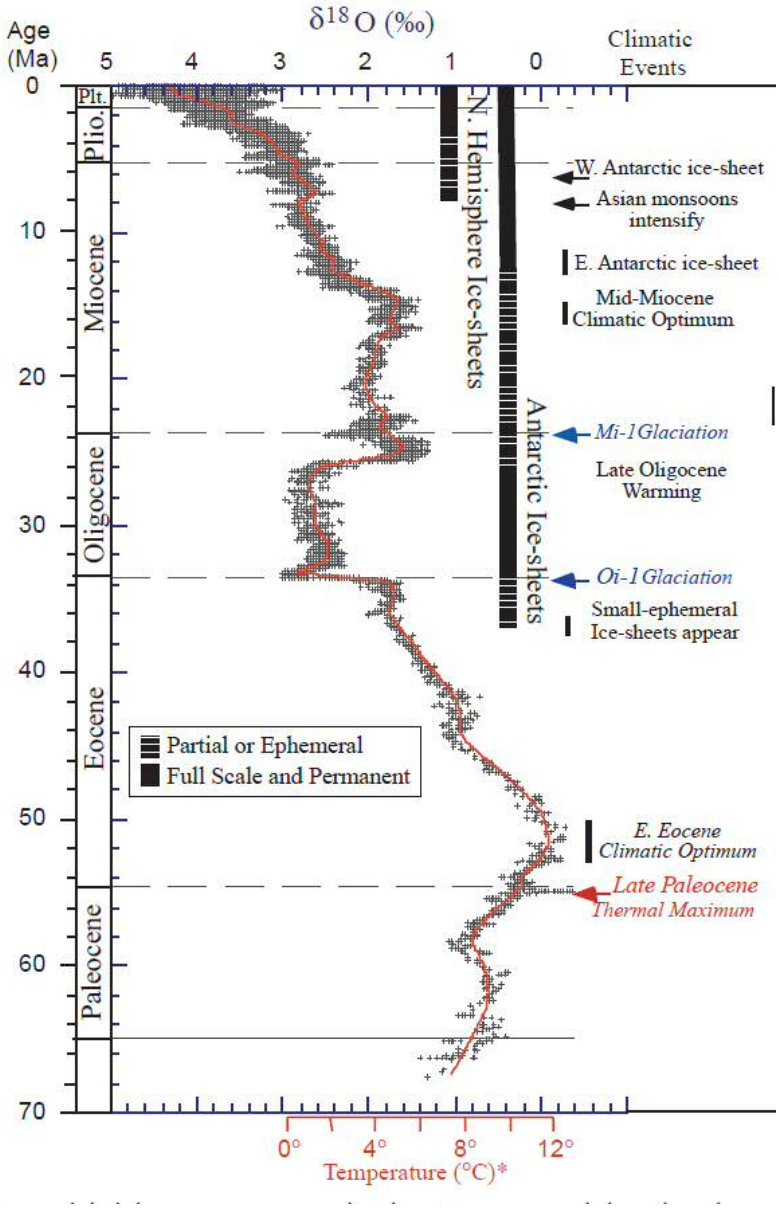


**Figure 2.1** Benthic foraminifera $\delta^{18}$O stack over the last 65Ma, a proxy for global air temperature and climatic change from Zachos et al. (2001).

elliptic (Figure 2.2a) (Berger et al., 1992). This is known as eccentricity, where high/low eccentricity corresponds to an elliptic/circular orbit. An elliptic orbit will force the Earth closer to the sun increasing the solar radiation received on our planet. However, it will also cause the earth to move faster along its pathway leading to hotter, but shorter summers. In turn, a circular orbit will have the opposite effect creating longer, but cooler summers. The eccentricity cycles present periodicities of

100kyr, 413kyr and roughly 2Ma (Laskar et al., 2004). Eccentricity appears to be the weakest forcing factor on insolation (Figure 2.3).

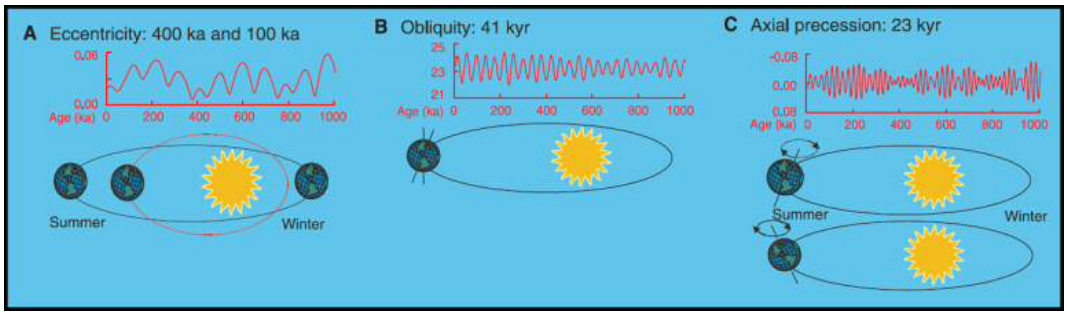


**Figure 2.2** Orbital parameters influencing insolation: (a) eccentricity, (b) obliquity, and (c) precession from Zachos et al. (2001). Typical cyclicity for each parameter noted at the top. Below, the Laskar et al. (2004) mathematical solution across the last 1Ma (red), and an idealised model showing the astronomical behavour.

The existence of gravitational forces between the planets cause additional alterations to the tilt of the earth's axis. The angle of the tilt varies between 22.4° and 24.5° on a 41kyr cycle (Laskar et al., 1993) which has a particular influence on seasonality in the high latitudes. A strong tilt leads to higher insolation in summer and lower insolation in winter, whereas a weak tilt causes less variability between summer and winter. Obliquity is strongly modulated by eccentricity leading to periods of high/low obliquity influence on insolation during maximum/minimum eccentricity (Figure 2.2b and 2.3) (Laskar et al., 2004). The earth is a body of mass rotating around its own axis. Gravitational pull towards other bodies of mass (e.g. other planets) impede a perfect rotation and cause the axis to describe a circular motion (Figure 2.2c). One axial "wobble", or precessional cycle, is completed in around 23kyr (Laskar et al., 2004). Precession has a particular importance for insolation at lower latitudes since the "wobble" motion is largest around the equator.

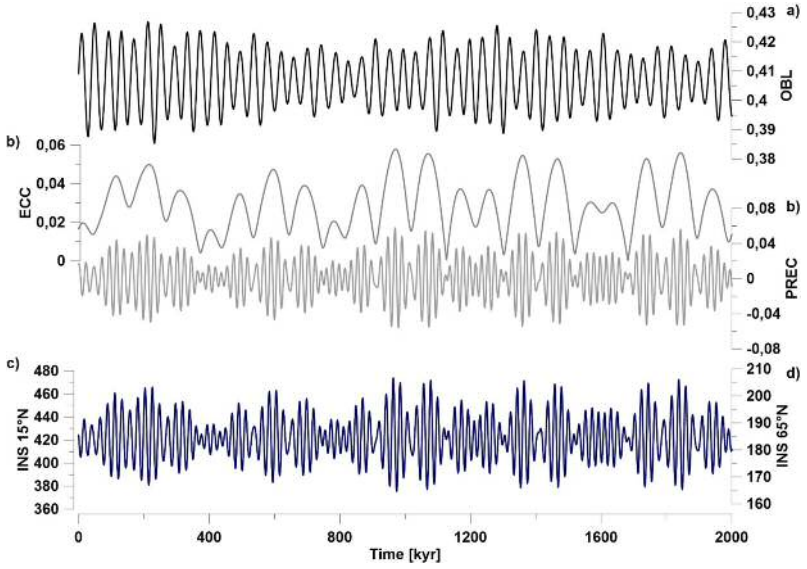


**Figure 2.3** The Laskar et al. (2004) mathematical solutions for the last 2Ma of obliquity (a), eccentricity (b), precession (c), and insolation at 15°N (tropical) (d) and 65°N (high latitudes)(e)

## 2.2 The Plio-Pleistocene (5.3Ma – 0.1Ma)

The Plio-Pleistocene combines two geological periods during which the earth's climate alternated between cold glacials and warm interglacials (Figure 2.4, 2.5). The Pliocene follows the Miocene epoch, with the onset defined at around 5.3 million years (Ma) in line with substantial cooling of the Earth's climate and a glaciated south pole. It is characterised by low amplitude high frequency glacial-interglacial cycles which follow a long-term decreasing trend from a warmer into a cooler world visible in $\delta^{18}$O stack data (Figure 2.4) (Lisiecki & Raymo, 2005; Zachos et al., 2001).

Temperature and atmospheric $CO_2$ concentrations are tightly coupled to $CO_2$ values oscillating between glacial 250ppm and interglacial 500ppm (Bartoli et al., 2011; Martínez-Botí et al., 2015; Seki et al., 2010). The Pliocene exhibits a warming phase between 5.33Ma and 2.58Ma termed the mid Pliocene Warm Period (mPWP) (e.g. Haywood et al., 2016). Recently, the mPWP has received increasing scientific attention, because of prevalent elevated $pCO_2$ levels around 400-500ppm (Berends

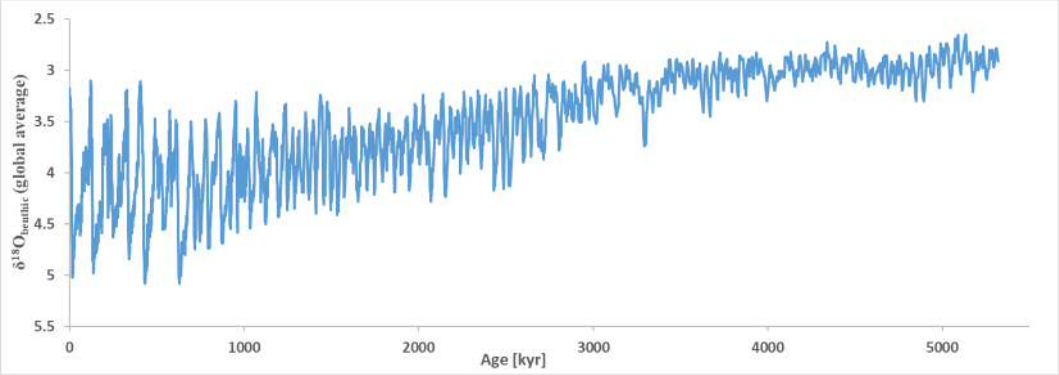


**Figure 2.4** Benthic foraminiferal calcite $\delta^{18}$O stack comprised of averaging 57 individual records showing the glacial-interglacial variability in ice volume and deep water temperature over the last 5.3Ma known as the Plio-Pleistocene (Lisiecki & Raymo, 2005).

et al., 2019; Martínez-Botí et al., 2015) which is comparable to the current future projections for 2100 (Burke et al., 2015). The mPWP is characterised by on average 3° - 9°C warmer temperatures than today (Dekens et al., 2007) which expresses itself in warmer surface waters (Dekens et al., 2007; Draut et al., 2003; Lawrence et al., 2009), overall enhanced ocean circulation (Ravelo & Andreasen, 2000), smaller ice caps (Austermann et al., 2015), enhanced cyclones (Yan et al., 2016) and expanded tropical ecosystems (Klaus et al., 2017). The end of the mPWP was most likely driven by northern hemisphere glaciation which occurred between 3.2Ma and 2.5Ma in line with long-term decrease of atmospheric $CO_2$ (Willeit et al., 2015) and the closure of the Panama isthmus (Bartoli et al., 2005; Driscoll & Haug, 1998; Haug & Tiedemann, 1998).

The Pleistocene (2.6Ma – 0.1Ma) differs in two fundamental ways from the Pliocene. First, it is governed by northern hemisphere glaciations (Lisiecki & Raymo, 2005). Unlike Antarctica which is limited by the surrounding liquid ocean, the northern hemisphere consists of large continental land masses. This provides stable ground for extensive lateral growth of ice sheets. Additionally, the closure of the panama straits led to a reorganisation of ocean circulation and set up a cross-equatorial northwards flowing surface current in the Atlantic Ocean (Bartoli et al., 2005; Haug & Tiedemann, 1998; O'Dea et al., 2016). This caused changes

in the salinity and temperature distributions of Atlantic surface waters leading to a modern-like salty and warm Gulf Stream (Karas et al., 2017). It is likely that the warm surface currents provided a new moisture source for growing northern hemisphere ice sheets (Bartoli et al., 2005). As such, Pleistocene glacial-interglacial cycles and ice sheet variability are enhanced (Figure 2.5). It has been shown that larger Pleistocene ice sheets respond more strongly to the integrated insolation over the summer duration (Huybers, 2006). As such, it causes early and middle Pleistocene climate cycles to phase-lock to the 41kyr obliquity pacing with medium amplitude and near-sinusoidal shaped cycles (Huybers, 2006; Meyers & Hinnov, 2010). Between 1.2Ma and 0.6Ma during the Mid-Pleistocene transition (see also chapter 2.4), periodicity, amplitude and shape of the cycles change without any shift in the astronomical forcing parameters (Figure 2.5). The periodicity expands from 41kyr to 100kyr parallel to increasing amplitude as glacials become colder in line with large-extent northern hemisphere ice sheets (Bintanja & Van De Wal, 2008). The formation of new phase-locking to 100kyr reorganised the interplay between earth intrinsic feedback mechanisms and caused a shift in the cycle shape from near-sinusoidal to asymmetrical saw-tooth shape (Lisiecki & Raymo, 2005).

For the last 0.8Ma, climate cycles are characterized by long-term glacial cooling followed by abrupt warming events (deglaciations or terminations) and short-term interglacials (Figure 2.5). Throughout the last glacial cycle, several abrupt climate oscillations known as the Daansgard-Oeschger cycles (Dansgaard et al., 1993; NGRIP, 2004), Bond cycles (Bond & Lotti, 1995) and Heinrich events (Heinrich, 1988) interrupt the mean climate state (Figure 2.6).

Rapid climate variability is likely driven by changes in the Atlantic meridional overturning circulation (AMOC) (Rahmstorf, 2002) potentially via ice sheet (Zhang et al., 2014) or $pCO_2$variability (Zhang et al., 2017). Reductions in the AMOC have been shown to cause cooling in the northern hemisphere (NH) and warming in the southern hemisphere (SH) due to the bipolar seesaw mechanism (Barker et al., 2009;

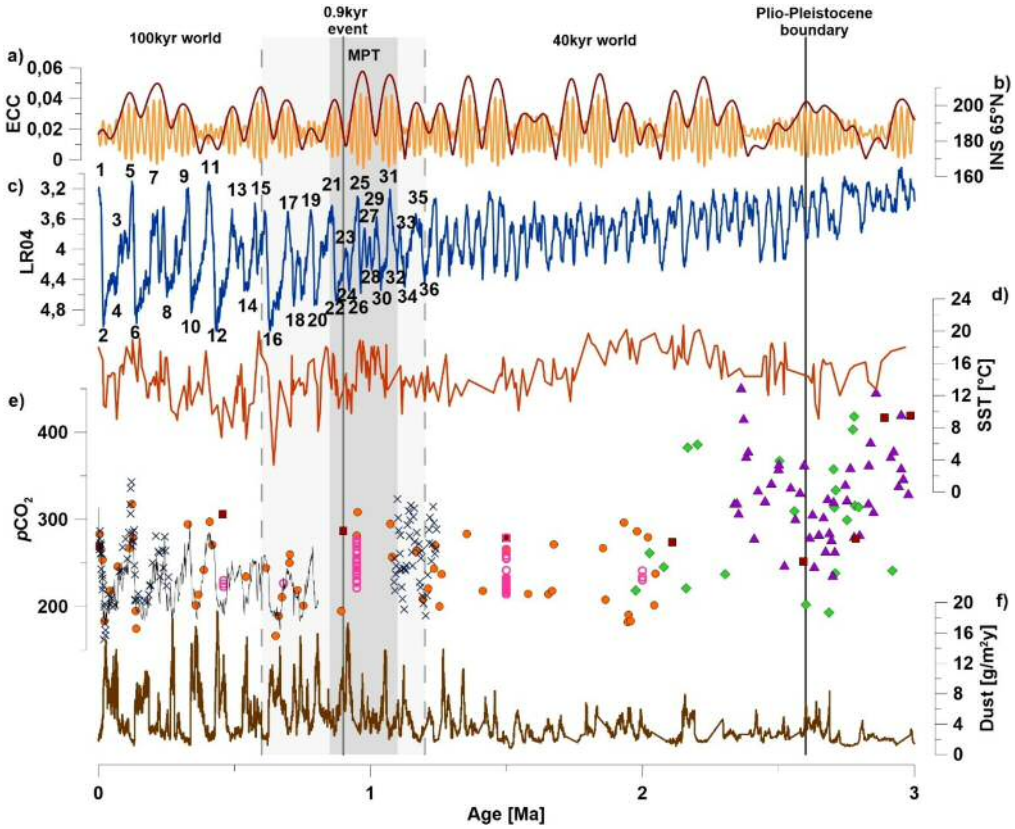


**Figure 2.5** Assembled climate date for the Pleistocene. (a) eccentricity (dark red) and (b) high latitude insolation (orange) from Laskar et al. (2004), (c) LR04 benthic $\delta^{18}$O stack (blue) (Lisiecki & Raymo, 2005) with Marine Isotope Stage labels for the last 35 climate cycles, (d) SST stack (red) from McClymont et al. (2013), (e) $pCO_2$ data from ice cores (thin dark blue line), blue ice (pink circles) and boron isotopes (filled circles) (for references see Figure 3.10), and (f) dust fluxes (brown) from Martinez-Garcia et al. (2011).

Stocker & Johnsen, 2003). It is debated whether rapid climate variability is also present during earlier Late Pleistocene glacial cycles. Barker et al. (2011) extend the 120kyr-long Greenland record by applying the bipolar seesaw mechanism to align NH and SH ice cores, then filter out the NH variability out of the 800kyr-long SH ice core record. The resulting variability suggests abrupt climate variability as a significant climate component of Late Pleistocene glacial cycles (Barker et al., 2011). Deglaciations also appear to be interrupted by abrupt climate events. In NH temperature records (NGRIP, 2004; Stuiver & Grootes, 2000), the last deglaciation begins with cold ice-rafting Heinrich event HS1 at 18kyr – 14.6kyr, followed by a warm spell (Bølling-Allerød), and a cold reversal around 12.8kyr – 11.5kyr (Younger

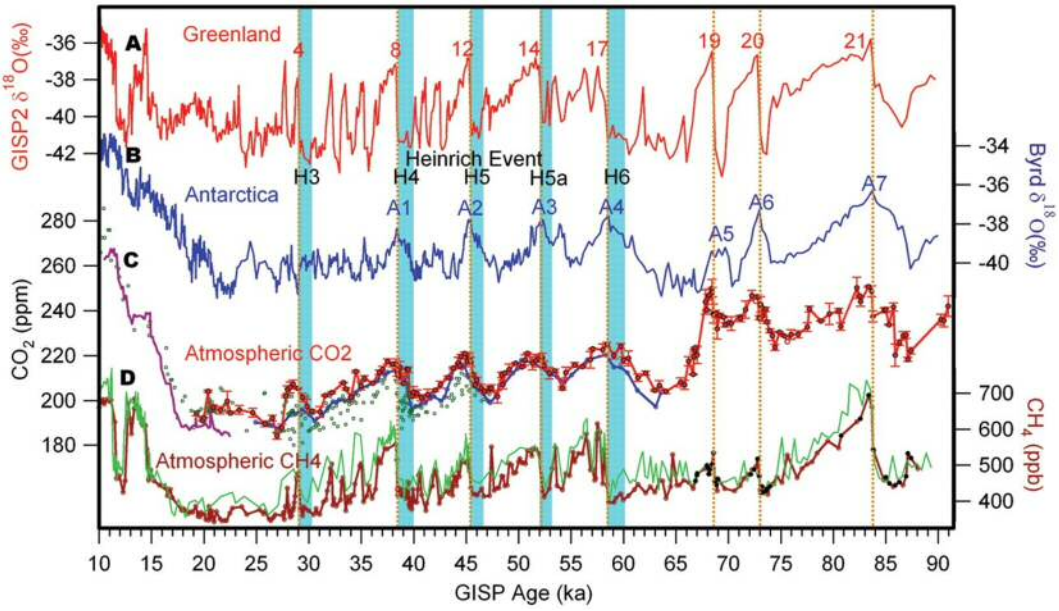


**Figure 2.6** Abrupt climate variability across the last glacial cycle. Compiled GISP2 (Greenland) (a) and Byrd (Antarctica) (b) $\delta^{18}$O ice core data, Antarctic ice core $CO_2$ (c) and $CH_4$ (d) for the last 90,000 years (90kyr) (Ahn & Brook, 2008).

Dryas) before reaching interglacial conditions (Figure 2.7). In line with the bipolar seesaw, Antarctic temperatures experienced gradual warming during NH cold periods, and slight cooling from 14.7kyr – 13kyr (Antarctic Cold Reversal) (see also Pedro et al., 2016) during the Bølling-Allerød (Barker et al., 2009). Deglacial climate variability was proposed to be governed by changes in ocean circulation via deep water formation reduction (Ritz et al., 2013; Thornalley et al., 2011). This can be achieved by disturbing density structures at NH deep water formation sites from input of ice sheet meltwater (Thornalley et al., 2010). Candidates for such forcing are phases of rapid sea level rise termed meltwater pulse 1A and 1B (Fairbanks, 1989) which occurred around 14,000 calendar years before present (cal yr B.P.) and 11,300 cal yr B.P., respectively (Bard et al., 2010). It was suggested that the Younger Dryas cooling resulted from a glacial lake outburst event and subsequent freshwater release into the North Atlantic (Broecker, 2006), potentially linked to meltwater pulse 1A and subsequent freshwater release from the Laurentide ice sheet (Tarasov & Peltier, 2005). This is widely debated as little geological evidence was found

for a glacial lake outburst (Broecker, 2006) and the extend of meltwater released during A1 can be explained from other sources (Clark et al., 1996). Instead, Barker et al. (2010) report a particularly vigorous AMOC during the Bølling-Allerød and propose that it resulted as an AMOC overshoot from fast increasing $pCO_2$, either from marine (Anderson et al., 2009; Skinner et al., 2010) or terrestrial (Köhler et al., 2014) sources. The Younger Dryas cold event may also be expressed as a transient climate phenomenon in response to an early interglacial-like B/A overshoot (Barker et al., 2010).

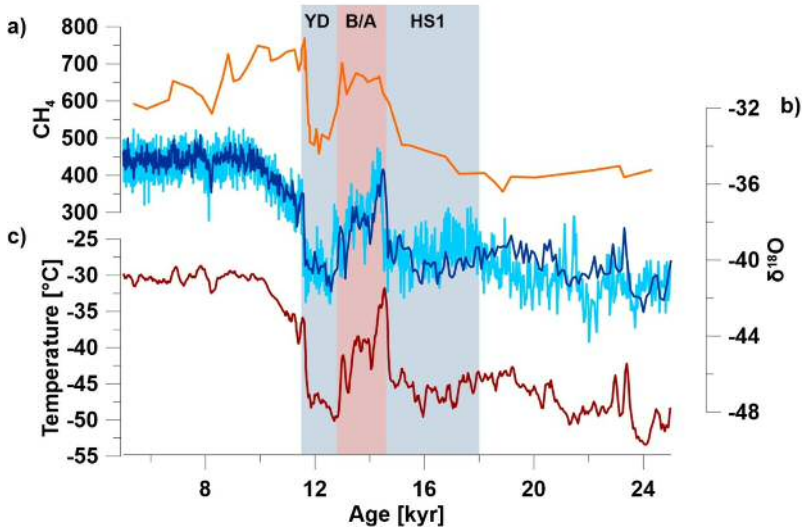


**Figure 2.7** Last deglaciation as evident in Greenland ice cores. (a) GISP2 methane concentrations from Brook et al. (1996) (orange), (b) $\delta^{18}$O from GISP2 (Grootes & Stuiver, 1997) (dark blue) and GRIP (Johnsen et al., 1997) (light blue), and (c) $\delta$D-derived temperature from GISP2 (Alley, 2000).

The Pleistocene ends around 10kyr, when the current interglacial known as the Holocene was established. Climate during interglacials such as the Holocene appears more stable than Late Pleistocene glacial variability (Figure 2.8). Yet, climatic changes are evident (e.g. Marcott et al., 2013) with a slightly warmer than modern global mean temperature around the Holocene climate optimum followed by a 5kr long cooling trend culminating in the “Little Ice Age” (Marcott et al., 2013). Since

then, global mean temperatures are increasing in line with anthropogenic $CO_2$ release (e.g. Mann et al., 1999).

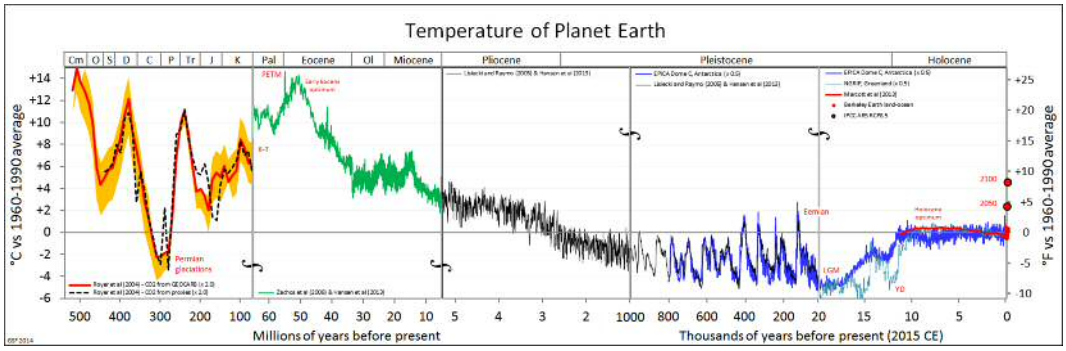


**Figure 2.8** Comparison of variability in global mean air temperature reconstructions over the last 500Ma plotted by G. Fergus using data from Royer et al. (2004) based on Veizer et al. (1999), Hansen et al. (2013) based on Zachos et al. (2008) and Lisiecki and Raymo (2005), Jouzel et al. (2007), NGRIP (2004), Marcott et al. (2013), Berkeley Earth project land ocean dataset (2014), and future scenarios from IPCC (2014).

## 2.3 $CO_2$ as a driver and feedback mechanism sustaining Late Pleistocene glacial-interglacial cycles

Throughout the late Pleistocene, atmospheric $CO_2$ varies between glacial 80-100ppm and interglacial 280-300ppm (Lüthi et al., 2008; Petit et al., 1999). It closely matches the development of ice volume and global mean temperature which all depict the characteristic sawtooth-shape cycles (Figure 2.5). This suggests tight coupling between ice volume, temperature and $pCO_2$, and underlines the non-linearity of the governing processes which control these three variables. Late Pleistocene glacials follow a saw-tooth shape with slow glaciation and abrupt terminations (Figure 2.5). A variety of mechanisms have been proposed to explain short-term termination $CO_2$ release. These are mostly linked to deglacial changes in ocean circulation and stratification exposing $CO_2$-rich isolated deep waters to the atmosphere (Anderson et al., 2009; Burke & Robinson, 2012; Skinner et al., 2010). Paleoclimate data suggests that the glacial ocean structure differed from the structure during the Holocene (Curry

& Oppo, 2005; McCave et al., 1995; Piotrowski et al., 2012; Spooner et al., 2018). In the glacial ocean, deep water circulation was shoaled (McCave et al., 1995) allowing heavy deep waters to fill the ocean abyss without engaging in overturning activity (Curry & Oppo, 2005). The shoaling is likely connected to Arctic sea ice extent and ocean surface reorganisations in the Arctic and Nordic Seas which led to reduced deep water convection and less dense northern-sourced deep waters (Thornalley et al., 2015). In contrast, extensive sea ice formation around Antarctica led to brine rejection and created particularly heavy water masses (Ferrari et al., 2014). As such, the glacial deep ocean filled up with southern-sourced waters (Curry & Oppo, 2005; Piotrowski et al., 2012) which became consecutively isolated due to circulation shoaling (Curry & Oppo, 2005), water stratification (Toggweiler, 1999) and polar sea ice (Ferrari et al., 2014; Stephens & Keeling, 2000) restricting deep water ventilation with the atmosphere.

Fast deglacial $CO_2$ release is possible by ventilating the glacial $CO_2$-rich deep water. Radiocarbon data from foraminifera show significant ageing of surface water masses during the termination (Burke & Robinson, 2012; Skinner et al., 2010). This can be interpreted as isolated deep water masses ventilating for the first time after significant periods of isolation (Burke & Robinson, 2012; Skinner et al., 2010). $CO_2$ concentration measurements from Antarctic ice cores show short-term $CO_2$ pulses which have been suggested to be linked to structural reorganisation in the Atlantic Ocean (Marcott et al., 2014). Conclusively, it is believed that deglacial $CO_2$ release occurs via break up of sea ice barriers, onset of deep ocean circulation, and re-ventilation of old $CO_2$-rich glacial deep waters around the Antarctic margin (Burke & Robinson, 2012; Skinner et al., 2010). Other areas have been proposed for additional deglacial $CO_2$ ventilation including the Arctic ocean (Thornalley et al., 2015) and the North Pacific (Rae et al., 2014).

The initiation of deglaciations is still under discussion. Palaeoclimate evidence is inconclusive whether initiation occurred via the northern or southern hemisphere.

According to Denton et al. (2010), initial changes in northern hemisphere insolation caused melting of NH ice sheets leading to large scale freshwater input into the North Atlantic (Hemming, 2004). This created a Heinrich event, during which the freshwater lens in the north supposedly inhibited the production of dense northern-sourced deep waters (Thornalley et al., 2010) and slowed ocean circulation and the northwards transport of warm surface currents (Barker et al., 2009). While the NH experienced cooling, the SH displayed significant warming (WAIS, 2015) due to the bipolar seesaw (Barker et al., 2009). This may have led to the abrupt breakdown of sea ice, and initial ventilation of $CO_2$ causing the onset of the termination (Anderson et al., 2009; Schmitt et al., 2012). Models are able to replicate this theory via north Atlantic hosing experiments (i.e. Liu et al., 2009). However, often unrealistic amounts of prescribed hosing are necessary to invoke a Heinrich event-like disturbance in ocean circulation. Others argue for a deglacial initiation from the SH (Knorr & Lohmann, 2003; WAIS, 2015). The WAIS Divide project members (2015) point out that Antarctic cold reversals begin before cold spells in the NH suggesting a SH driver. Subsequent modelling results show that SH warming can induce oceanic changes that are able to explain palaeoclimate data (Knorr & Lohmann, 2003; Zhang et al., 2017) and therefore provide evidence that deglaciations may be initiated via SH warming.

The mechanisms responsible for slow glacial uptake of $CO_2$ are less well understood. It has been widely suggested that glacial oceanic drawdown is linked to the establishment of glacial ocean circulation patterns (Adkins, 2013; Guihou et al., 2011) and sea ice-induced stratification (Stephens & Keeling, 2000), as well as shifts in the efficiency of the biological pump (Geider & La Roche, 2002; Martínez-García et al., 2014; Sigman et al., 2010). Evidence suggests that the glacial biological pump was strengthened, especially in the sub-Antarctic high nutrient low chlorophyll (HNLC) zone, due to fertilization from dust-blown iron (Fe) input (Lambert et al.,

2008; Martínez-García et al., 2014; Petit et al., 1999; Smetacek et al., 2012; Watson et al., 2000).

Glacial $CO_2$ uptake into the ocean interior appears gradual with two interspersed abrupt reduction events centred around 115kyr (-40ppm) and 70kyr (-35ppm) (Figure 2.9) (Hain et al., 2010). Cooling of ocean water causes an increase in carbonate dissolution leading to increased $CO_2$ uptake (Zeebe & Wolf-Gladrow, 2001). However, this effect is counteracted by increasing salinity (due to freeze out of water in ice sheets) and terrestrial organic carbon fluxes into the ocean (Hain et al., 2010; Zeebe & Wolf-Gladrow, 2001). These effects have therefore been previously assumed to cause a net-zero change in $pCO_2$ (Hain et al., 2010; Sigman & Boyle, 2000). According to box-model results by Hain et al. (2010), 36ppm can be explained by reduced upwelling due to sea ice extension and subsequent northwards shift of the intertropical convergence zone (ITCZ), and 40ppm due to changes in the biological pump. This leaves around 24ppm of a 100ppm decrease in $CO_2$ unexplained. Hain et al. (2010) assume that the biological pump is responsible in a yet unknown way. Indeed, the biological pump efficiency could be further increased through changes in the Redfield ratio (Geider & La Roche, 2002). However, so far biology seems to abide strictly by the ratio (Chester & Jickells, 2012). Others suggest that significant amounts of $CO_2$ may be drawn down due to changes in the oxygen content (Anderson et al., 2019) or changes in remineralisation depths (Wilson et al., 2019) and ballast sinking efficiency (Heinemann et al., 2019). Khatiwala et al. (2019) argue against the biological pump as the main drawdown mechanism after their model finds air-sea disequilibrium to have a significant effect on cooler sea temperatures and iron fertilisation in their model results. More work is needed to reconcile the different propositions and produce a new glacial $CO_2$ balance.

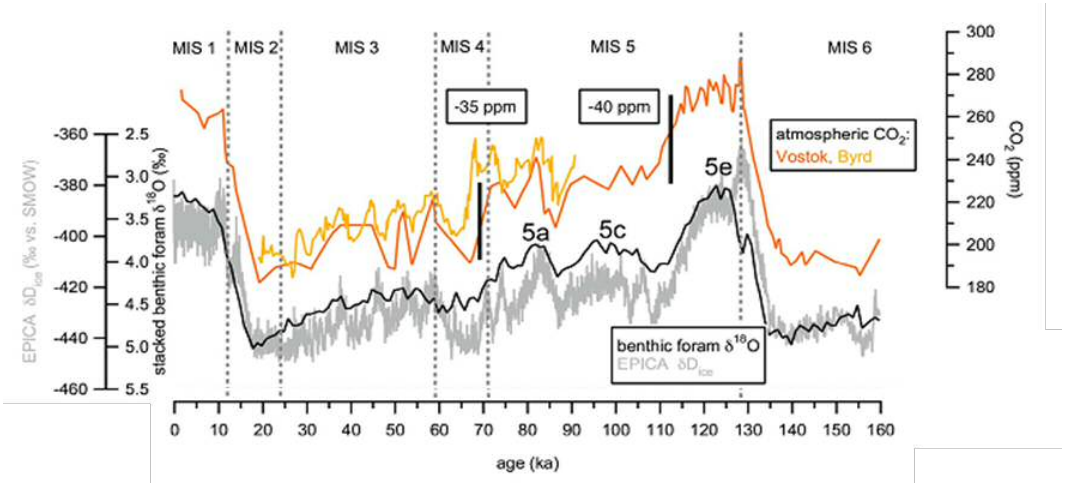


**Figure 2.9** $CO_2$ record during the last glacial cycle from the Vostok (orange) and Byrd (yellow) ice cores (Ahn & Brook, 2008; Petit et al., 1999). For comparison, global LR04 $\delta^{18}O$ stack (black) and the Antarctic EPICA ice core deuterium data (grey)(from Hain et al. (2010)).

## 2.4 The Mid-Pleistocene Transition (MPT)

The Mid-Pleistocene describes a period of multi-millennial scale climatic change during the Plio-Pleistocene (Figure 2.5). It is centred around a climatic shift around 1Ma ago. At that time, glacial-interglacial cycles expand their periodicity and amplitude without any significant changes in insolation (Figure 2.5). This was paralleled by a shift from virtually symmetrical to saw tooth-shaped cycles. Before the MPT, 40kyr periodicities in insolation are roughly reflected in the earth's climate (Lisiecki & Raymo, 2005). After the MPT, the periodicity of glacial-interglacial cycles increased to $\sim$100kyr which is also visible in eccentricity, but weak in insolation (Imbrie et al., 1993; Imbrie et al., 1992). This is known as the "100kyr problem". This has been reconciled by pointing out that the late Pleistocene 100kyr cycles are just "quasi-100kyr" which are made up of multiples of 40kyr (Huybers & Wunsch, 2005). Hence, the climate cycles are likely paced by obliquity-dominating insolation (Huybers & Wunsch, 2005), but strongly modulated through internal feedback mechanisms (Lisiecki, 2010; Paillard, 1998). Two questions remain. Why did the climate system switch from a strongly insolation driven state to a state where its glacial-interglacial cycles

are controlled by internal-feedback mechanisms and non-linearity? And how long did this switch take? Some suggest the MPT or Mid-Pleistocene revolution (MPR) as a long-term transition between 1.2Ma and 0.6Ma, starting as early as 2.5Myr according to spectral analyses in the LR04 benthic foraminiferal $\delta^{18}$O stack (Figures 2.4, 2.5) (Lisiecki & Raymo, 2007). Others propose a transition set between 1.1Ma and 0.85Ma during which long-term $CO_2$ estimates appear to decrease (Chalk et al., 2017; Hönisch et al., 2009) and glacial global ice volume increases (Paillard, 1998) (Figures 2.4, 2.5). Then again, some authors find short-term occurrences during specific glacial-interglacial cycles, such as the 900kyr event (Figure 2.5), which may have acted as a single climate trigger (Pena & Goldstein, 2014). Furthermore, it could be argued that climate triggers need triggers themselves suggesting that event-like changes are unlikely the sole cause of the MPT. In this thesis, I adopt the definition of transition and assume a transition starting point around 1.1Ma, and end point around 0.85Ma.

Explaining the processes that led to the MPT has proven to be a challenge. A complete hypothesis needs to include a proposition on the initial instigator of the MPT, and the following drivers and feedback mechanisms that pushed the MPT through. A variety of hypotheses have been proposed focusing mostly on the drivers and feedback mechanisms. Distinguishing the instigators of the MPT seems particularly difficult given the high cross-correlation characteristics of the climate system. Eight climate system parameters have been discussed as potential instigators and/or drivers. These include $pCO_2$ and nutrient dynamics (Chalk et al., 2017; Hönisch et al., 2009), ice volume changes (Bintanja & Van De Wal, 2008; Elderfield et al., 2012); sea surface and bottom temperature changes (McClymont et al., 2013; Sosdian & Rosenthal, 2009), ocean circulation collapse (Pena & Goldstein, 2014), ice sheet processes and/or interaction with basal regolith (Clark et al., 2006; Clark & Pollard, 1998), monsoonal shifts (Sun et al., 2019), closure of the Bering Straits

(Detlef et al., 2018; Kender et al., 2018), and climatic noise driven oscillators (Daruka & Ditlevsen, 2014; Mukhin et al., 2019; Rial et al., 2013).

### 2.4.1 The regolith hypothesis

The regolith hypothesis proposes that long-term Plio-Pleistocene waxing and waning of ice sheets led to the slow erosion of thick and soft lithogenic material, also referred to as regolith, at the base of NH ice sheets (Clark & Pollard, 1998). The hypothesis suggests that by the time of the MPT, nearly all regolith had been removed exposing harder crystalline rock (Clark & Pollard, 1998). This allowed the expansion of NH ice sheets, due to the reduction in basal friction and melt, and sustained them through periods of increasing insolation (Clark & Pollard, 1998). In combination with the albedo feedback, temperatures would have decreased leading to more extreme glacials and longer climate cycles (Clark et al., 2006; Clark & Pollard, 1998). Model results confirm the effect of regolith removal on ice sheets, but note that full 100kyr glacial cycles can only be reproduced with additional forcing from changing $pCO_2$ (Ganopolski & Calov, 2011; Willeit et al., 2019). Searching for geological evidence, Roy et al. (2004) collected lithogenic measurements from the Missouri delta. The mineral samples from late Pliocene to Pleistocene rock facies show that late Pliocene facies are depleted in crystalline rock lithologies and unstable minerals, while early and middle Pleistocene tills are enriched in the very same. In contrast, late Pleistocene tills include mostly major-element distributions similar of fresh shield bedrock. The authors suggest that this is in line with a removal of regolith over time and a strengthening of ice sheets due to exposure of crystalline rock at the base.

### 2.4.2 Ice sheet dynamics – driver of the MPT

Ice sheet dynamics have been proposed as sole driver of the MPT without the necessity of reduction in basal melt due to regolith removal (Bintanja & Van De Wal, 2008). Bintanja & van de Wal (2008) modelled the different effects of surface air temperature, ice volume and sea level on the LR04 foraminifera benthic $\delta^{18}$O stack. They show that northern hemisphere ice sheets began to sustain through insolation maxima and created oversized wet-based ice sheets which collapsed after reaching critical size and mass. The collapse occurred on a quasi-100kyr period causing the shift and change in cycle shape observed in the MPT. The increase in amplitude occurred via feedback mechanisms including albedo and temperature, and later ocean circulation during glacials. As such, the authors argue for a gradual change across multiple glacial cycles and an MPT transition rather than an event. Elderfield et al. (2012) reconstruct ice volume and bottom water temperature (BWT) components of benthic $\delta^{18}$O from the Chatham rise near New Zealand and confirm that ice volume has the stronger impact on benthic $\delta^{18}$O, but identify an abrupt shift after MIS 25 which appears as the first 100kyr cycle. The core location is known to record Antarctic lower circumpolar deep water which leads to the suggestion that the data records an increase in Antarctic ice volume at that time. As such, Elderfield et al. (2012) agree on ice volume as the driver of the MPT, but propose the MPT as an abrupt event.

### 2.4.3 Sea surface temperature and bottom water temperature changes as drivers for the MPT

Surface and bottom water temperatures have widely been discussed as the possible driver for the MPT (e.g. Sosdian and Rosenthal, 2009), and references therein). Sosdian & Rosenthal (2009) deconvolved the temperature and ice volume effect on benthic $\delta^{18}$O from a site in the north Atlantic. They find BWT decreasing between

MIS 30 and MIS 26, before the abrupt event at MIS23 reported by Elderfield et al. (2012). Spectral analysis shows that the 100kyr cyclicity seems to appear in temperature before sea level (Siddall et al., 2010). This leads to the proposition that long-term reduction in temperature, potentially due to $CO_2$ dynamics, cause a glacial pre-conditioning for larger growing ice sheets and allow ice sheet dynamics to cause the MPT-characteristic phase shifts in the climate cycles (Sosdian & Rosenthal, 2009). Surface ocean conditions support this hypothesis. Global sea surface temperatures (SST) present a long-term cooling trend starting around MIS35 paralleled by the emergence of the 100kyr cycle in the SST data (McClymont et al., 2013). The SST cooling is particularly evident during glacials, whereas interglacials experience low or no cooling (McClymont et al., 2013). This suggests a more gradual development of the MPT over several millennial cycles. Contrary, Medina-Elizalde & Lea (2005a) report the first obvious 100kyr cycle in SSTs from the western Pacific to occur abruptly after MIS25 arguing for a more event-like MPT.

### 2.4.4 Ocean circulation collapse as cause of the MPT

Neodymium (Nd) isotopes can be used as a proxy for ocean circulation (e.g. Piotrowski et al., 2012). Nd isotope data from the South Atlantic show a significant interglacial isotope excursion at MIS 23 after which the glacial Nd isotopes stay reduced throughout the late Pleistocene (Pena & Goldstein, 2014). The authors interpret their results as an interglacial ocean circulation collapse event at MIS23 which subsequently caused the first 100kyr cycle and the MPT. However, no proposition is made as to why ocean circulation may have collapsed around MIS23. So far, no Nd records exist showing the MIS23 ocean circulation collapse in other parts of the global ocean. Other circulation proxies give discordant results. Benthic carbon isotopes ($\delta^{13}$C) are often used as a non-conservative circulation proxy. $\delta^{13}$C profiles from the Atlantic Ocean show no change prior to MIS 17 (Poirier & Billups, 2014).

Sortable silt data from Chatham rise near New Zealand recording bottom current flow speeds show a significant step change later at MIS22 (Hall et al., 2001). This might suggest that ocean circulation was perturbed around 900kyr, but does not occur simultaneously on a global scale. Polar frontal movements and surface conditions have also been reconstructed from the South Atlantic and show contradicting results. Diekmann & Kuhn (2002) report a shift in the polar frontal movement cyclicity from around 1.2Ma until 0.65Ma to 130kyr. However, no significant change appeared around MIS23. Contrary, Kemp et al. (2010) track the polar front using multiple cores and show that it likely reached a most northern position at MIS22. Similarly, Schefuß et al. (2004) explain warming between MIS22 and MIS15 observed in the tropical Atlantic with a northwards shifted polar front. Robinson et al. (2019) present polar frontal movement reconstruction from the south Pacific and show that in the Pacific sector the polar front may have been in its most northern position since 1.2Ma or longer. They record a shift of the polar front southwards at MIS18. A northward shifted Antarctic polar front may be of significance to the MPT, because it expresses northward moved westerlies and therefore reduced upwelling around Antarctica (Kemp et al., 2010). This in turn will increase ocean stratification and the carbon storage potential in the deep ocean reducing atmospheric $CO_2$ concentrations (Toggweiler et al., 2006). Farmer et al. (2019) reconstructed productivity proxies and report an increase in the carbon storage potential of 50Gt between MIS25 and MIS22. According to the authors this occurs in line with the 20% reduction in ocean circulation evident in the Nd isotope data.

### 2.4.5 $CO_2$ and nutrient trends across the MPT

Long-term decline of atmospheric $CO_2$ has often been suggested as a key mechanism and potential driver of the MPT (e.g. Ganopolski and Calov, 2011; Lisiecki, 2010; Raymo, 1997; Willeit et al., 2019. Unfortunately, MPT $CO_2$ data are still sparse

allowing only limited understanding about the importance of $CO_2$ for the MPT. Hönisch et al. (2009) presented the first low resolution boron isotope-based $pCO_2$ reconstructions and suggest that $pCO_2$ decreased across the MPT. Later, Chalk et al. (2017) reconstructed $pCO_2$ from MIS33 to MIS36 and propose that glacial $CO_2$ levels decreased across the MPT due to dust fertilization. Indeed, dust fertilization increased exponentially during the MPT (Martínez-Garcia et al., 2011). Chalk et al. (2017) show a doubling of the sensitivity relationship between $CO_2$ and sea level when comparing the MIS33 – MIS36 record with the ice core period. They suggest that ice sheet dynamics either as a response to regolith removal or phase-locking instigated the MPT and led to the reduction of $CO_2$ during glacials via increased dust-fuelled productivity. Diester-Haass et al. (2018) reconstructed productivity from 7 sites across the Pacific and Atlantic Oceans and found potential evidence for increased productivity at the onset of the MPT (1.2Ma-1.0Ma), but state that these are heterogeneous and likely reflect regional patterns. The paper therefore argues against productivity as a major influence on the MPT carbon cycle.

### 2.4.6 The MPT as a response to oscillatory systems

By definition, the MPT describes the change in amplitude, periodicity and shape of oscillatory cycles. Therefore, drivers of the MPT can be determined using oscillatory models. Daruka & Ditlevsen (2014) produced an oscillator with two variables representing a temperature and ice volume-like climate. Their oscillator manages to reproduce an MPT-like phenomenon simply through shifts in phase-locking due to climatic noise. The shifts occur due to transcritical bifurcation systems that lead to a series of "canard oscillations" in the climate variables which may cause shifts in the periodicity and amplitude (Ashwin & Ditlevsen, 2015). Nyman & Ditlevsen (2019) suggest that this is the case when the internal period of a self-sustained oscillator interacts with the periodic component of a different oscillator, as is the

case with climate feedbacks and insolation. This led to the suggestion that the MPT might have no mechanistic instigator, but instead is a mere result of phase shifts and amplification through internal feedback mechanisms. This was also found by Quinn et al. (2018) who used a simple quaternary climate dynamics model and show that in absence of oscillatory astronomical forcing, earth's delayed feedback mechanisms lead to bi-stable behaviour. In this setting oscillations of ice volume coexist with a non-oscillatory equilibrium state (Quinn et al., 2018). When applying astronomical forcing with appropriate oscillations to the model, the forcing causes an eventual shift from small scale oscillations of 41kyr to large cycles with around 100kyr periodicity (Quinn et al., 2018). Mukhin et al. (2019) approached the question by applying a Bayesian data analysis system based on machine learning to the LR04 benthic foraminiferal $\delta^{18}$O stack to reveal potential statistical causes for the MPT. They accounted for internal climate dynamics, gradual trends, variations in insolation and millennial climate variability. The results suggest a strong phase locking between the distance to the next strong deglaciation and the meridional gradient of insolation. As such, the authors propose that the MPT as recorded in the benthic $\delta^{18}$O data was forced by intrinsic oscillatory characteristics which may well include stochastic behaviour. Using spectral analyses in connection with a numerical model, Rial et al. (2013) also find combined insolation-internal oscillation forcing to be the reason for the 100kyr climate cycles. In their model, the 100kyr cycles emerge at 1.2Ma as a result of phase-locking to the 413kyr eccentricity modulation. They hypothesise that the forced synchronisation occurred due to alignment between insolation changes and internal climate oscillations and the 413kyr eccentricity cycle (Rial et al., 2013).

### 2.4.7 The MPT in Asian monsoon systems

Palaeo-monsoon reconstruction has mostly focused on speleothems as ideal precipitation-recording archives (Cheng et al., 2016a; Wang et al., 2008). Unfortunately, like ice

cores, speleothems do not reach the age of the MPT (Cheng et al., 2016a). Therefore, little is known about the importance of monsoons for the MPT. However, some insights come from Chinese Loess which allows rough reconstruction of monsoonal strength using a variety of lithogenic proxies (Clemens et al., 2010; Heslop et al., 2002; Sun et al., 2019). Heslop et al. (2002) present magnetic susceptibility measurements from the Chinese loess plateau as a proxy for monsoon strength and find that monsoon strength weakened across the MPT while ice volume increased. They conclude that monsoon systems will likely not have played a role in the forcing or driving of the MPT. Contrary, Sun et al. (2019) present $\delta^{13}$C measurements from Chinese Loess carbonates as a proxy for monsoon-induced terrestrial vegetation changes. Their results indicate interesting phase shifts in the climatic system switching from a dominant 23kyr periodicity before 1.2Ma to combined 100-, 41-, 23kyr cycles after 0.7Ma. Modelling outputs indicate that the sensitivity of the monsoonal hydroclimate to insolation forcing may have changed as the northern hemisphere became increasingly glaciated (Sun et al., 2019). Additional proxy-model intercomparison analyses support this suggestion as temperature and precipitation responses seem different to astronomical forcing under varying ice/$CO_2$ boundary conditions (Sun et al., 2019). More research needs to be done to understand the monsoon systems and their 41kyr-world characteristics prior to the MPT.

# Chapter 3

# INTRODUCTION - ATMOSPHERIC $CO_2$ AND THE BORON ISOTOPE METHOD

## 3.1 The Marine Carbon Cycle – Mechanisms Controlling Atmospheric $CO_2$

On millennial timescales, the partial pressure of $CO_2$ ($pCO_2$) is controlled by ocean-atmosphere interactions (Takahashi et al., 2014). The deep ocean exhibits large storage capacities for carbon on the order of 38,000 peta-gram carbon (Pg C) (Denman et al., 2007). In comparison, the biosphere consists of about 500 Pg C, soils can hold up to 1,500 Pg C and the limit of the atmosphere lies at 750 Pg C (Denman et al., 2007). The largest carbon pool of 100,000,000 Pg C lies buried within the earth's crust as part of the lithosphere (Denman et al., 2007). Unlike carbon in the deep ocean, lithospheric carbon is tightly bound and only accessible through the weathering cycle. Conclusively, understanding the glacial-interglacial marine carbon cycle will advance the investigation of atmospheric $CO_2$ variability.

### 3.1.1 Inorganic carbon processes in the ocean

Carbon dissolves into the ocean at the air-sea interface, changing from atmospheric $CO_2$ into $CO_2$(*aqueous*) (Figure A.3.

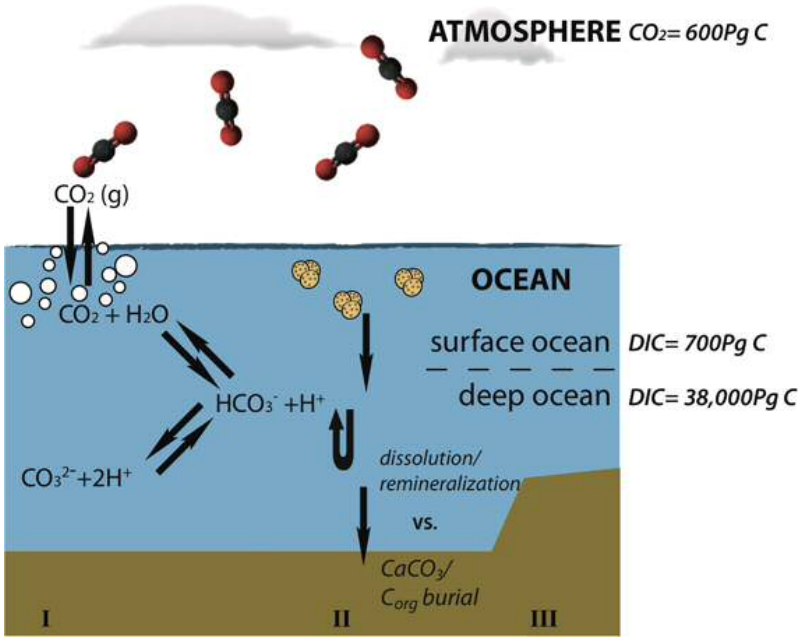


**Figure 3.1** Schematic of the marine carbon cycle (Kersten, 2012).

The dissolution of $CO_2$ occurs according to Henry's Law (EQN 3.1) with a theoretical equilibration time of roughly 12 days (Zeebe & Wolf-Gladrow, 2001).

$$[CO_2] = K_0(T,S) \times pCO_2 \tag{3.1}$$

Here, $CO_2$ represents the concentration and $pCO_2$ the partial pressure of $CO_2$ in the ocean. The solubility is expressed by the mainly temperature-dependent constant $K_0$(T,S) (Zeebe & Wolf-Gladrow, 2001) with higher solubility at lower temperature/salinity values.

Air-sea gas exchange between the ocean and the atmosphere is naturally moving towards equilibrium, meaning that the net $CO_2$ flux $\sim 0$. In the modern ocean, this is the case in large parts of the Indian Ocean, the western equatorial Pacific (WEP), and the south eastern equatorial Pacific (south EEP) (Takahashi et al., 2014)

(Figure 3.2). However, in some areas, such as the North Atlantic, North Pacific, Southern Ocean and below the EEP Inner tropical convergence zone (ITCZ) band, the natural equilibrium is inhibited (Takahashi et al., 2014). Here, surface water mixing processes between the upper 50-100m (surface mixed layer) and the underlying water masses interfere with setting up an equilibrium $CO_2$ flux. Examples of mixing processes are upwelling of deep water masses in upwelling areas (e.g. around the Southern Ocean), downwelling of surface water masses (e.g. in the ocean gyres), and wind stress-induced water mixing from Ekman forcing (e.g. under the ITCZ) (Figure 3.2). As a result, some areas become sinks, other areas become sources for atmospheric $CO_2$.

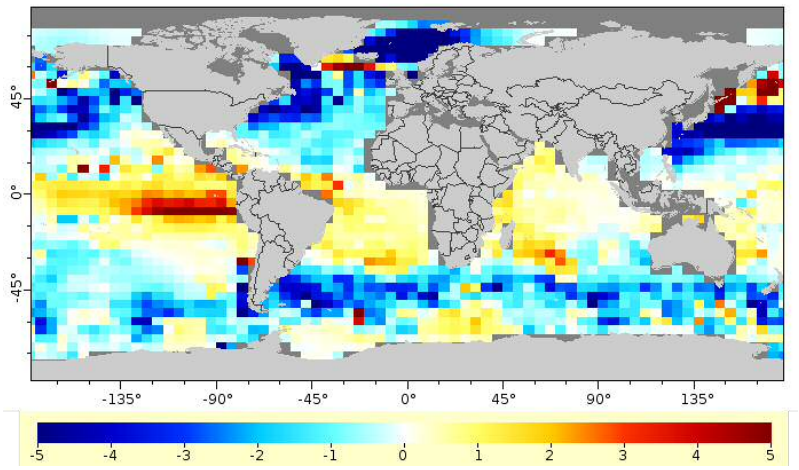


**Figure 3.2** Modern ocean $CO_2$ fluxes from Takahashi et al. (2014). Red shows areas with $CO_2$ release from the ocean, blue shows $CO_2$ uptake by the ocean.

After dissolution in seawater, $CO_2(aq.)$ forms carbonic acid ($H_2CO_3$). Some of it dissociates further creating bicarbonate ($HCO_3^-$) and carbonate ions ($CO_3^{2-}$) by releasing [$H^+$] (Figure 3.3).

The relative abundance of the three carbonate species in seawater is pH dependent. There are two pH values at which the concentration of two carbon species is equal. The values are known as the first and second equilibrium constants $pK_1^*$, and $pK_2^*$. When pH (seawater) = 5.68, [$CO_2$] = [$HCO_3^-$], respective to $pK_1^*$; and when pH(seawater) = 8.92, [$HCO_3^-$] = [$CO_3^{2-}$], respective to $pK_2^*$. The modern ocean

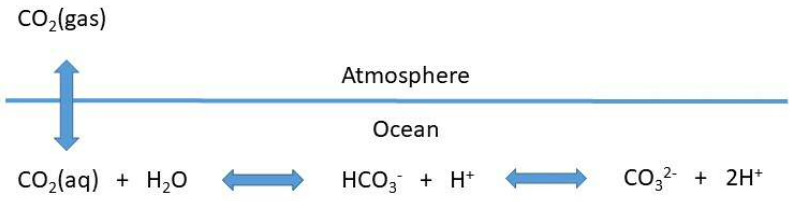


**Figure 3.3** Equilibration between the three soluble carbon species (after Zeebe and Wolf-Gladrow, 2001).

presents a pH of ∼8.1 (Zeebe & Wolf-Gladrow, 2001) which indicates that [$HCO_3^-$] is the most abundant species (Figure 3.4).

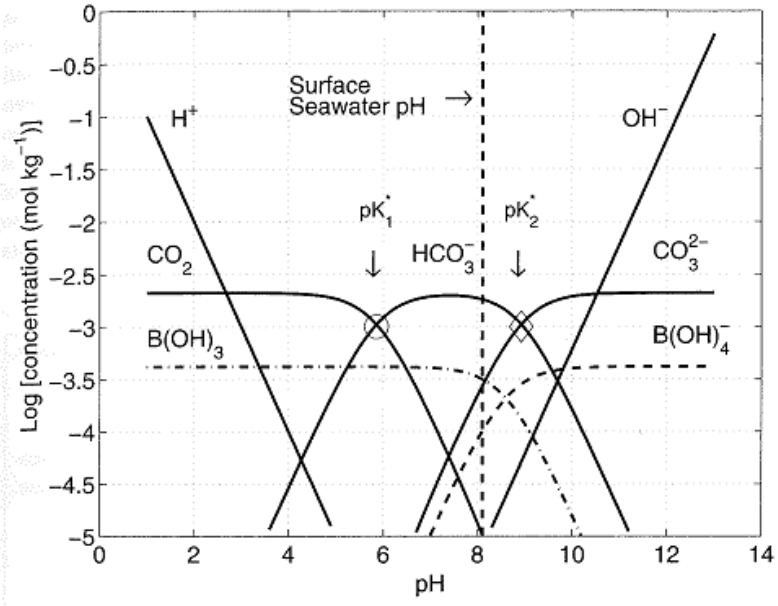


**Figure 3.4** Bjerrum plot for carbon and boron species in sea water (Zeebe & Wolf-Gladrow, 2001).

By adding up the concentrations of all three marine carbonate species, the total inorganic carbon content (DIC) can be calculated (EQN 3.2; Zeebe and Wolf-Gladrow, 2001). Likewise, using DIC in combination with $pK_1^*$, $pK_2^*$ and seawater pH determines the concentration of either marine carbon species (EQNs 3.2, 3.3, 3.4, and 3.5; Zeebe and Wolf-Gladrow, 2001).

$$DIC = \sum[CO_2] = CO_2 + [HCO_3^-] + [CO_3^{2-}] \tag{3.2}$$

$$[CO_2] = DIC/(1 + \frac{K_1^*}{[H^+]} + \frac{K_1^* K_2^*}{[H^+]}) \tag{3.3}$$

$$[HCO_3{}^-] = DIC/(1 + \frac{[H^+]}{K_1^*} + \frac{K_2^*}{[H^+]}) \tag{3.4}$$

$$[CO_3{}^{2-}] = DIC/(1 + \frac{[H^+]}{K_2^*} + \frac{[H^+]^2}{K_1^* K_2^*}) \tag{3.5}$$

The pH-dependency of inorganic carbon species in the ocean is of great importance as it provides a natural buffer system for the chemical state of the ocean (Figure 3.5). The carbonic ions serve as a buffer base neutralizing any protons added to the global oceans. As such, large amounts of acid are needed to shift the ocean pH to lower values. However, once the neutralizing base/buffer capacity is used up, meaning most of marine carbonate exists as $CO_2(aq.)$, only little acid is needed for significant pH decline. The modern anthropogenic addition of $CO_2$ to the earth's atmosphere causes a net flux of $CO_2$ into the global ocean as the system moves towards a new equilibrium state. Orr et al. (2005) note that the incoming oceanic $CO_2$ flux is comparable to an input of acid into the marine carbonate system. As a result, the marine carbonate buffer weakens and may eventually collapse leading to accelerated acidification of the global ocean.

There are several ways of quantifying the buffer capacity of the oceans. The most common one is known as alkalinity. Several definitions exist on how to calculate alkalinity (ALK) (see Zeebe and Wolf-Gladrow, 2001). Throughout this thesis, ALK is defined as the ionic state of the ocean summing up all conservative ions present in seawater proportional to their charges. At pH = 8.1, the prevalent conservative ions are effectively carbon and boron ions. Thus, alkalinity can be approximated using the following equation from Zeebe & Wolf-Gladrow (2001):

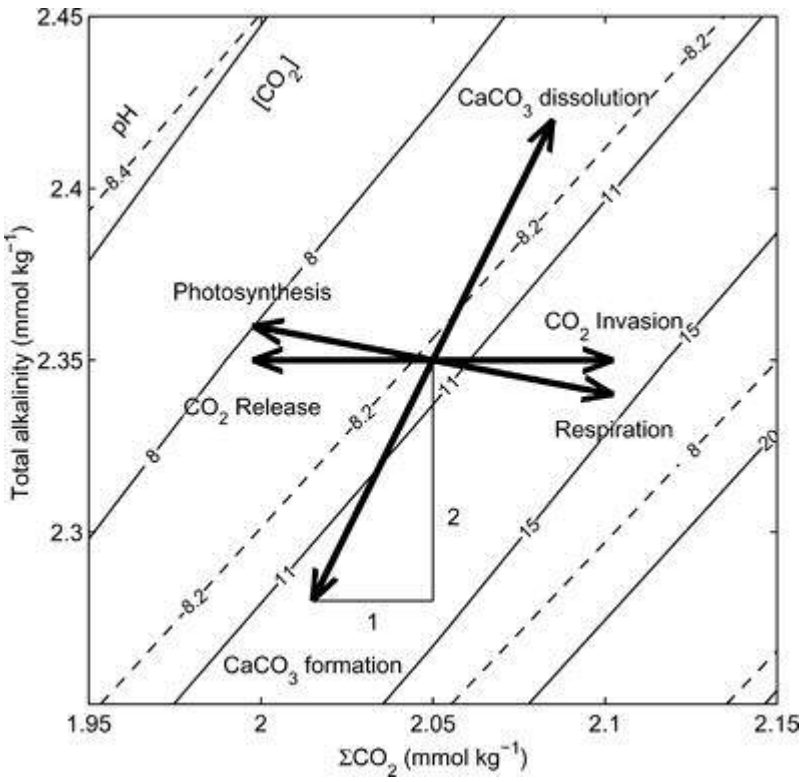


**Figure 3.5** Effects on DIC and ALK after various perturbations (Zeebe & Wolf-Gladrow, 2001).

$$ALK \approx [HCO_3^-] + 2[CO_3^{2-}] + [B(OH)_4^-] + [OH^-] - [H^+] \tag{3.6}$$

Both DIC and ALK are conservative quantities implying that they do not vary with temperature or pressure/depth.

### 3.1.2 Organic carbon processes in the ocean

The marine environment is a highly productive and species-rich environment. The annual marine carbon overturn is globally significant and comparable to that of the terrestrial biosphere (Longhurst, 1995). Highest organic carbon concentrations are found in the surface mixed layer and the upper thermocline (euphotic zone) where light availability fuels autotrophic photosynthetic phytoplankton production (Sigman & Hain, 2012) (Figure 3.6). Dead biomass is effectively remineralized and excreted

by several tropic layers throughout the water column. Repeated digestion leads to material clumping and the formation of organic pellets. Increased density and higher resistance to remineralisation cause the pellets (also known as marine snow) to sink to the ocean floor. There, they provide a source of food for a variety of benthic organisms. In the end, less than 1% of the initial organic material gets buried in oceanic sediments (Sigman & Hain, 2012).

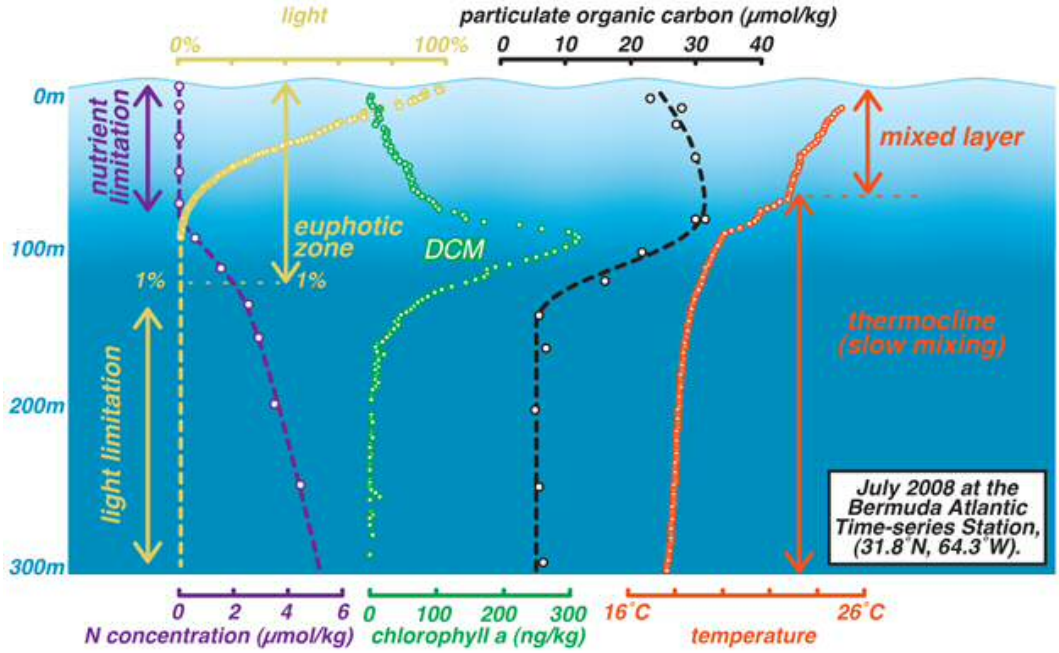


**Figure 3.6** Marine carbonate system in the modern ocean (Sigman & Hain, 2012).

In large parts of the modern global ocean, marine productivity is limited by the amount of nutrients available in the euphotic zone. Major nutrients include carbon (C), nitrogen (N) and phosphorus (P). It appears that plankton build up body mass according to a strict nutrient ratio of C:N:P – 106:16:1 known as the Redfield ratio (Redfield, 1934). As such, P is often considered the limiting nutrient. In some areas known as high-nutrient-low-chlorophyll (HNLC) belts, major nutrients are not used up to their full extent (Figure 3.7). Here, minor nutrients such as iron (Fe) or silicon (Si) limit biomass production. Today, we see this phenomenon in the Sub Antarctic Zone (SAZ), where a lack of Fe inhibits the efficient use of P, N, and C (Watson et al.,

2000). As a result, unused major nutrients (preformed nutrients) are exported from the Southern Ocean by deep water currents, which is equivalent to a "missed chance" of turning major nutrients into digestible carbon biomass (regenerated nutrients) (Sigman et al., 2010). In contrast, high nutrient usage and a low preformed vs. regenerated nutrient ratio is found in upwelling areas where nutrient rich deep waters reach the eutrophic zone.

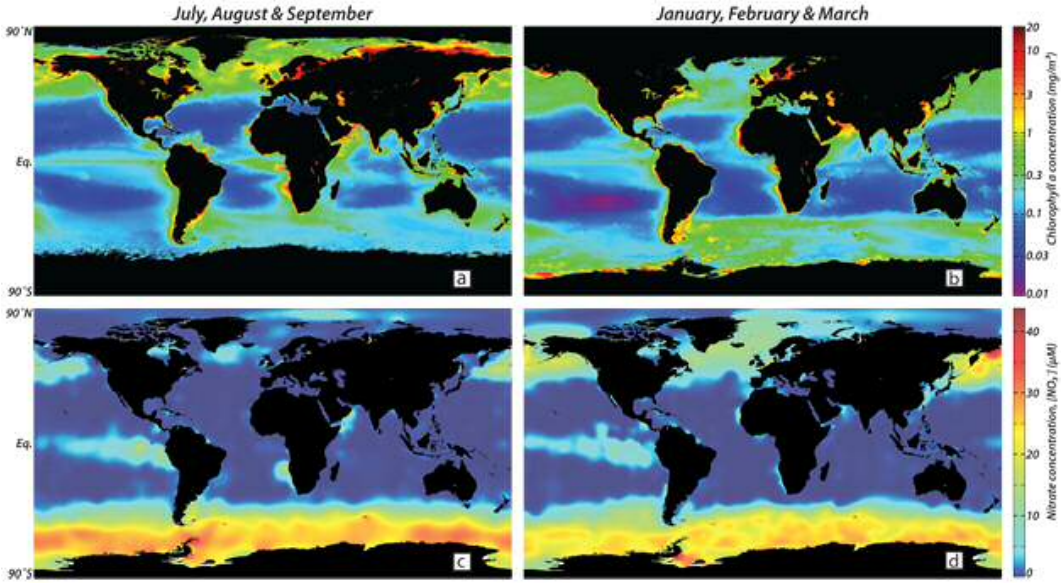


**Figure 3.7** Nitrate and chlorophyll a concentrations in the modern surface ocean (Sigman & Hain, 2012). Note high nitrate concentrations in the subantarctic zone suggesting inefficient nutrient recycling in this area.

The transport of organic carbon from the upper to the deep ocean has been referred to as the biological pump. This process has been proposed as one possible mechanism for storing $CO_2$ (initially from the atmosphere) in the deep ocean and reducing atmospheric $CO_2$ over glacial-interglacial timescales.

Organic carbon exists in two forms, either as soft-tissue (soft-tissue pump), or as calcium carbonate ($CaCO_3$) shells (carbon pump). Note that some authors use the term biological pump as a synonym for the soft-tissue pump (e.g. Sigman et al., 2010). However, here it will serve as an umbrella term for both pumps.

Only the soft-tissue pump may effectively transfer carbon from the top to the deep ocean and thus, contribute to the decrease in atmospheric $CO_2$. When soft-tissue is created from autotrophic photosynthetic organisms, $CO_2$ (*aq.*) is taken up in the surface mixed layer. After death, the body sinks to the deep ocean transferring the $CO_2$ out of the mixed layer into the deep. As a result, the equilibrium between $CO_2(aq.)$ and the carbonate ions shifts seawater pH in the upper ocean to a more basic value. This allows new atmospheric $CO_2$ to be drawn in. In contrast, the production of $CaCO_3$ removes not only $CO_2$, but also $Ca^{2+}$.

$$Ca^{2+} + CO_2(aq.) + H_2O \longleftrightarrow CaCO_3 + 2H^+ \tag{3.7}$$

The removal of $Ca^{2+}$ has significant implications for ALK and reduces it by 2 for 1 unit of carbon buried (Figure 3.5). As a result, the upper ocean carbon system shifts towards a more acidic and $CO_2(aq.)$-rich system promoting the release of 1unit carbon. In the end, one unit of carbon is buried, while one is released which results in no net-burial of $CO_2$.

### 3.1.3 Boron isotopes in planktonic foraminifera as proxy for palaeo-$pCO_2$

Natural boron forms two stable isotopes $^{10}B$ and $^{11}B$ accounting for approximately 19.82% and 80.18% of the total natural boron present. In the ocean, boron exists as planar trigonal boric acid ($B(OH)_3$), and as negatively charged tetrahedral borate ion ($B(OH)_4^-$) (Zeebe & Wolf-Gladrow, 2001), with the total boron concentration $B_T$ defined as the sum of the two.

$$B(OH)_3 = H_2O \leftrightarrows B(OH)_4^- + H^+ \tag{3.8}$$

$$B_T = B(OH)_3 + B(OH)_4^- \tag{3.9}$$

Isotopic fractionation occurs between $B(OH)_3$ and $B(OH)_4^-$, with $B(OH)_3$ enriching in $^{11}B$, and $B(OH)_4^-$ in $^{10}B$. The isotopic fractionation can be described with the fractionation factor $\varepsilon$

$$\varepsilon = 1000 \times (\alpha_b - 1) \tag{3.10}$$

where $\alpha_b$ is the equilibrium constant of the fractionation.

Boron isotopic measurements are conducted to a reference standard resulting in the final isotopic ratio of $^{11}B/^{10}B$ being expressed as delta-notation.

$$\delta^{11}B = (\frac{^{11}B/^{10}B_{sample}}{^{11}B/^{10}B_{standard}}) \times 1000 \tag{3.11}$$

In seawater, the prevalent chemical state of boron is determined by pH. The relative concentrations of $B(OH)_3$ and $B(OH)_4^-$ are defined by the dissociation constant $pK_B^*$, which equals 8.60 at 25°C temperature, and 35psu salinity. Boron isotopic fractionation is therefore linked to seawater pH (Figure 3.8).

It has been shown that trace amounts of boron are taken up by calcifying marine organisms as $B(OH)_4^-$ (Rae, 2018). As such, marine biogenic carbonates are specifically light ($14‰ < \delta^{11}B_{carbonates} < 23‰$) compared to the surrounding seawater $\delta^{11}B_{seawater}$ = 39.61‰, (Foster et al., 2010), with a fractionation factor that is correlated to seawater pH (Rae, 2018). Boron isotopes in marine biogenic carbonates can therefore be used as a proxy for seawater pH. This property is widely applied in palaeoclimate research, where boron isotopes in planktonic foraminiferal tests allow the reconstruction of past atmospheric $CO_2$ concentrations, using the $\delta^{11}B$ proxy in addition to one other marine carbonate system parameter, often an estimate of alkalinity.

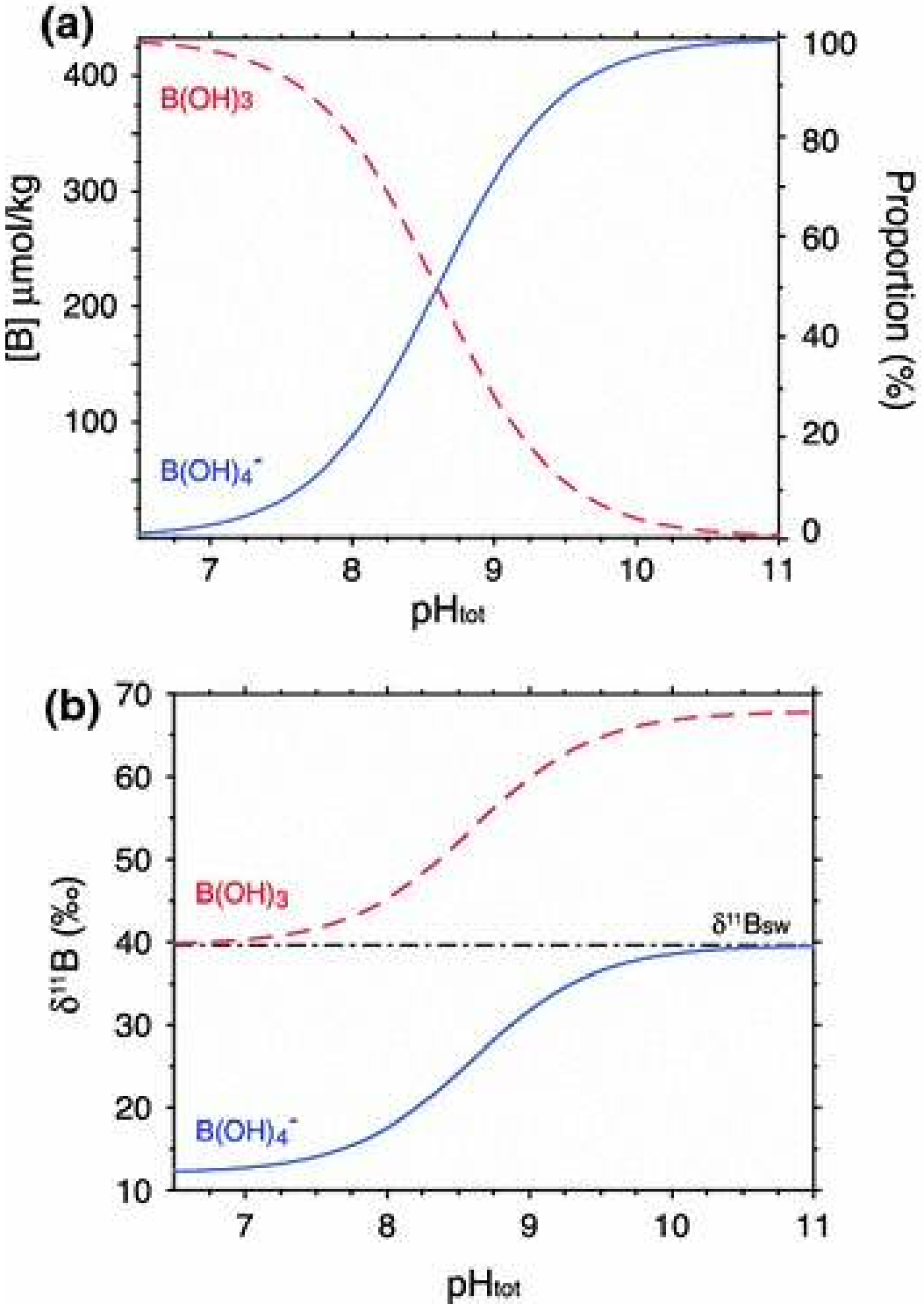


**Figure 3.8** Boron isotope chemistry in seawater (from Rae, 2018). (a) Total boron concentration (left axis) as a function of seawater pH for $B(OH)_3$ and $B(OH)_4^-$. The proportion of total boron of either boron species is shown on the right axis. (b) Boron isotopic value ($\delta^{11}B$) of $B(OH)_3$ and $B(OH)_4^-$ as a function of seawater pH.

$$pH = pK_B - log(\frac{-(\delta^{11}B_{sw} - \delta^{11}B_{foraminifera})}{\delta^{11}B_{sw} - \alpha_b \times \delta^{11}B_{foraminifera} - \varepsilon}) \tag{3.12}$$

where $pK_B$ is the dissociation constant of boric acid at in situ temperature, pressure, salinity (per Dickson, 1990), $\delta^{11}B_{sw}$ and $\delta^{11}B_{foraminifera}$ are the isotopic signatures of seawater and the foraminiferal sample, respectively, $\alpha_b$ is the equilibrium constant, and $\varepsilon$ is the fractionation factor. The two parameters can then be used to calculate palaeo-$pCO_2$. A more accurate calculation has recently been proposed by Rae (2018)

$$pH = -log\frac{K_B \times {}^{\frac{11}{10}}R_{B(OH)_4^-} - K_B \times {}^{\frac{11}{10}}R_{SW} + \alpha_b \times K_B \times {}^{\frac{11}{10}}R^2_{B(OH)_4^-} - \frac{\alpha_b \times K_B \times {}^{\frac{11}{10}}R_{SW} \times {}^{\frac{11}{10}}R_{B(OH)_4^-}}{\alpha_b \times {}^{\frac{11}{10}}R_{B(OH)_4^-} - \alpha_b \times {}^{\frac{11}{10}}R_{B(OH)_4^-}}}{{}^{\frac{11}{10}}R_{SW} + {}^{\frac{11}{10}}R_{SW} \times {}^{\frac{11}{10}}R_{B(OH)_4^-} -} \tag{3.13}$$

where $K_B$ is the equilibrium constant of the reaction ($K_B \sim 10^{-8.6}$ according to Rae 2018), ${}^{\frac{11}{10}}R$ stands for the ratio between $^{11}B$ and $^{10}B$ of either $B(OH)_4^-$ or seawater (sw), and $\alpha_b$ is the equilibrium fractionation of 27.2‰ (Klochko et al., 2006).

It has been shown that the fractionation of $\delta^{11}B$ in planktonic foraminifera deviates from the fractionation observed during inorganic carbonate precipitation by ±2-3‰, and between different planktonic foraminifera species up to 4‰ (**Henhanetal_2013**; Hönisch et al., 2003; Sanyal et al., 1996)This suggests that $\delta^{11}B_{calcite} \neq \delta^{11}B_{borate}$ in planktonic foraminifera, and species specific calibrations are necessary. Hönisch et al. (2003) show that the offset between different special boron fractionation factors occur due to species-specific biological processes, also known as vital effects. These processes, including the cultivation of photosynthetic symbionts or the production of gametogenic calcite during the reproductive cycle, can influence

the micro-environment pH, and therefore alter the species-specific boron isotope fractionation (Hönisch et al., 2003). Calibrations defining the boron isotopic offset from that measured in inorganic calcite are mostly determined through culturing and comparison with core-top values (e.g. Henehan et al., 2016). At the time of this thesis, calibrations exist for five planktonic foraminifera species including Globigerinoides ruber, Trilobatus sacculifer (formerly known as Globigerinoides sacculifer; see Spezzaferri et al. (2015)), Orbulina universa, Globigerina bulloides, and Neogloboquadrina pachyderma (Henehan et al., 2016) (Figure 3.9).

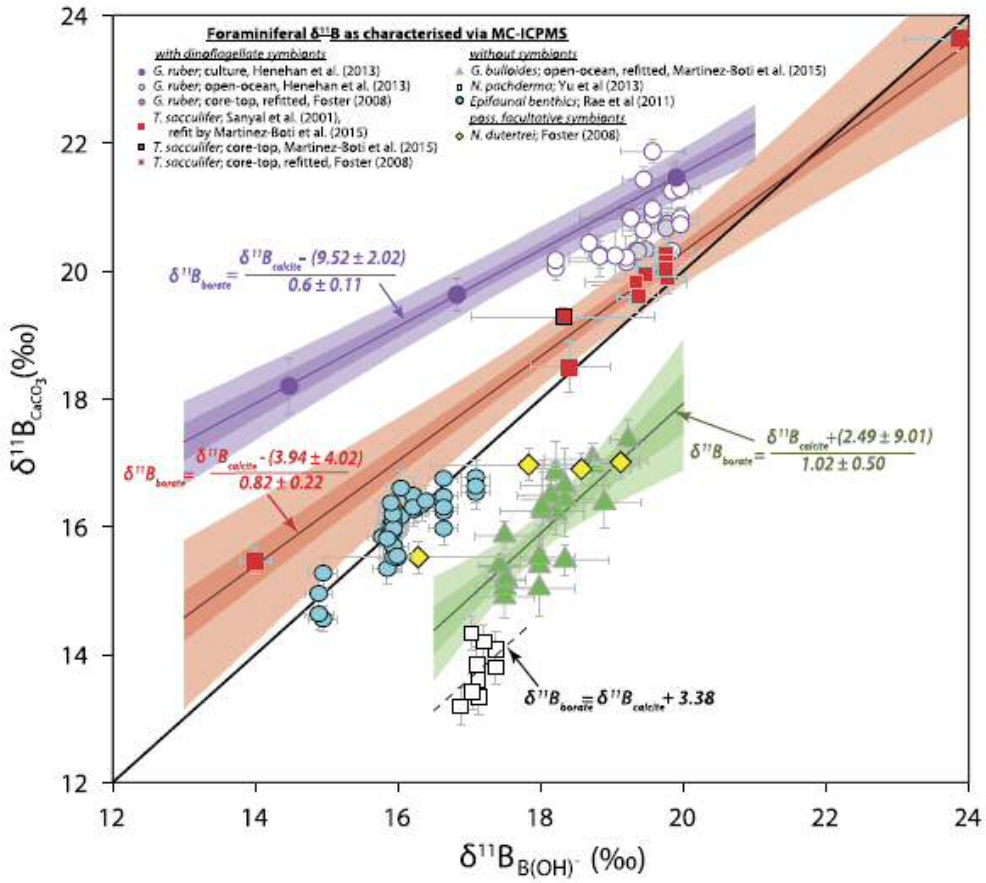


**Figure 3.9** Existing planktonic foraminiferal boron isotope calibrations from a mixture of core-top and culture data. Figure from Henehan et al. (2016)

### 3.1.4 Plio- pleistocene boron isotope records

Atmospheric $CO_2$ concentrations are well known across the last 800,000 years thanks to ice core archives. However, beyond that estimates of earlier $CO_2$ concentrations used to be sparse. This was mostly due to the lack of reliable $CO_2$ proxies from older climate archives. Over the last decades, two proxies have been developed that allow the reconstruction of $CO_2$ using foraminiferal calcite from ocean sediment cores. Foraminifera are calcifying heterotrophic single-celled organisms that live ubiquitously in the ocean. Their existence goes back millions of years and their calcified shells accumulate on the ocean floor. The local climate influences the chemical composition of their shell during shell calcification. As such, they can be used to reconstruct past climates over millions of years (for more information see chapter Materials & Methods 5). The boron isotope (Foster, 2008; Hemming & Hanson, 1994; Hönisch et al., 2009) and alkenone (Pagani et al., 2005) proxies enabled the reconstruction of $pCO_2$ beyond the ice core record (Figure 3.10). So far, the record is still patchy, and much work needs to be done to create a high resolution long-term $pCO_2$ record.

The Plio-Pleistocene is characterised by climate oscillations with warm interglacial and cold glacial endmembers (Lisiecki & Raymo, 2005). $CO_2$ correlates closely with these cycles suggesting it plays a significant role in shaping the oscillations (Bereiter et al., 2015; Chalk et al., 2017; Hönisch et al., 2009; Martínez-Botí et al., 2015; Tierney et al., 2019). $CO_2$ reconstructions from both proxies show close to modern interglacial values around 400ppm and glacial values around 250ppm (Figure 3.10) (Martínez-Botí et al., 2015; Zhang et al., 2013). Given that the interglacial $pCO_2$ values are similar to today, this period is of particular interest to study natural $CO_2$ processes and climatic links. During the early and middle Pleistocene (2.58Ma – 1.1Ma), $CO_2$ reconstructions are still sparse (Figure 3.10). Low resolution measurements suggest $CO_2$ levels around 280ppm during interglacials

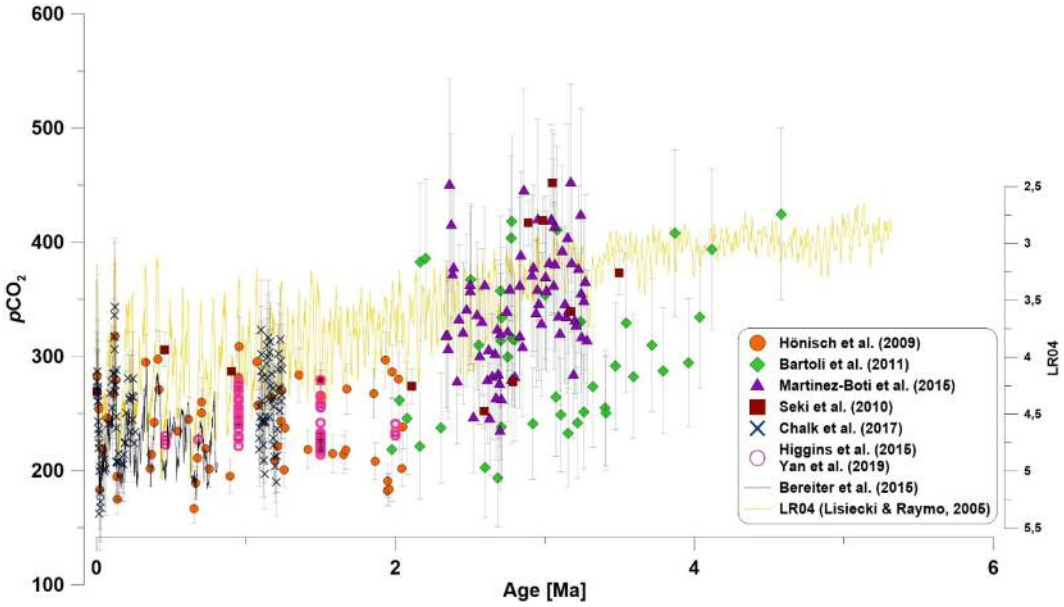


**Figure 3.10** Available assembled atmospheric $CO_2$ reconstructions from boron isotopes for the Plio-Pleistocene. For comparison, LR04 benthic $\delta^{18}O$ stack in yellow, continuous ice core $pCO_2$ in black, and discontinuous Allan Hills blue ice in pink.

and 200ppm during glacials (Hönisch et al., 2009). High resolution results across two glacial-interglacial cycles suggest similar glacial, but slightly higher interglacial $pCO_2$ levels at 320ppm (Chalk et al., 2017). No reconstructions, apart from highly variable sporadic blue ice measurements (Higgins et al., 2015), exist between 1.1Ma and the onset of the ice core record at 800,000 years.

# Chapter 4

# INTRODUCTION - THE AGULHAS SYSTEM

## 4.1 The Agulhas System and its hydrography

The Agulhas System describes the current system along the eastern margin of the African continent in the western Indian Ocean. Upstream, it connects to the Mozambique Channel system, and downstream it ends in the Agulhas Leakage and current retroflection. The Agulhas Leakage represents an important aspects of global ocean circulation and plays a key role in the modulation of global climate (Beal et al., 2011; Biastoch et al., 2009; Lutjeharms, 2006). It describes the eddying of warm and salty waters from the Indian Ocean into the South Atlantic at the cape of Good Hope (Beal et al., 2011) (Figure 4.1). The eddies are shed off during the retroflection process of the Agulhas current. As the Agulhas current flows westward around the tip of Africa, it meets the eastward flowing Antarctic circumpolar current and is forced to turn by 180° (Figure 4.1). Most of the current waters retroflect flowing back into the southern Indian Ocean. Only small amounts are shed off as the leakage. Importantly, the salt content in the eddies is significantly higher than that

of the surrounding South Atlantic making the Agulhas Leakage an important salt supply for the Atlantic meridional overturning circulation (AMOC).

Further upstream, the Agulhas current travels along the eastern African continent as a western boundary current. Durgadoo et al. (2017) define four main source waters for the Agulhas system. These include Indonesian throughflow (ITF) waters (62%), Tasman leakage waters (28%), Arabian Peninsula waters (10%), and retroflected Agulhas current waters recirculated via the southwest Indian Ocean subgyre (see also Simon et al., 2013; Simon et al., 2015). Northern sources, such as the ITF and Arabian water masses, arrive at the Agulhas system via the Mozambique Channel. Southern sources, i.e. Tasman leakage and recirculating Indian Ocean gyre waters, cross the Indian Ocean directly and entrain south of Madagascar (Durgadoo et al., 2017; Lutjeharms, 2006; Sætre & Da Silva, 1982). In the modern, ITF outflow waters provide the largest volume flow. After entering the Indian Ocean, they form the South Equatorial Current (SEC) travelling westward along 10°S. At the Madagascan margin, the SEC flow is interrupted forcing it to split into a northern and southern limb. The northern limb enters the Agulhas system via the Mozambique Channel, while the southern limb feeds straight into the Agulhas current south of Madagascar. The two limbs entrain different proportions of ITF, Arabian Peninsula and Tasman leakage waters which cross the Indian Ocean westwards, southwards and northwestwards, respectively. Despite high evaporation rates, their hydrographic signature can be traced across the Indian Ocean into the northern Mozambique Channel (Backeberg et al., 2012; Le Bars et al., 2013; Rodgers et al., 2000; Talley, 2005).

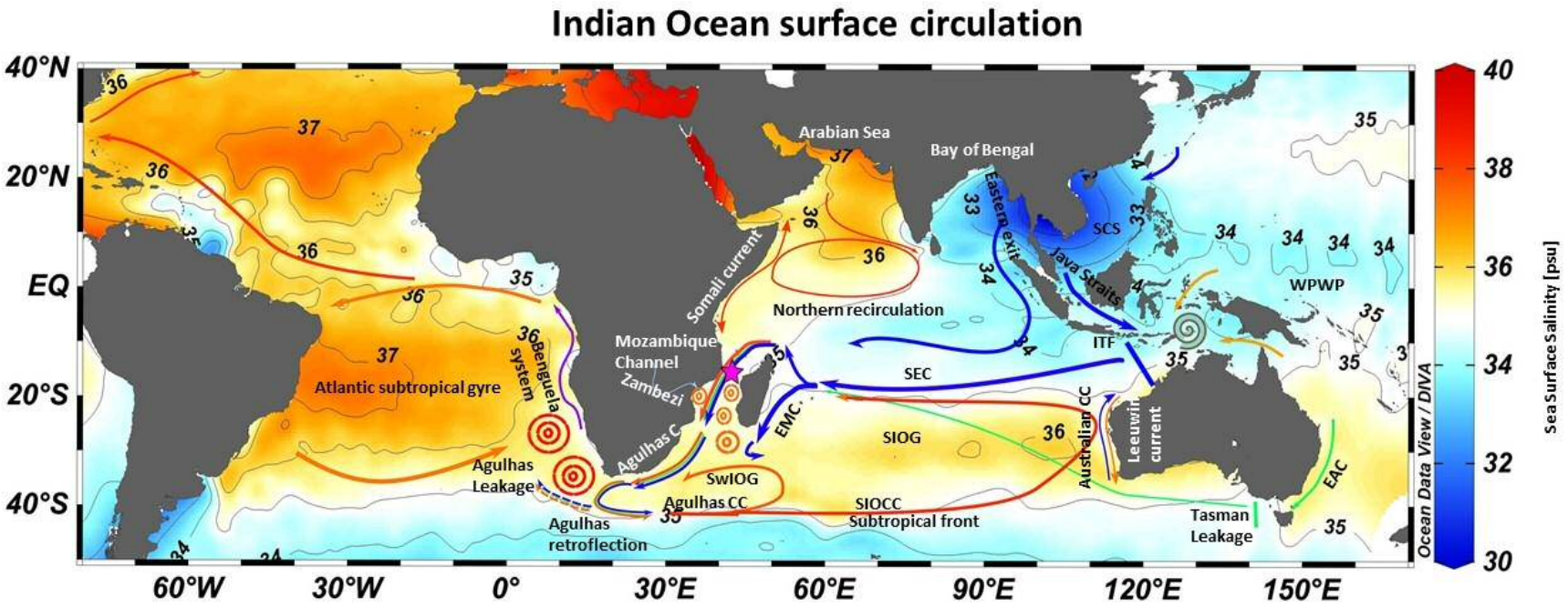


**Figure 4.1** Indian Ocean surface circulation indicated as arrows ontop of modern sea surface salinity from GLODAP V2 which was interpolated using DIVA in ocean data viewer (ODV). Orange/blue arrows indicate saltier/fresher surface waters. Green arrows show a small contribution from the Tasman Leakage. High eddy activity is identifyable by spiral symbols. Impotant currents and geographical features are labelled in black and white writing.

## 4.2 Implications for global climate and the Mid-Pleistocene Transition

The process of leaking salt into the South Atlantic via the Agulhas Leakage has been shown to significantly impact global climate on short- (Beal et al., 2011; Biastoch et al., 2009; Biastoch et al., 2015) and long-term timescales (Bard & Rickaby, 2009; Beal et al., 2011; Peeters et al., 2004). The high salinity surface eddies interact with the Benguela upwelling system and eventually mix in with northwards flowing Atlantic surface currents (Garzoli et al., 1997; Garzoli et al., 1996). Eventually, Atlantic surface currents reach deep water formation sites in the Nordic Seas where greater salt content leads to heavier density potentials in surface waters and deeper sinking. This has the potential of creating a deeper and more vigorous overturning circulation. Changes in the vigor and overturning depth of global ocean circulation have widely been discussed as one of the primary climate shaping mechanisms (e.g. Broecker, 1991; see also chapters 2.2, 2.3). As such, the Agulhas Leakage could play a vital role in the evolution of glacial-interglacial ocean circulation changes. Understanding the mechanisms that control the Agulhas Leakage is therefore key to understanding glacial-interglacial climate variability.

The Mid-Pleistocene transition (MPT) is known as the most recent step change in orbital scale climate dynamics (see chapter 2.4). Quaternary glacial-interglacial climate cycles lengthened their periodicity from 41kyr to quasi-100kyr, and switch from virtually symmetrical to distinctly saw-tooth shaped cycles with greater amplitude post-MPT. The transition occurs without any notable change in the orbital parameters. This necessitates a change to Earth's internal feedback mechanisms which may respond to a long-term decrease in atmospheric $pCO_2$ (Chalk et al., 2017; van de Wal et al., 2011). The onset, duration and completion of the MPT are still subject to discussion (see chapter 2.4 for discussion and references). However, it

is generally accepted that the climate system reorganisation occurred somewhere between 1.2 million years (Ma) and 0.6Ma (see chapter 2.4). The increase in amplitude appears to be mostly driven via intensification of glacials in parallel with further reduction in atmospheric $pCO_2$ (e.g. Chalk et al., 2017). The uptake and release of carbon on multi-millennial timescales is closely linked to global overturning depth and vigor (see chapter 2.3 for discussion and references). Ocean circulation has been suggested previously as a significant contributor to the MPT (Pena & Goldstein, 2014). Therefore, multi-millennial changes in the efficiency of the Agulhas salt leakage may reflect a key aspect of potential changes in the global thermohaline circulation across the MPT.

## 4.3 Possible controls on the modern Agulhas Leakage efficiency

The mechanisms by which the Agulhas Leakage is controlled in the modern are still discussed. On multi-annual to decadal timescales, the Agulhas Leakage may be driven by i) changes in the Agulhas current transport (Loveday et al., 2014; Rouault et al., 2009; Van Sebille et al., 2009b), ii) changes in the location of the retroflection (Loveday et al., 2014), and iii) changes in the westerly wind strength (Biastoch et al., 2015; Durgadoo et al., 2013).

Rouault et al. (2009) report that an increase in the Agulhas current transport will increase the Agulhas Leakage due to larger volume flow. In contrast, Van Sebille et al. (2009b) show a decrease of the leakage with increasing current transport as a result of a stronger and further eastward located retroflection. Biastoch et al. (2009) propose the westerly wind system as a main driver of the Agulhas Leakage stating that a southward shift of the westerlies will increase leakage due to a shift in the location of the retroflection further south of the African continent.

This would allow higher volume transport to flow through the gap between the STF and the African continent which strengthens the leakage. Durgadoo et al. (2013) reconcile the different findings by using a high-resolution eddy model nested within a global general circulation model. Their study confirms that changes in the strength of the westerlies exert the most control on the Agulhas Leakage, either via intensification, or meridional change. Contrary to the initial suggestion in Biastoch et al. (2009), the Agulhas Leakage weakens with a southward shift of the westerly wind belt. A southward movement of the westerlies will reduce the wind stress curl and equatorward transport of the interior water masses, leading to a diminished Sverdrup transport and therefore weaker westward transport of water masses south of Africa (Durgadoo et al., 2013). Loveday et al. (2014) comments that Agulhas Leakage modelling is highly dependable on the resolution modelled. Using the same nested model as Durgadoo et al. (2013), they clarify that the Agulhas Leakage is likely decoupled from the Agulhas current and is not directly driven by changes in the Agulhas current volume transport. Conclusively, it is likely that on short monthly or decadal timescales the Agulhas Leakage is controlled mostly by intensification of westerly winds (Biastoch et al., 2015; Durgadoo et al., 2013) without a direct link between the Agulhas current and the leakage (Durgadoo et al., 2013; Loveday et al., 2014).

## 4.4 Millennial to multi-millennial climate controls on the Agulhas Leakage

On millennial to multi-millennial timescales, mechanisms that exert control on the Agulhas Leakage might deviate slightly from the ones active today as longer-term ocean circulation effects have to be taken into account. The current compilation of paleoclimate data available from the Agulhas system present two robust features.

First, faunal assemblage datasets show a spike in tropical species during glacial terminations (Bard & Rickaby, 2009; Caley et al., 2011; Caley et al., 2012; Peeters et al., 2004). Second, planktonic foraminifera and alkenone paleo-salinity reconstructions show high salinities in glacial maxima and fresh conditions during interglacials (Kasper et al., 2014; Martinez-Mendez et al., 2010; Petrick et al., 2015; Simon et al., 2013; Simon et al., 2015), often with significant termination salinity spikes (Marino et al., 2013).

Paleoclimate studies suggest a variety of mechanisms that may explain the above trends. These include i) low latitude monsoon forcing via changes in the Agulhas current (Peeters et al., 2004), ii) movements of the subtropical front (Bard & Rickaby, 2009; Caley et al., 2011; Caley et al., 2012), iii) southern hemisphere high latitude forcing (Caley et al., 2011; Caley et al., 2012), and iv) changes in the southwest Indian Ocean subgyre dynamics (Simon et al., 2013; Simon et al., 2015).

Peeters et al., (2004) introduce tropical faunal assemblage counts (Agulhas Leakage fauna, ALF) as a proxy for Agulhas Leakage strength. They find a weak precessional beat in their counts leading them to hypothesize that Agulhas Leakage efficiency is driven by low latitude monsoon forcing. Bard & Rickaby (2009) present alkenone sea surface temperatures (SST) and foraminiferal stable isotopes from further upstream, and see distinct glacial-interglacial variability in both. They propose that on longer timescales shifts in frontal zones, such as the southern hemisphere subtropical front (STF), control the leakage by reducing the width of the Agulhas current south of the African tip causing a decrease in the leakage via a decrease in the throughflow. This suggestion is similar to the initial proposal made by Biastoch et al. (2009) then argued by Durgadoo et al. (2013). However, on longer timescales, changes in the wind belts may lead to changes in deep water formation fluxes which may shift frontal zones (Durgadoo et al., 2013). Caley et al. (2011; 2012) also reconstructed faunal assemblages off South Africa in a different location, but rather find a strong obliquity signal in their data. They agree that southern

hemisphere forcings, such as changes in the STF, are responsible for changes in the Agulhas Leakage. Reducing the through flow area for the Agulhas current south of Africa might have influences on the paleo-location of the retroflection which has been proposed to influence leakage (Van Sebille et al., 2009a). Using Strontium isotopes in bulk sediment, Franzese et al. (2006) reconstructed the source regions of sediment grains on the Agulhas plateau and inferred that the Agulhas current retroflection did not significantly move between the Holocene and last glacial maximum (LGM). Simon et al. (2013) present high resolution SST and hydrographical data as well as faunal assemblage counts and conclude that large variability exists within the Agulhas system. They infer that short-term southwest Indian Ocean subgyre dynamics may influence the salt and heat content of Agulhas current waters and influence the leakage on millennial timescales. As such, contrary to decadal timescales, both the Agulhas current strength and the width of the gateway seem to influence the leakage on longer timescales across glacial-interglacial cycles.

# Chapter 5

# MATERIALS AND METHODS

## 5.1 Ocean sediment cores as climate archives

### 5.1.1 Natural Archives

The Earth's climate history is recorded in a variety of geological and biological archives. These include tree rings, pollen records (from soil, lake or ocean sediment cores), corals, speleothems, and ice cores. They are of great value for climate science due to their intrinsic property of providing reasonably undisturbed lamination which can be related to time. Choosing the right archive is of importance, as different archives appear in diverse geospatial settings and record climate in different biological and chemical ways. This project is investigating glacial-interglacial cycle dynamics which calls for an archive that has good coverage and reasonably high resolution across the Plio-Pleistocene (11.7kyr-5.3 Ma), when waxing and waning of ice sheets played a significant role in changing global climate.

Deep ocean sediment cores present undisturbed continuously laminated records spanning several millions of years in the past. In locations with high sedimentation (e.g drift deposits), rates of 2.5cm/100 yrs can be found (e.g. Jansen et al., 1996). More commonly, sedimentation rates reach from 2cm/1000 yrs (e.g. Hall et al.,

2017) to 0.5cm/1000 yrs in the deep basins (Ericson et al., 1961). The material is often rich in calcareous and siliceous micro- and nanofossils which record the prevailing oceanic state in the shell chemistry. Isotope and trace element analyses in planktonic and benthic foraminiferal calcite found in calcareous microfossil oozes are particularly useful to extract climatic information from ocean sediment cores.

### 5.1.2 Foraminiferal calcite as climate proxies

A variety of ocean sediment cores are highly abundant in calcareous microfossils. Often, the taxonomic group of foraminifera prevails the assemblage. Foraminifera are sand-grain-sized single cell organisms in the oceans which create characteristic calcium shells around a soft tissue body (Hemleben et al., 1989). They can be divided into planktonic and benthic species, with planktonic species living in the upper water column with some species inhabiting deeper waters down to the thermocline, and benthic species inhabiting the ocean floor (faunal) or burying into it (infaunal) (Hemleben et al., 1989). Throughout their life span, most planktonic foraminifera are filter feeders largely eating small plankton. Prey is caught using long, pseudopodia spines. A variety of planktonic species keep photosynthetic symbionts including dinoflagellates, diatoms and chlorophytes (Spero, 1998). Reproduction occurs sexually and asexually throughout the life cycle (Bè & Anderson, 1976). Some planktonic species reject their symbionts before meiosis and strengthen the outer shell wall with gametogenic calcite. It has been proposed that some species sink to greater depths during meiosis to promote release of symbionts (Erez et al., 1991). Overall, little is still known about depth migrating patterns of specific planktonic species.

During shell calcification, foraminifera substitute calcite ions for other trace metals in the carbonate lattice. This often occurs according to certain environmental conditions, which makes foraminiferal calcite a valuable source for climate recon-

struction. As such, the trace metal ratio of a variety of elements to calcite can be used as proxies for different environmental parameters. Most commonly used are Mg/Ca as a proxy for water temperature (e.g. Barker et al., 2005; Rosenthal et al., 2000), Sr/Ca as measure for land surface weathering (e.g. Lear et al., 2003), Ba/Ca as a nutrient (e.g Lea and Spero, 1992) or river run-off indicator (e.g. Hönisch et al., 2011), Cd/Ca as a productivity measure (e.g. Boyle, 1988) and B/Ca as a proxy for seawater [$HCO_3^-$] (e.g. Yu et al., 2007).

Isotopic ratios in foraminiferal calcite of various elements can also be used for climate reconstructions . Isotopes are atoms of the same element, with equal proton numbers, but variable amounts of neutrons leading to differences in total atomic mass. Often, foraminifera prefer taking up one isotope over the other leading to biogenic fractionation between the element's isotopes in the organism and its surrounding. In some cases, the fractionation process occurs according to prevalent environmental conditions. Hence, the ratio between the lighter and heavier isotope of a specific element can be used as a proxy for certain environmental conditions. Traditional isotopic systems used in palaeoceanography are oxygen isotopes ($\delta^{18}$O) as a proxy for ice volume (Shackleton, 1987) and deep water temperature (Elderfield et al., 2012), carbon isotopes ($\delta^{13}$C) as a way of assessing the ocean carbonate system or as a tracer for ocean water masses (Curry & Oppo, 2005), neodymium isotopes ($\varepsilon$Nd) as conservative tracers for ocean water masses (e.g. Rutberg et al., 2000), and boron isotopes as a proxy for seawater pH (e.g. Hönisch and Hemming, 2005).

After death, the foraminifera soft tissue is largely remineralised throughout the water column and the calcium test becomes buried in ocean sediments (Sigman & Hain, 2012). The shells may be preserved for millions of years, depending on the corrosiveness of overlying ocean and pore waters. This allows the assessment of million-year-old environments by using foraminfera as a medium and isotope and trace metal analyses as a method to extract palaeo-climate information.

### 5.1.3 Biogenic calcite preservation issues

The state of foraminiferal calcite preservation in the core is important as it influences their usefulness in climate reconstruction. Edgar et al. (2015) differentiate between three distinct processes by which diagenetic effects on foraminiferal calcite may influence geochemical analyses post-mortem in the water column or the sediments (Pearson & Burgess, 2008). These include (i) partial dissolution, (ii) calcite overgrowth, and (iii) calcite recrystallization.

#### Partial dissolution

Some foraminifera species produce thick gametogenic calcite layers shortly before gamete release. This is often connected to changes in depth habitat. This leads to different thicknesses in calcite layers between ontogenetic and gametogenic calcite. Due to the thinner layer, ontogenetic calcite is more susceptible to dissolution potentially biasing the geochemical analysis towards ratios representing the gametogenic calcite and the climate at deeper depths (Edgar et al., 2015). The same effect is valid for carbonate layers deposited under warmer climates, where calcite deposition leads to thinner calcification layers (Barker et al., 2005). This can cause cold-biases in Mg/Ca-reconstructed temperatures, if warmer layers were preferentially dissolved post-mortem due to undersaturated pore waters (Brown & Elderfield, 1996; Rosenthal et al., 2000; Rosenthal & Boyle, 1993).

#### Calcite overgrowth

Post-depositional inorganic overgrowth, such as ferro-manganese crusts, can present significantly different elemental/calcium ratios than the ontogenetic foraminiferal calcite, and may therefore alter geochemical measurements (Edgar et al., 2015). Crusts should be visible on high resolution images of foraminiferal tests depending on their size. Ferro-manganese crusts can also be identified through measurement

of Fe/Mg and Al/Mg in foraminiferal calcite. If a strong correlation exists between Fe or Mn and Mg, it is likely that large amounts of magnesium leached from a ferro-manganese crust and overprint the ontogenetic Mg signature. Barker et al. (2003) show that concentrations <0.1 mol/mol Fe/Mg, Al/Mg, or Mn/Mg are too small to have significant effects on the Mg/Ca measurements. I therefore adopt the contamination limit of 0.1mol/mol as a guidance for "dirty samples".

#### Calcite recrystallization

Calcite recrystallization processes may cause alterations to the original geochemical signature of the ontogenetic calcite (Edgar et al., 2015; Pearson & Burgess, 2008). During recrystallization, the ontogenetic microgranular calcite structure is replaced by larger and blockier calcite crystals (Pearson & Burgess, 2008; Sexton et al., 2006; Sorby, 1879). Recrystallized calcite can be easily identified under the microscope as having a "frosty" appearance. In contrary, unaltered calcite looks more "glassy" to the specialist eye. Additionally, changes in the crystal structure can be identified on high resolution images.

## 5.2 Core U1476 location and hydrography

Core U1476 was drilled on Davie Ridge at 15°49.25'S; 41°46.12'E during the International Ocean Drilling Program (IODP) expedition 361 which collected ocean sediment cores along the southeast African coast (Figure 5.1) (Hall et al., 2017). U1476 is located at the northern entrance of the Mozambique Channel, and represents the most northern drilled site during the expedition (Figure 5.1). Sediments are rich in calcareous oozes with particularly well preserved microfossils during the Plio-Pleistocene (11.7kyr - 5.3Ma) and low degrees of bioturbation (Hall et al., 2017).

The Mozambique Channel is connected to the Agulhas system via a net-southwards surface transport, mostly characterised by three large quasi stationary eddies (Lut-

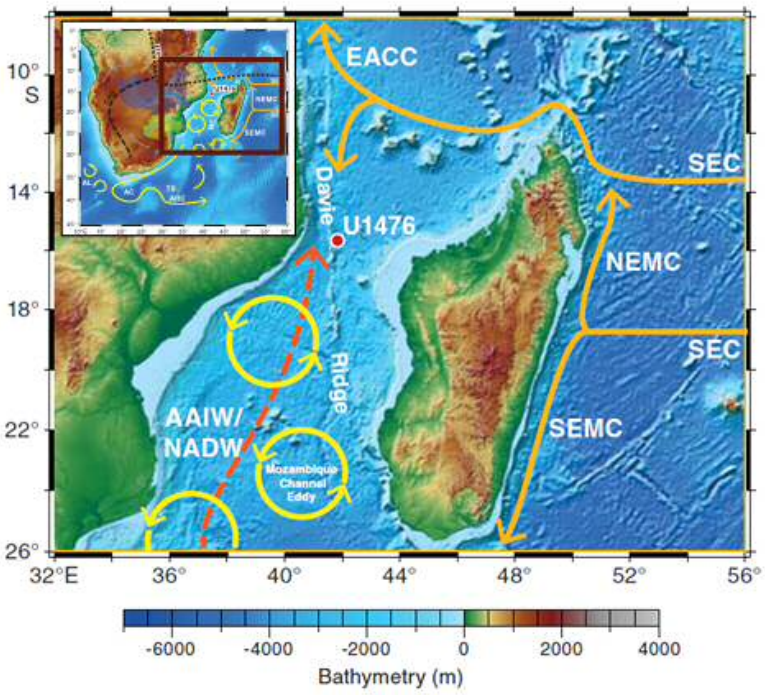


**Figure 5.1** Bathymetry map of the Mozambique channel and core site U1476 within the western Indian Ocean. Regional ocean surface circulation patterns are indicated with arrows from Hall et al. (2017).

jeharms, 2006; Figure 5.1). Additional shorter-lived smaller eddies appear in the channel and can last from monthly to yearly timescales (Sætre & Da Silva, 1982). Depending on their location and direction of spin, they may create short-term northwards flowing boundary currents along Africa and Madagascar (Lutjeharms, 2006; Sætre & Da Silva, 1982). Coastal hydrography is influenced by a strong seasonal monsoon cycle which brings freshwater to the channel via the Zambezi river (Weldeab et al., 2014). Surface waters in the channel are mainly influenced by light subtropical surface water (STSW), South Indian central water (SICW), Indonesian Throughflow waters (ITFW) and tropical surface waters (TSW) (Ullgren et al., 2012). Source waters include south equatorial current waters, northern-sourced Indian ocean waters, recirculating southern-sourced Indian ocean waters and Tasman Leakage waters (Durgadoo et al., 2017). Generally, warmer and fresher TSW and ITFW are found in the northern part, while more saline STSW dominates in the southern part of the

channel (Ullgren et al., 2012). Depending on seasonality and interannual variability, anti-clockwise rotating quasi-stationary eddies transport highly saline Red Sea waters southwards which sink under the fresher surface waters and may create strong salinity boundaries between RSW and the fresher northwards flowing underlying Mozambique Undercurrent (Ullgren et al., 2012). The variability seen in the STSW in figure 5.2 is a result of variable salinity regimes depending on annual and interannual variability in the pre-dominance of either ITFW, TSW, or RSW within the STSW surface water (Ullgren et al., 2012).

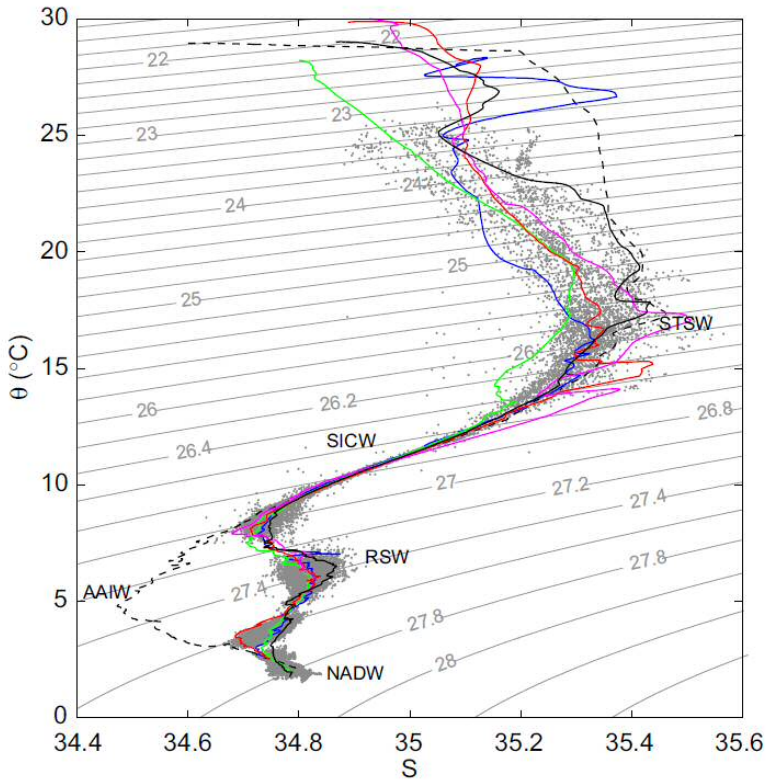


**Figure 5.2** $\theta$-S diagram from Ullgren et al. (2012) showing mooring data from an east-west cross-section at 15°N across the northern Mozambique Channel. Characteristic water masses are identified as NADW, AAIW, RSW, SICW, and STSW.

Less data is currently available on intermediate and deep water characteristics in the Mozambique Channel. Globally, deep oceans are mainly influenced by two water masses originating either at deep water convection sites in the North Atlantic producing NADW, or at deep water convection sites around Antarctica

creating southern-sourced waters (SSW) such as Antarctic Bottom water (AABW) or Antarctic Intermediate waters (AAIW) (Curry & Oppo, 2005). Unlike NADW, AABW is primarily produced by brine rejection processes leading to the production of the planet's heaviest deep water mass (Curry & Oppo, 2005). It is therefore most likely found in the ocean's abyss. The source of different deep water masses can be identified using carbon isotopes ($\delta^{13}$C). After its ventilation and deep water formation, the water mass collects highly fractionated organic carbon that rains down from the biologically active surface ocean. This alters its $\delta^{13}$C signature over time and creates a unique footprint which can trace NADW and SSW across the deep oceans (Figure 5.3).

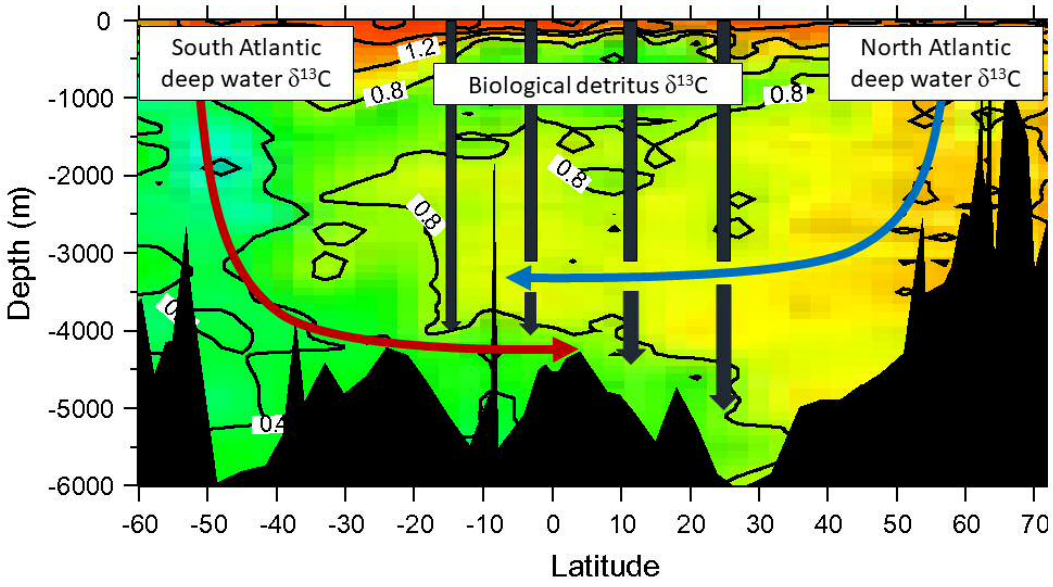


**Figure 5.3** North-south cross section across the Atlantic ocean showing the development of water mass benthic $\delta^{13}$C over time. Modern water mass $\delta^{13}C_{benthic}$ signatures in the background with contours (adapted from Curry & Oppo (2005)). Arrows indicate pathways of different carbon inputs that influence the $\delta^{13}C_{benthic}$ signature of the water masses.

For the Mozambique Channel, Hall et al. (2017) and Ullgren et al. (2012) suggest that the northwards flowing Mozambique Undercurrent consists of NADW, overlain by smaller amounts of diluted AAIW. My $\delta^{13}$C data from the foraminifer *Cibidoides wuellerstorfi* over the last 1.2Ma (for preparation and analytical methods see chapter 5.3) confirm relatively pure NADW as the major deep water mass in the northern

Mozambique Channel (Figure 5.4), after comparing the $\delta^{13}$C record against other 1.2 million year-long records of young NADW (core ODP983), mid-aged NADW (core U1304), old NADW (core U1088), and SSW (core U1089 and core U1090). This suggests that NADW surrounds the African continent westwards without significant mixing with SSW.

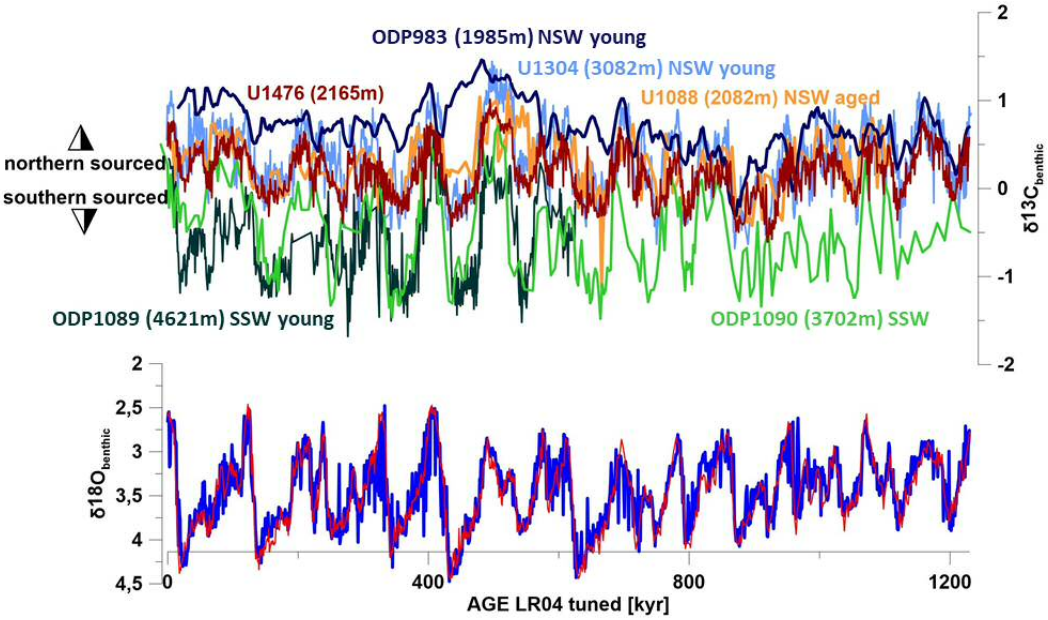


**Figure 5.4** Benthic $\delta^{13}$C for U1476 (red, Barker et al., unpublished) and for different deep water masses. Northern-sourced and southern-sourced water masses are labelled NSW, and SSW, respectively. $\delta^{13}C_{benthic}$ from 983 (Raymo et al., 2004) in dark blue, U1304 (Hodell et al., 2009) in light blue, ODP1088 (Hodell et al., 2003) in orange, ODP1089 (Hodell et al., 2003) in dark green, and ODP1090 (Hodell et al., 2003) in light green. Core locations are plotted in Figure 5.5

The modern Mozambique Channel is known as a high biodiversity hotspot (Obura et al., 2019). Due to its tropical location at 15°S and its warm sea surface temperatures around 29.5°C in summer and 26°C in winter (Fallet et al., 2010), primary productivity is flourishing. Fallet et al. (2010) have studied modern *Globigerinoides ruber* (*G. ruber*) at the site using plankton tows and compare foraminiferal Mg/Ca-derived SST to in-situ measured and monthly averaged SST for 2.5 years. Their results show that annual averages of reconstructed SSTs using *G. ruber* calcite plot close to annual averages calculated from in-situ measurements. This suggests

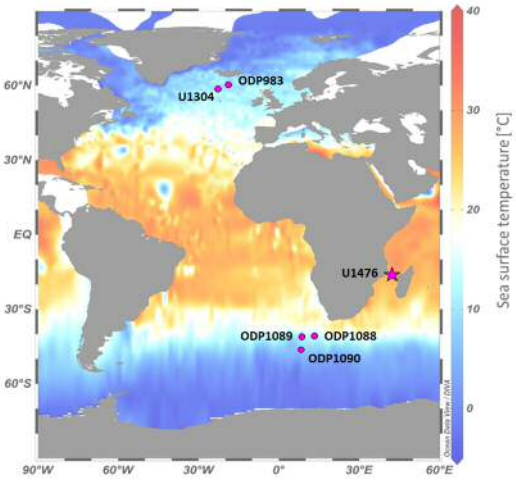


**Figure 5.5** Map showing the core locations of cores referenced in Figure 5.4.

that *G. ruber* tests from the northern Mozambique Channel record annual surface ocean climatology and can be a useful tool for the reconstruction of past sea surface hydrography and climate.

## 5.3 Sample preparation and analyses

### 5.3.1 Core sampling and sample preparation

Core U1476 was spliced and sampled at a vertical resolution of 2cm which roughly equates to a resolution of 1kyr per sample. Each sample contains approximately 35cm$^3$ of ocean floor mud of which 3cm$^3$ were set aside as archive. Ocean sediment samples were washed through a 63$\mu$m sieve. The coarse fraction was collected and dried in the oven at 40°C. The fine fraction was also collected and left to settle. Then the supernatant was syphoned off and the residual fine material was left to dry in the oven at 40°C. Dry bulk weights, and fine and coarse weights were collected before and after washing. For benthic and planktonic foraminiferal analysis, benthic species *C. wuellerstorfi* and planktonic species *G. ruber* were picked from the coarse fraction at >150$\mu$m, and 300-355$\mu$m, respectively. 1-3 specimen of *C. wuellerstorfi* were used for stable isotope analysis, while 30 specimen of *G. ruber*

were picked. This is due to high reproducibility in stable isotope results from benthic species, while greater variability exists in planktonic species. *G. ruber* tests were weighed on a microbalance, then carefully crushed between two glass slides. After homogenisation, an aliquot of 20% total sample was taken for stable isotope analysis. *C. wuellerstorfi* tests were analysed whole.

The following steps were carried out in a fume hood equipped with HEPA filters. All acids used in this method were teflon-distilled in-house in a Savillex teflon distiller. For stable isotope analysis, 1-3 whole uncleaned benthic foraminiferal tests, and a split of 20% of the crushed planktonic foraminiferal sample were used. The remaining 80% of *G. ruber* test fragments underwent standard clay and organics cleaning procedure as described by Barker et al. (2003) (Figure 5.6) for trace element analysis. Clays were removed by suspending the sample, then briefly allowing all foraminifera fragments to settle before syphoning off the clayey supernatant using a pipettor. This procedure was repeated 4 times in 18.2MΩ·cm resisting MilliQ de-ionized water, and twice in Methanol. Between cycles, samples were ultrasonicated for 1 minute to ensure the release of clays from the shell fragments. After clay removal, samples were heated to 80°C in a 1% sodiumhydroxide (NaOH) buffered hydrogen peroxide ($H_2O_2$) solution over 10 minutes to release organic residue from shell fragments. At minutes 2.5, 5, and 7.5, samples were swiftly taken out and air bubbles released by tapping the sample rack firmly on the bench. At minute 5, samples were briefly ultrasonicated for 5 seconds. This step was repeated. No reductive cleaning step was conducted as there were no signs of significant ferromanganese crust coatings (Figures 5.15 and 5.16). After the full oxidative cleaning procedure, samples were quickly checked under the microscope. If significantly discoloured calcite fragments and/or black specs were visible, they were picked out by hand using a cow's eyelash brush. Clean foraminifera test fragments were dissolved overnight in 0.065M $HNO_3$.

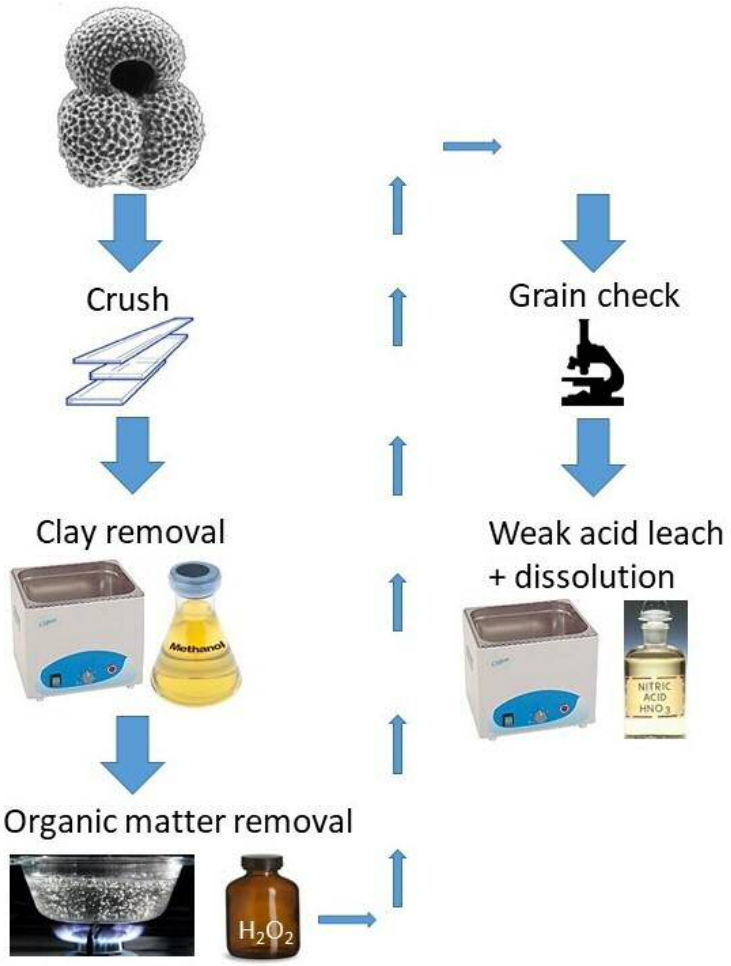


**Figure 5.6** Flow chart showing the order of different preparation and cleaning steps before trace element and boron isotope analyses of planktonic foraminifera samples.

### 5.3.2 Stable isotope analysis

Planktonic and benthic foraminifera were analysed for stable isotopes at the Earth & Ocean Science department of Cardiff University by laboratory technician Alexandra Nederbragt. The analysis was conducted on a Thermo MAT253 mass spectrometer with a Kiel IV carbonate preparation device. The device drips phosphoric acid onto the whole shells and dissolved the calcite. This process releases $CO_2$ gas which is then analysed for its oxgen and carbon isotopes. Samples are interspersed with carrara marble in-house standard (BCT63) which gives a longterm standard deviation of 0.035‰ for oxygen, and 0.024‰ for carbon isotopes. In comparison, the average standard deviation for single sample oxygen and carbon isotope ratios is

0.032‰, and 0.024‰, respectively. For data quality purposes, the output files record acid temperature, leak rate, and total $CO_2$. Data points are excluded by Alexandra Nederbragt, if they fall outside a 3x standard deviation envelope, or have reasons to be removed due to methodological failure.

### 5.3.3 Trace element analysis

Cleaned and dissolved planktonic *G. ruber* were analysed for a suite of trace element to calcite ratios at three laboratories. This resulted from splitting samples into three batches. These include trace element-only samples, boron-isotope samples for scoping out the potential of the core using a conventional method, and boron isotope samples using a new boron separation method. To gain a good $\delta^{11}$B-based seawater pH reconstruction, trace elements must be measured on direct splits of the boron samples. We therefore combined the trace element data from the trace-element only samples with trace element data from $\delta^{11}$B analysis.

Trace element-only samples (n=190) were analysed on a Thermo Scientific ELEMENT XR mass spectrometer at the Cardiff University CELTIC laboratories, while trace element data from $\delta^{11}$B analyses were collected at the STAiG laboratories in St. Andrews, and the Foster Lab laboratories in Southampton. In St. Andrews, trace element samples (n=198) were analysed on an Agilent Triple Quadrupole mass spectrometer. In Southampton samples (n=36) were measured on a Thermo Scientific Element XR mass spectrometer. In all three laboratories, samples were spun in a centrifuge prior to analysis to reduce risk of undissolved particle contamination. Then an aliquot of 10$\mu$L in Cardiff, 3$\mu$L in St. Andrews, and 20$\mu$L in Southampton (Henehan et al., 2015), was diluted and pre-run for calcium (Ca) concentrations. In Cardiff, matrix matched standards were created for each sample below a concentration of 2mM calcite. Samples with a concentration >2mM calcite were diluted to set standard concentrations at 2mM, 2.5mM, 3mM, 3.5mM, and 4mM. In St. Andrews,

and Southampton (Henehan et al., 2015), samples were matched to a 0.5mM or 1mM Ca standard, depending on boron concentrations of the sample. The following ratios were collected at all three institutions: Mg25/Ca43, B11/Ca43, Sr88/Ca43, Cd111/Ca43, U238/Ca43, Al27/Ca43, Mn55/Ca43, Li7/Ca43, Nd146/Ca43, and Ba138/Ca43 (Figure 5.7).

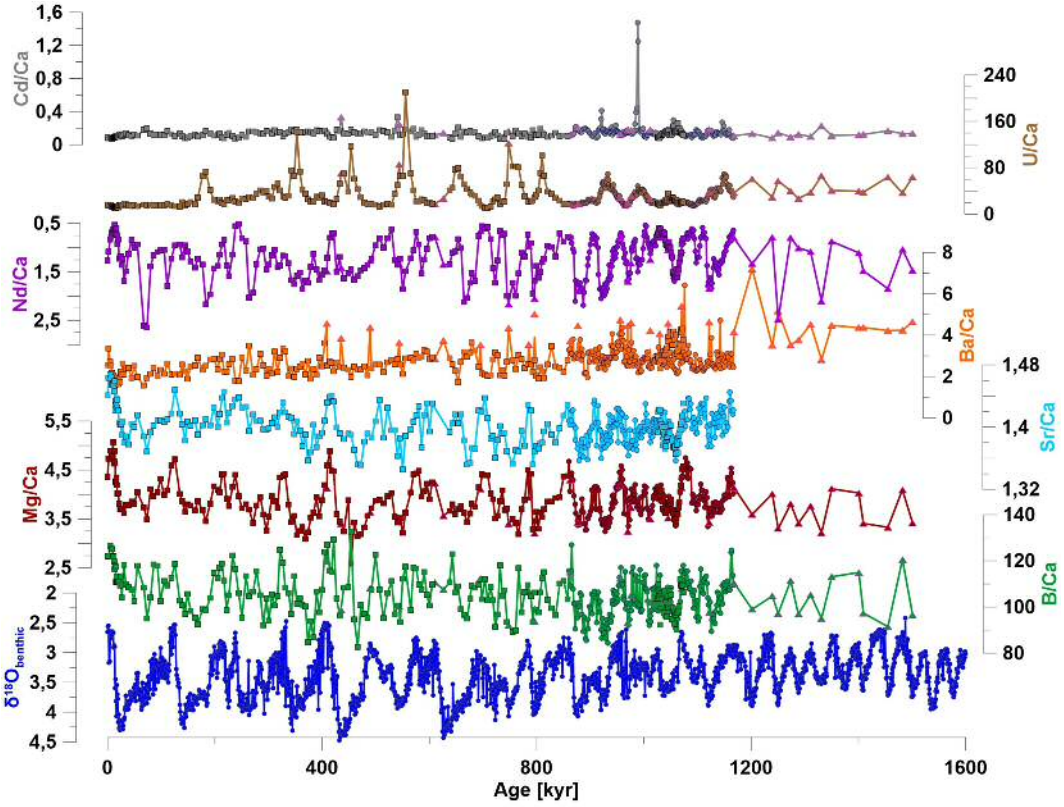


**Figure 5.7** Benthic $\delta^{18}O$ with a complete set of U1476 trace element/Ca ratios across the last 1.6Ma measured for this thesis. Samples were analysed in three locations including Cardiff University (filled circles with dark blue outline), University of St Andrews (squares with black outline), and National Oceanographic Centre Southampton (triangles with pink outline).

Long-term reproducibility from in-house standards for Cardiff, St. Andrews, and Southampton are listed in Table 5.1 at the end of this subchapter. For comparison, average relative standard deviations (RSD) from the sample batches are listed in Table 5.2. Long-term reproducibility for the Foster Lab in Southampton is also referenced in Henehan et al. (2015).

Raw-data quality was tested by calculating the signal/noise ratio for B11/Ca43 as

$$\frac{B11_{Sample}[cps]}{B11_{previousblank}[cps]} \tag{5.1}$$

and the sample-standard matrix match in [%] as

$$\frac{Ca43_{Sample}[cps] - Ca43_{previousstandard}[cps]}{Ca43_{previousstandard}[cps]} * 100 \tag{5.2}$$

where [cps] stands for counts per second.

I chose these quality checks, because boron concentrations can be very small in samples and provide a good measure of signal/noise ratio when compared to blank measurements. Additionally, it is important that sample and bracketing standard are matrix matched well, since poor matrix matching can lead to matrix effects on the mass spectrometer and may influence the final measurement of concentration or isotopic signature if the plasma conditions and long-term machine drift are somewhat unstable. Samples which had a signal/noise ratio for B11 <5, or a matrix match >30% were scrutinised and considered for exclusion (Figure 5.8). Data points were only excluded in circumstances where all element ratios were well out of the naturally occurring range of that ratio.

Some samples experienced difficulties during the analysis (see Figure 5.9). These included samples that were (i) run with a dirty blank pot, (ii) left uncapped for 24 hours due to plasma shutdown, (iii) showed signs of dilution problems or high contamination tracer concentrations, or (iv) were re-picked and re-run after sample loss during preparation. Dirty blank pot samples (i) were blank corrected using an average of the clean blanks also used in the run as a better representation of blank. During one run, the plasma shutdown due to a pressure drop in argon gas. These samples (ii) were re-run in their respective beakers 24 hours later using the blank and standard pots from the original run. As such, contamination accumulation over the 24 hours was also representative in the blanks and standards and was corrected

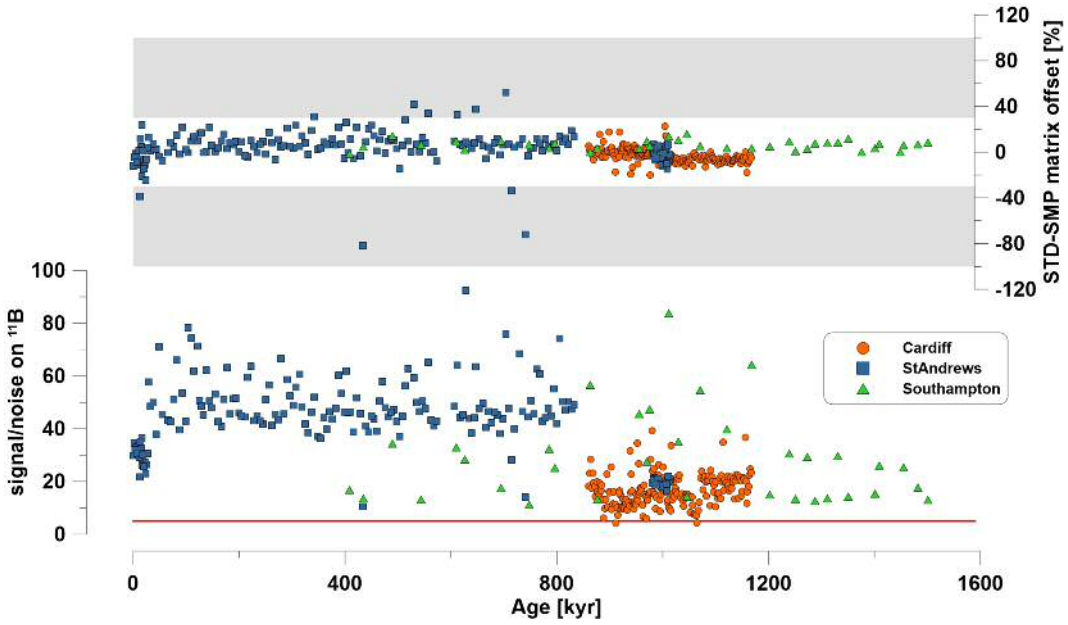


**Figure 5.8** sigal/noise ratio for B11, and standard-sample matrix offset for the three sample batches run in Cardiff (orange circles), St. Andrews(blue squares), and Southampton (green triangles). The red line, and grey bars indicate boundary levels, respectively. Samples that fall below the red line, or within the grey bars were subject to quality scrutiny.

for through the bracketing method. Samples with dilution problems (iii) can be problematic, because of differences in the standard and sample calcium concentration. This can lead to errors in the sample measurement, as not all matrix effects are accounted for by the standard bracketing. If matrix effects are small during certain runs, moderate sample-standard differences may be acceptable. Therefore, I did not correct or exclude any wrongly diluted samples. Samples with high contamination tracers (Al/Ca, Fe/Ca, Mn/Ca) were only excluded if a strong correlation existed between the contamination tracer and the climate variable. This was never the case. Some samples experienced high rates of carbonate loss during the preparation steps. These samples were re-picked and re-run. No further issues occurred to the re-picked samples(iv). Again, data points were only excluded if trace element ratios plotted well outside the naturally occurring range of that ratio. In the final record, one Mg/Ca data point was excluded due to plotting four times higher than the natural range, and one B/Ca data point was not analysed by the mass spectrometer.

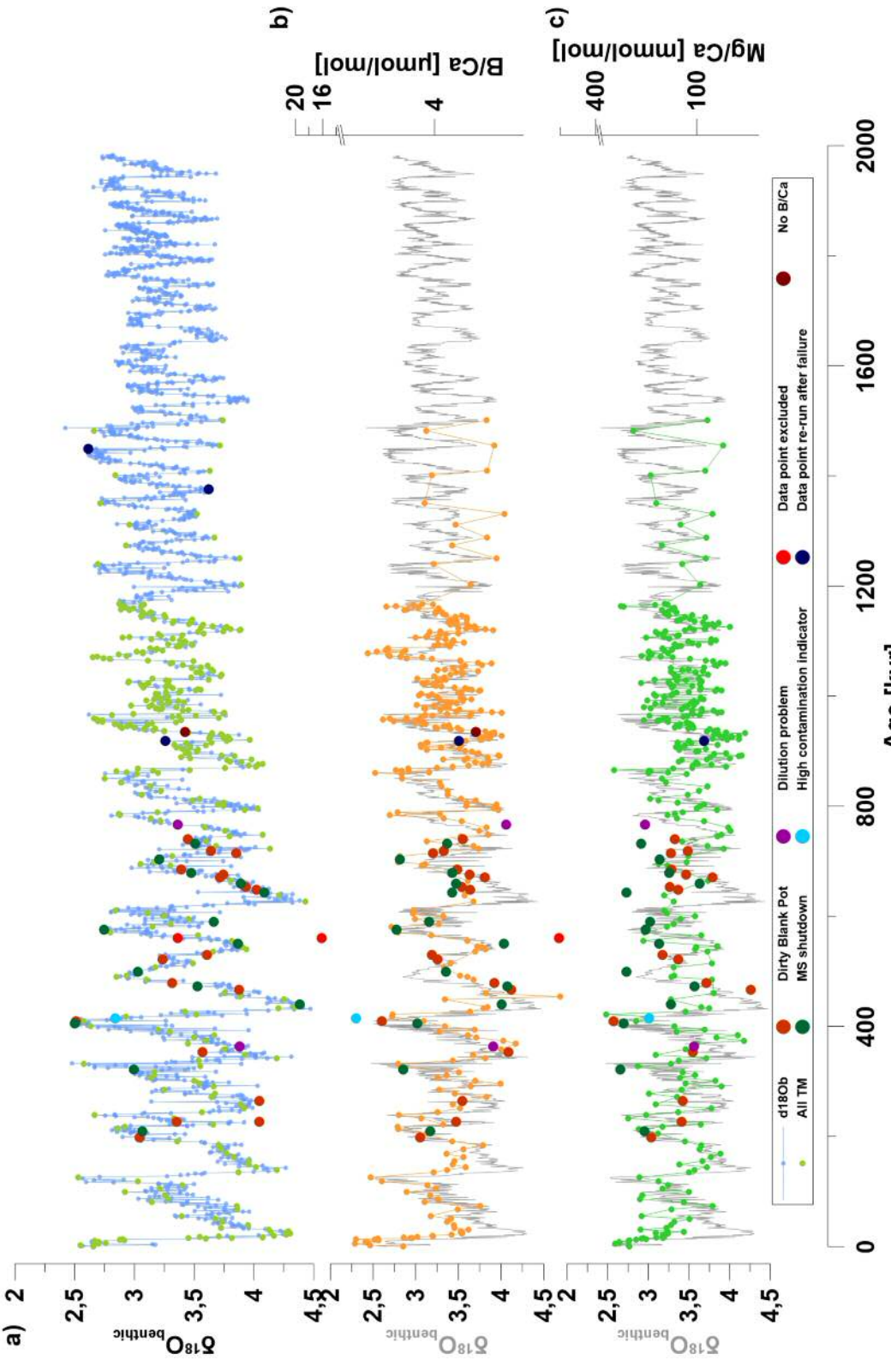


**Figure 5.9** Plot of samples having experienced measurement difficulties. To highlight the respective samples in their temporal space, they were plotted representatively as values of $\delta^{18}O_{benthic}$ (a). 17 large orange circles show samples subject to dirty blank pots. 14 large grey circles show samples subject to mass spectrometer shutdown and therefore long exposure to laboratory air. 2 large yellow circles represent samples with concentration mismatch between samples and standards. 1 large light blue circle represents a sample subjected to high contamination. 1 large light green circle shows the excluded data point. 3 large dark blue circles represent data points that were re-run. 1 large brown circle shows a data point where B/Ca was not measured. For comparison, small grey circles show all data points measured for trace elements in this thesis, and small blue circles show all samples measured for stable isotopes. This also represents the sampling density of the core. Influence of sample measurement difficulties on Mg/Ca and B/Ca are visible in (b) and (c).

### 5.3.4 Interlaboratory standard comparison

Here, I combine trace element data from three laboratories. I therefore conducted a series of standard measurements from the exact same standard at Cardiff and St. Andrews. The Southampton laboratory did not take part in this study, since the samples produced there are only a small subset of the main data cloud (36 samples out of 388 total samples). I analysed a subset of trace element ratios of the Cardiff consistency in-house standards *CS1 Cardiff* and *CS2 Cardiff* at both laboratories using the same Cardiff in-house bracketing standard *MCS-A*. These included Mg25/Ca43, B11/Ca43, Li7/Ca43, Sr88/Ca43, Cd111/Ca43, U238/Ca43, Al27/Ca43, and Mn55/Ca43. I then compared the two sample distributions using a Welch 2-sample t-test with a null hypothesis stating that the two distributions are the same. The null hypothesis was rejected for all $p<0.05$, as was the case for Mg/Ca, Sr/Ca, Mn/Ca and B/Ca for standard *CS1 Cardiff*, but only Mg/Ca and Al/Ca for standard *CS2 Cardiff*, respectively (see boxplots in Figure 5.10 and Table 5.3). As such, there was no clear result for Sr/Ca, Mn/Ca, Al/Ca, and B/Ca. I therefore did not consider a correction for either of these element ratios.

The null hypothesis for Mg/Ca was rejected for both standard analyses. The standard difference between St. Andrews and Cardiff resulted in -0.043, and 0.106 for *CS1 Cardiff*, and *CS2 Cardiff* respectively. This result does not point towards a systematic standard offset between the two laboratories, since the offset is negative for *CS1 Cardiff*, but positive for *CS2 Cardiff*. Additionally, offsets were smaller in Cardiff between defined standard values and average measured values, than in St. Andrews suggesting that a correction factor might be appropriate for samples measured in St. Andrews. Then again, *CS1 Cardiff*, and *CS2 Cardiff* are Cardiff in-house standards, where the laboratory set-up is tuned to provide accurate measurements for *CS1 Cardiff*, and *CS2 Cardiff*. When comparing laboratory-specific long-term

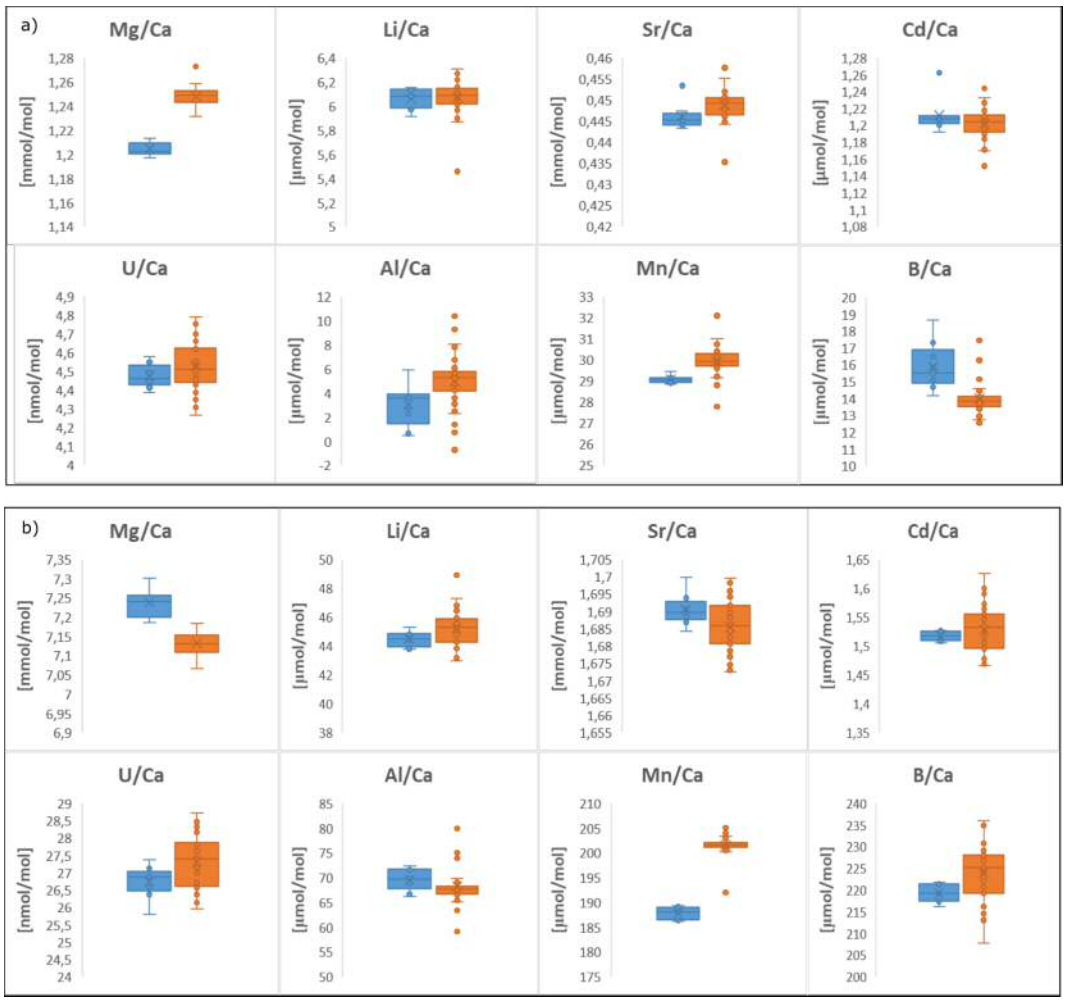


**Figure 5.10** Boxplots for eight element ratios comparing consistency standards *CS1 Cardiff* (a) and *CS2 Cardiff* (b) measured in St. Andrews (blue), and Cardiff (orange). Number of samples (n) for St. Andrews and Cardiff are 9, and 35, respectively.

reproducibility standards, both laboratories provide excellent reproducibility for their respective consistency standards (see Table 5.1).

To ultimately decide whether a consistent offset should be used for Mg/Ca, I picked and ran 24 foraminiferal test samples from section D4-2 and D4-3 in U1476 ($\sim$1.1Ma) both in Cardiff, and in St. Andrews (Figure 5.11).

A Welch 2-sample t-test found no difference between the datasets ($p = 0.853$) at a significance level of 5% (Figure 5.12). For comparison, this section also includes four Southampton Mg/Ca measurements which plot well within the Cardiff-St. Andrews

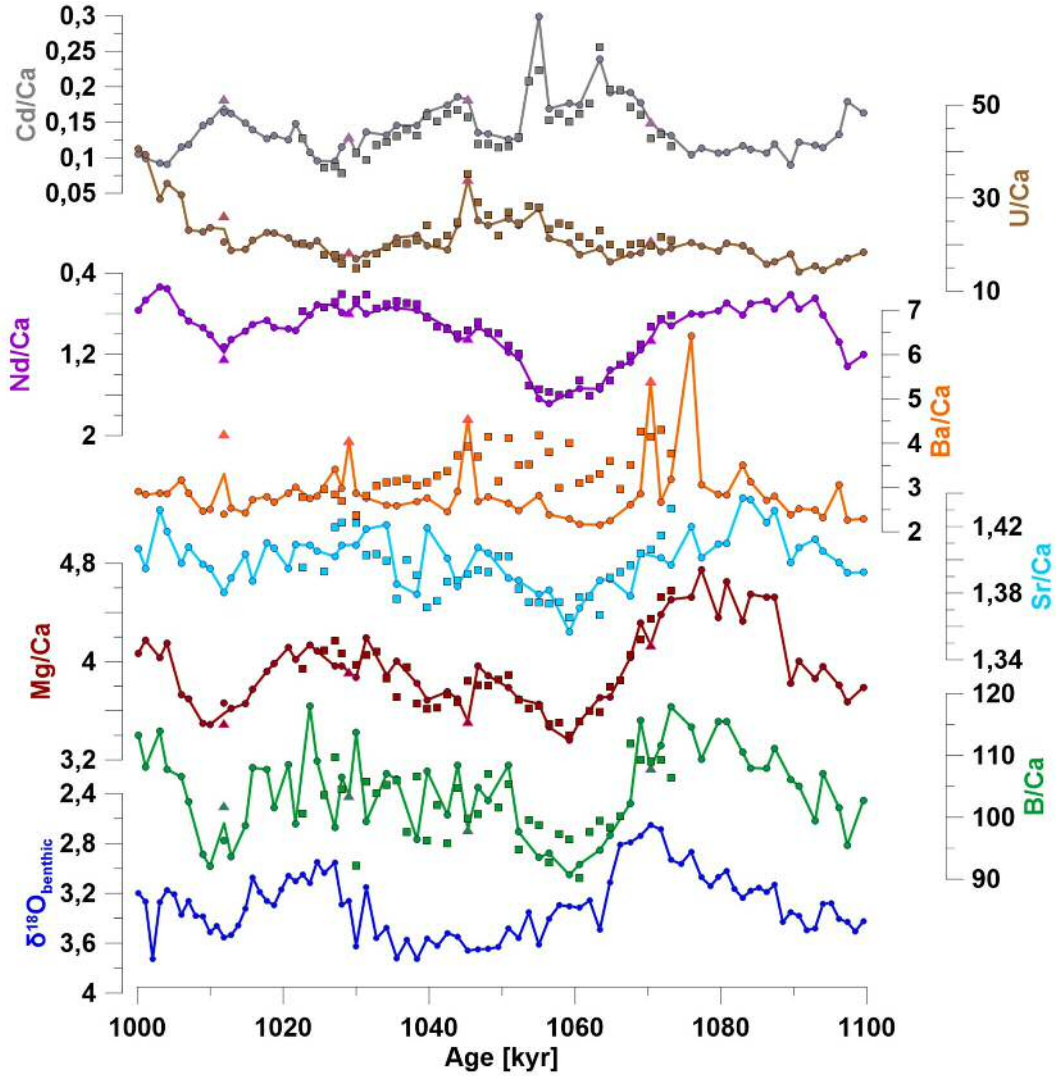


**Figure 5.11** Comparison of trace element ratios from the same samples measured in Cardiff (circles), St. Andrews (squares), and Southampton (triangles) across time period MIS30.

dataset (Figure 5.11). I therefore concluded that no correction factor will be used on the Mg/Ca datasets.

Elements which were not tested in this standard comparison include Ba138/Ca43, and Nd146/Ca43. I assessed their comparability through same sample measurements, as done previously with Mg/Ca. Figures 5.7 and 5.11 show no consistent offset between laboratories in Nd/Ca, but hint towards a potential offset in Southampton Ba/Ca compared to Cardiff and St. Andrews Ba/Ca. As such, Southampton Ba/Ca values were excluded from any analysis conducted with Ba/Ca data.

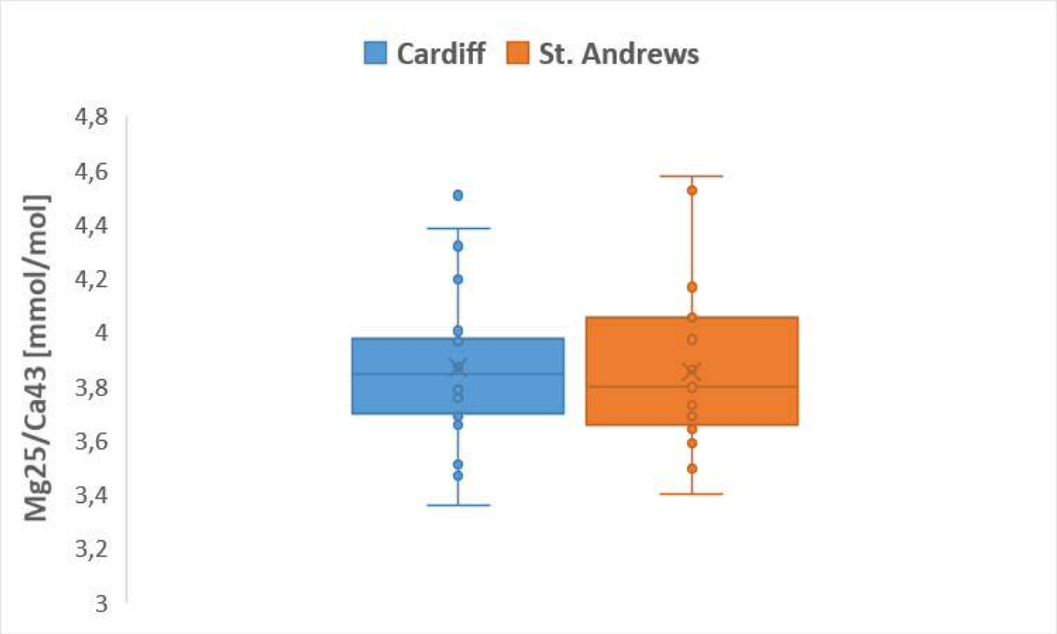


**Figure 5.12** Boxplot of 24 identical samples which were picked and measured once in Cardiff, and again in St. Andrews.

### 5.3.5 Foraminiferal sample preservation

Dissolution potential and saturation state may vary across time and could have potentially caused partial dissolution in the past. To assess whether foraminifera were subject to dissolution, I took high resolution images under a microscope. The images show well preserved glassy tests with fine pores and micro-structures, without significant amounts of blocky calcite visible (Figure 5.13).

Changes in partial dissolution over time due to movements in the lysocline should lead to variability in foraminiferal shell weights (Broecker & Clark, 2001; Lohmann, 1995). Before geochemical analysis on U1476 samples, 25 foraminiferal tests were weighed from each sample, and their average weight/test was calculated. I see no glacial-interglacial changes in the average *G. ruber* (300-355$\mu$m) shell weights/test over the last 1.2Ma (Figure 5.14) which stay around 16.1$\mu$g/shell (2sd = 2.61).

Tests may be overgrown with inorganic crusts rich in Al, Mn and Fe. All samples are below the (2003) threshold for Fe/Mg ratios ((Figure 5.15b), and only few *G. ruber* (300-355$\mu$m) calcite samples show slightly elevated Al/Mg or Mn/Mg (Figure

**Figure 5.13** High-resolution light microscope image of a *G. ruber* specimen from ocean sediment core U1476. Calcite shell structures are well preserved with no indication for dissolution.

5.15). Furhermore, I find no correlation between Fe and Mg, or Mn and Mg in my samples (Figure 5.16). This supports that my foraminiferal tests are unaffected by significant partial dissolution or inorganic overgrowth.

**Table 5.1** Trace element ratio consistency standards and long-term reproducibility for the CELTIC, STAiG, and Foster Lab laboratories

| STD | Ratio | Unit | STD value | Bracketing STD | Average | Reproducibility (2SD[a]) | RSD [%][b] | n[c] |
|---|---|---|---|---|---|---|---|---|
| | | | | *CELTIC, Cardiff* | | | | |
| *CS1 Cardiff* | Mg25/Ca43 | [mmol/mol] | 1.24 | MCSB | 1.26 | 0.026 | 1% | 14 |
| | Li7/Ca43 | [$\mu$mol/mol] | 6.09 | MCSB | 6.12 | 0.400 | 3% | 14 |
| | Sr88/Ca43 | [mmol/mol] | 0.45 | MCSB | 0.45 | 0.004 | 0% | 14 |
| | Cd111/Ca43 | [$\mu$mol/mol] | 1.25 | MCSB | 1.23 | 0.043 | 2% | 14 |
| | U238/Ca43 | [nmol/mol] | 4.49 | MCSB | 4.70 | 0.230 | 2% | 14 |
| | Al27/Ca43 | [$\mu$mol/mol] | 4.38 | MCSB | 20.8 | 34.895 | 84% | 14 |
| | Mn55/Ca43 | [$\mu$mol/mol] | 28.86 | MCSB | 29.42 | 0.838 | 1% | 14 |
| | B11/Ca43 | [$\mu$mol/mol] | 13.40 | MCSB | 15.61 | 3.422 | 11% | 14 |
| | Fe56/Ca43 | [$\mu$mol/mol] | 56.06 | MCSB | 65.19 | 29.468 | 23% | 14 |
| *CS2 Cardiff* | Mg25/43 | [mmol/mol] | 7.15 | MCSB | 7.19 | 0.063 | 0% | 14 |
| | Li7/Ca43 | [$\mu$mol/mol] | 45.12 | MCSB | 45.20 | 3.566 | 4% | 14 |
| | Sr88/Ca43 | [mmol/mol] | 1.69 | MCSB | 1.69 | 0.012 | 0% | 14 |
| | Cd111/Ca43 | [$\mu$mol/mol] | 1.56 | MCSB | 1.51 | 0.041 | 1% | 14 |
| | U238/Ca43 | [nmol/mol] | 27.21 | MCSB | 27.25 | 0.901 | 2% | 14 |
| | Al27/Ca43 | [$\mu$mol/mol] | 69.70 | MCSB | 71.44 | 7.402 | 5% | 14 |
| | Mn55/Ca43 | [$\mu$mol/mol] | 201.70 | MCSB | 202.80 | 3.728 | 1% | 14 |
| | B11/Ca43 | [$\mu$mol/mol] | 221.95 | MCSB | 220.82 | 7.007 | 2% | 14 |
| | Fe56/Ca43 | [$\mu$mol/mol] | 2.09 | MCSB | 2.12 | 0.051 | 1% | 14 |

Table 5.1 continued

| | | | *STAiG, St. Andrews* | | | | | |
|---|---|---|---|---|---|---|---|---|
| *CS1 St. Andrews* | Li7/Ca43 | [$\mu$mol/mol] | 12.57 | STGTE | 12.51 | 0.475 | 2% | 15 |
| | B11/Ca43 | [$\mu$mol/mol] | 205.81 | STGTE | 211.56 | 26.006 | 6% | 15 |
| | Na23/Ca43 | [mmol/mol] | 5.37 | STGTE | 5.36 | 0.079 | 1% | 15 |
| | Mg24/Ca43 | [mmol/mol] | 1.34 | STGTE | 1.27 | 0.138 | 5% | 15 |
| | Mg25/Ca43 | [mmol/mol] | 1.22 | STGTE | 0.99 | 0.405 | 20% | 15 |
| | Al27/Ca43 | [$\mu$mol/mol] | 19.95 | STGTE | 19.41 | 1.147 | 3% | 15 |
| | Mn55/Ca43 | [$\mu$mol/mol] | 14.55 | STGTE | 15.02 | 0.300 | 1% | 15 |
| | Sr88/Ca43 | [mmol/mol] | 0.47 | STGTE | 0.47 | 0.005 | 1% | 15 |
| | Cd111/Ca43 | [$\mu$mol/mol] | 0.04 | STGTE | 0.04 | 0.007 | 9% | 15 |
| | Ba138/Ca43 | [$\mu$mol/mol] | 1.57 | STGTE | 1.56 | 0.038 | 1% | 15 |
| | Nd146/Ca43 | [$\mu$mol/mol] | 1.14 | STGTE | 1.13 | 0.051 | 2% | 15 |
| | U238/Ca43 | [nmol/mol] | 3.96 | STGTE | 3.98 | 0.475 | 4% | 15 |
| *CS3 St. Andrews* | Li7/Ca43 | [$\mu$molmol/mol] | 39.40 | STGTE | 39.02 | 1.457 | 2% | 15 |
| | B11/Ca43 | [$\mu$mol/mol] | 38.92 | STGTE | 51.49 | 26.81 | 26% | 15 |
| | Na23/Ca43 | [mmol/mol] | 15.89 | STGTE | 15.84 | 0.300 | 1% | 15 |
| | Mg24/Ca43 | [mmol/mol] | 7.55 | STGTE | 7.64 | 0.119 | 1% | 15 |
| | Mg25/Ca43 | [mmol/mol] | 7.54 | STGTE | 7.45 | 0.710 | 5% | 15 |
| | Al27/Ca43 | [$\mu$mol/mol] | 100.28 | STGTE | 96.60 | 6.415 | 3% | 15 |
| | Mn55/Ca43 | [$\mu$mol/mol] | 37.38 | STGTE | 38.17 | 0.431 | 1% | 15 |
| | Sr88/Ca43 | [mmol/mol] | 1.84 | STGTE | 1.84 | 0.035 | 1% | 15 |
| | Cd111/Ca43 | [$\mu$mol/mol] | 0.18 | STGTE | 0.17 | 0.013 | 4% | 15 |
| | Ba138/Ca43 | [$\mu$mol/mol] | 3.04 | STGTE | 3.04 | 0.088 | 1% | 15 |
| | Nd146/Ca43 | [$\mu$mol/mol] | 11.22 | STGTE | 11.20 | 0.249 | 1% | 15 |
| | U238/Ca43 | [nmol/mol] | 47.59 | STGTE | 47.78 | 2.111 | 2% | 15 |

Table 5.1 continued

| *Foster Lab, Southampton* | | | | | | | | |
|---|---|---|---|---|---|---|---|---|
| *SCS1* | Li7/Ca43 | [$\mu$mol/mol] | 12.48 | SMG2 | 12.51 | 0.592 | 2% | 4 |
| | B11/Ca43 | [$\mu$mol/mol] | 199.86 | SMG2 | 190.19 | 15.889 | 4% | 4 |
| | Na23/Ca43 | [mmol/mol] | 5.00 | SMG2 | 5.12 | 0.412 | 4% | 4 |
| | Mg24/Ca43 | [mmol/mol] | 1.00 | SMG2 | 0.96 | 0.006 | 0% | 4 |
| | Mg25/Ca43 | [mmol/mol] | 1.00 | SMG2 | 0.95 | 0.030 | 2% | 4 |
| | Al27/Ca43 | [$\mu$mol/mol] | 12.01 | SMG2 | 13.49 | 1.305 | 5% | 4 |
| | Mn55/Ca43 | [$\mu$mol/mol] | 14.96 | SMG2 | 14.43 | 1.036 | 4% | 4 |
| | Sr86/Ca43 | [mmol/mol] | 0.50 | SMG2 | 0.51 | 0.006 | 1% | 4 |
| | Sr87/Ca43 | [mmol/mol] | 0.50 | SMG2 | 0.50 | 0.003 | 0% | 4 |
| | Cd111/Ca43 | [$\mu$mol/mol] | 0.03 | SMG2 | 0.03 | 0.003 | 5% | 4 |
| | Ba138/Ca43 | [$\mu$mol/mol] | 1.50 | SMG2 | 1.44 | 0.023 | 1% | 4 |
| | Nd146/Ca43 | [$\mu$mol/mol] | 1.00 | SMG2 | 1.02 | 0.023 | 1% | 4 |
| | U238/Ca43 | [nmol/mol] | 5.28 | SMG2 | 5.18 | 0.088 | 1% | 4 |
| | Fe56/Ca43 | [$\mu$mol/mol] | 9.02 | SMG2 | 8.33 | 0.035 | 0% | 4 |
| *SCS2* | Li7/Ca43 | [$\mu$mol/mol] | 24.98 | SMG2 | 25.18 | 0.029 | 0% | 4 |
| | B11/Ca43 | [$\mu$mol/mol] | 499.94 | SMG2 | 481.05 | 11.710 | 1% | 4 |
| | Na23/Ca43 | [mmol/mol] | 10.00 | SMG2 | 10.09 | 0.550 | 3% | 4 |
| | Mg24/Ca43 | [mmol/mol] | 3.00 | SMG2 | 2.80 | 0.011 | 0% | 4 |
| | Mg25/Ca43 | [mmol/mol] | 3.00 | SMG2 | 2.89 | 0.109 | 2% | 4 |
| | Al27/Ca43 | [$\mu$mol/mol] | 55.02 | SMG2 | 55.66 | 2.582 | 2% | 4 |
| | Mn55/Ca43 | [$\mu$mol/mol] | 29.98 | SMG2 | 29.58 | 1.326 | 2% | 4 |
| | Sr86/Ca43 | [mmol/mol] | 1.00 | SMG2 | 1.00 | 0.003 | 0% | 4 |
| | Sr87/Ca43 | [mmol/mol] | 1.00 | SMG2 | 1.00 | 0.004 | 0% | 4 |
| | Cd111/Ca43 | [$\mu$mol/mol] | 0.10 | SMG2 | 0.10 | 0.003 | 1% | 4 |
| | Ba138/Ca43 | [$\mu$mol/mol] | 2.50 | SMG2 | 2.35 | 0.031 | 1% | 4 |
| | Nd146/Ca43 | [$\mu$mol/mol] | 8.01 | SMG2 | 8.18 | 0.047 | 0% | 4 |
| | U238/Ca43 | [nmol/mol] | 25.25 | SMG2 | 24.83 | 0.174 | 0% | 4 |
| | Fe56/Ca43 | [$\mu$mol/mol] | 56.02 | SMG2 | 58.18 | 1.755 | 2% | 4 |

Table 5.1 continued

| | | | | | *Foster Lab, Southampton* | | | |
|---|---|---|---|---|---|---|---|---|
| *SCS3* | Li7/Ca43 | [$\mu$mol/mol] | 40.02 | SMG2 | 40.04 | 0.593 | 1% | 4 |
| | B11/Ca43 | [$\mu$mol/mol] | 29.91 | SMG2 | 26.80 | 6.529 | 12% | 4 |
| | Na23/Ca43 | [mmol/mol] | 15.00 | SMG2 | 14.99 | 0.542 | 2% | 4 |
| | Mg24/Ca43 | [mmol/mol] | 6.50 | SMG2 | 6.50 | 0.046 | 0% | 4 |
| | Mg25/Ca43 | [mmol/mol] | 6.50 | SMG2 | 6.59 | 0.330 | 3% | 4 |
| | Al27/Ca43 | [$\mu$mol/mol] | 120.00 | SMG2 | 120.91 | 1.022 | 0% | 4 |
| | Mn55/Ca43 | [$\mu$mol/mol] | 100.02 | SMG2 | 97.28 | 3.139 | 2% | 4 |
| | Sr86/Ca43 | [mmol/mol] | 2.00 | SMG2 | 1.98 | 0.010 | 0% | 4 |
| | Sr87/Ca43 | [mmol/mol] | 2.00 | SMG2 | 1.98 | 0.009 | 0% | 4 |
| | Cd111/Ca43 | [$\mu$mol/mol] | 0.20 | SMG2 | 0.20 | 0.008 | 2% | 4 |
| | Ba138/Ca43 | [$\mu$mol/mol] | 3.50 | SMG2 | 3.40 | 0.099 | 1% | 4 |
| | Nd146/Ca43 | [$\mu$mol/mol] | 12.01 | SMG2 | 12.27 | 0.195 | 1% | 4 |
| | U238/Ca43 | [nmol/mol] | 50.30 | SMG2 | 49.71 | 0.414 | 0% | 4 |
| | Fe56/Ca43 | [$\mu$mol/mol] | 87.02 | SMG2 | 90.71 | 7.590 | 4% | 4 |

[a]2SD: 2 x standard deviation [b]RSD: relative standard deviation [%] [c]n: number of samples

**Table 5.2** Average relative standard deviations (RSD) for the sample batches

| X/Ca ratio | Unit | Average RSD | n[a] |
|---|---|---|---|
| *CELTIC, Cardiff* | | | |
| Mg25/Ca43 | [mmol/mol] | 3% | 190 |
| B11/Ca43 | [$\mu$mol/mol] | 182% | 189 |
| Sr88/Ca43 | [mmol/mol] | 1% | 190 |
| Cd111/Ca43 | [$\mu$mol/mol] | 1% | 190 |
| U238/Ca43 | [nmol/mol] | 65% | 190 |
| Al27/Ca43 | [$\mu$mol/mol] | 40% | 190 |
| Fe56/Ca43 | [$\mu$mol/mol] | 309% | 190 |
| Mn55/Ca43 | [$\mu$mol/mol] | 232% | 190 |
| Li7/Ca43 | [$\mu$mol/mol] | 24% | 190 |
| Li6/Ca43 | [$\mu$mol/mol] | 69% | 190 |
| Nd146/Ca43 | [$\mu$mol/mol] | 2% | 190 |
| Ba138/Ca43 | [$\mu$mol/mol] | 4% | 190 |
| *STAiG, St. Andrews* | | | |
| Li7/Ca43 | [$\mu$mol/mol] | 3% | 198 |
| B11/Ca43 | [$\mu$mol/mol] | 2% | 198 |
| Na23/Ca43 | [mmol/mol] | 2% | 198 |
| Mg24/Ca43 | [mmol/mol] | 2% | 198 |
| Mg25/Ca43 | [mmol/mol] | 2% | 198 |
| Al27/Ca43 | [$\mu$mol/mol] | 5% | 198 |
| Mn55/Ca43 | [$\mu$mol/mol] | 2% | 198 |
| Sr88/Ca43 | [mmol/mol] | 2% | 198 |
| Cd111/Ca43 | [$\mu$mol/mol] | 5% | 198 |
| Ba138/Ca43 | [$\mu$mol/mol] | 2% | 198 |
| Nd146/Ca43 | [$\mu$mol/mol] | 3% | 198 |
| U238/Ca43 | [nmol/mol] | 3% | 198 |
| *Foster Lab, Southampton* | | | |
| Li7/Ca43 | [$\mu$mol/mol] | 2% | 36 |
| B11/Ca43 | [$\mu$mol/mol] | 2% | 36 |
| Na23/Ca43 | [mmol/mol] | 3% | 36 |
| Mg24/Ca43 | [mmol/mol] | 1% | 36 |
| Mg25/Ca43 | [mmol/mol] | 1% | 36 |
| Al27/Ca43 | [$\mu$mol/mol] | 6% | 36 |
| Mn55/Ca43 | [$\mu$mol/mol] | 1% | 36 |
| Sr86/Ca43 | [mmol/mol] | 1% | 36 |
| Sr87/Ca43 | [mmol/mol] | 1% | 36 |
| Cd111/Ca43 | [$\mu$mol/mol] | 3% | 36 |
| Ba138/Ca43 | [$\mu$mol/mol] | 2% | 36 |
| Nd146/Ca43 | [$\mu$mol/mol] | 2% | 36 |
| U238/Ca43 | [nmol/mol] | 2% | 36 |
| Fe56/Ca43 | [$\mu$mol/mol] | 1% | 36 |

[a]n: number of samples

**Table 5.3** Interlaboratory comparison of Standards *CS1 Cardiff* and *CS2 Cardiff*

| X/Ca ratio | Unit | STD value | St. Andrews average | Cardiff average | p-value |
|---|---|---|---|---|---|
| | | | *CS1 Cardiff* | | |
| Mg25/Ca43 | [mmol/mol] | 1.24 | 1.21 | 1.25 | $2.18e^{-12}$ |
| B11/Ca43 | [$\mu$mol/mol] | 13.40 | 15.88 | 14.01 | 0.0035 |
| Sr88/Ca43 | [mmol/mol] | 0.45 | 0.45 | 0.45 | 0.0256 |
| Cd25/Ca43 | [$\mu$mol/mol] | 1.25 | 1.21 | 1.20 | 0.2240 |
| U238/Ca43 | [nmol/mol] | 4.49 | 4.48 | 4.52 | 0.1265 |
| Al27/Ca43 | [$\mu$mol/mol] | 4.38 | 3.03 | 4.96 | 0.0124 |
| Mn55/Ca43 | [$\mu$mol/mol] | 28.86 | 29.06 | 29.92 | $1.10e^{-7}$ |
| Li7/Ca43 | [$\mu$mol/mol] | 6.09 | 6.05 | 6.07 | 0.7182 |
| | | | *CS2 Cardiff* | | |
| Mg25/Ca43 | [mmol/mol] | 7.15 | 7.24 | 7.13 | 0.0354 |
| B11/Ca43 | [$\mu$mol/mol] | 221.95 | 219.21 | 223.84 | 0.2122 |
| Sr88/Ca43 | [mmol/mol] | 1.69 | 1.69 | 1.69 | 0.0691 |
| Cd111/Ca43 | [$\mu$mol/mol] | 1.56 | 1.69 | 1.52 | 0.3513 |
| U238/Ca43 | [nmol/mol] | 27.21 | 26.75 | 27.32 | 0.2373 |
| Al27/Ca43 | [$\mu$mol/mol] | 69.70 | 69.57 | 68.36 | 0.0398 |
| Mn55/Ca43 | [$\mu$mol/mol] | 201.70 | 187.77 | 201.58 | 0.9804 |
| Li7/Ca43 | [$\mu$mol/mol] | 45.12 | 44.47 | 45.22 | 0.0691 |

number of samples (n) for St. Andrews and Cardiff are 9, and 35, respectively.

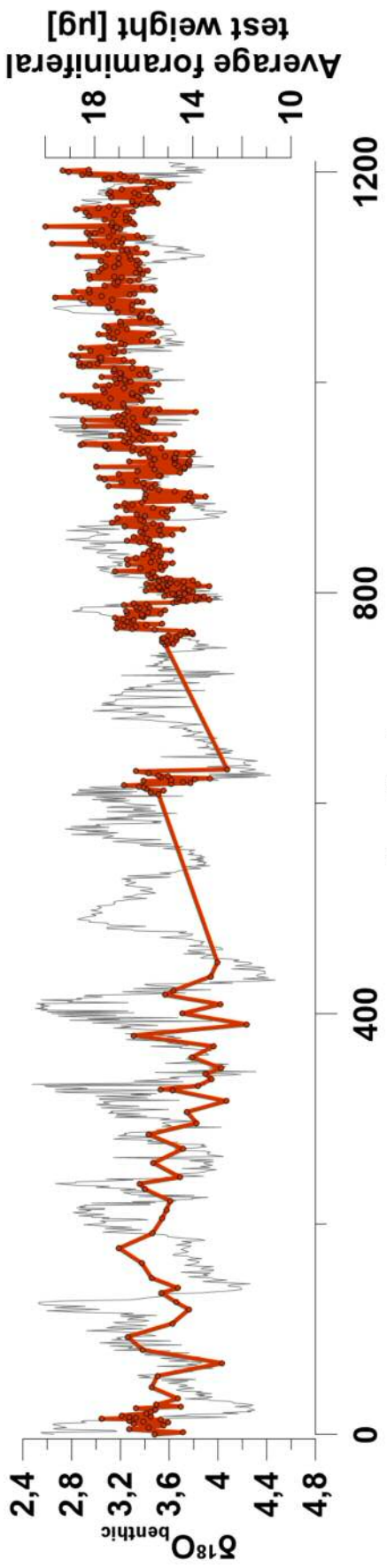


**Figure 5.14** Average test weight in $\mu g$ for single foraminifera shells from ocean sediment core U1476 across the Late Pleistocene (orange). For comparison, benthic oxygen isotopes in grey.

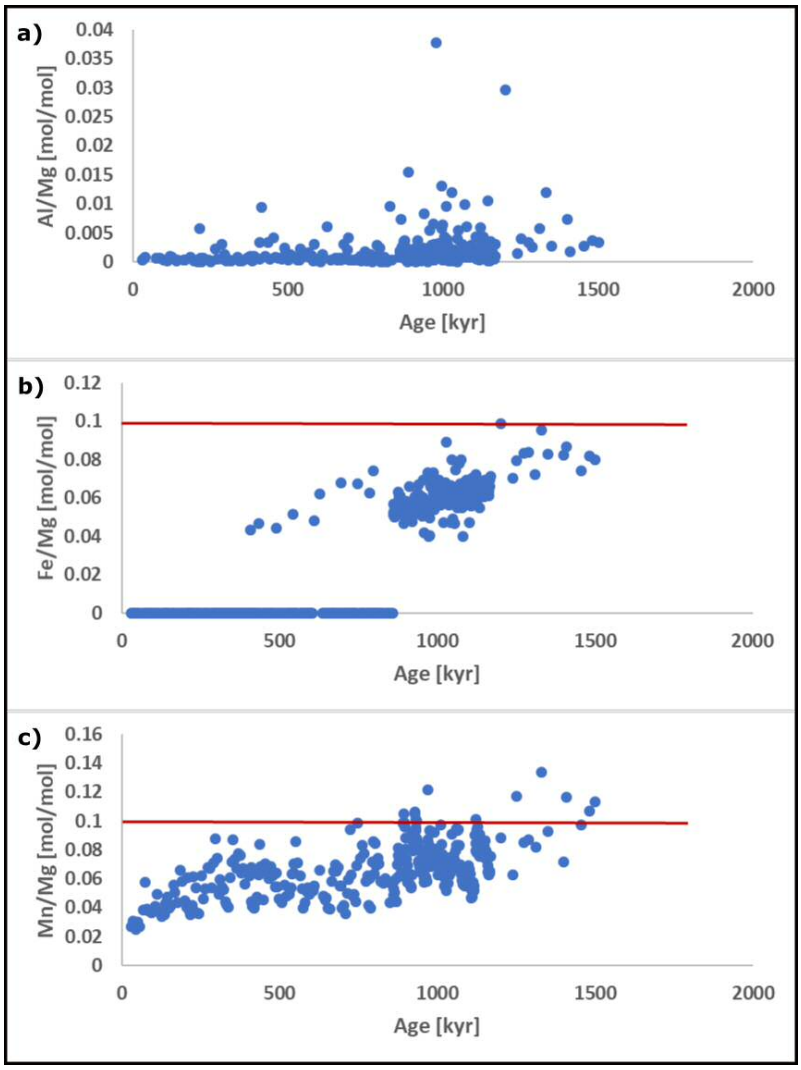


**Figure 5.15** Al/Mg (a), Fe/Mg (b), and Mn/Mg (c) ratios from *G. ruber* (300-355$\mu$m) for core U1476 across the last 1.5Ma. The red line indicates the cleanliness threshold identified by Barker et al. (2003). Samples above the threshold should be considered with caution, as they might contain contamination from clays or organic material which may contain other elements such as Mg, or B. In this case, trace element ratios from these samples may be biased towards the signature of the contaminant. Note that not all analytical analyses included Fe/Mg measurements. All samples that have no Fe/Mg measurement were plotted as 0.

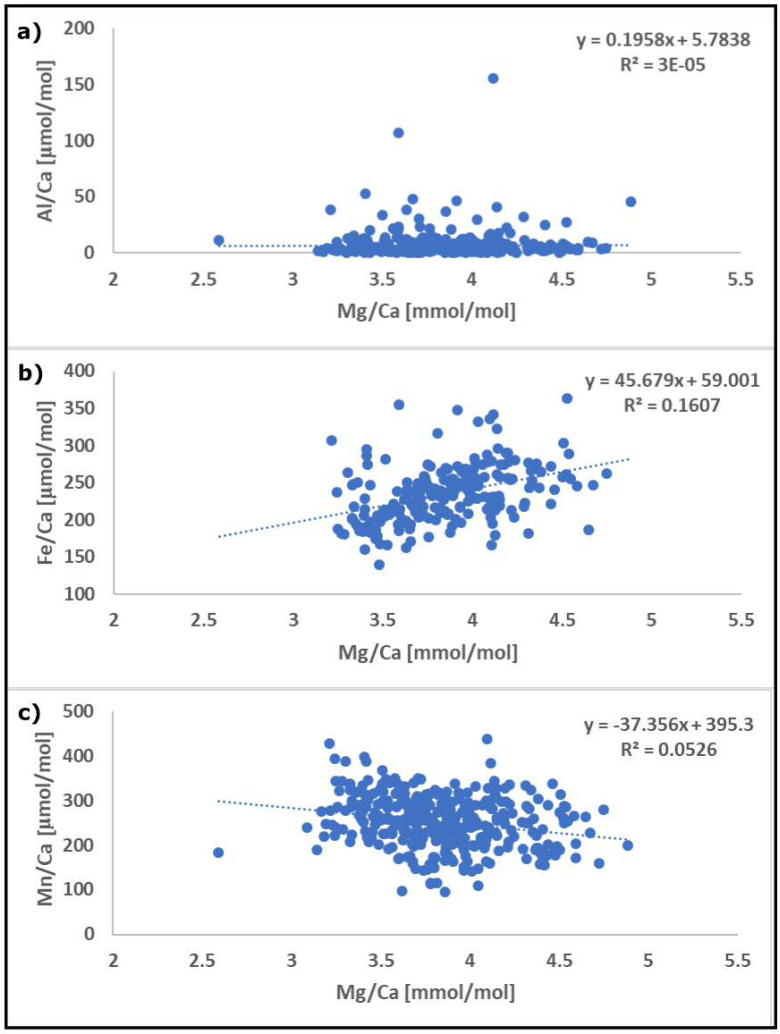


**Figure 5.16** Correlation plots for Al/Ca (a), Fe/Ca (b), and Mn/Ca (c) against Mg/Ca in *G. ruber* (300-355$\mu$m) from U1476. Trend lines and $R^2$ values indicate no correlation in any of the plots. Mg is common in clays, inorganic calcite overgrowth, and organic material. Correlations of contamination tracers against Mg are therefore a useful tool to identify possible influences of contamination sources on foraminiferal calcite trace element ratios.

## 5.4 Age model

The age model for U1476 was created by aligning benthic foraminiferal $\delta^{18}$O from *C. wuellerstorfi* to the benthic LR04 $\delta^{18}$O stack from Lisiecki & Raymo (2005) using 1-3 tiepoints per glacial cycle (Figure 5.17) (Barker et al., unpubl.). The LR04 stack averages benthic $\delta^{18}$O measurements from 57 globally located cores across the last 5.3Ma (Lisiecki & Raymo, 2005) effectively removing local variability and presenting a global signature. The LR04 has therefore been interpreted as overall changes in global climate across this time (Lisiecki & Raymo, 2005). Climate on glacial-interglacial timescales is known to be paced by insolation forcing. Changes in insolation are well understood for the last 5.3Ma (Laskar et al., 1993; Laskar et al., 2004) and provide a tight time constraint for climate signals that follow it. The LR04 has been tuned to the insolation curve aligning each deglaciation to increases in insolation. Now, the insolation timeline can be adopted for the LR04 benthic $\delta^{18}$O stack and acts as reference for other benthic $\delta^{18}$O records.

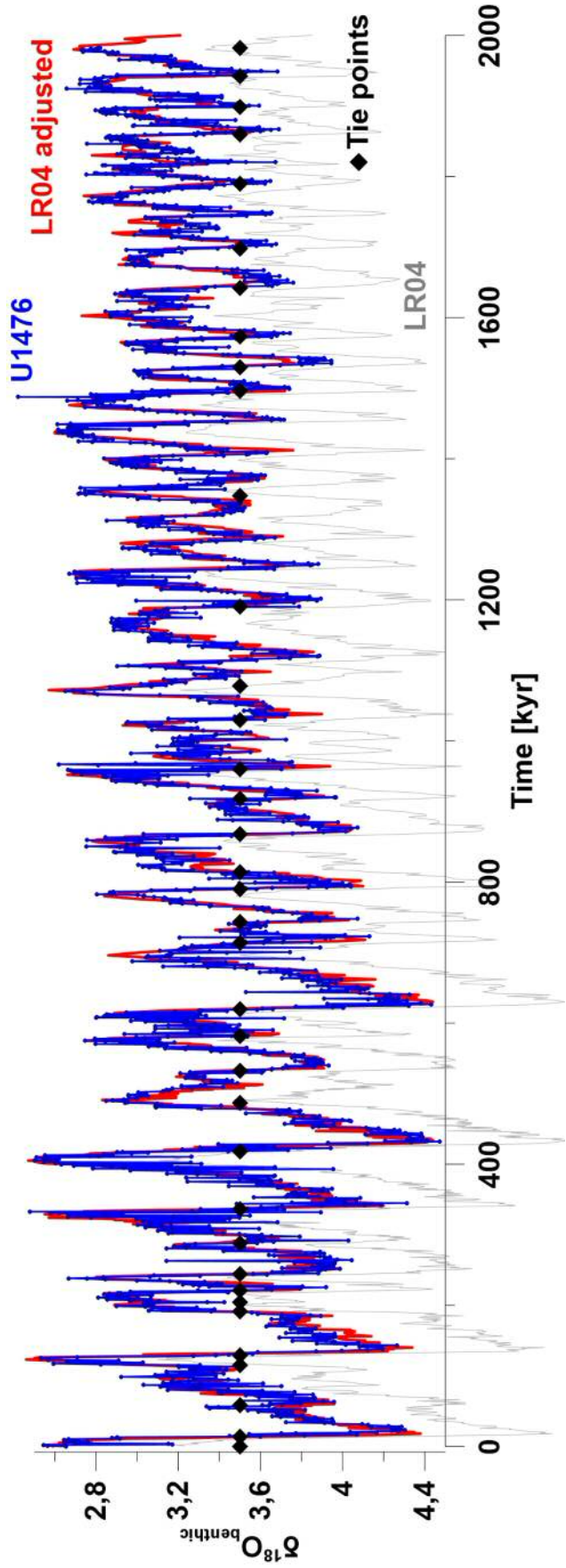


**Figure 5.17** Age model for U1476 (Barker et al., unpubl.). Tie points for U1476 in black diamonds aligning $\delta^{18}O_{benthic}$ to the LR04 benthic stack (Lisiecki & Raymo, 2005). The original stack (in grey) was shifted by -0.64 (in red) to align with the $\delta^{18}O_{benthic}$ record of U1476.

# Chapter 6

# A STUDY OF SAMPLE PREPARATION AND ANALYTICAL BORON ISOTOPE PROCEDURES USING PLANKTONIC FORAMINIFERA

## 6.1 Abstract

Boron isotopes in planktonic foraminifera are widely used as a proxy for palaeo-seawater pH and palaeo-$pCO_2$. Yet, sample preparation and analytical measurements are still difficult, due to small sample sizes and low concentrations, and have mostly been developed for multi-collector inductively plasma mass spectrometry (MC-ICPMS) using a Thermo Neptune mass spectrometer. Here, I present two studies investigating (a) the cleanliness of large samples using conventional planktonic foraminifera cleaning methods which have been designed for small samples, and (b)

the analytical accuracy and precision of boron isotopic standards on a Nu plasma II MC-ICPMS. I find that conventional cleaning methods are sufficient for large samples of up to 200 foraminiferal tests without the need of upscaling the volumes of the cleaning reagents. Additionally, I show that left-over residue or black particles in clean samples have small potential for contamination of B/Ca and Mg/Ca. However, large contamination of IRD, particularly quartz, may alter the final elemental ratio. Under optimal conditions, my accuracy and precision on a Nu plasma II equates to 0.04 ($\pm$0.26; 2x standard deviation) for a 200ppb solution, and 0.06 ($\pm$0.41; 2x standard deviation) for a 50ppb solution of NIST 951. I find that high precision can only be achieved through management of short-, medium-, and long-term mass bias. According to my data, short-term mass bias can be controlled by minimizing mass bias instability, as opposed to tuning for optimal B intensity, whereas medium-, and long-term mass bias are corrected for with effective standard bracketing. I propose that effective standard bracketing can be achieved through shortening the bracketing time by introducing a washout-enhancing method. Finally, I identify that internal errors on single measurements are inherently important for the external precision and provide two options of how to improve internal errors on a Nu plasma II by decreasing the signal to noise ratio. These include increasing the concentration of the sample, or the resistivity on faraday cup collectors.

## 6.2 Introduction

Boron isotopes from foraminiferal calcite has become an important tool for the reconstruction of palaeo-seawater pH and atmospheric $CO_2$ (e.g. Foster, 2008; Hönisch et al., 2009; Martínez-Botí et al., 2015; Rae et al., 2018) However, sample preparation and analysis can be challenging.

Foraminiferal calcite cleaning is important for the boron isotope procedure, due to potentially high boron concentrations in marine sedimentary clays. Planktonic

foraminiferal samples are generally cleaned using the Mg-cleaning method described in Barker et al. (2003), Rosenthal et al. (1997), and Boyle & Keigwin (1985) (Farmer et al., 2016; Foster, 2008; Misra et al., 2014; Rae et al., 2018). This includes removal of clays through 18.2 MΩ MilliQ de-ionized water and Methanol washes, as well as organic matter removal using $H_2O_2$ in a hotbath at 80°C. Reductive cleaning for the removal of ferro-manganese crusts is often omitted (Foster, 2008), as little accumulation of boron was found in ferro-manganese crusts (Boyle & Keigwin, 1985), and trace element measurements may be biased through increased calcite dissolution (Barker et al., 2003).

Due to low concentration of boron in planktonic foraminifera, large samples are often needed to gain a measurable final boron concentration. However, the Mg-cleaning method described by Barker et al. (2003) was primarily developed for small samples up to 25 foraminifera, a representative sample size for trace element ratio analyses. Additionally, no in-depth study was undertaken to identify the contamination potential of ice-rafted debris or microscopic black particles, both commonly found in ocean sediment samples. Instead, the method suggests a time intensive microscope step during which the cleaned sample is carefully checked and any pieces of discoloured calcite, ice-rafted debris, or microscopic black particles are removed using a cow's eyelash brush (Barker et al., 2003). Here, I test whether conventional foraminiferal calcite cleaning methods, which were developed for sample sizes of up to 25 tests, are effective on large samples including up to 200 tests. I then investigate the contamination potential of ice-rafted debris and microscopic black particles on Mg/Ca and B/Ca ratios to understand whether the time consuming microscope step is necessary.

Analytical boron isotope measurements are exceedingly difficult, due to the occurrence of only two natural isotopes, small sample sizes often combined with low sample concentrations, and high potential for contamination. Current published analytical procedures are conducted using a multi-collector inductively coupled

plasma mass spectrometer from Thermo Scientific (Foster, 2008; Rae et al., 2018). For analysis, the samples are purified prior to measurement using column chemistry (Foster, 2008; Rae et al., 2018). Due to the high volatilisation potential of boron which can lead to fractionation, the purified boron samples may not be dried down after collection, and must be run at their elution concentration instead (Foster, 2008; Rae et al., 2018). This necessitates the use of micro-columns which enable elution volumes in the $\mu$L range. Additionally, boron concentrations in planktonic foraminiferal calcite are low, with B/Ca ratios ranging from as low as 40$\mu$mol/mol in *G. bulloides* up to 120$\mu$mol/mol in *G. ruber* (Rae, 2018). As such, 100 *G. ruber* tests usually provide 20ng boron diluted in 600$\mu$L elution acid which amounts to concenctrations around 25ppb (see also Rae, 2018). In the second part of this chapter, I apply published analytical prodedures to a new mass spectrometer in the new CELTIC isotope laboratory facility. I present analytical measurements of boron isotope standards conducted on a Nu plasma II produced by Nu instruments, and give suggestions to the optimal front-end set-up when measuring boron isotopes on a Nu plasma instrument.

## 6.3 Methods

### 6.3.1 Sample preparation for foraminiferal sample cleaning studies

Three tests were conducted investigating (a) the influence of conventional cleaning methods for large samples, as well as the contamination potential of (b) ice-rafted debris residue, and (c) microscopic black particles, on Mg/Ca and B/Ca from planktonic foraminiferal calcite.

Samples were picked from ocean sediment core U1476 (Figure 4.1) for the large sample study, and from ODP982 for the contamination tracer studies (see Table 6.1).

**Table 6.1** Core site, section, and depth for all samples used in the cleaning studies

| Sample code | Core site | Core section | Depth |
|---|---|---|---|
| *Cleaning large samples* | | | |
| *A* | U1476 | CC[a] | 17-19 |
| *B* | U1476 | CC[a] | 27-29 |
| *C* | U1476 | CC[a] | 37-39 |
| *D* | U1476 | CC[a] | 47-49 |
| *E* | U1476 | CC[a] | 07-09 |
| *F* | ODP982 | A3-5 | 60-62 |
| *G* | ODP982 | A4-3 | 70-72 |
| *IRD influence on cleanliness* | | | |
| *H* | ODP982 | A1-1 | 67-69 |
| *I* | ODP982 | A1-1 | 77-79 |
| *J* | ODP982 | A1-1 | 87-89 |
| *K* | ODP982 | A1-1 | 97-99 |
| *L* | ODP982 | A1-1 | 107-109 |
| *Black particle influence on cleanliness* | | | |
| *M* | ODP982 | A1-1 | 67-69 |
| *N* | ODP982 | A1-1 | 77-79 |
| *O* | ODP982 | A1-1 | 87-89 |
| *P* | ODP982 | A1-1 | 97-99 |
| *Q* | ODP982 | A1-5 | 40-42 |
| *R* | ODP982 | A1-5 | 42-44 |
| *S* | ODP982 | A1-5 | 48-50 |
| *T* | ODP982 | A1-5 | 50-52 |

[a]CC: Core catcher sample

Samples will be referred to by their sample code from herein). Core ODP982 was chosen due to its location at 1150m in the North Atlantic on the Rockall plateau (Figure 6.1; Jansen et al., 1996) which causes particularly clay- and organic-rich samples with high concentrations of IRD. All samples were crushed between glass slides and homogenized before division into sub-samples. All samples were cleaned using the Mg-cleaning method by Barker et al. (2003) (see also chapter Materials & Methods 5.3). Before acid-leach, samples were checked under a microscope for residual grains pieces of discoloured calcite. These were picked out by hand using

a cow's eyelash brush. Trace element ratios of Al/Ca, Fe/Ca, Mn/Ca, Mg/Ca and B/Ca were measured on a Thermo X Series ICP mass spectrometer (see also chapter Materials & Methods 5.3). Samples were considered clean if Al/Mg, Fe/Mg and Mn/Mg ratios were below the threshold of 0.1mol/mol (Barker et al., 2003).

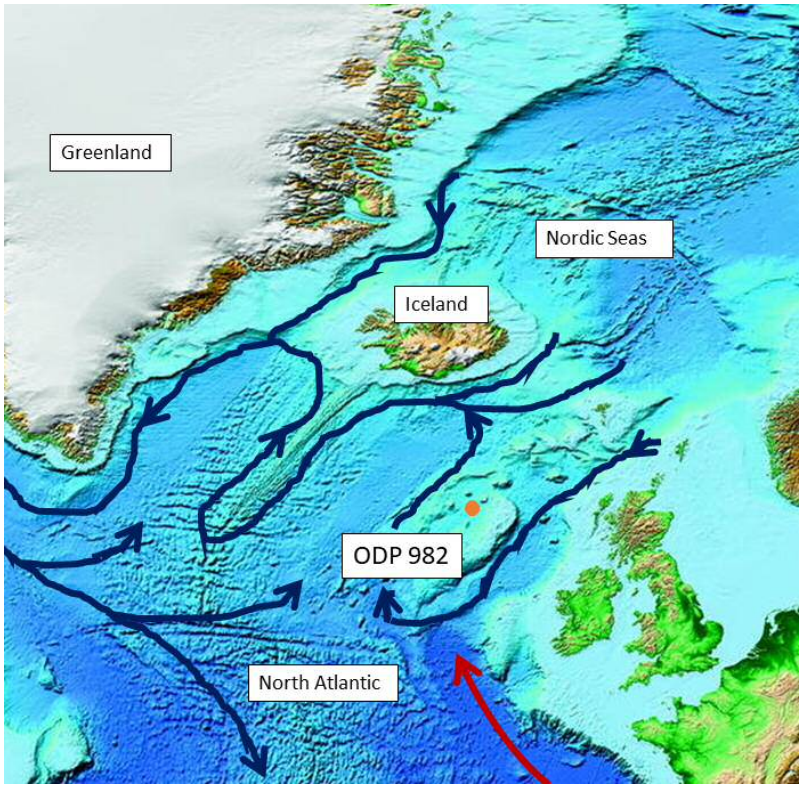


**Figure 6.1** Bathymetry map of the North Atlantic and Nordic Seas showing the location of ODP982 on the Rockall plateau (orange filled circle). Surface and deep water currents indicated with red and blue arrows, respectively.

### 6.3.2 Cleaning study designs

To test the influence of size on sample cleanliness, 600 individual *G. bulloides* tests were divided into sub-samples with each 20, 40, 60, 80, 100, 100, and 200 tests, respectively (Figure 6.2). Samples "20", "40", "60", "80", and "100a" were cleaned in 0.5mL acid-cleaned Eppendorf tubes, while samples "100b" and "200" were cleaned in 1.5mL acid-cleaned Eppendorf tubes.

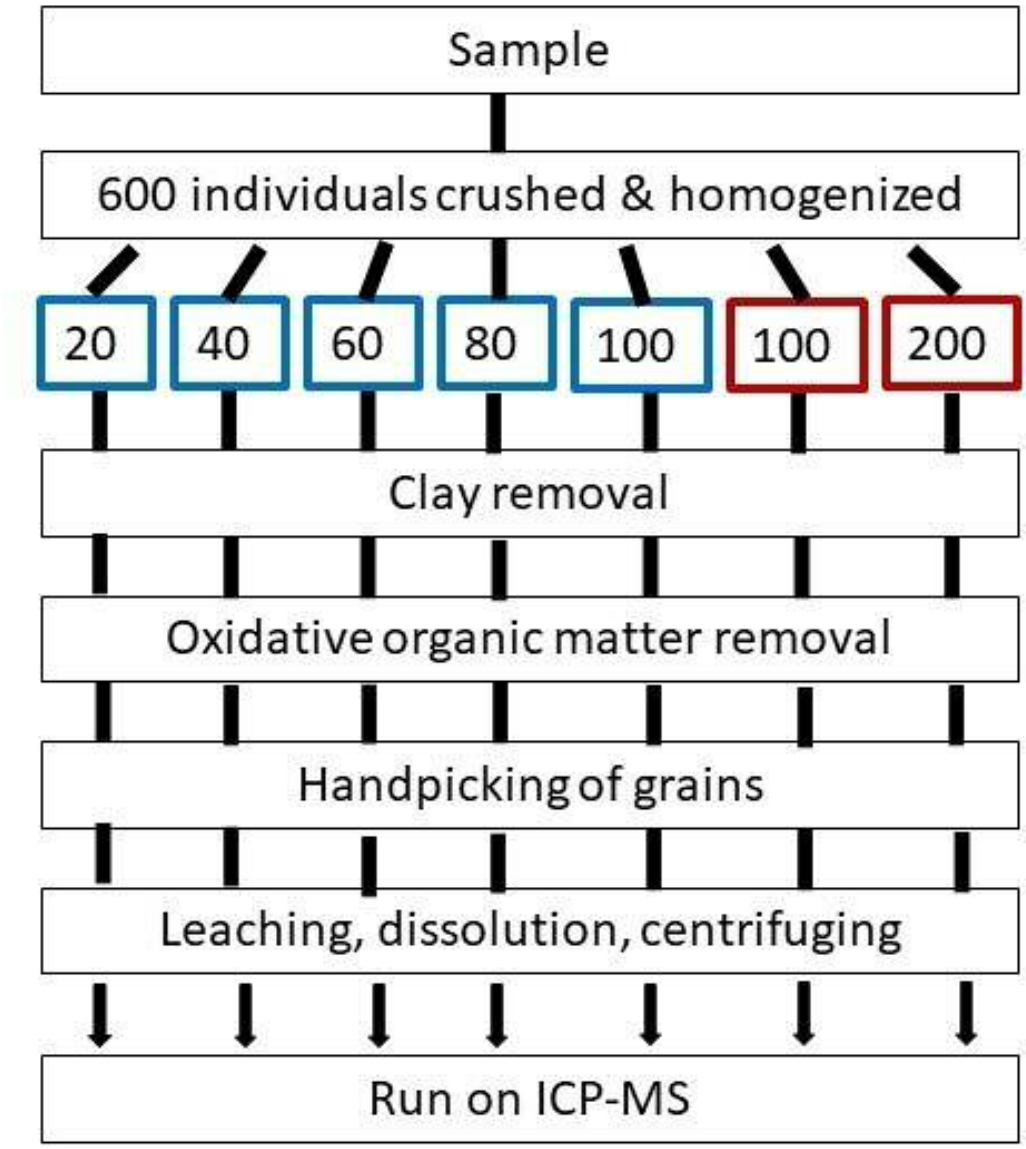


**Figure 6.2** Flow chart showing the study design for the cleaning of large foraminiferal samples. The amount of foraminiferal tests in each sub-sample is shown by the large numbers. Blue squared sub-samples indicate crushing and cleaning conducted in 0.5mL vials, and red squared sub-samples in 1.5mL vials. The different stages refer to cleaning steps undertaken for each sample. Arrows show which cleaning step was conducted for which sub-sample.

To investigate the influence of IRD and microscopic black particles on sample cleanliness, 250 individual *G. bulloides* tests were picked from consecutive glacial samples, and sub-divided into samples containing 25 tests (see Figures 6.3 and 6.4).

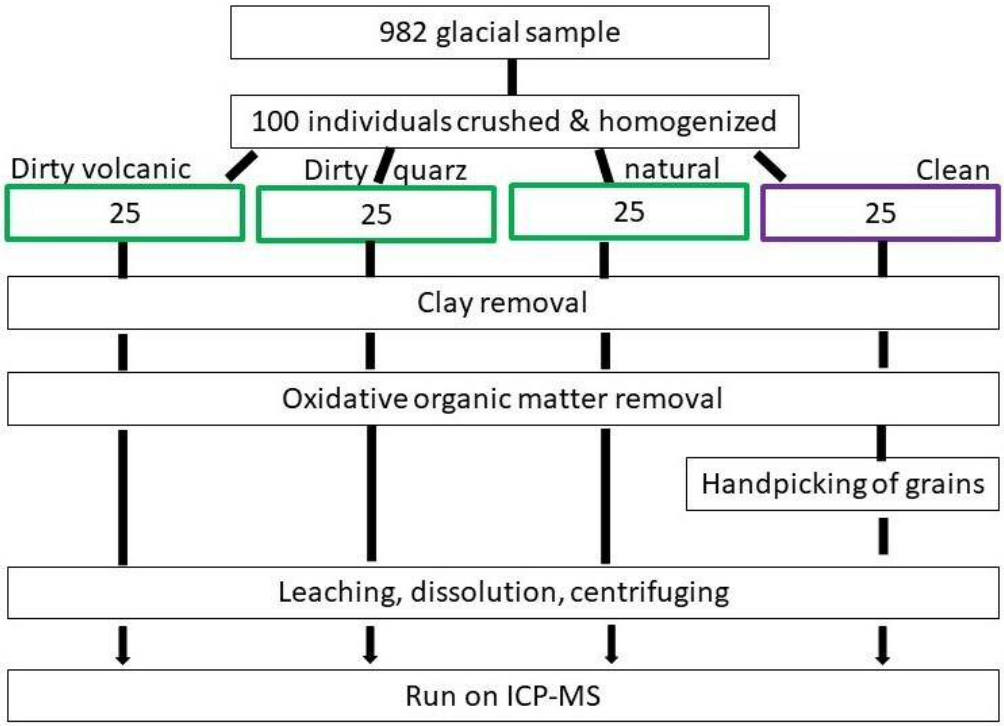


**Figure 6.3** Flow charts showing the study design for testing the influence of IRD contamination on the cleanliness and elemental ratios of planktonic foraminiferal calcite samples. The amount of foraminiferal tests in each sub-sample is shown by the large numbers. Green boxes indicate samples with additional IRD or IRD residue, while the purple box shows the clean control. The different stages refer to cleaning steps undertaken for each sample. Arrows show which cleaning step was conducted for which sub-sample.

The different sub-samples received varying treatments. For the IRD study, these included (i) addition of volcanic IRD grains picked from the same sample ("dirty volcanic"), (ii) addition of quartz IRD grains picked from the same sample ("dirty quartz"), (iii) omitting the cow's eyelash brush picking stage ("normal"), and (iv) fully cleaned control ("clean"). For the black particle study, sub-samples were divided into samples of (i) fully cleaned control, and (ii) additionally added black particles from cleaned control samples.

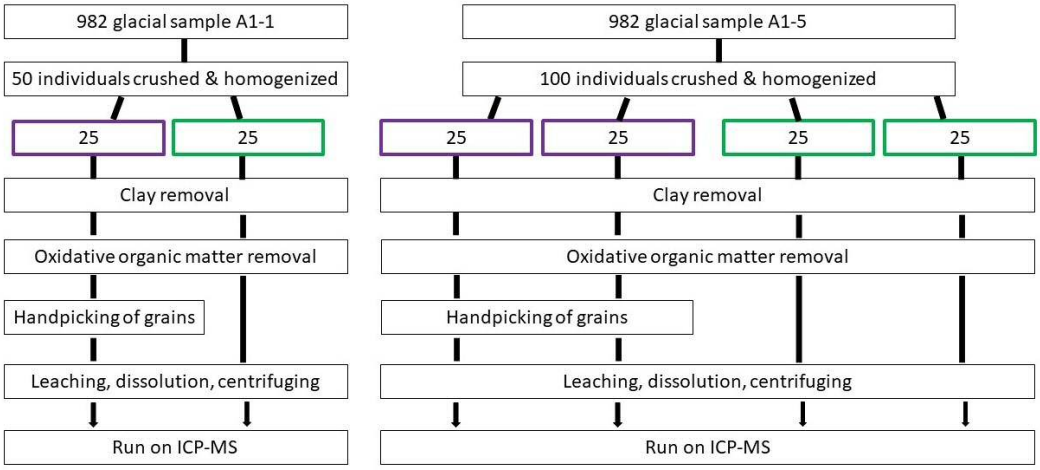


**Figure 6.4** Flow chart showing the study design for testing the influence of black particle contamination on the cleanliness and elemental ratios of planktonic foraminiferal calcite samples. The top box indicates the original ocean sediment sample. The amount of foraminiferal tests in each sub-sample is shown by the large numbers. Green boxes indicate samples with additional black particles, while purple boxes show the clean control. The different stages refer to cleaning steps undertaken for each sample. Arrows show which cleaning step was conducted for which sub-sample.

### 6.3.3 Analytical development and Nu plasma II MC-ICPMS set-up

The most widely used analytical protocols for boron isotope measurements include the methods described by Foster (2008) and Rae et al. (2018). In these protocols, purified boron samples are analysed on a Thermo Neptune or Neptune Plus mass spectrometer equipped with Faraday cups in positions L3, and H3 connected to either $10^{11}\Omega$ or $10^{13}\Omega$ resistors. Sample introduction occurs via self-aspirating nebulisers at low flow rates of either $50\mu$L/min or $35\mu$L/min and aerosol formation in a PFA barrel spray chamber connected to a Sapphire injector torch. Analytical measurements are conducted following a standard-bracketing procedure where samples are compared to the boric acid reference standard NIST 951 with a defined $\delta^{11}B$ ratio of 0. To improve bracketing time, washout-enhancing methods are used. These include inlet of gaseous $NH_3$ (Foster, 2008), and HF-addition (Rae et al., 2018). Standard and

sample precision are published as ±0.3‰ for the Foster (2008), and as ±0.23‰ for the Rae et al. (2018) protocols, respectively.

I employed a comparable set-up on the Nu plasma II, with sample injection occurring through a 100$\mu$L/min flow rate PFA self-aspirating nebulizer connected to a PFA barrel spray chamber and a sapphire injector. Nebulizer uptake rates were generally between 50 and 60 seconds. Ions collected were transferred to volts on faraday cups in positions L3, and H9, and amplified by $10^{11}\Omega$ resistors with a settling response time of 2 seconds. Here,I designed my methods with traditional washout procedures without washout-enhancers.

I present my initial results for standard measurements conducted on a Nu plasma II in reference to boric acid standard NIST 951. The accuracy and precision of the instrument are assessed by calculating the average and 2x standard deviation ($\sigma$) of bracketed standard measurements. Each measurement is the result of multiple measurements integrated over a time t. To assess the error on bracketing measurements, I calculate the internal error defined as standard deviation $\sigma/\sqrt{n}$, where n is the number of integrations conducted during integration time t.

### 6.3.4 Boron standard preparation for analytical method testing

Multiple boron isotope standards exist. Here, I use two boric acid-based boron isotope standards NIST 951 ($\delta^{11}B$=0), and ERM AE121 ($\delta^{11}B \sim 19.9\pm0.6$) (Brand et al., 2014) at different concentrations ranging from 25ppb to 200ppb. Standards were diluted using 0.5M $HNO_3$ which consisted of in-house distilled concentrated $HNO_3$, and 18.2MΩ resisting de-ionized MQ water. All dilutions were conducted in ultra-clean laminar flow hoods equipped with boron-free HEPA filters to reduce contamination.

## 6.4 Cleaning large samples for boron isotopic analyses

### 6.4.1 Conventional cleaning methods suitable for large planktonic foraminifera samples

There is no consistent offset in cleanliness (Al/Mg, Fe/Mg, Mn/Mg) with sample size, suggesting the cleaning method is effective in cleaning small and large samples irrespective of tube size. Contaminant tracers Al/Mg and Fe/Mg are below the 0.1 mol/mol contamination line for nearly all sub-samples (Figure 6.5).

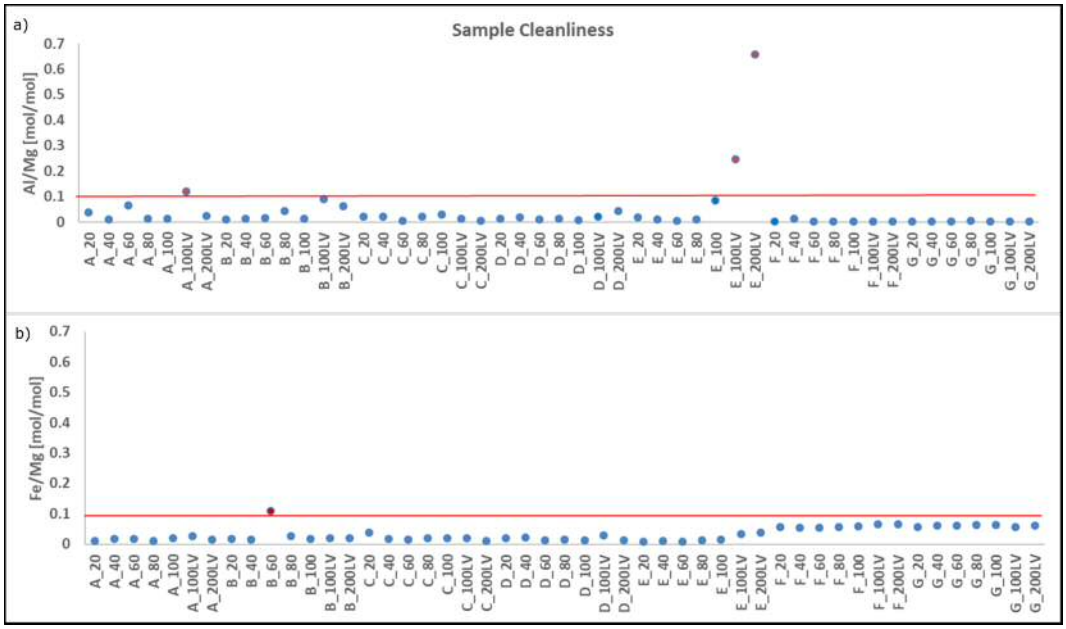


**Figure 6.5** Cleanliness indicators, Al/Mg (a) and Fe/Mg (b), for sub-samples from the sample size analysis. The red line indicates the cleanliness threshold of 0.1mol/mol (see also (2003)). Sub-samples with Al/Mg and Fe/Mg concentrations below the threshold are considered clean. 7 samples were used for sub-sampling (samples A-G; see also 6.1). Sub-samples are labelled as 20, 40, 60, 80, 100, 200 which corresponds to the foraminiferal test number within each sub-sample. Sub-samples cleaned in large 1.5mL vials are labelled as LV.

Three sub-samples present higher Al/Ca, including two "100b" samples cleaned in large vials. This could suggest that cleaning procedures are not optimised for large samples cleaned in large vials. However, all three samples were cleaned in the

same batch hinting towards inconsistencies between batches cleaned rather than a size effect. Only one sample presents high Fe/Ca values. This hints towards spot contamination from the tube rather than an insufficient cleaning method.

B/Ca and Mg/Ca ratios also show no significant effect with sample size (Figure 6.6) providing evidence that contamination levels in large samples are sufficiently reduced to reproduce the signature of B/Ca and Mg/Ca in small samples.

After normalization to the distribution mean, B/Ca ratios of large samples ("200") appear to plot as averages of smaller samples suggesting that larger samples might yield better average sample results (Figure 6.7). Normalized Mg/Ca of samples "200" plots slightly higher than the small sample average, however well within the 2x standard deviation of $\pm 0.19$.

In summary, the results support current cleaning methods as useful preparation methods for elemental and isotopic analyses on large planktonic foraminiferal samples. Current methods have the potential of up to 50% carbonate loss during cleaning (Barker et al., 2003). The results above confirm that no scaling of the cleaning reagents is needed for samples of up to 200 planktonic foraminifera. This suggests that cleaning may currently be too rigorous, and reducing reagent strength could help to lower carbonate loss. Additionally, it may reduce the degree of cleaning-induced partial dissolution which has been reported as a concern for accurate and precise elemental ratios (Barker et al., 2003).

### 6.4.2 Influence of mafic- and quartz-based ice-rafted debris (IRD) residue and black particle residue on Mg/Ca and B/Ca in planktonic foraminifera

Conventional cleaning methods for planktonic foraminifera do not include a specific step concerned with the removal of IRD-based residue. It is suggested in the protocol by Barker et al. (2003) to remove any residue or discoloured calcite by hand using

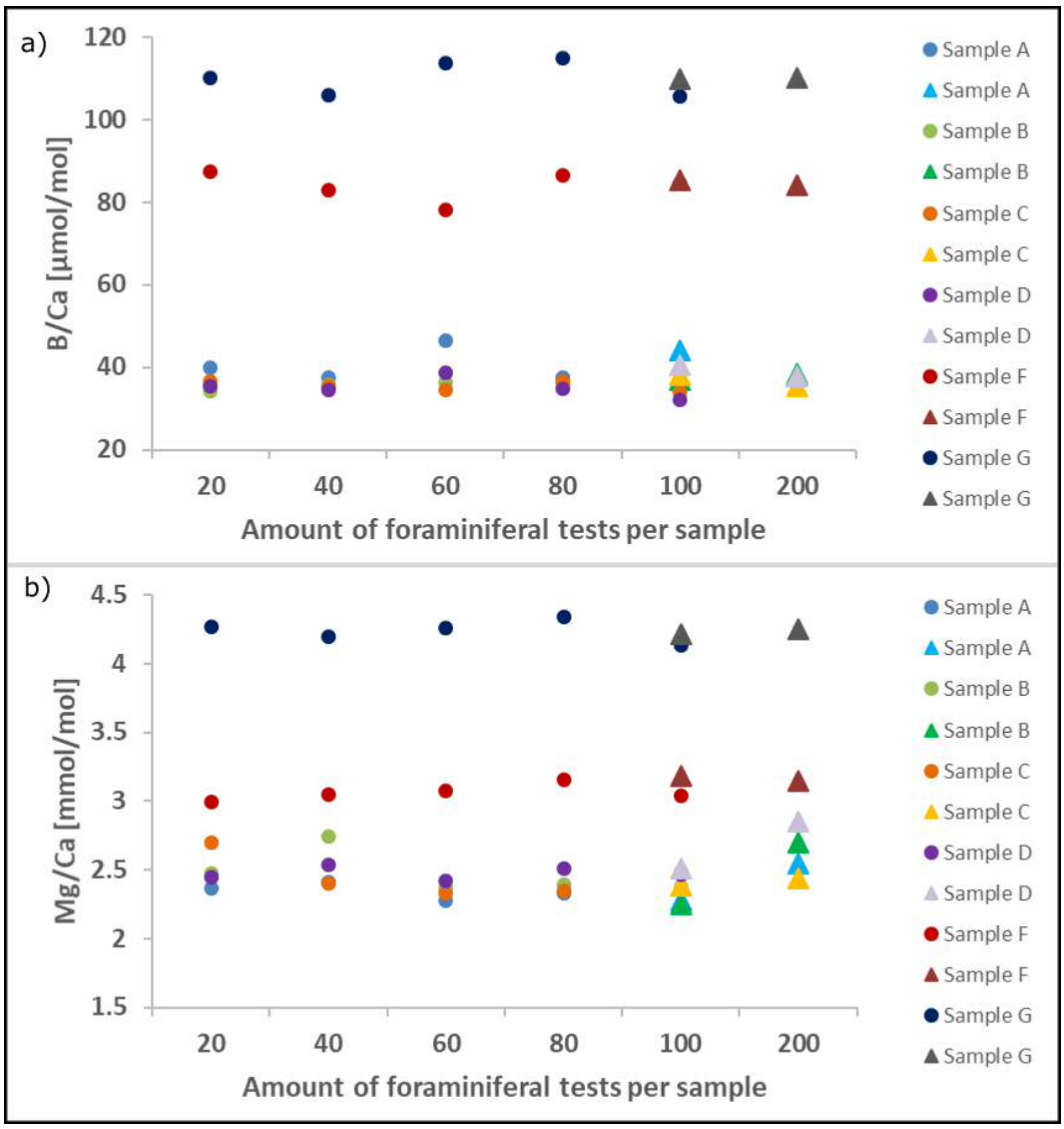


**Figure 6.6** B/Ca (a) and Mg/Ca (b) for different sized sub-samples. Sub-samples are plotted according to sample size (amount of foraminiferal tests per sample). Sub-samples cleaned in small 0.5mL Eppendorf vials are indicated by filled circles. Sub-samples cleaned in large 1.5mL vials are plotted as triangles. Sub-samples from the same sample (A-G; see also table 6.1) are plotted in the same colour. For better comparison, triangle-sub-samples from the same sample are plotted in a different shade.

a cow's eyelash brush. This involves transferring the clean sample to an indented picking slide and examining it under a microscope which carries risk for post-clean-contamination.

My data show an increase for Al/Mg and Fe/Mg above the threshold of 0.1mol/mol for "dirty quartz" and "dirty mafic" samples, reaching up to 1.5mol/mol Al/Mg for

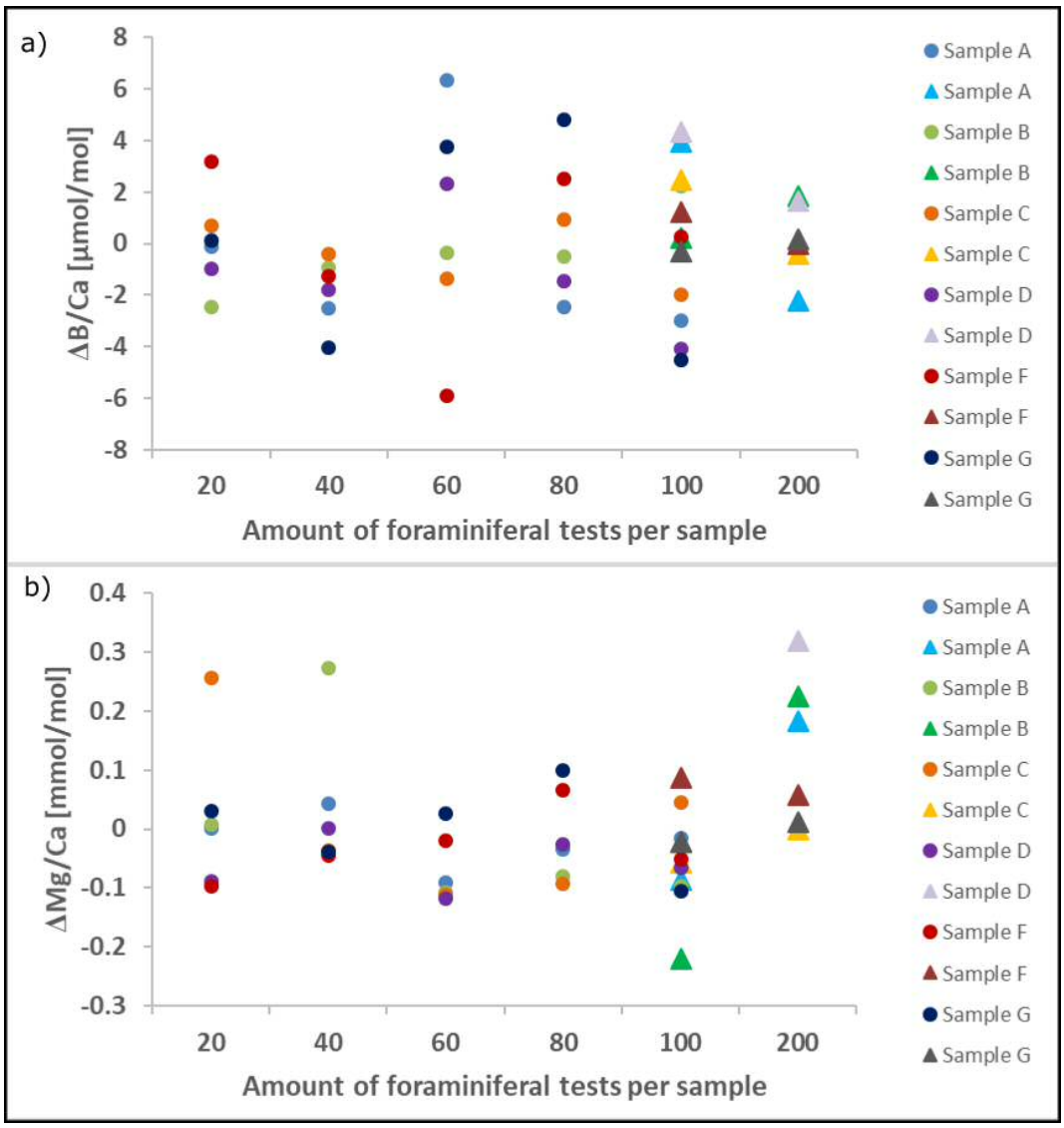


**Figure 6.7** B/Ca (a) and Mg/Ca (b) for different sized sub-samples normalised to the sample mean. Sub-samples are plotted according to sample size (amount of foraminiferal tests per sample). Sub-samples cleaned in small 0.5mL Eppendorf vials are indicated by filled circles. Sub-samples cleaned in large 1.5mL vials are plotted as triangles. Sub-samples from the same sample (A-G; see also table 6.1) are plotted in the same colour. For better comparison, triangle-sub-samples from the same sample are plotted in a different shade.

dirty mafic in sample J (Figure 6.8). In comparison, Al/Mg and Fe/Mg are below the threshold of 0.1mol/mol in all "clean" and "normal" samples (Figure 6.8). This suggests that that IRD grains have a high potential for sample contamination in Al and Fe, particularly mafic IRD. Conversely, I see no difference between "clean" and

"normal" samples, clarifying that contamination only occurs in samples with large IRD content unnatural in hand-picked foraminiferal samples.

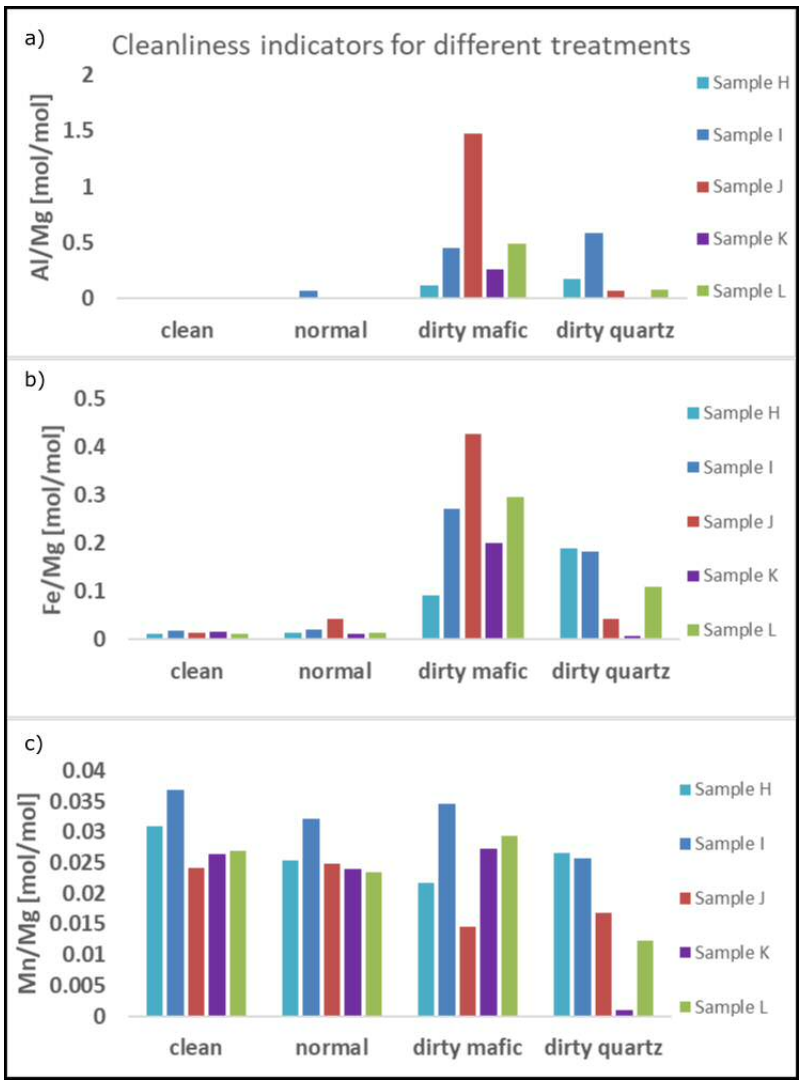


**Figure 6.8** Cleanliness indicators Al/Mg (a), Fe/Mg (b), and Mn/Mg (c) for five glacial samples (H-L; see also table 6.1) with four different contamination treatments including clean control, normal, dirty mafic and dirty quartz. For comparison, samples above the cleanliness threshold of 0.1mol/mol are considered contaminated.

Contamination is particularly concerning if complexed to climate-proxy-elements such as Mg, or B. After averaging Mg/Ca and B/Ca across treatments to get a representative glacial value, I find that there is no significant difference between B/Ca ratios in all treatments, and Mg/Ca ratios in "clean" and "normal" samples (Figure 6.9). In contrast, Mg/Ca in "dirty mafic" and "dirty quartz" plot outside

the 2x standard deviation of the clean average across samples with "dirty quartz" samples showing the largest offset (Figure 6.9).

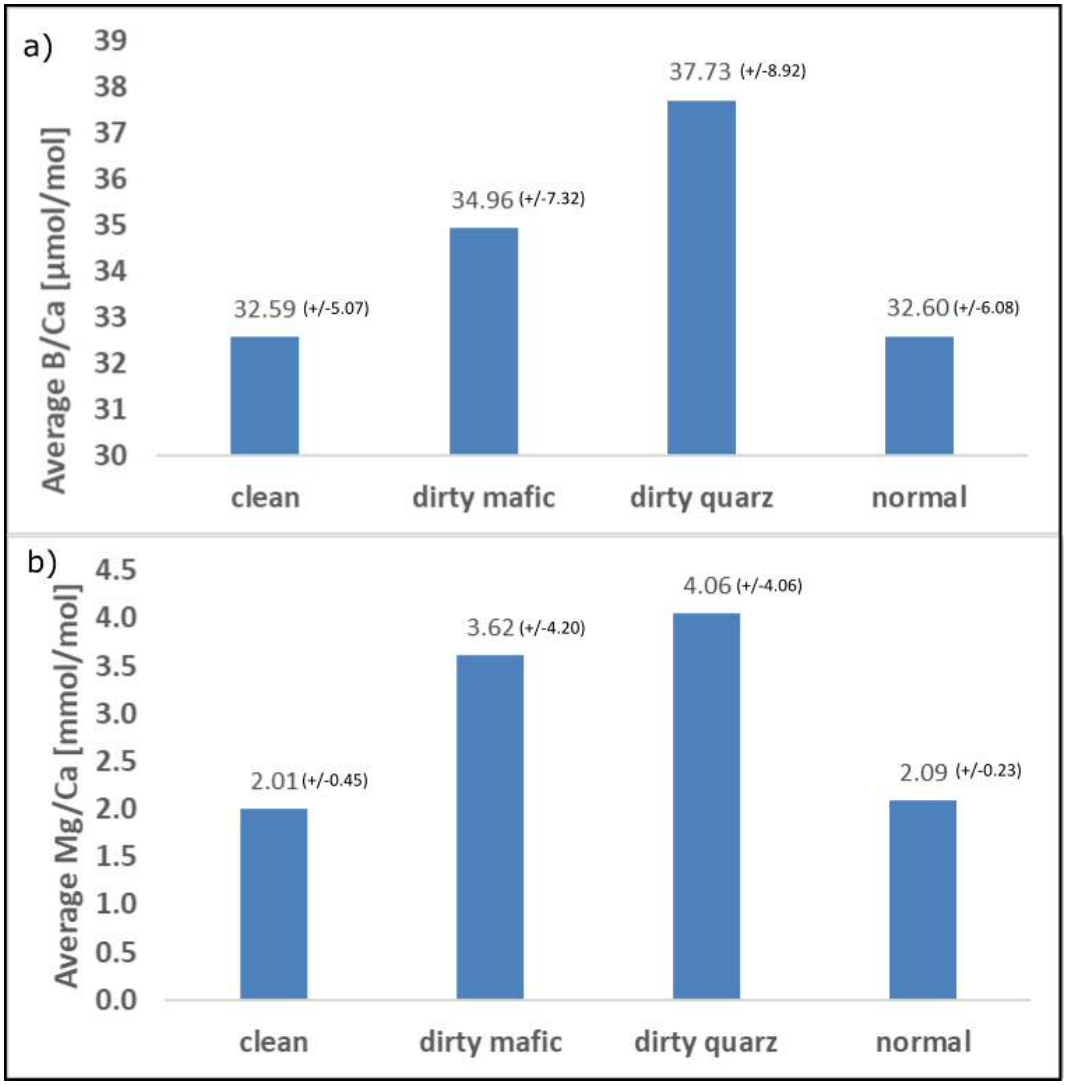


**Figure 6.9** (a) B/Ca after averaging 5 glacial samples (H-L; see also table 6.1), and (b) Mg/Ca after averaging 4 glacial samples (H-J,L). Averages and 2x standard deviations ($\sigma$) are printed above the bars. $\sigma$ values are high due to temperature-induced offsets between samples H-L. Averages between treatments are still comparable, since the offset is constant between treatments.

B/Ca values for "dirty quartz" show an offset of $\sim$0.06 above 2x standard deviation, which approximates the measurement error for B/Ca, and is therefore insignificant (Figure 6.9a).

Similar conclusions can be drawn from the black particle test. To analyse whether there is a difference between particle and no-particle sub-samples, I first averaged

particle and no-particle sub-samples from glacial sample A1-1, and A1-5 individually assuming that differences between subsamples within A1-1, and A1-5 are small. I then combined the resulting averages from both samples into one dataset per treatment. This resulted in two distributions with each 8 values for particle, and no-particle, respectively. Plotting the distributions as boxplots shows that medians for B/Ca and Mg/Ca fall within the $1^{st}$ and $3^{rd}$ quantiles, or the error of these, of either distribution (Figure 6.10). Therefore, there is no difference between the two treatments in either B/Ca or Mg/Ca suggesting that the existence of black particles in samples has no effect on final B/Ca or Mg/Ca measurements. In fact, I noticed that cleaning the samples was in itself efficient in removing black particles assumingly due to the water wash steps. As such, the "particle" samples lost some of their previously added black particles during the cleaning, with residual black particle densities not causing any contamination in B/Ca or Mg/Ca as shown above. Picking black particles by hand is therefore unnecessary.

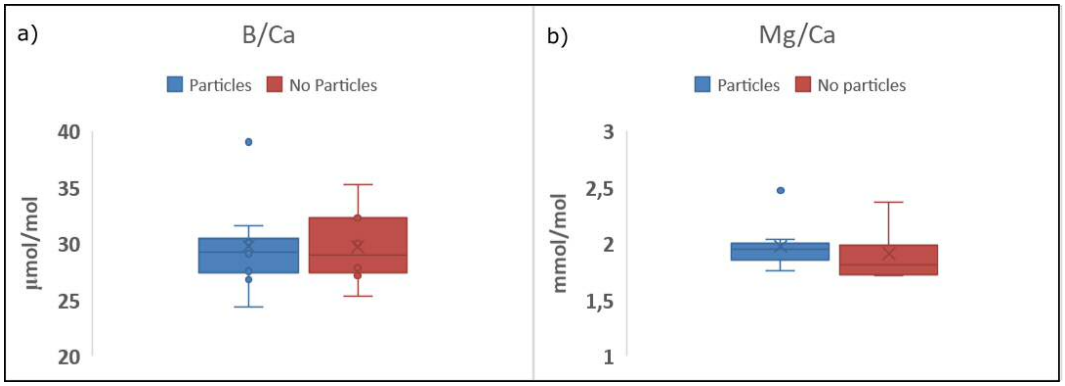


**Figure 6.10** Boxplots for B/Ca (a) and Mg/Ca (b) showing the different distributions of all sub-samples with and without black particle contamination. The distributions were created by combining sub-samples from A1-1 with averaged sub-samples from A1-5 (see also table 6.1). The line in the middle of the box shows the median of the distribution. The lower and upper limits on the box represent the $1^{st}$ and $3^{rd}$ quantiles of the datasets.

This is also supported by the contamination tracers which show Al/Mg and Fe/Mg to be below the threshold for all samples (suplementary Figure 6.11).

Surprisingly, a suite of particle-cleaned samples from glacial interval A1-5 present high Mn/Mg values of up to 0.27mol/mol (Figure 6.12).

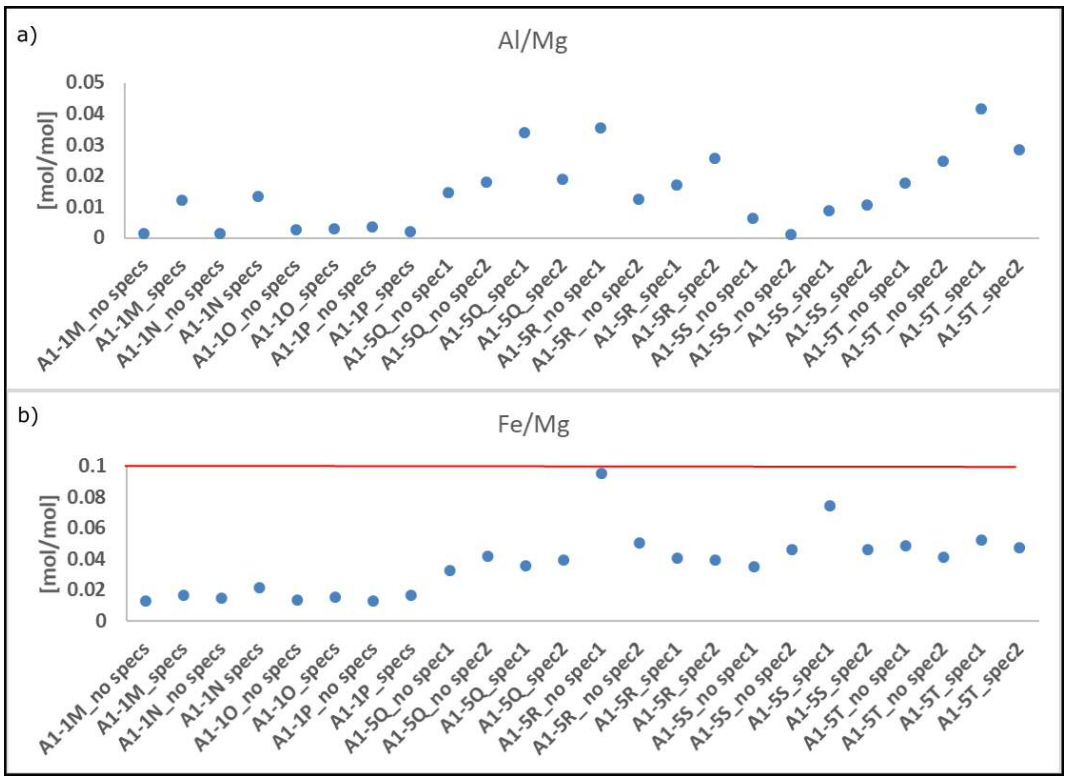


**Figure 6.11** Contamination indicators Al/Mg (a) and Fe/Mg (b) for the black particle ("spec") study. "Spec"-samples contain added black particles, while "no spec"-samples are clean controls. Sub-samples were picked from several samples (M-T; see also table 6.1). Samples M-P, and Q-T, originated from glacial intervals A1-1, and A1-5, respectively.

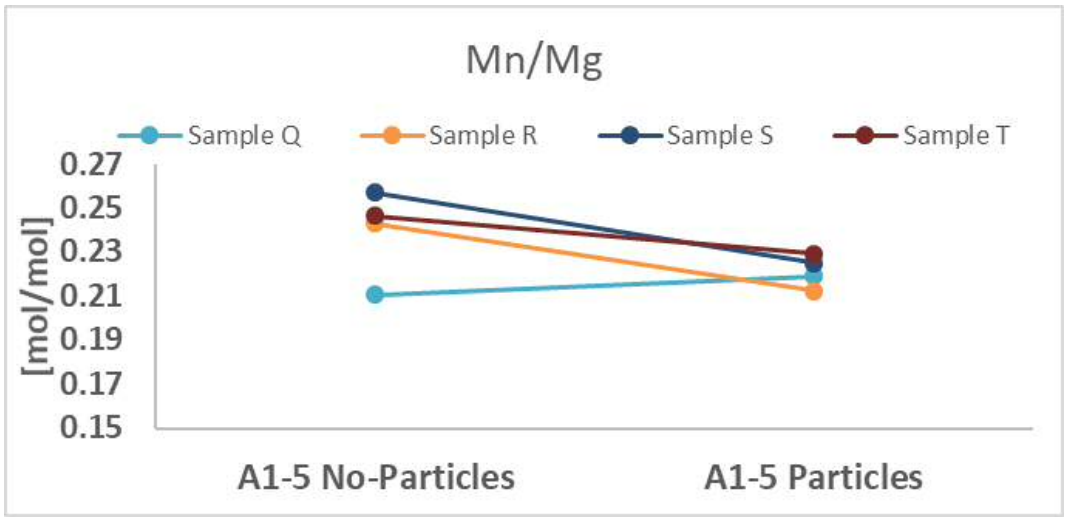


**Figure 6.12** Mn/Mg ratios for sub-sample averages from glacial interval A1-5 plotted according to treatment. Note, all Mn/Mg ratios are above the cleanliness threshold of 0.1mol/mol and are therefore classified as contaminated.

These do not correlate with high Fe confirming that Mn was not released from potential ferromanganese crusts (Figure 6.13). It appears that no-particle samples have marginally more Mn in 3 out of 4 samples (Figure 6.12). This potentially suggests that picking the specs leads to Mn contamination through the brush or microscope. However, the effect cannot be significant as the other suite of samples have very low Mn/Mg values (<0.035mol/mol). The two suites were cleaned as batches on different days (Figure 6.13). It is therefore likely that one batch received Mn contamination during cleaning on this specific day.

In conclusion, I find significant leaching potential in mafic- and quartz-based IRD grains for Mg/Ca, but not B/Ca, with higher leachate concentrations from mafic-based IRD. Amounts of black particles left after cleaning show no leaching potential. Quartz-based IRD grains present the greatest influence on Mg/Ca suggesting that quartz-sourced leachates carry potential for Mg contamination. This however was only the case in unnaturally enriched IRD samples which are unlikely in hand-picked planktonic foraminiferal calcite samples. I could not find any influence of potential IRD-based residue on Mg/Ca or B/Ca in "normal" samples. As such, I propose omitting the cow's eyelash picking step under the microscope. Instead I recommend checking the sample after cleaning by eye under the microscope by opening the lid of the Eppendorf vial and and visually inspecting it. Based on the results from this study, I suggest that picking out residue or discoloured calcite is only necessary in samples with high visual residue or particle density (>10 particles visible at the same time in a cleaned sample with 25 foraminifera). In other samples, picking out residue or particles may lead to unnecessary contamination.

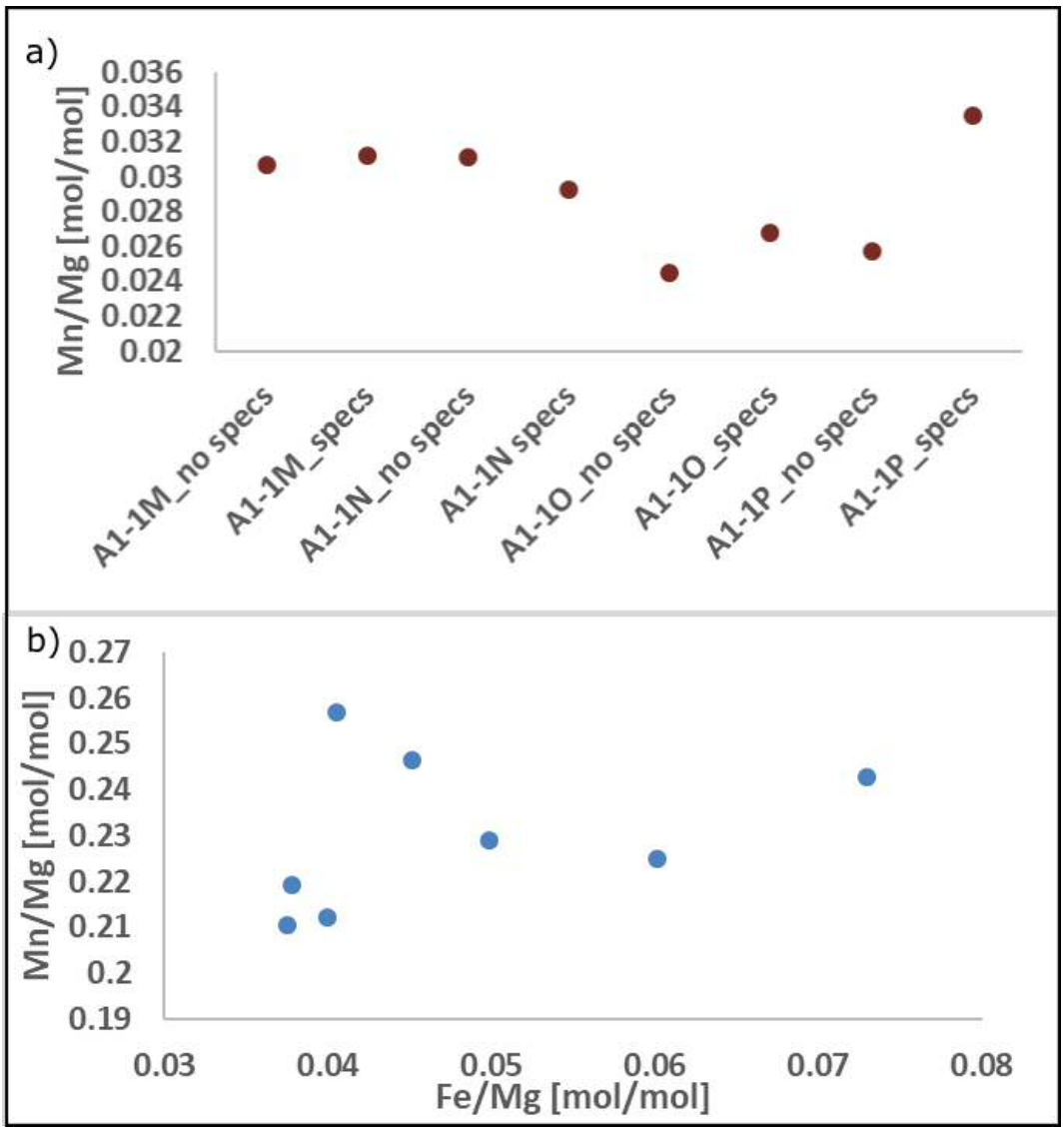


**Figure 6.13** (a) Mn/Mg ratios for sub-samples from glacial interval A1-1. All samples plot below the threshold of 0.1mol/mol and are therefore considered clean. (b) Cross-plot between Fe/Mg and Mn/Mg as indication of whether Mn-contamination is sourced from ferromanganese crusts. There is no correlation suggesting different sources for Mn.

## 6.5 Analytical analyses of boron isotopic standards on a Nu plasma II

### 6.5.1 Resulting accuracy and precision from glass cyclonic and PFA cyclonic compared to PFA barrel spray chambers on a Nu plasma II

PFA barrel spray chambers in combination with low rates self-aspirating Savillex nebulizers are typical for Thermo Neptune boron set-ups. Here, I tested instrument accuracy and precision using a PFA barrel spray chamber with a 66$\mu$L flow rate Savillex self-aspirating nebulizer on a Nu plasma II. Standards were integrated over 2 minutes, and bracketed by 0.5M $HNO_3$ blank measurements integrated over 1 minute. Between measurements, the instrument was washed out for 3 minutes using 0.5M $HNO_3$ from a different vial. 25ppb NIST 951 standard intensities for $^{11}B$ were generally around 100mV, with blank measurements around 1mV. For 6 bracketed 25ppb NIST951 standard measurements, accuracy and precision resulted in -0.08($\pm$0.58) (Figure 6.14).

To investigate whether other types of spray chambers give better precision for NIST 951 on a Nu plasma II, I repeated the NIST 951 standard runs using a PFA (polytetrafluoroethylene) cyclonic and a glass (borosilicate) cyclonic spray chamber. Accuracy and precision using PFA cyclonic resulted in 0.12($\pm$0.49) for 31 bracketed 25ppb, and -0.06($\pm$0.41) for 10 bracketed 50ppb NIST 951 standards (Figure 6.15).

Using a glass cyclonic spray chamber, precision degraded over the duration of a day from 0.00($\pm$0.25) to 0.40($\pm$0.91) (Table 6.2, Figure 6.16).

Accuracy and precision improved to -0.01($\pm$0.24) when increasing washout times on the glass spray chamber to 4min, but degraded to 0.19($\pm$0.53) when reducing the NIST 951 concentration from 50ppb to 25ppb keeping a 4 minute washout. As

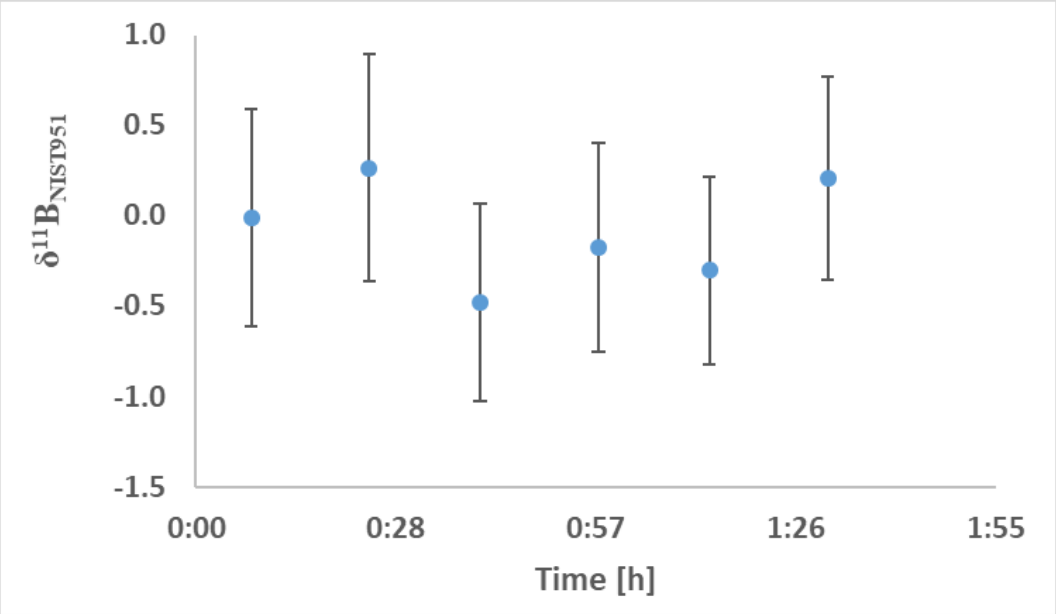


**Figure 6.14** Blank-corrected boron isotope ratios on a 25ppb NIST 951 solution measured during a run employing a PFA barrel spray chamber and 66$\mu$L flowrate Savillex nebulizer.

**Table 6.2** Changes in accuracy and precision of six 50ppb NIST951 brackets over time using a glass cyclonic spray chamber

| | | **Test A** | **Test B** | **Test C** |
|---|---|---|---|---|
| **Accuracy** | $\bar{\chi}$ | 0.00 | -0.20 | -0.40 |
| **Precision** | $\sigma$ | $\pm$0.25 | $\pm$0.38 | $\pm$0.91 |
| **Propagated internal errors** | $\sigma/\sqrt{n}$ | $\pm$0.23 | $\pm$0.25 | $\pm$0.22 |

such, the glass spray chamber did not improve precision, despite higher intensities of 540mV, compared to 340mV for a 50ppb NIST 951 solution. The results are likely due to the increased boron memory effect in a glass spray chamber, whereby glass appears to worsen the washout process. This was also evident from blank measurements which show glassware backgrounds around 9mV, compared to 1-3mV in PFA-ware.

To exclude the memory effect on accuracy and precision, I collected a series of continuous NIST 951 standard measurements during which the probe never left the standard. Accuracy and precision were similar at 0.10($\pm$0.57) for 8 continuous NIST

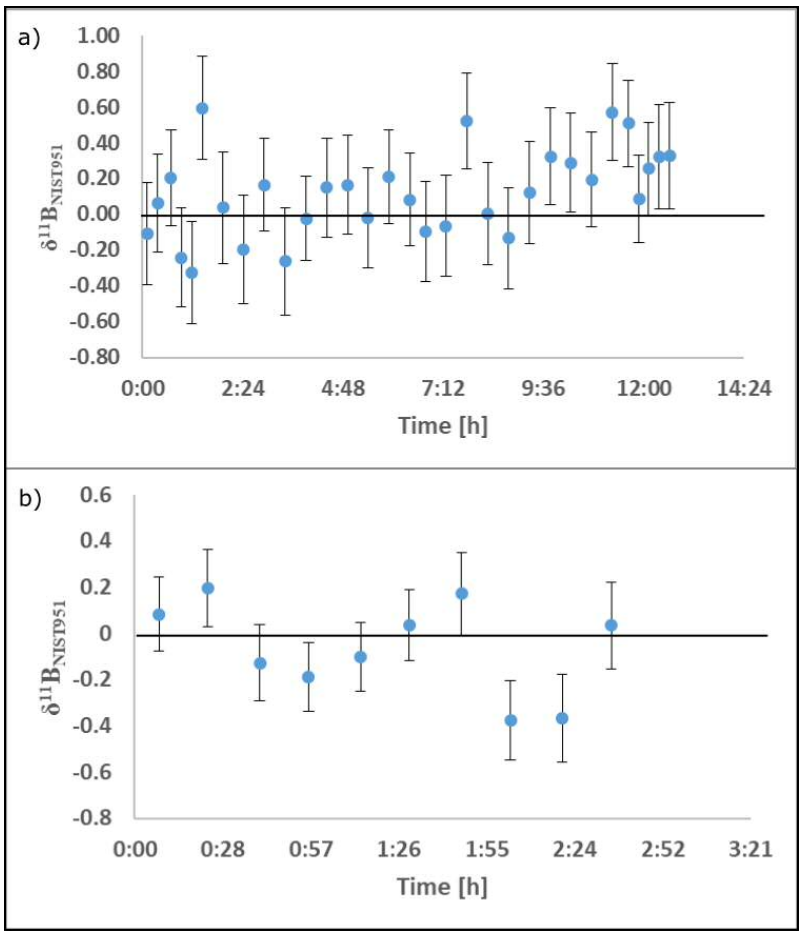


**Figure 6.15** Blank corrected boron isotope ratios of NIST 951 for a 25ppb (a) and 50ppb (b) solution during runs conducted with a PFA cyclonic spray chamber and a 100$\mu$L flowrate ESI nebulizer.

951 brackets. The results show however, that the precision was linked to 2 outliers within the 8 measured NIST 951 values (Figure 6.17).

If these were removed, accuracy and precision for that run evolve to 0.08($\pm$0.21). I found no correlation between $^{11}B/^{10}B$ ratio and intensity suggesting instabilities in short-term mass bias. This was reproducible at lower concentrations for a different standard AE121 (Figure 6.18).

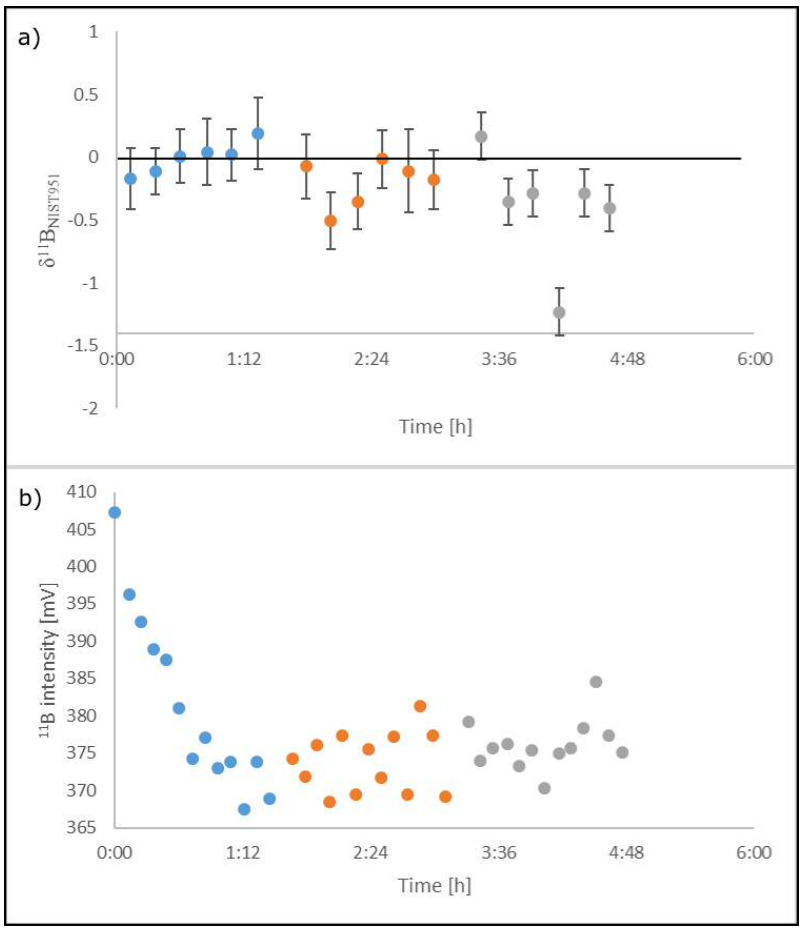


**Figure 6.16** Blank corrected boron isotopic ratios (a) and $^{11}$B intensities (b) of NIST 951 for a 50ppb solution using a glass cyclonic spray chamber and a 100$\mu$L flowrate ESI nebulizer. The run was conducted in three separate sub-runs that were started consecutively, without significant interruption. For identification, the three sub-runs are colour-coded in blue (run 1), orange (run 2), and grey (run 3), respectively.

### 6.5.2 Characterising instrument mass bias through accuracy and precision of NIST 951 standard measurements on a PFA cyclonic spray chamber

Poor analytical precision can be a result of short-term changes in the instrument-specific fractionation of the isotopes, also known as mass bias changes. To investigate the influence of mass bias on precision and accuracy, I ran a series of continuous NIST 951 standard measurements where the probe never left the standard. Accuracy and precision of NIST 951 $\delta^{11}B$ measurements generally improved throughout a

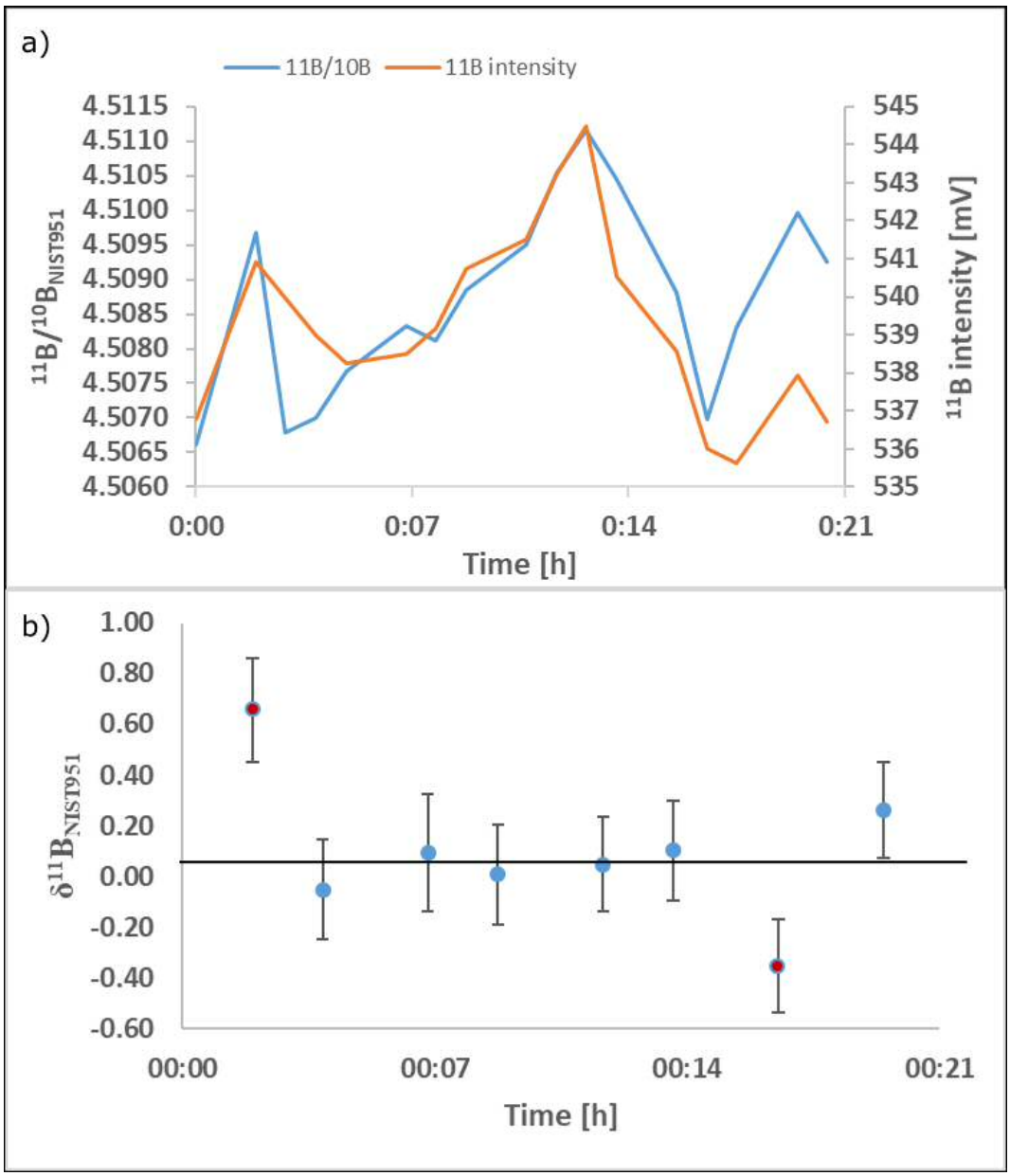


**Figure 6.17** (a) $^{11}B/^{10}B$ ratios (blue) and $^{11}B$ intensities (orange) from continuous measurements of 50ppb NIST 951 solution using a glass cyclonic spray chamber, during which the probe did not leave the standard vial. (b) Resulting $\delta^{11}B$, after bracketing every second continuous measurement. Two outliers correlating to short-term changes in intensity lead to a significant reduction in the precision.

day from around 0.18($\pm$1.08) in the morning, to around -0.03($\pm$0.31) in the evening. This suggests that the precision on boron isotopic standard measurements can be significantly improved with an instrument that stabilised with time. However, in several runs precision was compromised due to short-term changes in intensity

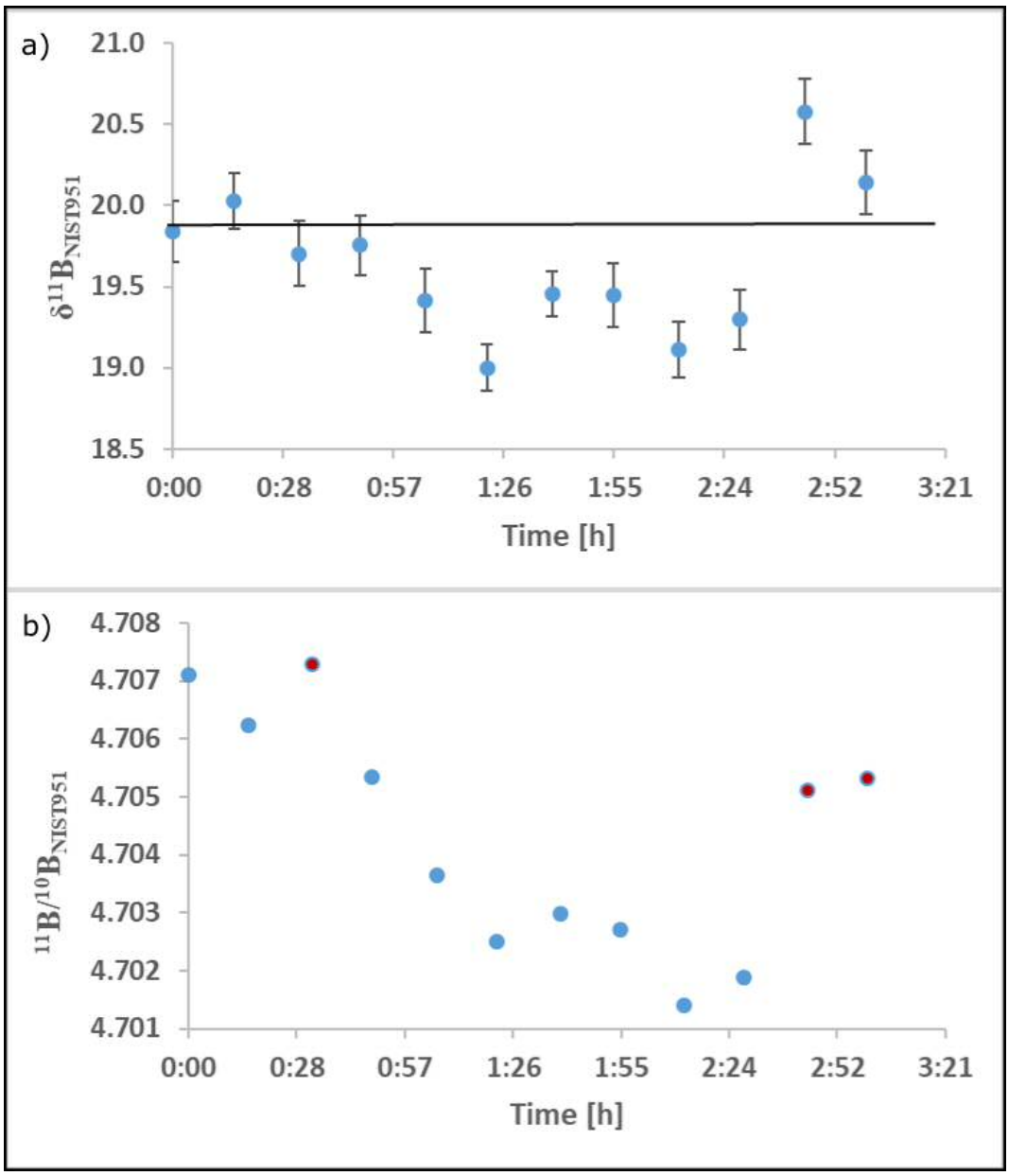


**Figure 6.18** $\delta^{11}$B (a) and boron isotopic ratio $^{11}$B/$^{10}$B (b) for boron standard AE121 at 25ppb concentration using a glass cyclonic spray chamber. The defined $\delta^{11}$B standard value is indicated with a black line. Red filled circles show $^{11}$B/$^{10}$B ratios which appear as outliers compared to the other measurements, likely due to changes in short-term mass bias.

which likely inflicted a change in mass-bias during the integration of a NIST 951 measurement (Figure 6.19).

To improve changes in short-term mass bias, I applied a boron-ratio specific mass bias tune prior to analysis of NIST 951. The mass bias tune identifies a plateau in the $^{11}B/^{10}B$ ratio in relation to changing sample gas pressure (Foster, 2008). The

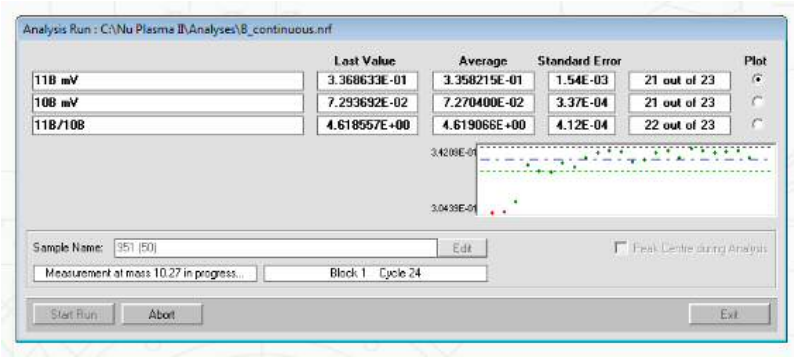


**Figure 6.19** Screenshot of a live window during a single analysis showing short-term measurements whose average creates the final output measurement. Average and 3x standard error of the measurements are listed above the graph, and plotted as grey and green dashed lines. All points that lie within the 3x standard error envelope are plotted as green filled circles. Any measurements that lie outside the boundaries are plotted in red and automatically excluded from the final integrated average. This analysis shows an example of short-term changes in mass bias resulting in short-term shifts in intensity. Here, the shift covers nearly 40mV in a few seconds.

optimal mass bias tuning setting may deviate from the optimal intensity setting. However, due to stabilised instrumental mass bias, precision and accuracy of $\delta^{11}B$ measurements may increase.

Accuracy and precision on 10 blank-corrected brackets of 50ppb NIST 951 standard were -0.06($\pm$0.41). The mass bias tune did not significantly improve precision, but stabilised short-term changes in mass bias (Figure 6.20b). The poor precision is likely due to long-term mass bias drift which led to a shift of 3.35‰ between the first and last $\delta^{11}B$ value. A longer analysis of 25ppb NIST 951 showed that the long-term drift stabilized after around 10h (Figure 6.20a). During this run, precision improved from $\pm$0.43 for the first 5 brackets to $\pm$0.35 for the last 5 brackets. However, accuracy deteriorated from -0.03 to -0.21. This could be due to slightly too long bracketing times. As such, medium-term mass bias changes may not be accounted for by the standard-sample bracketing procedure.

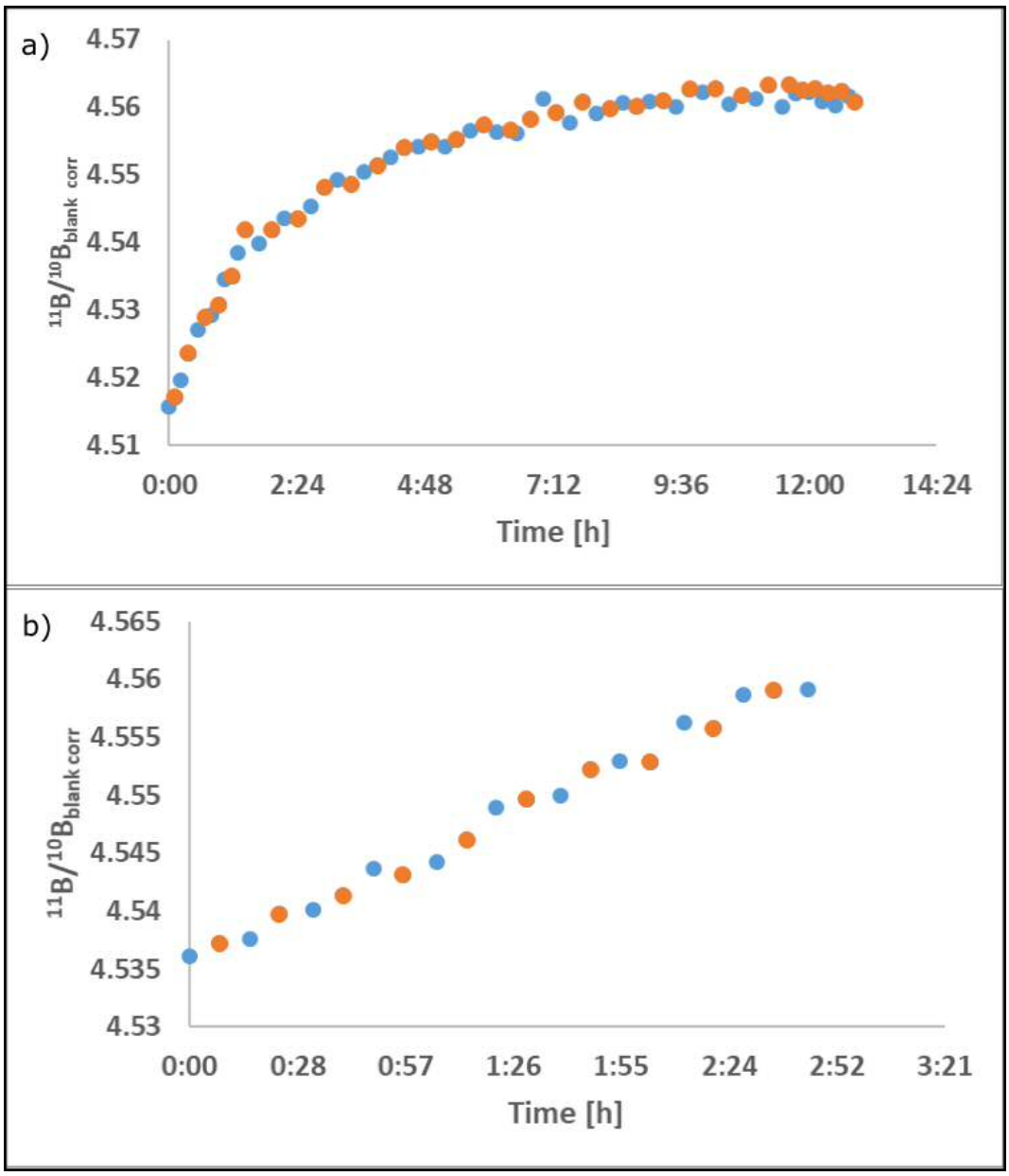


**Figure 6.20** NIST 951 boron isotopic ratio over 14h (a) and 3h (b) after tuning for mass bias. The mass bias tune has effectively reduced short-term changes in the ratio. The medium-and long-term mass bias drifts become visible. The $\delta^{11}B$ values for the 14 hour and 3 hour runs are shown in Figure 6.15. The bracketed ratios that were treated as samples are plotted in orange.

### 6.5.3 Influence of bracketing times on accuracy and precision of boron isotope standards

Medium-term mass bias can be corrected for by tight standard-sample bracketing.

During optimal bracketing time, mass-bias changes are minimal between standard

and sample measurements, leading to well-corrected $\delta^{11}B$ sample values. However, during longer standard-sample bracketing times, medium-term mass bias changes may cause changes in the $^{11}B/^{10}B$ ratio measured for the same standard. This can lead to increases in accuracy and precision due to poor standard-bracketing.

Here, I identify the influence of standard-bracketing time on accuracy and precision of $\delta^{11}B$ from a 50ppb NIST 951 solution. Changes in bracketing time were achieved by varying the washout time between 2 and 3 minutes, and keeping standard and blank 0.5M $HNO_3$ measurements constant at 125 seconds. I then trialled significantly shortening the bracketing time in a continuous standard run, by simulating the timing of wash/blank and standard measurements. During this test run, the probe never left the standard pot, but collected two types of measurements where "wash+blank" measurements took 3 minutes, and "standard" measurements took 125 seconds. As such I decreased the bracketing time by 3.08 minutes, without inducing a wash-related memory effect. Accuracy and precision of 9 brackets of 50ppb NIST 951 resulted in 0.00($\pm$0.48) for a 3 minute washout, and 8 brackets in 0.01($\pm$0.62) for a 2 minute washout (Figure 6.21).

My idealised continuous run with significantly shorter bracketing time presented an accuracy and precision of -0.01($\pm$0.25) on 9 brackets of NIST 951 (Figure 6.22). This confirms that precision will improve with shorter bracketing times. However, my results further suggest that shortening bracketing times by reducing washout time is insufficient, as it increases the memory effect and therefore reduces precision on the standard measurements. Therefore, other methods of reducing the bracketing time or improving the precision are necessary.

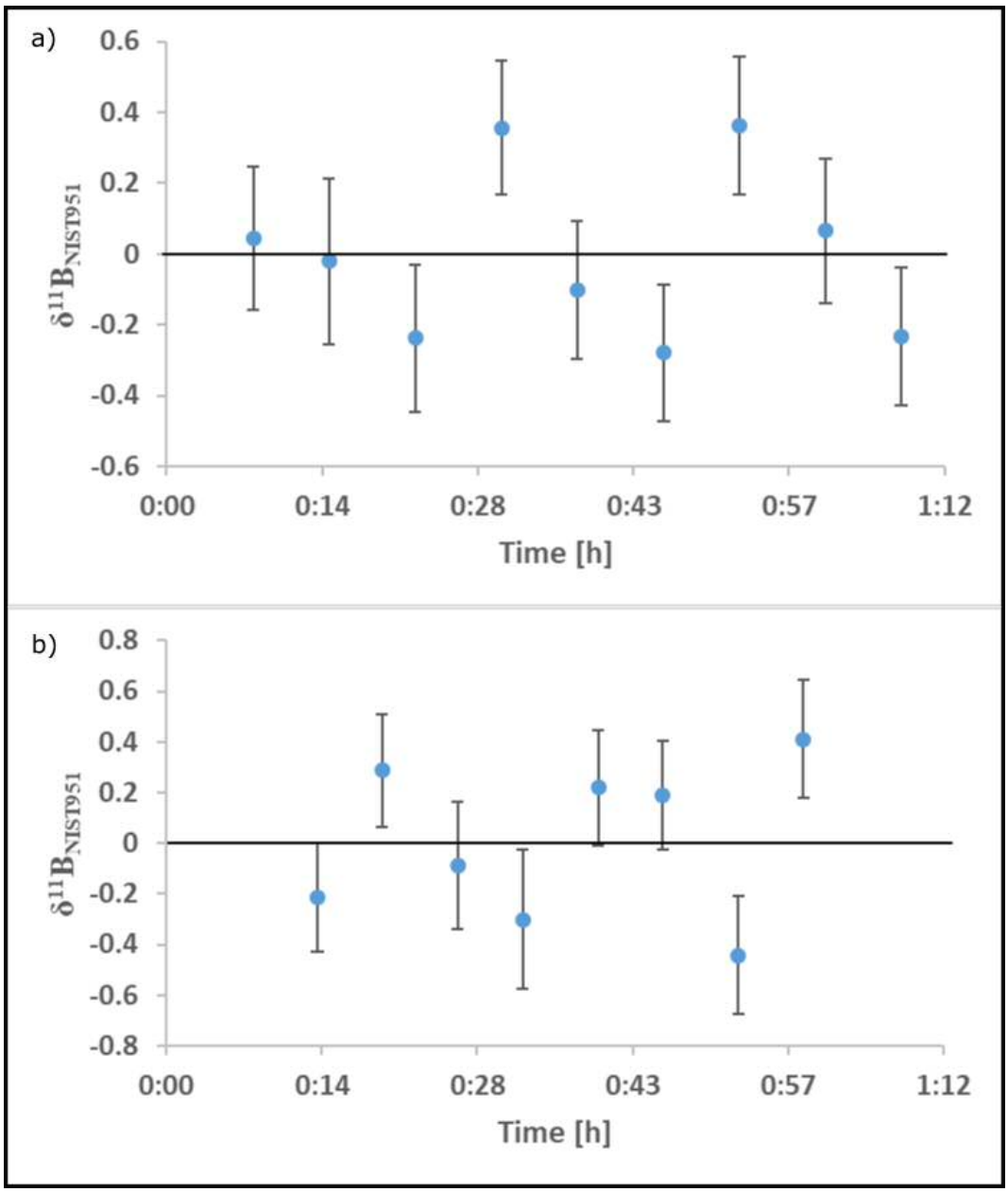


**Figure 6.21** Testing the efficiency of bracketing time by varying washout time on $\delta^{11}B$ of 50ppb NIST 951, with a 3 minute washout (a), and a 2 minute washout (b). NIST 951 $\delta^{11}B$ standard value shown as black line. Error bars are propagated errors for each measurement.

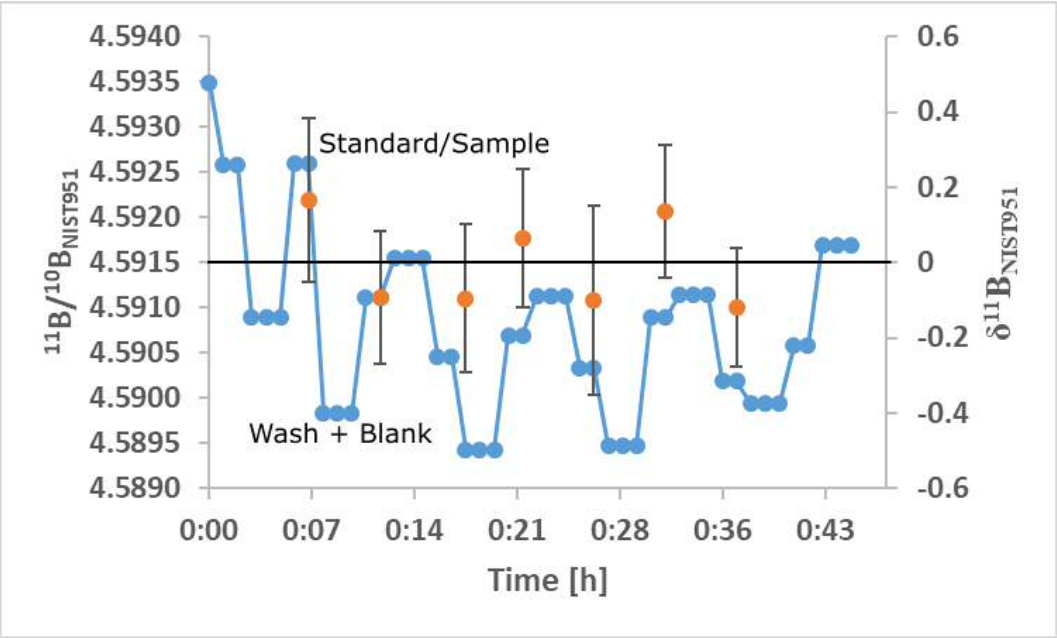


**Figure 6.22** $^{11}B/^{10}B$ ratio (a) (blue) and resulting $\delta^{11}B$ (b) (orange filled circles) for a continuous run of 50ppb NIST 951 standard which simulated the times of different measurements during a normal blank- and washout-including analysis. During the continuous run, the probe never left the standard vial. Measurement time needed for "washout + blank" are simulated in the group of 3 blue filled circles. The measurements that were assumed to be "samples" and "standards" are plotted as the group of 2 blue filled circles.

### 6.5.4 Enhancing accuracy and precision on NIST 951 boron isotope measurements through improvement of internal errors

Statistically, the standard deviation between bracketed $\delta^{11}B$ measurements is directly dependent upon the standard error of the measurements themselves. As such, the precision of a run which is expressed as 2x standard deviation between the measurements can be improved by decreasing the standard error of each measurement. I tested two methods to investigate the influence of changing internal errors on precision and accuracy. First, I increased the standard concentration from 50ppb to 200ppb as a means of increasing the signal/noise ratio. Second, I exchanged the $10^{11}\Omega$ resistors with $10^{12}\Omega$ resistors to enhance the electric signal given by a small standard concentration.

Propagated internal errors were typically around ±0.20 for $\delta^{11}B$ measurements conducted on a 50ppb NIST 951 solution using a PFA cyclonic spray chamber. After increasing the concentration to 200ppb and adapting the washout time from 3 to 3.5 minutes, internal errors resulted in around ±0.15 for single integrated measurements. Under these conditions, accuracy and precision of 8 NIST 951 measurements resulted in 0.04(±0.26) (Figure 6.23) confirming that higher signal/noise ratios can significantly improve the accuracy and precision of boron isotope measurements.

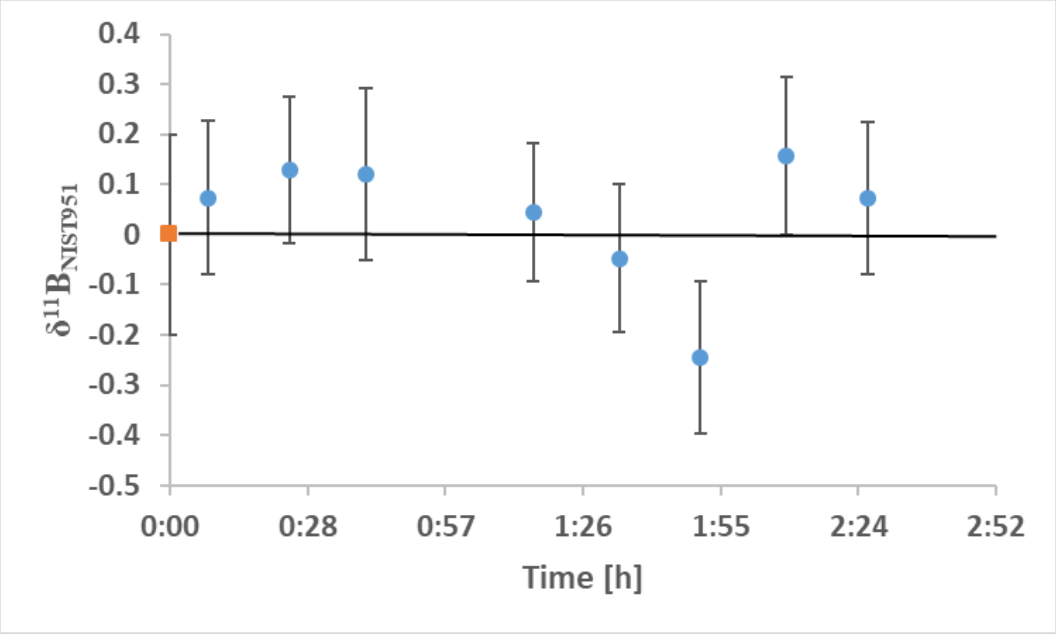


**Figure 6.23** $\delta^{11}B$ and measurement standard error for a 200ppb NIST 951 analysis (blue filled circles) with 3.5 minutes washout time. For comparison the average measurement standard error of a 50ppb NIST 951 analysis plotted as error bars on the orange square.

Installation of $10^{12}\Omega$ resistors require adaptation of the magnet delay time, due to longer response times of higher Ω resistors. I therefore systematically tested the internal errors of measurements for different magnet delay times and measurement integration times. I found that smallest internal errors can be reached with 600 seconds measurement integration time, and 12 seconds magnet delay time (Figure 6.24).

Resulting internal errors of single measurements of a 200ppb NIST 951 standard solution were around 0.13. Accuracy and precision from the same 8, and from

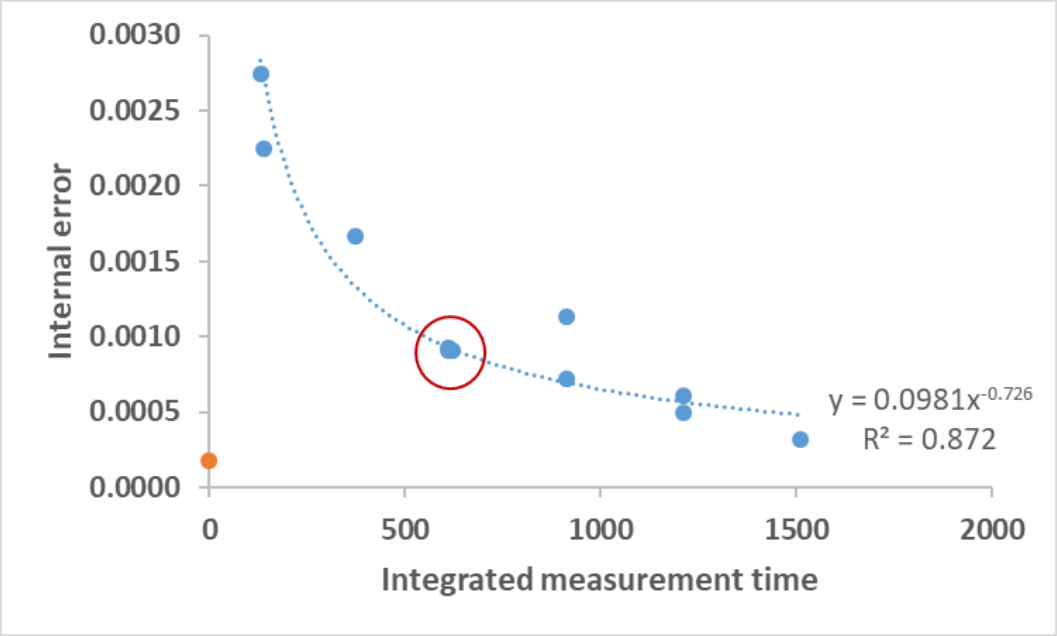


**Figure 6.24** Changes in internal error (blue) as a function of integrated measurement time using $10^{12}\Omega$ resistors (blue closed circles). The optimal setting is found where both internal errors and integrated measurement time are minimal. This is the case at integrated measurement time of around 600 seconds, after which the gain in internal error happens at a significant cost in integrated measurement time. For comparison, average internal errors on $10^{11}\Omega$ resistors are plotted in orange.

further 24, bracketed $\delta^{11}B$ NIST 951 measurements reported at 0.26($\pm$0.62), and 0.04($\pm$0.85), which is significantly worse than results for $10^{11}\Omega$ resistors. According to Ohm's law R=U/I, where R = resistance in $\Omega$, U = voltage in V, and I = current in A, a higher resistor will create a higher voltage and therefore more concentrated signal. This should have the same effect as increasing the concentration of the standard solution. Given that I increased the concentration and the resistors simultaneously, I would have expected a significant improvement in the internal errors in comparison to the concentration-only test. This however is not the case, as both internal errors are comparable. Given my highest intensity at 570mV for 200ppb (see Figure 6.25, I exclude the possibility of resistor oversaturation. Instead, I propose that the degradation of average and precision with resistor type is due to an increase in the bracketing time between standards and samples because of longer magnet delay

times. This causes inefficiency of the brackets when correcting for medium- and long-term changes in mass bias.

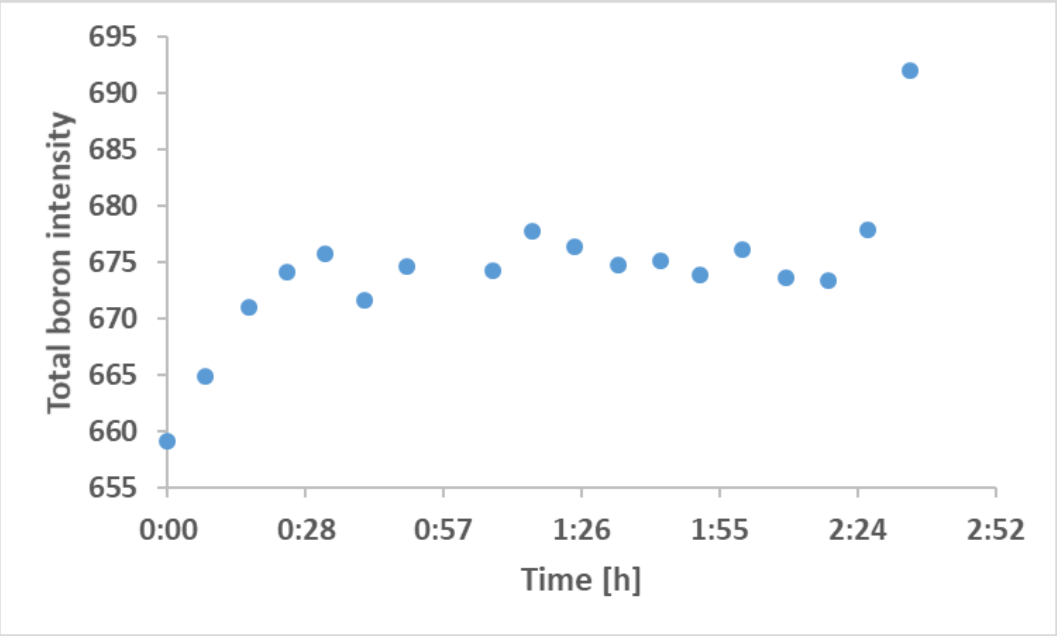


**Figure 6.25** Total boron intensity for 200ppb NIST 951 on $10^{12}\Omega$ resistors, after applying a 0.1 scaling factor, which allows the voltage to be plotted on a $10^{11}\Omega$ resistor scale. The complementary $\delta^{11}B$ values are plotted in Figure 6.23.

## 6.6 Conclusions

Analytical measurements of boron isotopes in planktonic foraminifera using MC-ICPMS are known to be challenging due to small sample sizes often combined with low concentrations. This causes planktonic foraminifera boron samples to be significantly larger than samples for other geochemical analyses. In this study, I revisited two important steps in the boron isotope analysis chain, including foraminiferal sample cleaning, and analytical sample measurement on a Nu plasma II.

I find that conventional cleaning methods are sufficient for samples containing up to 200 foraminifera in Eppendorf tubes of either 0.5mL or 1.5mL, without necessity of up-scaling the volumes of cleaning reagents. In fact, my results suggest that current cleaning methods might be too rigorous for small samples and cleaning-

induced calcite loss could be reduced by re-scaling reagent volumes to smaller samples. Furthermore, I confirmed that picking of residues and black particles after cleaning is unnecessary in the majority of ocean sediment-derived foraminiferal samples. My data show some leaching potential from mafic and quartz IRD, with quartz leachates potentially carrying Mg contamination. However, this was the result of enhanced IRD contamination which is unlikely in hand-picked foraminifera samples.

In this study, I also present new boron isotopic measurements from standards NIST 951, and ERM AE121, conducted on a Nu plasma II. I gained highest and most consistent accuracy and precision with a PFA cyclonic spray chamber, compared to a PFA barrel and a glass cyclonic spray chamber. My data shows optimistic results for some analyses conducted using the glass cyclonic spray chamber. However, I believe using a PFA spray chamber is superior, due to its potential for lower backgrounds, faster washouts, and potential for introduction of strong acids and bases such as HF or $NH_3$ as washout-enhancers. Furthermore, I show that short-term mass bias can be controlled by tuning for boron isotopic mass bias. Additionally, I find that short bracketing times, complete washouts, and low internal errors are important for high precision boron analyses on a Nu plasma II, to control medium- and long-term instrument mass bias through efficient standard-sample bracketing. Internal errors may be efficiently reduced by increasing the sample concentration, or the Faraday cup resistor. I could not improve bracketing times other than by reducing the washout below 3 minutes. I therefore propose a washout-enhancing method when analysing boron isotopes on a Nu plasma II.

# Chapter 7

# A HIGHLY SALTY AGULHAS LEAKAGE LINKED TO GLACIAL INDIAN OCEAN SALINIFICATION

## 7.1 Abstract

Leakage of salty surface waters from the Indian Ocean to the North Atlantic are thought to play an important role in shaping glacial-interglacial climate through controlling Agulhas Leakage efficiency. It is proposed that a strong Agulhas Leakage supplies warm and salty Indian ocean surface waters to Atlantic surface currents influencing convective potential at North Atlantic deep-water formation sites. While changes in the volume strenth of the Agulhas Leakage have been previously studied, variability in its salt content has not been investigated. Here, I present new planktonic foraminiferal Mg/Ca and stable isotope-derived salinity reconstructions for the last 1.2Ma from the northern Mozambique channel. I find salinity increases prior to terminations during peak glacial conditions after correcting for ice volume related

whole ocean salinity changes, followed by early decreases before glacial inception. I present a possible link between the hydrography of the northern Mozambique channel and glacial-interglacial changes in Indian Ocean salinity due to unique Indian ocean surface circulation variations. Despite being a mostly tropical and subtropical ocean, salinity in the modern tropical Indian Ocean is lower than at comparable latitudes in the Atlantic or Pacific. This is due to the inflow of low salinity waters from the Indonesian throughflow (ITF) and surface water loss through a strong Agulhas Leakage. I suggest that a reduction in the ITF coupled to a weakened Agulhas Leakage during glacials drove higher surface salinities in the western Indian ocean. I hypothesise that the closure of these two gateways caused isolation of Indian Ocean surface waters and encouraged the development of a strong subtropical Indian Ocean gyre which led to increased surface water temperatures and salinities through higher net evaporation. The release of this salty water to the North Atlantic, particularly during terminations, may drive or enhance rapid climate change.

## 7.2 Introduction

Surface circulation in the Indian ocean forms part of the upper limb of the global overturning circulation (Beal et al., 2011; Gordon, 1986). Surface waters enter the Indian Ocean via the South equatorial current fed by the Indonesian Throughflow (ITF) and leave the basin as Agulhas Leakage eddys (Figure 7.1). By providing the northwards flowing Atlantic surface currents with excess salt, the Agulhas Leakage and ultimately the Indian ocean are important for the formation of North Atlantic deep water (NADW)and thus the global overturning circulation (Beal et al., 2011; Biastoch et al., 2009; Biastoch et al., 2015). It has been proposed that the Agulhas Leakage efficiency varies with glacial-interglacial climate, controlled by latitudinal movements in the subtropical front (STF) (Bard & Rickaby, 2009). According to this hypothesis, a northward/southward shift of the STF would reduce/enlarge the

outflow area between the front and the African continent, decreasing/increasing the efficiency of the leakage (Bard & Rickaby, 2009).

Flow through the Indonesian Throughflow (ITF), the other Indian Ocean gateway, has also been shown to reduce during glacials (Holbourn et al., 2011; Petrick et al., 2019), most likely due to reduced sea level and subsequent exposure of modern shelves (Petrick et al., 2019). Changes in the surface topography within the ITF also influence atmospheric circulation and potentially lead to a particularly dry eastern and wet western Indian Ocean (DiNezio et al., 2018) with an increased SST gradient across the equatorial Indian Ocean (DiNezio et al., 2018), and higher SST variability in the east (Thirumalai et al., 2019). The modern South Equatorial Current is comparatively fresh (Talley, 2005), due to low salinity ITF surface waters (Figure 7.1). This is mainly driven by a combination of Pacific low salinity surface water and large monsoonal rainwater input which enter the ITF region through the South China Sea (SCS) and cause a stratification-induced cool and fresh thermocline ITF outflow (Sprintall et al., 2014). Sea level-induced exposure of ITF shelves could therefore enhance SSTs and salinity in the glacial SEC.

Changes in the outflows of these two gateways during glacials may significantly increase the salinity of the glacial Indian Ocean. Palaeoclimate evidence, such as foraminiferal abundance counts (Peeters et al., 2004), show a particularly strong Agulhas Leakage during terminations. Given that glacial Indian Ocean surface waters may have been saltier than today (Simon et al., 2013; Simon et al., 2015), due to reduced volume flows through the gateways, the volume spikes in Agulhas Leakage during terminations could have been particularly salty (Kasper et al., 2014; Marino et al., 2013).

To investigate this question, I present new geochemical analyses from well preserved planktonic foraminifera collected on the International Ocean Discovery Programme expedition 361 in the northern entrance of the Mozambique Channel spanning the Late Pleistocene and Mid-Pleistocene transition. I combine my proxy

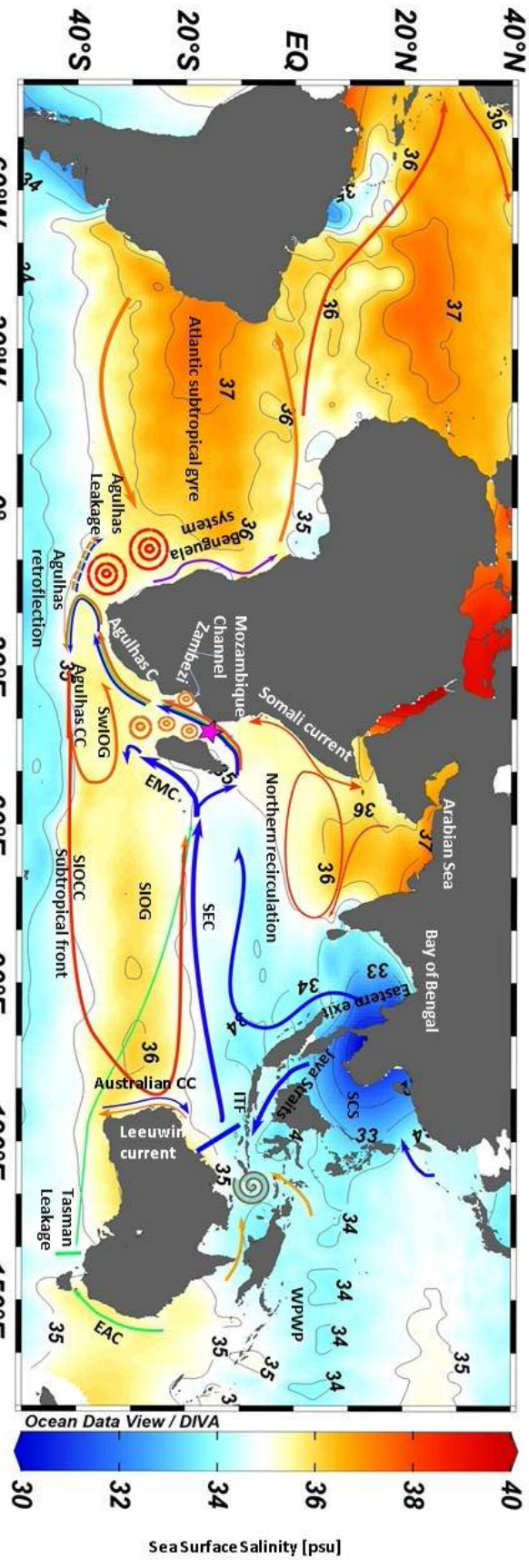


**Figure 7.1** Indian Ocean surface circulation. Fresher and saltier water masses are highlighted in blue and orange, respectively. Background colours represent modern sea surface salinity from the GLODAP V2 dataset and interpolated using the DIVA setting in ocean data viewer (ODV). The core location for U1476 (depth at 2166m) is highlighted with a pink star.

reconstructions with modelling results using a topography model coupled to an ice-sheet model and an earth system model to understand the importance of changing sea levels on the land exposure in the ITF, and salt input into the South Atlantic on global ocean circulation. I use my new analyses to investigate the influence of changes in the SEC and the Agulhas Leakage on western Indian Ocean surface salinity and temperature. The northern Mozambique Channel is an ideal location for this study, because ITF-sourced SEC waters travel across the equatorial Indian Ocean and enter the Mozambique Channel in the north (Durgadoo et al., 2017; Talley, 2005). At the same time, the channel has been identified as an upstream source region for the Agulhas Leakage (Lutjeharms, 2006). As such, it is possible to trace changes in whole Indian Ocean surface hydrography transported by the SEC without direct influence of the smaller southwest Indian Ocean recirculation patterns.

## 7.3 Methods

### 7.3.1 Core location and hydrography

Samples were taken from ocean sediment core U1476. The core was drilled during the International Ocean Drilling Program (IODP) expedition 361 which collected ocean sediment cores along the southeast African coast (Hall et al., 2017). U1476 is located at the northern entrance of the Mozambique Channel in 2166m water depth, and is bathed by North Atlantic deep water (NADW) (Figure 5.4). The core presents well preserved foraminiferal oozes (Hall et al., 2017) useful for climate reconstruction (see chapter Materials & Methods 5.3.5).

The core site is located on Davie Ridge at 15°49.25'S; 41°46.12'E. Source waters include south equatorial current waters, northern-sourced Indian ocean waters, recirculating southern-sourced Indian ocean waters and Tasman leakage waters (Durgadoo et al., 2017). A net southwards transport connects the channel to the

Agulhas system, mostly characterised by three large quasi stationary eddies located mostly south of site U1476 (Lutjeharms, 2006). Additional shorter-lived smaller eddies appear in the channel and can last from monthly to yearly timescales (Sætre & Da Silva, 1982). Depending on their location and direction of spin, they may create short-term northwards flowing boundary currents along Africa and Madagascar (Lutjeharms, 2006; Sætre & Da Silva, 1982). Coastal hydrography is also influenced by a strong seasonal monsoon cycle which brings freshwater to the channel via the Zambezi river (Hall et al., 2017; Weldeab et al., 2014).

### 7.3.2 Sea surface temperature calculation

To investigate changes in sea surface temperature (SST) and salinity (SSS), I collected Mg/Ca and $\delta^{18}$O from surface-dwelling foraminifera *G. ruber*. SST was calculated from Mg/Ca using the *G. ruber* calibration by Gray et al. (2018) and the R script published in Gray & Evans (2019) (see also Figure 7.2):

$$\frac{Mg}{Ca} = e^{0.060(\pm 0.008)\times T + 0.033(\pm 0.022)\times S - 0.83(\pm 0.73)\times (pH-8) - 1.07(\pm 0.80)} \quad (7.1)$$

where T is sea surface temperature, S is salinity and pH is the negative decadic logarithm of $H^+$ ions.

SST uncertainties are calculated using Monte Carlo analysis. The R script allows for iterative calculation of T, by simultaneously solving for S and pH at each time step. S is varied in a normal distribution of $\pm$0.5psu about the modern value (Gray & Evans, 2019). pH is calculated using the SEACARB function, with alkalinity and $p\mathrm{CO}_2$ as carbonate system input parameters. Alkalinity varies in a flat distribution of -25 to +75 $\mu$mol/kg (Gray & Evans, 2019), with a modern alkalinity value of 2300 (Fallet et al., 2010). Ice core atmospheric $\mathrm{CO}_2$ was linearly interpolated to the

LR04 benthic $\delta^{18}$O stack beyond 800kyr years (Figure 7.3). Tests looking into the sensitivity of SST to the different input variables are described in the results.

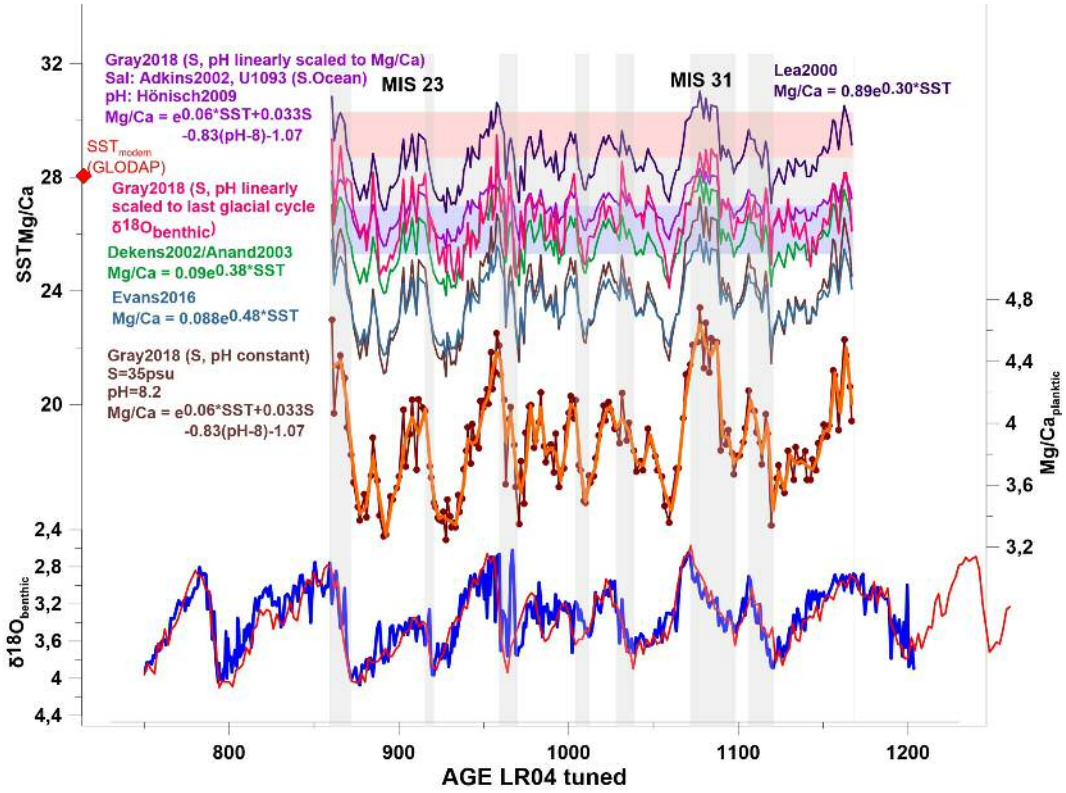


**Figure 7.2** Application of different SST-Mg/Ca calibrations to a subset of the whole Mg/Ca dataset. Different applied calibrations in dark purple (Lea et al., 2000), light purple ((Gray et al., 2018) using Adkins et al. (2002) and Hönisch et al. (2009) to vary salinity and temperature linearly scaled to Mg/Ca, pink (Gray et al., 2018) using Adkins et al. (2002) and Hönisch et al. (2009) to vary salinity and temperature linearly scaled to benthic $\delta^{18}O$, green (Anand et al., 2003; Dekens et al., 2002), blue (Evans et al., 2016), and brown (Gray et al., 2018) where salinity and temperature are kept constant. Below, Mg/Ca$_{G.\ ruber}$ in dark red with 5kyr running mean (orange). $\delta^{18}O_{benthic}$ in blue and LR04 in red.

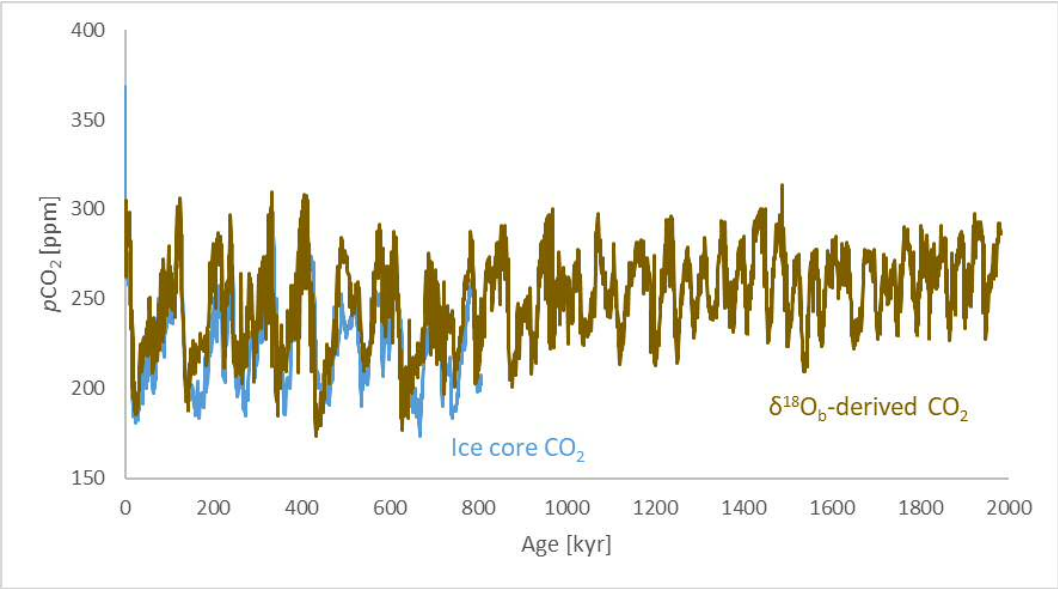


**Figure 7.3** Comparison of LR04-derived $pCO_2$ to ice core $pCO_2$ (Bereiter et al., 2015). $pCO_2$ was linearly interpolated to LR04 to enable the iterative caclulation of SST across 1.2Ma using the R script by Gray & Evans (2019).

### 7.3.3 Calculating local surface water $\delta^{18}O$

Planktonic $\delta^{18}$O is frequently used to reconstruct local hydrographic changes in the past. This requires correction for variability induced by temperature and global ice volume changes. Then, the residual can be interpreted as variability in the salinity component of the local surface water mass.

$$\delta^{18}O_{sw} = \delta^{18}O_{planktonic} - \delta^{18}O_{temperature} - \delta^{18}O_{ivc} \tag{7.2}$$

where $\delta^{18}O_{sw}$ is the $\delta^{18}$O of local seawater, $\delta^{18}O_{planktonic}$ is the $\delta^{18}$O of *G. ruber*, and $\delta^{18}O_{temperature}$ and $\delta^{18}O_{ivc}$ are the equivalents of temperature and ice volume in $\delta^{18}$O space. After testing a suite of potential transfer functions (see Figure 7.4), planktonic $\delta^{18}$O was corrected for temperature using the calibration of Bovier-Soumagnac & Duplessy (1985), as it was calibrated using planktonic foraminifera from the Indian Ocean.

$$\delta^{18}O_{sw,ivc} = (\delta^{18}O_{planktonic} + 0.20) - \frac{T - 15.4}{-4.81} \tag{7.3}$$

where $\delta^{18}O_{sw}$ is given in VSMOW and $\delta^{18}O_{planktonic}$ in VPDB, respectively.

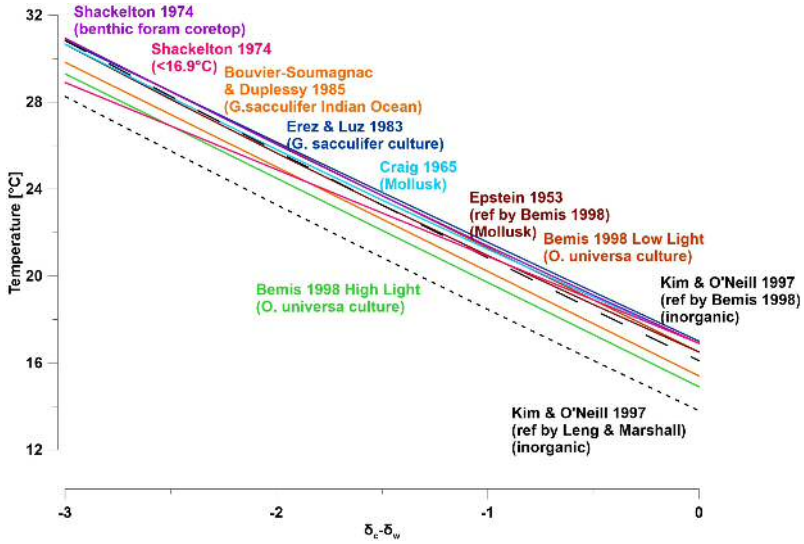


**Figure 7.4** Different carbonate SST - $\delta^{18}O_{sw}$ calibrations. Bouvier-Soumagnac & Duplessy (1985) was chosen to calculate U1476 $\delta^{18}O_{sw}$ as it is based on planktonic foraminiferal calcite (Globigerinoides *sacculifer*) from the Indian Ocean.

To compare between VSMOW and VPDB, I apply a conversion factor of +0.20 (see also Bemis et al., 1998; Pearson, 2012).

To establish the influence of global ice volume changes on relative sea level in the northern Mozambique channel, I modelled RSL and $\delta^{18}O_{icevolume}$ using the ANICE ice sheet model and U1476 benthic $\delta^{18}$O (see Chapter 7.3.6). I then corrected $\delta^{18}O_{sw,ivc}$ for the modelled $\delta^{18}O_{icevolume}$ to obtain $\delta^{18}O_{sw}$.

To allow better relative comparison between different glacial cycles, the $\delta^{18}O_{sw}$ record was detrended. To detrend the record, I developed an algorithm capable of identifying the middle of each termination and glacial cycle. Other ways of detrending were also tested and are described in chapter 7.3.4. The algorithm requires initial subjective inputs at what time interglacial minima and glacial maxima occurred. It then uses that time as a starting point and applies a moving window of

10kyr to search for the true minimum/maximum value in the data (compare Figure 7.5).

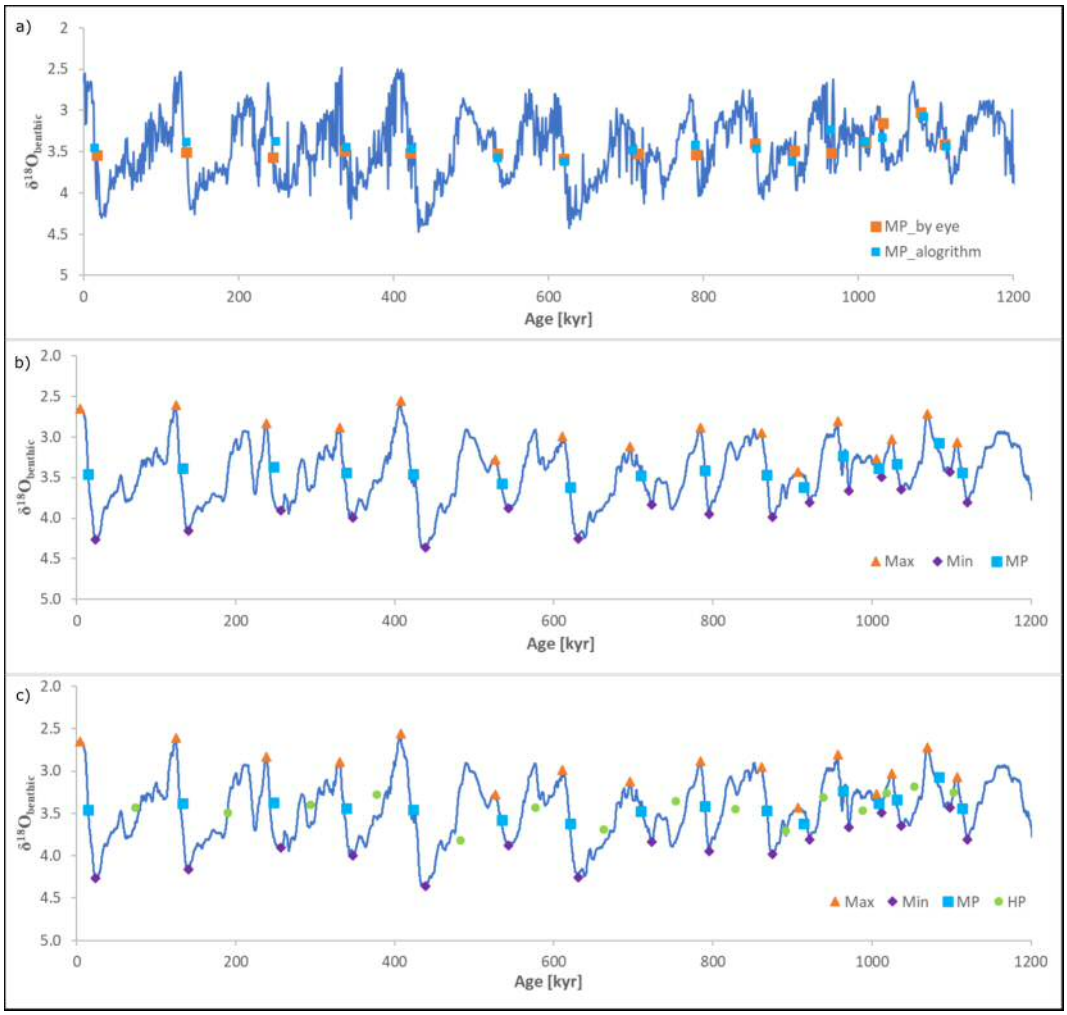


**Figure 7.5** Deglacial midpoints (MP) and glacial half points (HP) for U1476 $\delta^{18}O_{benthic}$. (a) Comparison of midpoints that were chosen by eye (orange), and calculated by the algorithm (bright blue) plotted on $\delta^{18}O_{benthic}$. (b) Maxima (orange triangles), minima (purple diamonds), and calculated midpoints (bright blue squares) on $\delta^{18}O_{benthic}$ (blue), as identified by the algorithm for $\delta^{18}O_{benthic}$. (c) as in (b) with additional halfpoints (green filled circles) as calculated by the algorithm.

A termination midpoint (MP) is defined as the half-point between the glacial maximum and the interglacial minimum. The time at which the MP occurs is calculated as follows:

$$t(MP) = \frac{t(glacial_{max}) - t(interglacial_{min})}{2} + t(interglacial_{min}) \qquad (7.4)$$

where t(MP) is the time at which midpoint MP is occurring, and t(glacialmax) and t(interglacialmin) are the times at which climatic maximum and minimum occur. $\delta^{18}O_{benthic}$ (MP) is estimated as the average between $\delta^{18}O_{benthic}$ at interglacial minimum and glacial maximum (Figure 7.5). Glaciation half-points (HP) were also calculated and are defined as the time at which half the glaciation has already happened. As such:

$$t(HP) = \frac{t(interglacial_{min}) - t(glacial_{max})}{2} + t(glacial_{max}) \tag{7.5}$$

and $\delta^{18}O_{benthic}$ at t(HP) was estimated by calculating the average between $\delta^{18}O_{benthic}$ at the previous interglacial minimum and the following glacial maximum (Figure 7.5). The same method was used to identify deglacial mid-points and glacial half-points in the $\delta^{18}O_{sw}$ record (Figure 7.6).

Glacial half-points were used to define the length of a glacial cycle for detrending the $\delta^{18}O_{sw}$ record. A glacial cycle occurs from one glacial half-point to the following glacial half-point, so that the cycle centres around a termination midpoint. All points within a glacial cycle were detrended by using the respective midpoint value as reference:

$$\delta^{18}O_{sw-MPdetrend} = \delta^{18}O_{sw-raw} - \delta^{18}O_{sw-at\,t(\delta^{18}O_b(MP))} \tag{7.6}$$

where $\delta^{18}O_{sw-MPdetrend}$ is the detrended value of $\delta^{18}O_{sw}$, $\delta^{18}O_{sw-raw}$ is the $\delta^{18}O_{sw}$ before detrending, and $\delta^{18}O_{sw-\delta^{18}O_{benthic(MP)}}$ is the $\delta^{18}O_{sw}$ value at the termination midpoint time defined in the $\delta^{18}O_{benthic}$ data (Figure 7.7).

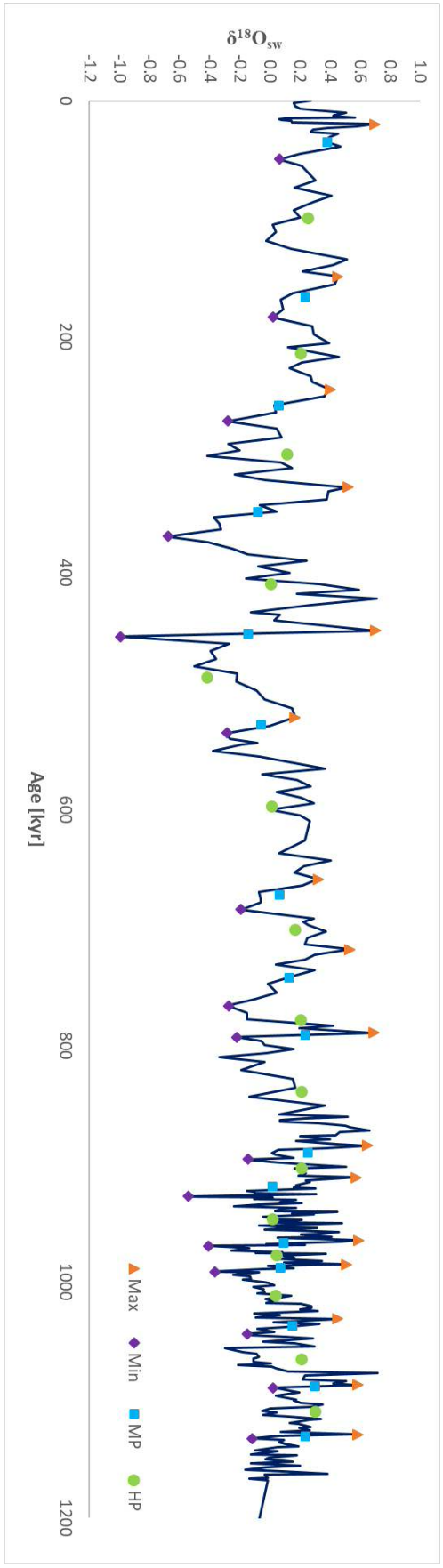


**Figure 7.6** Interglacial maxima (orange), glacial minima (purple), midpoints (bright blue), and glacial half-points (green) for the raw (not detrended) $\delta^{18}O_{sw}$ (dark blue line).

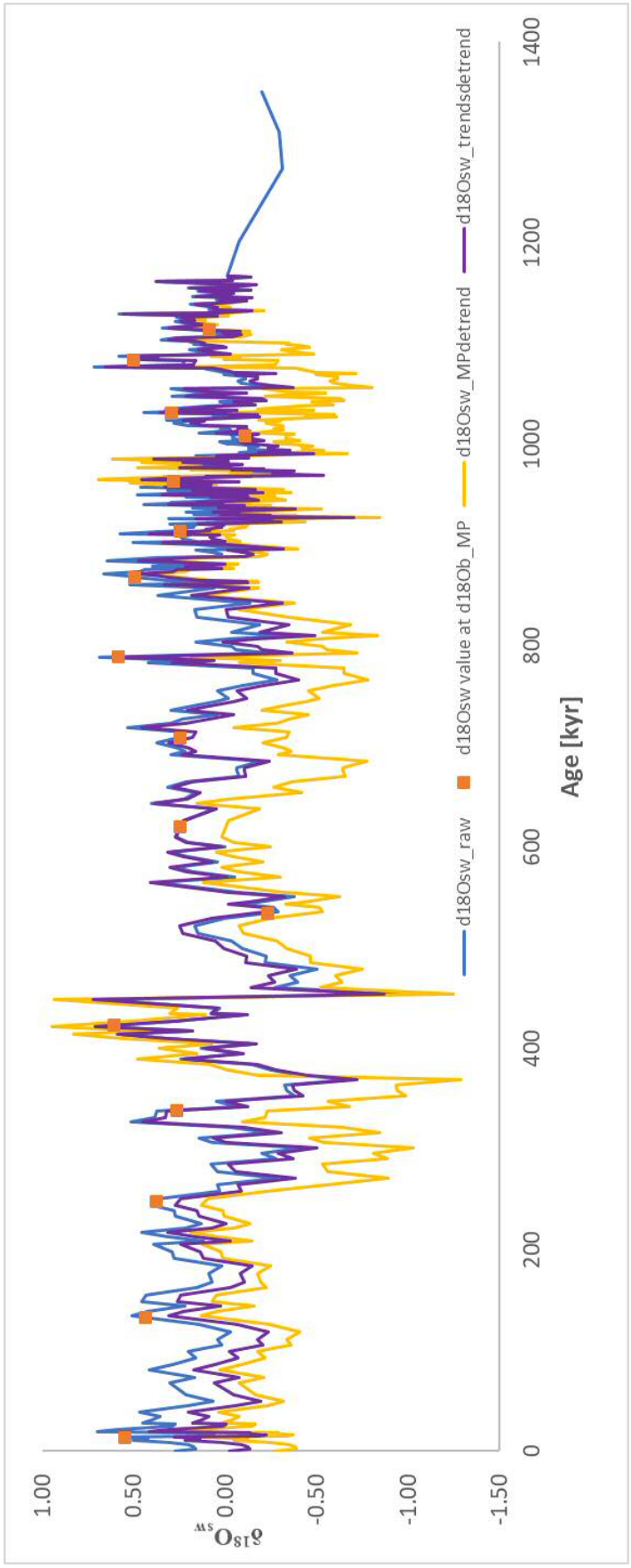


**Figure 7.7** Comparison of different $\delta^{18}O_{sw}$ detrend methods showing the original record (blue), the record using the 3-linear detrend method (purple) and the mid-point detrend method (yellow). Orange squares represent termination mid-points as identified from the $\delta^{18}O_{benthic}$ record.

### 7.3.4 Other approaches tested for dentrending the $\delta^{18}O_{sw}$ record

Additionally to the algorithm approach described in section 7.3.3, I tested three further approaches to identify midpoints of terminations and glacial cycles. These include (a) by-eye-trend approach, (b) $1^{st}$ derivative method, and (c) $2^{nd}$ derivative method.

For approach (a), I identified three diverging trends within the record by eye (Figure 7.8).

Trend 1 occured from 0.86-1.2Ma (positive), trend 2 from 0.45-0.86Ma (negative), and trend 3 from 0-0.45Ma (positive). I then corrected the three time periods in the $\delta^{18}O_{sw}$ record for its respective trend. The resulting $\delta^{18}O_{sw}$ record is plotted in Figure 7.7.

Approach (b) assumes that termination midpoints occur during times of greatest slope values which should be visible as slope value spikes in the $1^{st}$ derivative of the curve (Barker et al., 2015). The $1^{st}$ derivative at time t was solved iteratively using

$$Time\,t = \frac{t2 - t1}{2} + t1 \tag{7.7}$$

and

$$Slope\,m(at\,t) = \frac{y2 - y1}{t2 - t1} \tag{7.8}$$

where y1 and y2 are subsequent $\delta^{18}O_{benthic}$ data points occurring at times t1 and t2, respectively.

Approach (c) uses the $2^{nd}$ derivative of the record to identify inflexion points in the curve. These may correlate with interglacial maxima and glacial minima in a climate signal. The $2^{nd}$ derivative is calculated at time t(m) using the same equations as above, but taking the $1^{st}$ derivative curve as input-function.

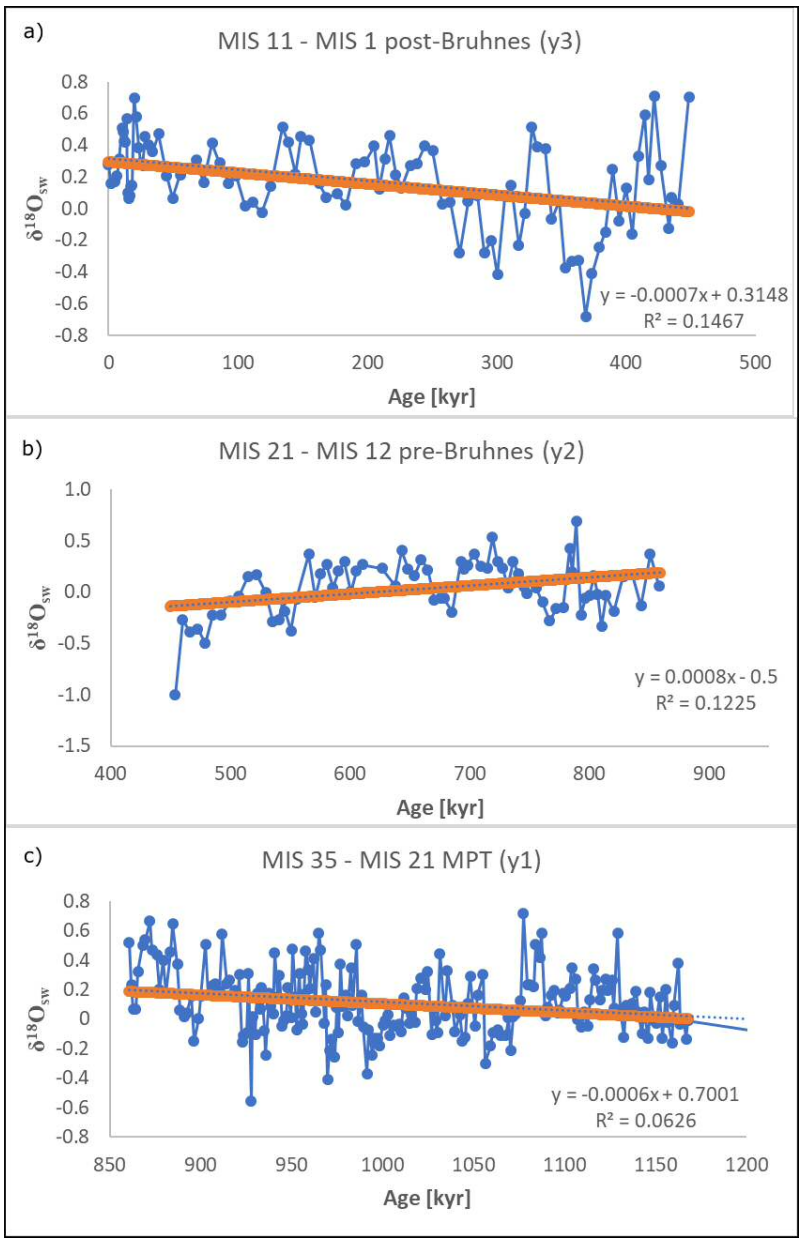


**Figure 7.8** Long-term trends identified in the $\delta^{18}O_{sw}$ record. (a) trend 1 from 0-450kyr, (b) trend 2 from 450-860kyr, (c) trend 3 from 860-1200kyr.

$$Time\,t(m) = \frac{tm2 - tm1}{2} + tm1 \tag{7.9}$$

and

$$Slope\,m2(at\,tm) = \frac{m2 - m1}{tm2 - tm1} \tag{7.10}$$

where m1 and m2 are subsequent data points on the $1^{st}$ derivative curve occurring at times tm1, and tm2, respectively. The middle of a termination is then defined as the time T occurring between two inflexion points.

Approaches (b) and (c) require smoothed records to reduce the amount of false positives due to short-term variability in the data. I therefore tested them on a 5kyr- (Figure 7.9) and a 10kyr- (Figure 7.10) smoothed record.

However, due to the significant change in termination-slopes between 40kyr-world deglaciations and 100kyr-world deglaciations, I could not find a single cut-off point that was able to correctly identify termination mid-points (Figures 7.9, 7.10).

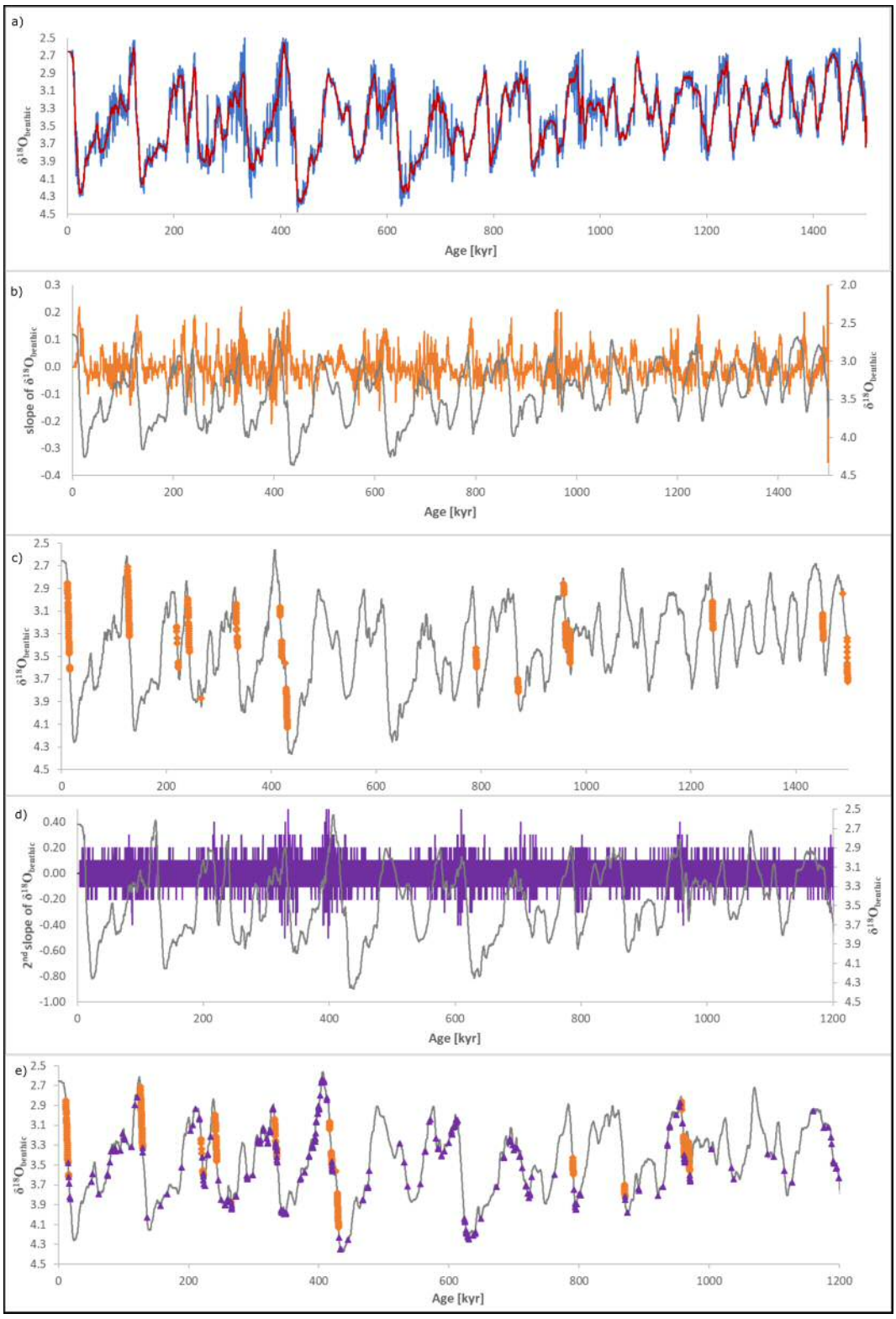


**Figure 7.9** Identification of termination midpoints (MP) using the slope of $\delta^{18}O_{benthic}$. (a) U1476 $\delta^{18}O_{benthic}$ record (blue) and 5kyr-smooth (red). (b) 5kyr-smoothed record (grey) and $1^{st}$ derivative of the $\delta^{18}O_{benthic}$ 5kyr-smoothed record (orange). (c) Slope values > 0.15 (orange) plotted on the 5kyr-smoothed $\delta^{18}O_{benthic}$ record (grey). (d)5kyr-smoothed record (grey) and $2^{nd}$ derivative of the $\delta^{18}O_{benthic}$ 5kyr-smoothed record (purple). (e) Slope values > 0.15 (orange filled circles), and $2^{nd}$ slope values <-0.2 (purple triangles) plotted on the 5kyr-smoothed $\delta^{18}O_{benthic}$ record (grey).

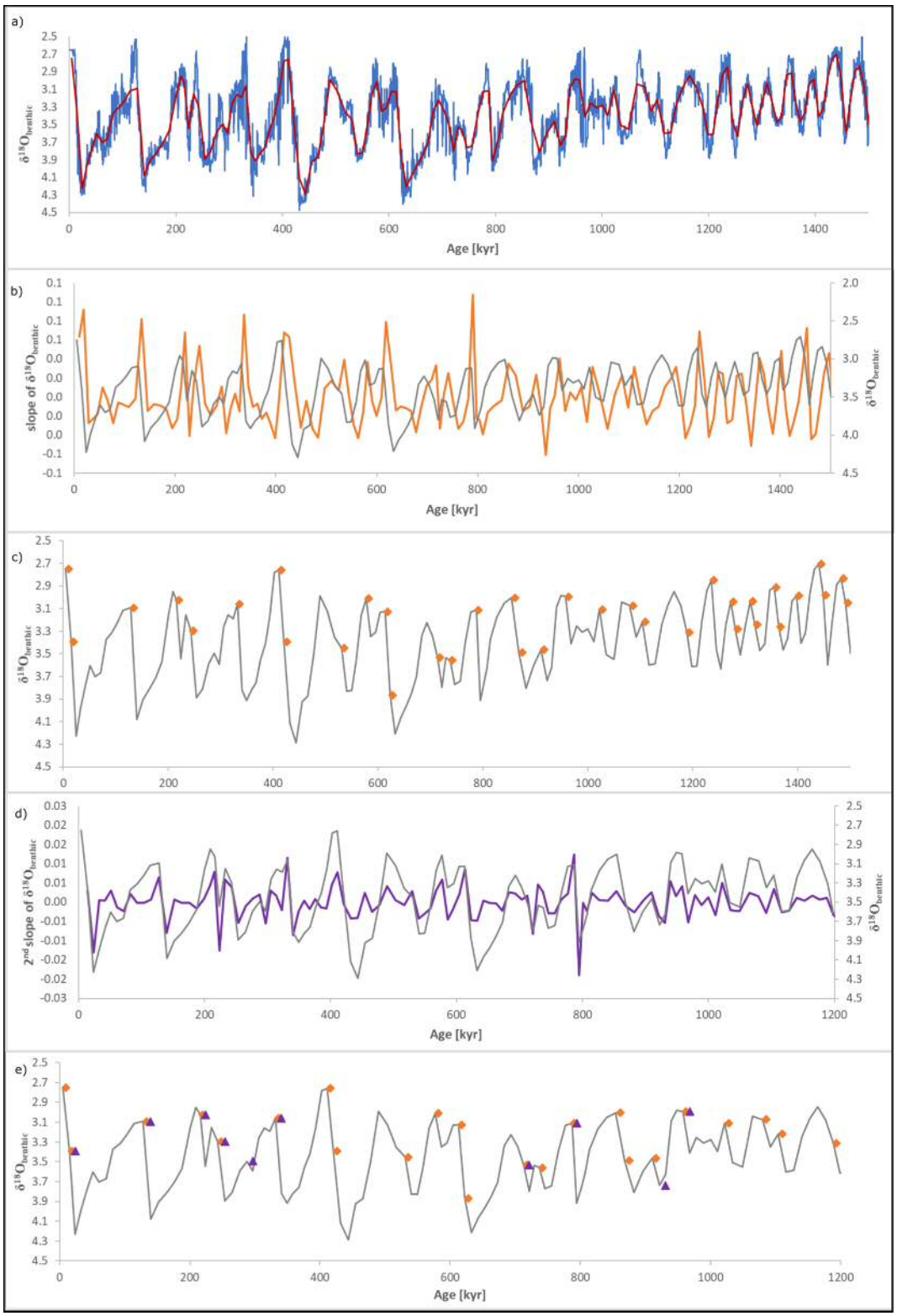


**Figure 7.10** Identification of termination midpoints (MP) using the $2^{nd}$ slope of $\delta^{18}O_{benthic}$. (a) U1476 $\delta^{18}O_{benthic}$ record (blue) and 10kyr-smooth (red). (b) 10kyr-smoothed record (grey) and $2^{nd}$ derivative of the $\delta^{18}O_{benthic}$ 10kyr-smoothed record (orange). (c) Slope values > 0.02 (orange) plotted on the 10kyr-smoothed $\delta^{18}O_{benthic}$ record (grey). (d)10kyr-smoothed record (grey) and $2^{nd}$ derivative of the $\delta^{18}O_{benthic}$ 10kyr-smoothed record (purple). (e) Slope values >0.02 (orange filled circles), and $2^{nd}$ slope values <-0.005 (purple triangles) plotted on the 10kyr-smoothed $\delta^{18}O_{benthic}$ record (grey).

### 7.3.5 Lead-lag time analysis using EPOC

Lead-lag time quantification was also tested using superimposed EPOC analysis. The analysis requires $\delta^{18}O_{benthic}$−midpoint times for each glacial cycle, then aligns all glacial cycles with their respective midpoint centred at 0, and other variables (e.g. $\delta^{18}O_{sw}$) are aligned accordingly. The stacked glacial cycles are averaged and plotted with 25 and 75 quantile error envelopes. The analysis was successful in identifying lead-lag relationships for the last 4 glacial cycles (Figure 7.11), but was unable to portray relationships for all 16 glacial cycles, due to the change in cycle periodicity and shape (Figure 7.12).

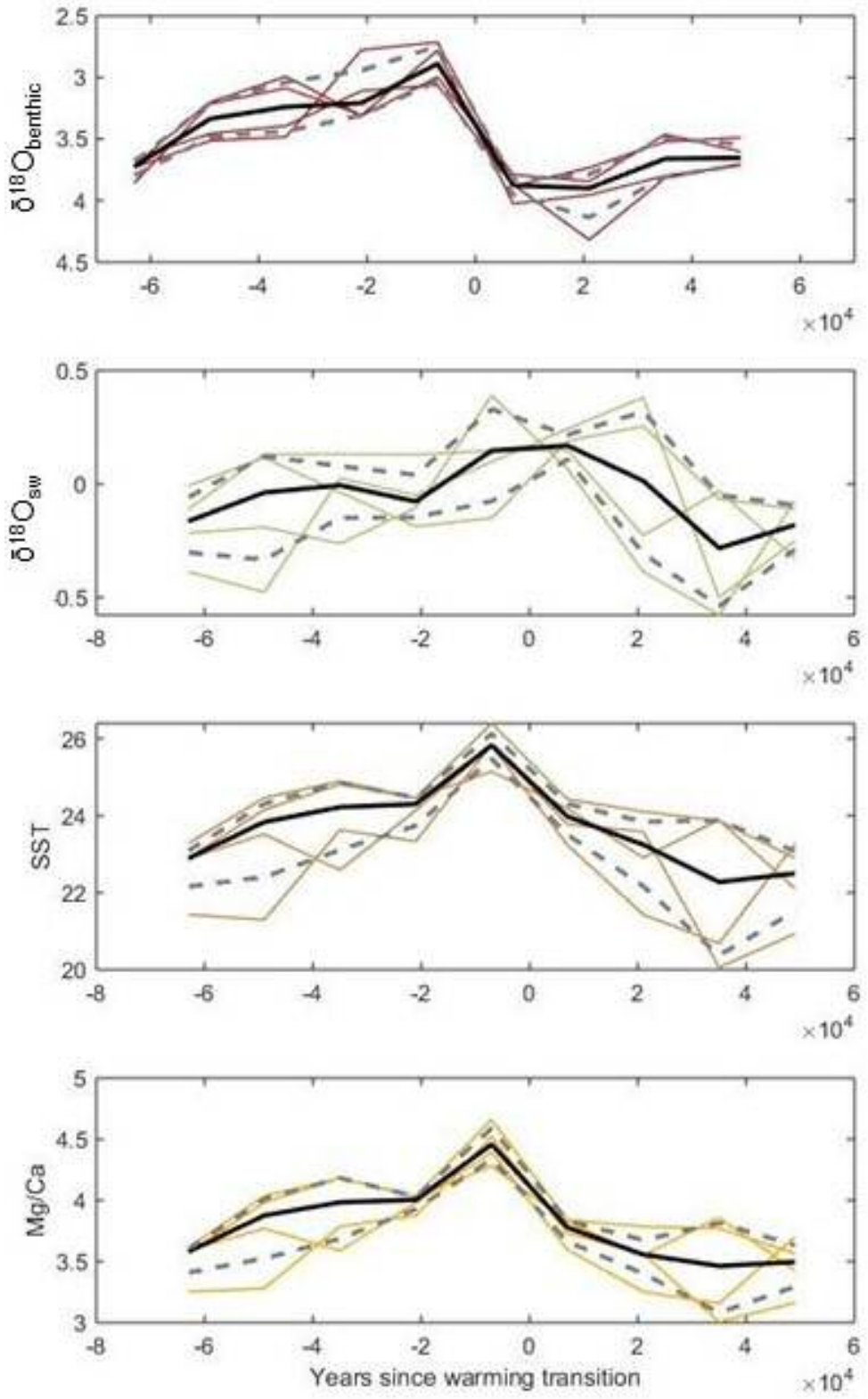


**Figure 7.11** Superimposed EPOC analysis output for the last 4 glacial-interglacial cycles from MIS5 to MIS11 for $\delta^{18}O_{sw}$, SST, and Mg/Ca with an analysis time of 70kyr either side of the respective termination midpoint.

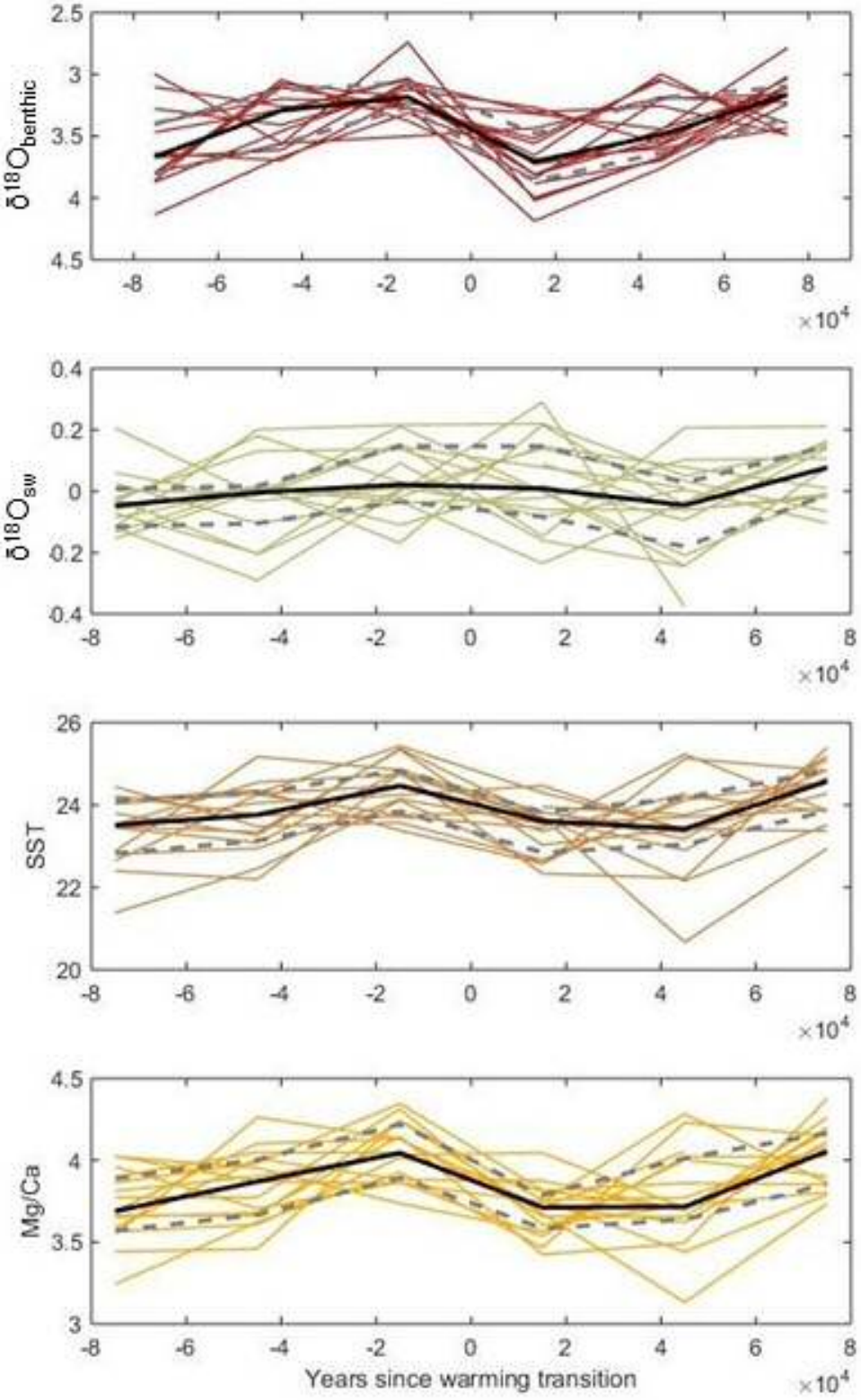


**Figure 7.12** Superimposed EPOC analysis output for all 16 glacial-interglacial cycles from MIS1 to MIS33 for $\delta^{18}O_{sw}$, SST, and Mg/Ca with an analysis time of 90kyr either side of the respective termination midpoint.

### 7.3.6 Global ice-sheet, sea level and topography simulations using ANICE and SELEN

Global ice volume and sea-level change where simulated using an inverse modelling approach with the global 3D ice-sheet model ANICE (de Boer et al., 2014a). Here I use the benthic $\delta^{18}$O data from U1476 to derive ice volume and deep-ocean temperature changes contributing to the benthic $\delta^{18}$O signal. A surface-air temperature anomaly is calculated every 100 years and used to adapt present-day temperature and precipitation over the ice-sheet regions to simulate ice volume. Following mass conservation of $\delta^{18}$O of ice-sheets and ocean volume I determine the ice-volume contribution to sea water $\delta^{18}O_{ivc}$. The deep-water temperature change is derived using a time-lag temperature relation relative to the surface-air temperature anomaly, and its contribution to benthic $\delta^{18}$O is determined using a linear relationship following Duplessy et al. (2002).

The ice-sheet model calculates ice volume over Antarctica, Greenland, North America and Eurasia. In ANICE, the shallow ice and shallow shelf approximations are used to simulate ice dynamics over long time scales. Following this procedure, I ran simulations with the ANICE-SELEN model (de Boer et al., 2014b), a fully coupled ice-sheet sea-level model. Ice-sheet thickness on land is passed to SELEN every 1kyr, whereas global relative sea level (RSL) changes modelled by SELEN are fed back into ANICE. RSL change is given by the difference between the sea surface elevation change and the vertical deformation of the solid Earth. Modelled global RSL in SELEN includes the gravitational changes due to water and ice load changes, influences of the Earth's rotation, glacial isostatic adjustment of the solid Earth and considers migration of coastlines over the globe. SELEN calculates RSL changes on a 1D radial viscoelastic Earth, using a lithospheric thickness of 96km and 3-layer rheology of 3, 1 and 0.5 x $10^{21}$ Pa s, for the lower, middle and upper mantle respectively.

## 7.4 Results

Ice volume corrected $\delta^{18}O_{sw}$ and Mg/Ca-derived SSTs show repeated cyclic features (Figure 7.13).

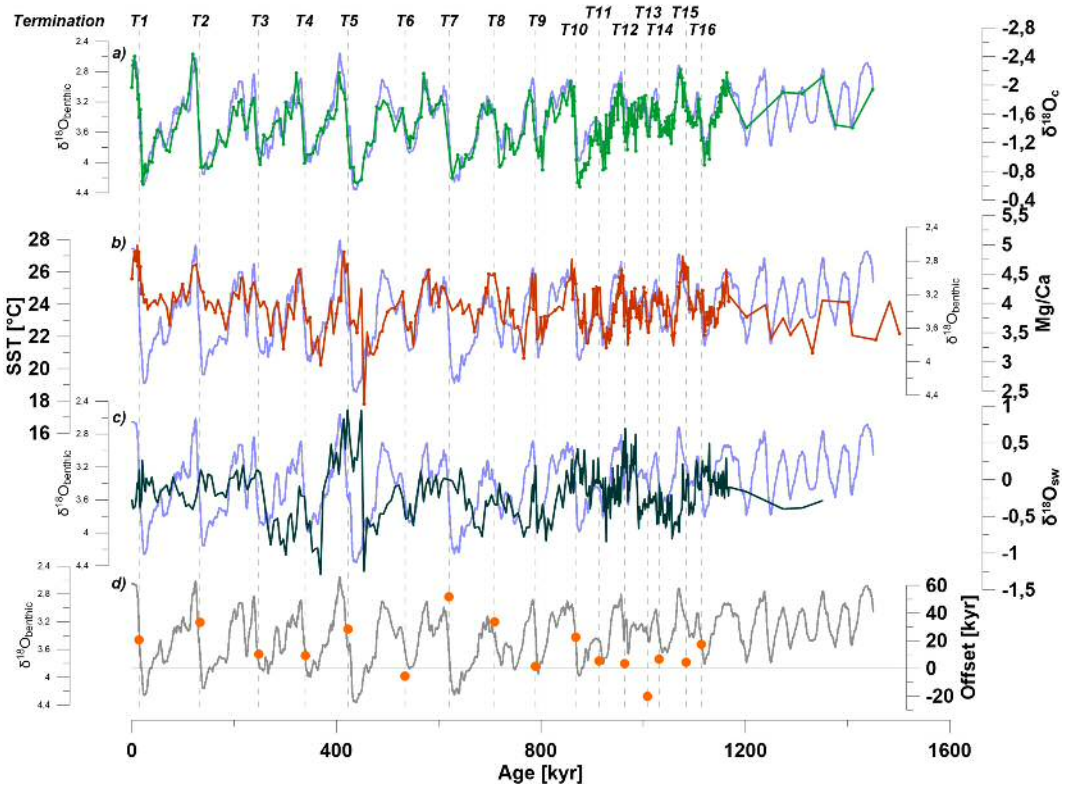


**Figure 7.13** U1476 (a) $\delta^{18}O_{G.\ ruber}$ (green), (b) Mg/Ca-derived SST (red), and (c) $\delta^{18}O_{sw}$ (dark green) from *G. ruber*, with U1476 $\delta^{18}O_{benthic}$ in light blue.(d) Age offsets between termination midpoints of $\delta^{18}O_{sw}$ and $\delta^{18}O_{benthic}$ (orange filled circles). Positive/negative offsets show $\delta^{18}O_{sw}$ terminating before/after $\delta^{18}O_{benthic}$.

Consistently, $\delta^{18}O_{sw}$ increase abruptly in the second half of the glacial cycle, in parallel with more gradual increases in SSTs. Both proxies then decrease before or during interglacial maximum, with $\delta^{18}O_{sw}$ showing more abrupt changes and SSTs reducing more gradually. Highest SSTs are around 28°C, while lowest SSTs fall to 18°C before termination 5 (T5). This fits well with a modern average of 28°C (Fallet et al., 2010), and a yearly seasonal variability of $\pm$2.5°C (Figure 7.14).

Early Holocene values of $\delta^{18}O_{sw}$ reach modern values of around 0.55‰ (Fallet et al., 2010), with slight reduction to around 0.3 for the core-top sample.

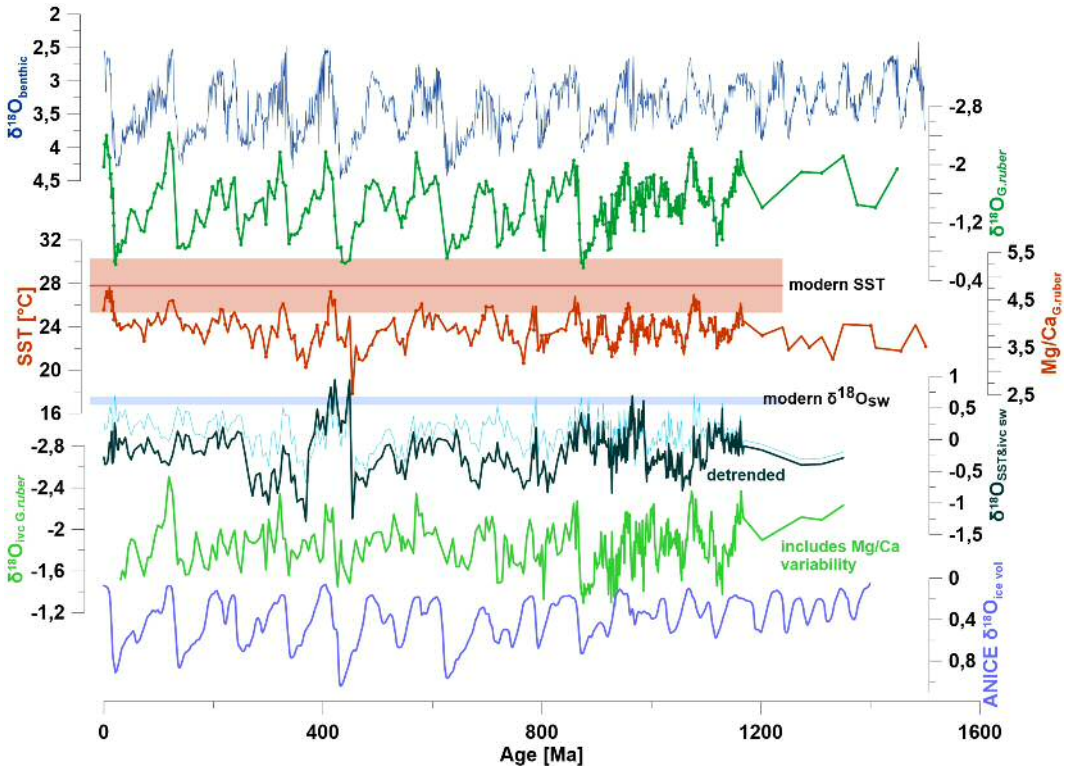


**Figure 7.14** Calculation of U1476 $\delta^{18}O_{sw}$ from $\delta^{18}O_{G.\ ruber}$ and Mg/Ca. (a) $\delta^{18}O_{benthic}$ (blue). (b) $\delta^{18}O_{G.\ ruber}$ (green). (c) Mg/Ca$_{G.\ ruber}$ (red). (d) $\delta^{18}O_{sw}$ (ivc & SST corrected)(ice blue), and mid-point detrended (dark blue). (e) $\delta^{18}O_{sw}$ (ivc-only corrected) (light green). (f) ANICE-modelled $\delta^{18}O_{ivc}$. Shaded horizontal areas represent modern values. Note that some y-axes are flipped for plotting consistency.

Ice volume corrected $\delta^{18}O_{sw}$ can be interpreted as relative changes in sea surface salinity (SSS). SST and SSS correlate closely implying that warm surface waters are salty, while cool surface waters are fresher. Deglacial SST and SSS both lead benthic $\delta^{18}$O by several thousand years (Figure 7.13). The result is consistent when SST and SSS are compared to RSL instead of benthic $\delta^{18}$O) (Figure 7.15.

In 14 out of 16 deglaciations, SSS terminates on average 17.5kyr earlier than $\delta^{18}O_{benthic}$, with the longest lead-lag relationship during T7 where SSS increases 51.8kyr before $\delta^{18}O_{benthic}$ (Table 7.1). T6, and T13 are the exception, where SSS responds in line with, or slightly lags $\delta^{18}O_{benthic}$. However, these glacial cycles are known as abnormal in shape (multi-peaked), and alternative solutions for interglacial highstands exist.

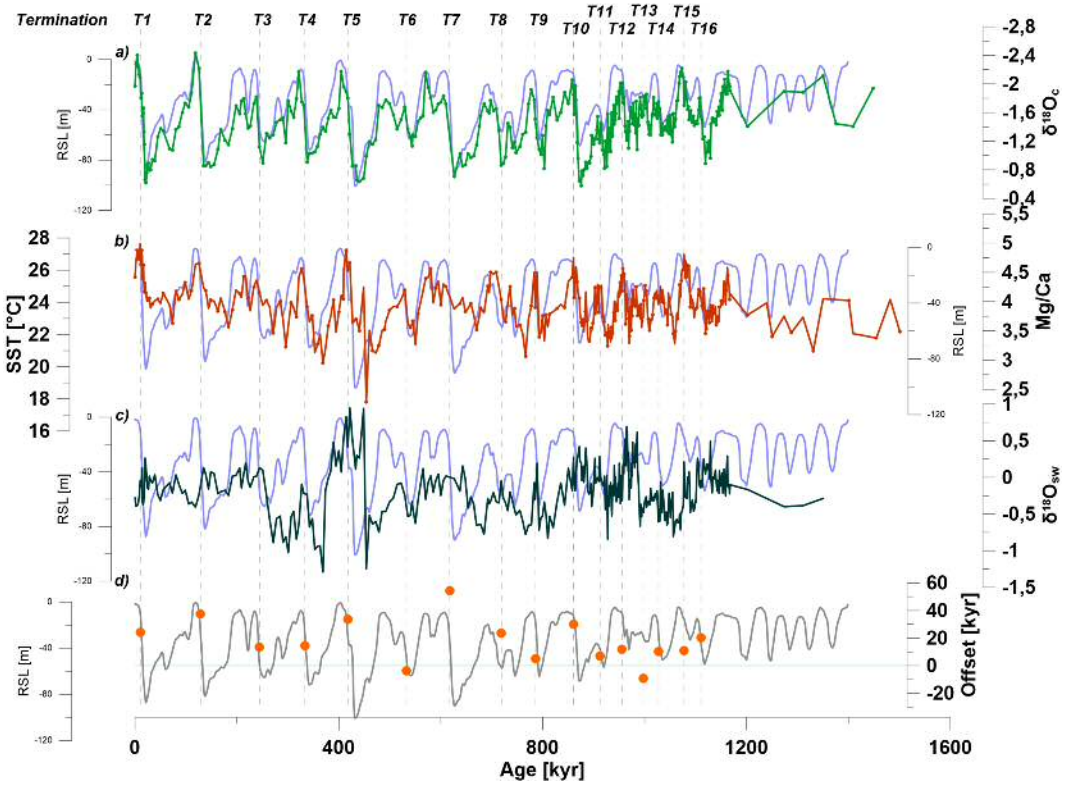


**Figure 7.15** U1476 (a) $\delta^{18}O_{G.\ ruber}$ (green), (b) Mg/Ca-derived SST (red), and (c) $\delta^{18}O_{sw}$ (dark green) from *G. ruber*, with U1476 relative sea level (RSL) in light blue.(d) Age offsets between termination midpoints of $\delta^{18}O_{sw}$ and RSL (orange filled circles). Positive/negative offsets show $\delta^{18}O_{sw}$ terminating before/after RSL.

To understand the sensitivity of SSTs to input parameters, I tested the effect of prescribed vs. varying pH, salinity (S), and pH-influencing alkalinity on resulting SSTs. Varying parameters were calculated iteratively. I prescribed pHs of 8.1, and 8.2 (Figure 7.16), and varied pH, while S=35, and while S was varied itself.

The difference between scenarios with prescribed S and varied S are indistinguishable and plot on-top of each other (Figure 7.17), while the maximum difference between prescribed and varied pH scenarios is 3°C (Figure 7.17b).

pH is calculated assuming a value of alkalinity. I therefore tested the influence of prescribed (ALK=2300) and varying alkalinity (starting ALK = 2300) values on final SST calculations. Differences in SSTs are less than 1°C between prescribed and changing alkalinity (Figure 7.18).

**Table 7.1** Times for $\delta^{18}O_{benthic}$ and $\delta^{18}O_{sw}$ midpoints, and their difference defined as Age ($MP_{\delta^{18}O_{sw}}$) - Age ($MP_{\delta^{18}O_{benthic}}$)

| Termination | Age ($MP_{\delta^{18}O_{benthic}}$) *[kyr]* | Age ($MP_{\delta^{18}O_{sw}}$) *[kyr]* | **Difference *[kyr]*** |
|---|---|---|---|
| T1 | 13.9 | 34.8 | **20.9** |
| T2 | 132.8 | 166.1 | **33.3** |
| T3 | 247.8 | 257.9 | **10.2** |
| T4 | 338.8 | 348.0 | **9.2** |
| T5 | 422.9 | 451.2 | **28.4** |
| T6 | 534.3 | 528.7 | **-5.6** |
| T7 | 620.3 | 672.0 | **51.8** |
| T8 | 709.0 | 742.5 | **33.6** |
| T9 | 789.5 | 791.0 | **1.5** |
| T10 | 867.9 | 890.4 | **22.5** |
| T11 | 914.1 | 919.6 | **5.5** |
| T12 | 963.8 | 967.3 | **3.5** |
| T13 | 1008.5 | 988.4 | **-20.1** |
| T14 | 1031.0 | 1037.7 | **6.7** |
| T15 | 1084.1 | 1088.5 | **4.4** |
| T16 | 1113.6 | 1131.0 | **17.4** |

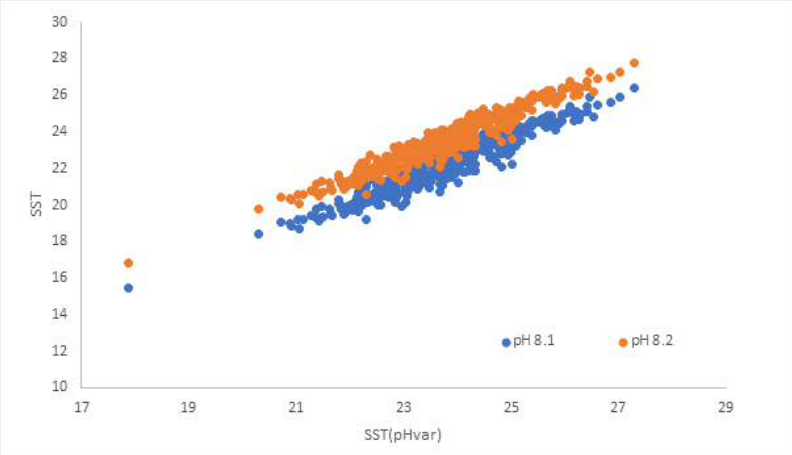


**Figure 7.16** Sensitivity test of the SST response to prescribed and varying pH and salinity (S) as crossplot between iteratively varying pH scenarios (x-axis) and prescribed pH scenario (y-axis). The test was conducted using two different pH starting values. The different responses are plotted in orange and blue. This plot shows that differences in calculated SST are minimal between iteratively varying pH and constant pH. The choice of starting pH minimally influences the absolute value of SST, but does not influence the $pH_{var}$-$pH_{constant}$ relationship.

For varying alkalinity, a modern starting value must be inserted. Hence, I additionally tested five potential modern starting values for varying alkalinity. These

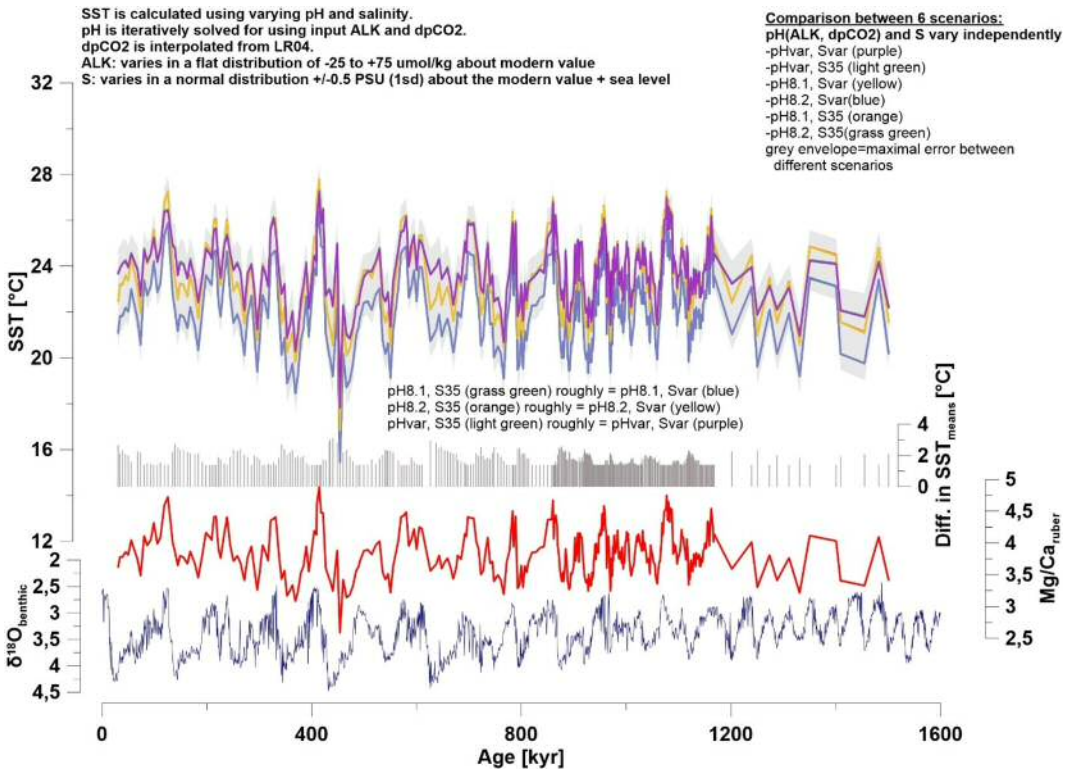


**Figure 7.17** Sensitivity test of SST to prescribed and varying pH and salinity (S). From top to bottom: (a) calculated SSTs for different pH, S scenarios. Difference between S=35, and S=varying is minimal making the S35 scenarios invisible. Monte Carlo $95^{th}$ quantile errors represented as grey envelope. (b) Difference between lowest and highest scenario for each measurement point in grey vertical bars. (c) U1476 $Mg/Ca_{G.\ ruber}$ (red). (d) U1476 $\delta^{18}O_{benthic}$ data (blue).

include ALK=2350 (default value in the R script), ALK=2345 (GLODAP dataset alkalinity value for the northern Mozambique channel), ALK=2300 (used in Fallet et al. 2010 for the northern Mozambique channel), ALK=2292.5 calculated using Lee et al (2006) for the Indian Ocean, and ALK=2285 (low ALK endmember). Again, maximum SST differences are <1°C (Figure 7.19).

Changes in central Mozambique $\delta^{18}O_{sw}$ from the coast have previously been linked to East African monsoon variability (Weldeab et al., 2014). Ba/Ca ratios have been proposed to track riverine freshwater input due to increased Ba concentrations in riverine waters from suspended continental estuarine muds compared to the surrounding coastal seawater (Schmidt & Lynch-Stieglitz, 2011; Weldeab et al., 2014). Near the Zambezi river mouth south of U1476, Weldeab et al. (2014) report

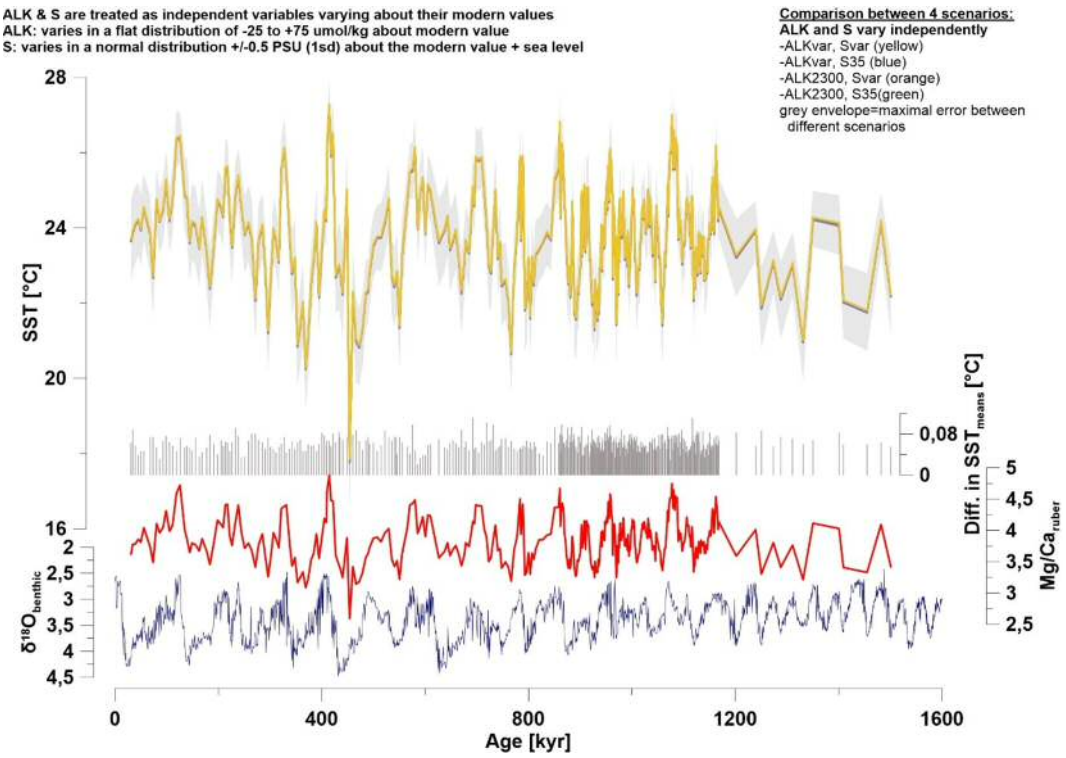


**Figure 7.18** Sensitivity test of SST to prescribed and varying alkalinity (ALK) and salinity (S). From top to bottom: (a) calculated SSTs for different ALK, S scenarios. Difference between scenarios is minimal causing scenarios to plot on top of each other. Monte Carlo errors represented as grey envelope. (b) Difference between lowest and highest scenario for each measurement point plotted as grey vertical bars. (c) U1476 $Mg/Ca_{G.\ ruber}$ (red). (d) U1476 $\delta^{18}O_{benthic}$ data (blue).

a tight correlation between Ba/Ca and $\delta^{18}O_{sw}$ suggesting that coastal $\delta^{18}O_{sw}$ is controlled by Zambezi freshwater input which is closely correlated to the East African monsoon. At U1476, I do not find a correlation between $\delta^{18}O_{sw}$ and Ba/Ca (Figure 7.20).

This could be due to U1476 being located outside of the Zambezi river plume and therefore not recording changes in riverine input. However, Ba/Ca values at U1476 plot around 2-8 $\mu$mol/mol (Figure 7.20; see also Figure 5.7 in chapter 5.3.3) which is much higher than Ba/Ca values at the Zambezi river mouth. Saraswat et al. (2013) also observed comparably high Ba/Ca values in the Arabian Sea and suggest that the proxy might be overprinted by additional Ba from pore waters due to high productivity. The modern Mozambique Channel is known as a biodiversity hotspot

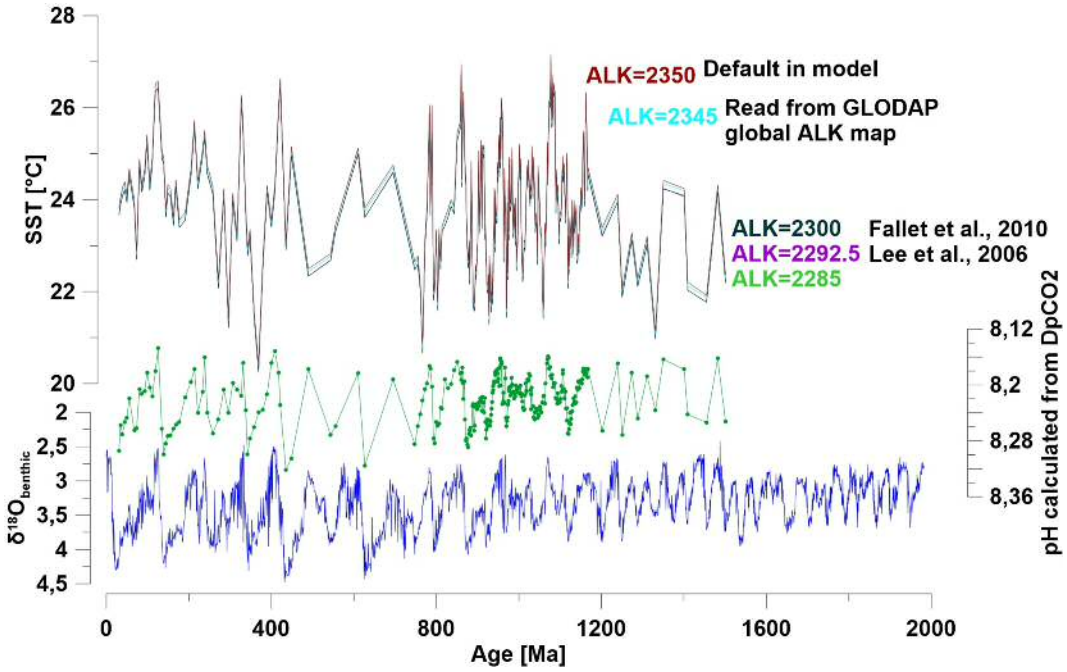


**Figure 7.19** (a) Resulting SST calculations using the iteratively solving R-script of Gray & Evans (2019) with different modern alkalinity estimates as starting values. (b) Calculated pH for different ALK estimates. Differences in pH plot on top of each other. (c) For comparison, U1476 $\delta^{18}O_{benthic}$.

with high modern productivity rates (Obura et al., 2019). Ba concentrations may increase in sediment pore waters at locations with high productivity, due to increases in sedimentary sulfate reduction and dissolution of barite ($BaSO_4$) (Agnihotri et al., 2003). As such, Ba/Ca ratios at U1476 may be overprinted by post-depositional Ba increase, and represent changes in productivity rather than Zambezi riverine outflow. Still, given the distance between the Zambezi river mouth and U1476, it is unlikely that riverine plumes provide a first order control on the $\delta^{18}O_{sw}$ at U1476. I therefore suggest that $\delta^{18}O_{sw}$-derived SSSs and SSTs at U1476 are driven by changes in the hydrography of Indian Ocean water masses entering at the northern mouth of the Channel.

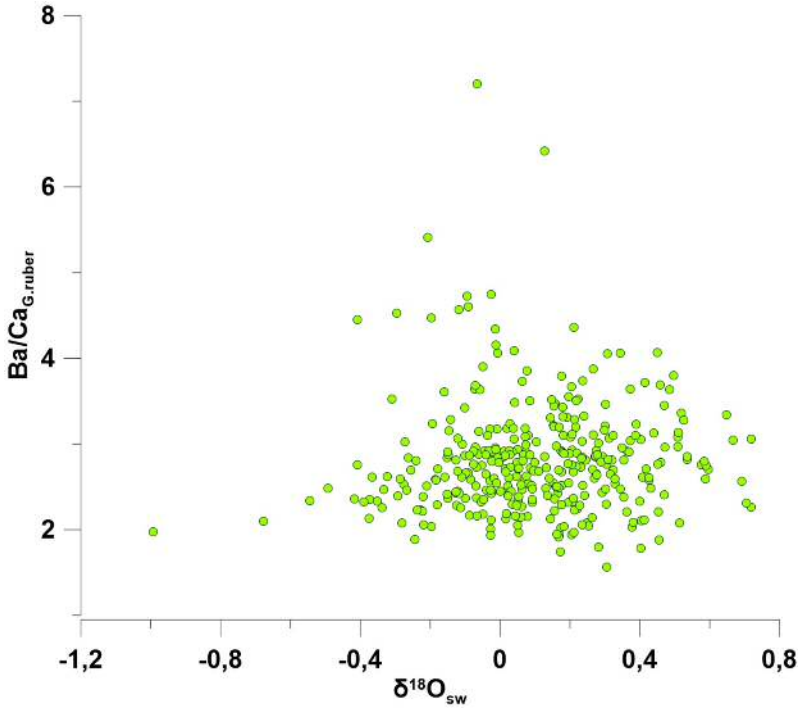


**Figure 7.20** Cross-plot between Ba/Ca and $\delta^{18}O_{sw}$ as indicator for potential influence of riverine freshwater on U1476 surface salinity variability. The lack of correlation suggests little to no influence of riverine input on U1476 surface hydrography.

## 7.5 Discussion

In the Mozambique Channel, changes in SSS and SST lead climate terminations over the last 1.2 Ma. I propose that the multi-millennial SSS and SST variability in the Mozambique Channel is the result of shifts between different Indian Ocean surface waters controlled by glacial-interglacial ITF dynamics coupled with changes in the strength of the Agulhas Leakage.

To understand past influences on SSS and SST, I first identify modern drivers of SSS in the Indian Ocean. Modern surface circulation in the tropical and subtropical Indian Ocean differs from the Atlantic and Pacific in that it does not exhibit highly saline surface waters in the Indian Ocean gyre. This is due to the inflow of fresh and cool ITF-waters travelling westwards along the South Equatorial Current (SEC) (Talley, 2005), as well as the loss of saline and warm surface waters to the Atlantic Ocean through the Agulhas Leakage (Figure 7.1). Palaeoclimate evidence suggests

that both the ITF (Holbourn et al., 2011; Xu et al., 2008; Xu et al., 2006), and the Agulhas Leakage (Caley et al., 2012; Caley et al., 2014; Peeters et al., 2004) were reduced during peak glacial conditions. This may alter the salinity and temperature patterns in the glacial Indian Ocean surface waters, and ultimately define the salinity concentrations in the Agulhas Leakage. I see an increase in glacial SSTs and available SSS data throughout the glacial Indian Ocean (Figure 7.21; for core sites see Figure 7.22) suggesting a large-scale reorganisation of SSTs and SSSs during glacial periods. The mechanisms responsible for those reorganisations must be intrinsic to the Indian Ocean, as no comparable glacial warming can be seen in Indian Ocean source regions, such as the South China Sea (SCS), and the western Pacific warm pool (WPWP) (Figure 7.23)

The glacial increase in SST and SSS is also found in the immediate Agulhas Leakage source regions (Figure 7.24; Simon et al., 2013; Simon et al., 2015) suggesting that it will have a direct effect on the salt content of the Agulhas Leakage itself.

I propose that these large-scale glacial hydrographic changes are linked to the interplay between reduced inflow of cooler freshwater from the ITF and reduced outflow of warmer salty water through the Agulhas Leakage. This would have supported greater recirculation of surface waters in the glacial Indian Ocean, enhancing net-evaporation, and leading to warming and salinification. As such, the glacial Indian Ocean may have presented a subtropical gyre system much more like the salty and warm subtropical gyres present in the modern Atlantic and Pacific Oceans (Figure 7.25).

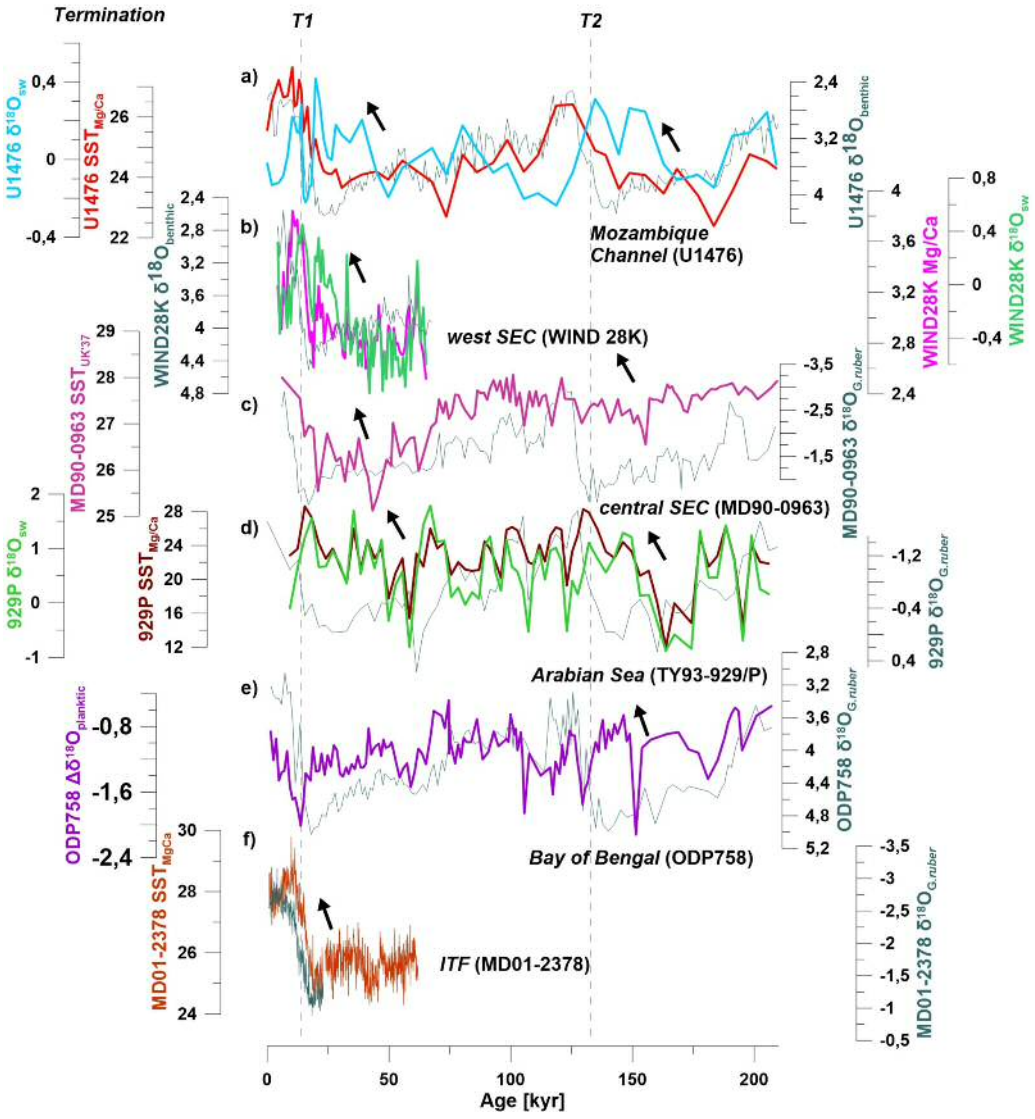


**Figure 7.21** Comparison of lead-lag relationships in the Indian Ocean. SST and available SSS data plotted in comparison to core-respective benthic or planktonic $\delta^{18}O$ as proxy for global ice volume. All $\delta^{18}O_{benthic}$ data in blue. (a) Mozambique Channel SST (red) and $\delta^{18}O_{sw}$ light blue) (this study). (b)Mg/Ca (pink) and $\delta^{18}O_{sw}$ (green) from the western SEC (Kiefer et al., 2006). (c) central SEC SSTs (light purple) (Bassinot et al., 1994). (d) Arabian Sea SSTs (brown) and $\delta^{18}O_{sw}$ (light green) (Barker et al. unpubl.; Rostek et al., 1997). (e) relative changes in $\delta^{18}O_{sw}$ from the Bay of Bengal (Bolton et al., 2013). (f) SSTs (orange) from the ITF outflow region (Xu et al., 2008; Zuraida et al., 2009). Early increases in SST/SSS are indicated with black arrows.

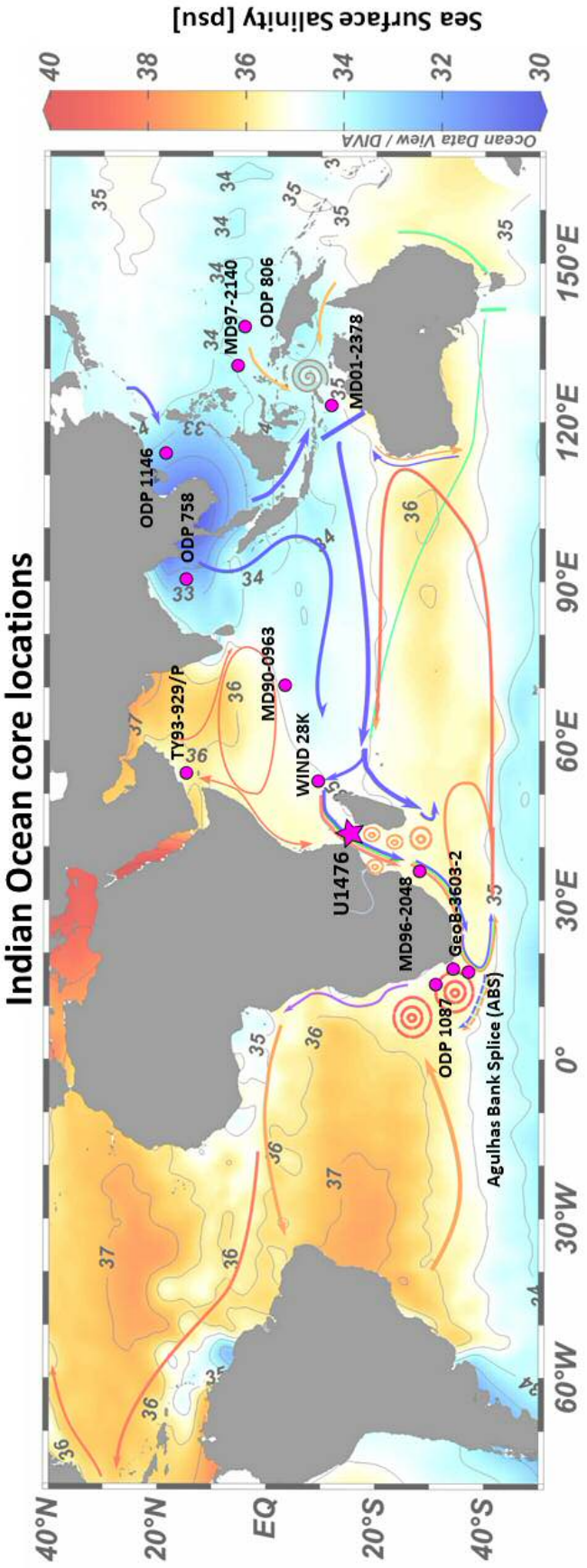


**Figure 7.22** Spatial compilation of published core locations and U1476 from the Indian Ocean, Indonesian archipelago, and Agulhas system plotted on modern ocean sea surface salinity.

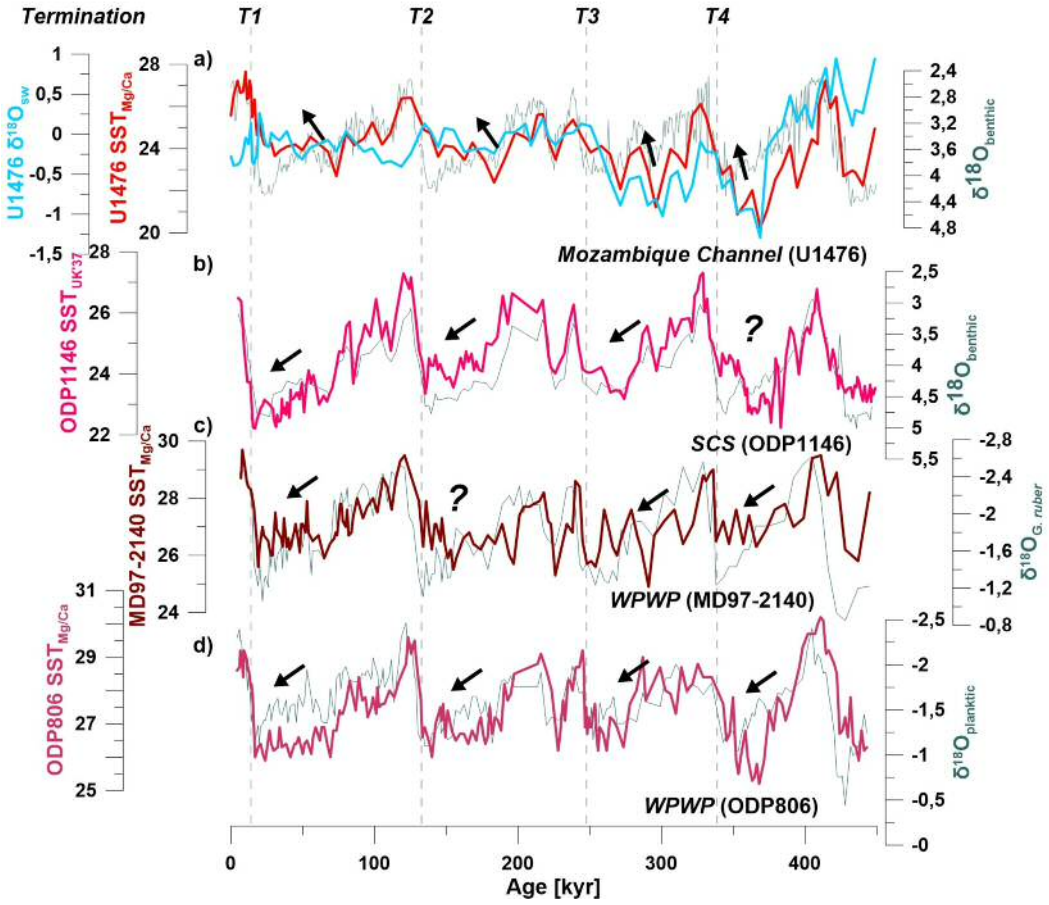


**Figure 7.23** Comparison of lead-lag relationships in the South China Sea (SCS) and western Pacific warm pool (WPWP). SST and available SSS data plotted in comparison to core-respective benthic or planktonic $\delta^{18}O$ as proxy for global ice volume. All $\delta^{18}O_{benthic}$ data in blue. (a) Mozambique Channel SST (red) and $\delta^{18}O_{sw}$ light blue) (this study). SSTs from the SCS (pink) (Herbert et al., 2010) (b), and the WPWP (brown) (c) (De Garidel-Thoron et al., 2005), (purple) (d) (Medina-Elizalde & Lea, 2005b). Termination-related increases are indicated by black arrows.

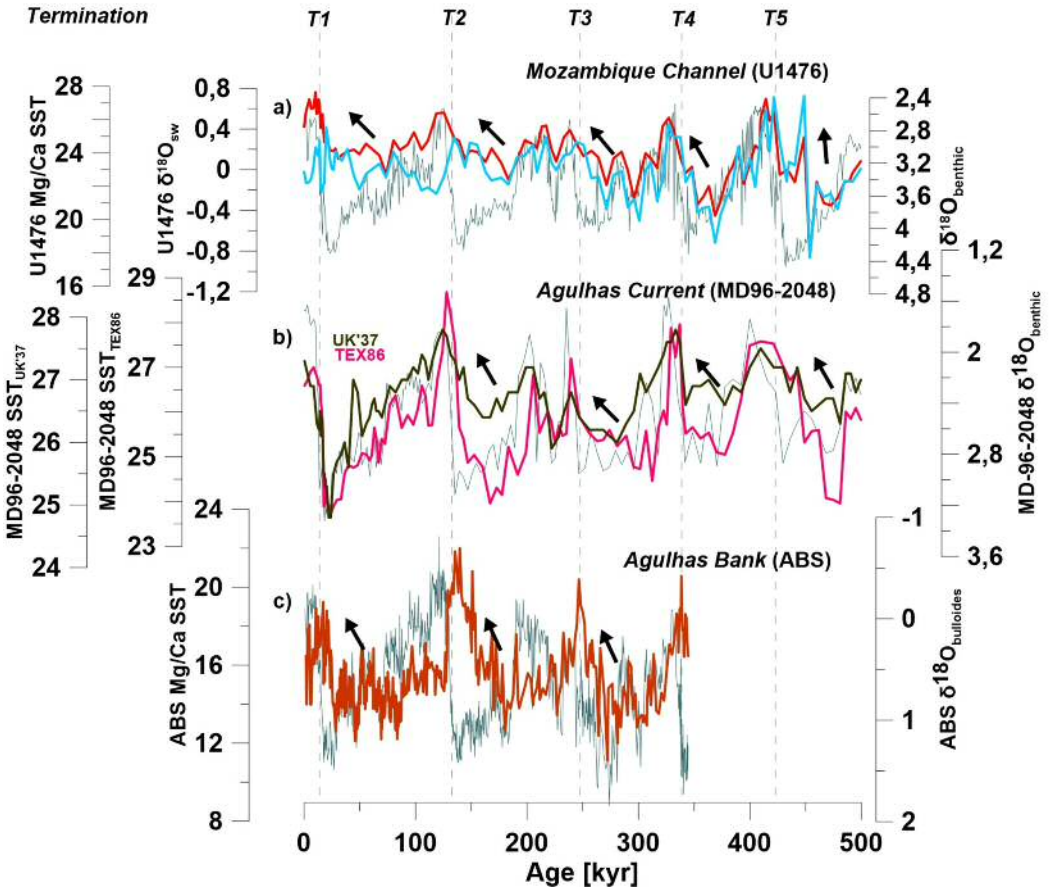


**Figure 7.24** Comparison of lead-lag relationships in the upstream Agulhas system. SST and available SSS data plotted in comparison to core-respective benthic or planktonic $\delta^{18}O$ as proxy for global ice volume. All $\delta^{18}O_{benthic}$ data in blue. (a) Mozambique Channel SST (red) and $\delta^{18}O_{sw}$ light blue) (this study). (b) UK'$^{37}$ (dark brown) and TEX86 (pink) -derived SST from the Agulhas Current (Caley et al., 2011). (c) SST (orange) from the Agulhas Bank (Martinez-Mendez et al., 2010). Early increases in SST/SSS are indicated with black arrows.

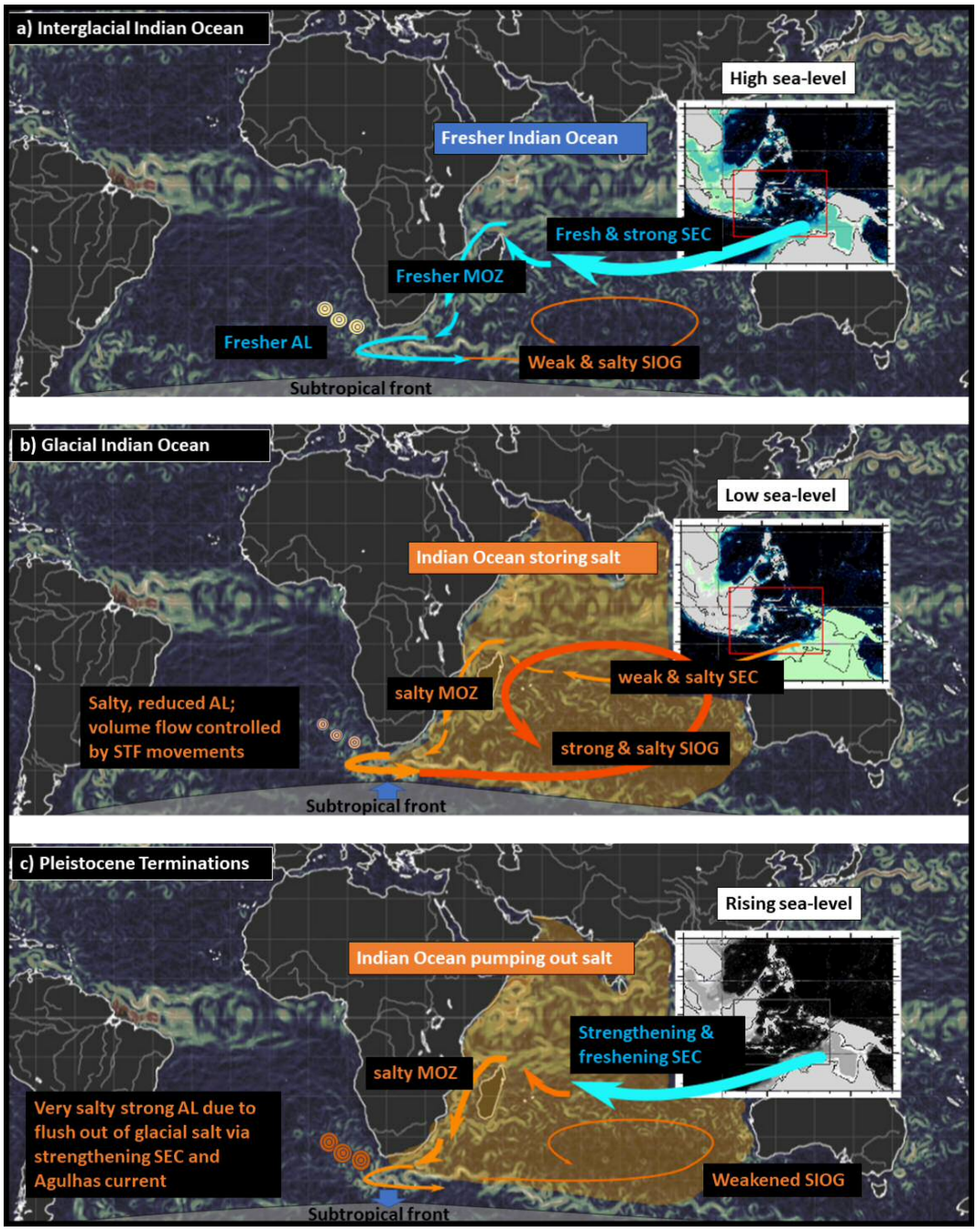


**Figure 7.25** Conceptualisation of Indian Ocean salt content and circulation during (a) interglacial, (b) glacial, and (c) terminations. Orange/blue colouring suggests higher/lower salt content. Ocean circulation pathways indicated by arrows.

### 7.5.1 Glacial ITF reduced by changes in relative sea level

It has been previously suggested that the glacial ITF was reduced due to lowering of sea level and the exposure of Indonesian and Australian shelves (Holbourn et al., 2011; Linsley et al., 2010; Petrick et al., 2019). To identify whether changes in sea level and ITF reduction occur in concert, I created a relative sea level curve by inputting the U1476 $\delta^{18}O_{benthic}$ into a 3D ice-sheet model (ANICE) (see also Figure 7.26).

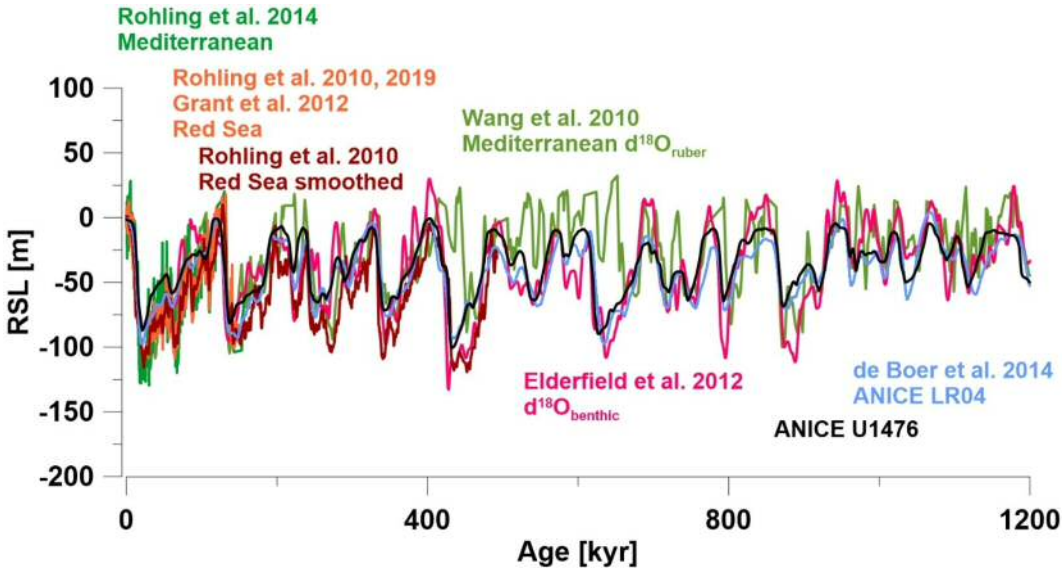


**Figure 7.26** Comparison of different relative sea level reconstructions for the last 1.2Ma. ANICE model results from U1476 (this study, black) and LR04 (light blue) are plotted with sea level reconstructions from the Mediterranean (dark green, light green), the Red Sea (dark red, orange), and ODP1123 (pink).

RSL covaries closely with $\delta^{13}C_{benthic}$ from the ITF (Figure 7.27) providing evidence that reduction in sea level across the Indian archipelago can cause a reduction in ITF.

To further investigate the drivers of a reduced ITF, I reconstructed the changes in above-sea-level topography using an ice sheet-topography coupled model (ANICE-SELEN). The results produce two major changes in above-sea-level topography across the Indonesian archipelago when crossing a ∼50m below modern sea level threshold. These include exposure of the North Australian shelves and closure

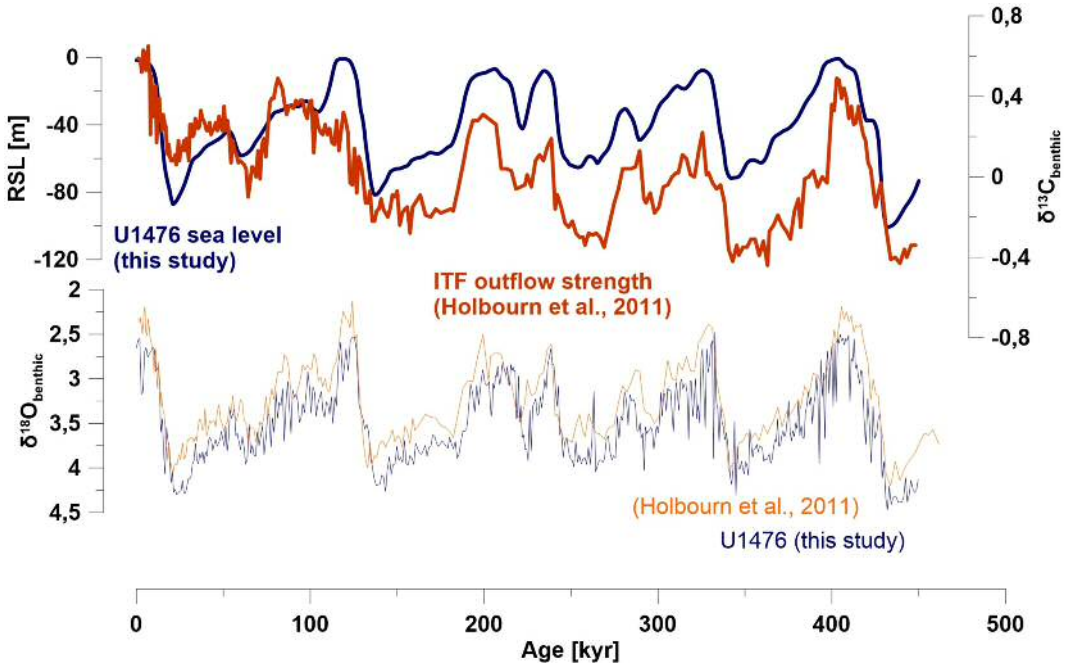


**Figure 7.27** Close correlation between U1476 RSL (blue) and a reconstruction of ITF outflow strength using benthic $\delta^{13}$C (Holbourn et al., 2011). Benthic $\delta^{18}$O in light blue (U1476) and orange (MD01-2378) for age model comparison.

of the Java Straits (Figure 7.28). The relative elevation of the Australian shelves will restrict the Timor Straights which have been identified as the main outflow of the ITF (Sprintall et al., 2014). Additionally, closure of the Java Straits would isolate the South China Sea from the ITF, cutting-off its source for freshwater input. Palaeobotanical evidence supports a complete closure of the Java Straits during glacials (Bird et al., 2005), suggesting that SCS-sourced freshwater lenses were missing from the glacial ITF transforming it into a warm, salty surface outflow (Holbourn et al., 2011; Xu et al., 2008; Xu et al., 2006).

Using the PMIP model ensemble, DiNezio et al. (2013; 2016) show that exposure of Australian shelves and Java Straits lead to changes in Indian Ocean-wide rainfall patterns, which drive increases/decreases in eastern/western modelled Indian Ocean salinity. However, if Indian Ocean SSS were mainly driven by atmospheric teleconnections, one would expect a fresher surface water signature in the western

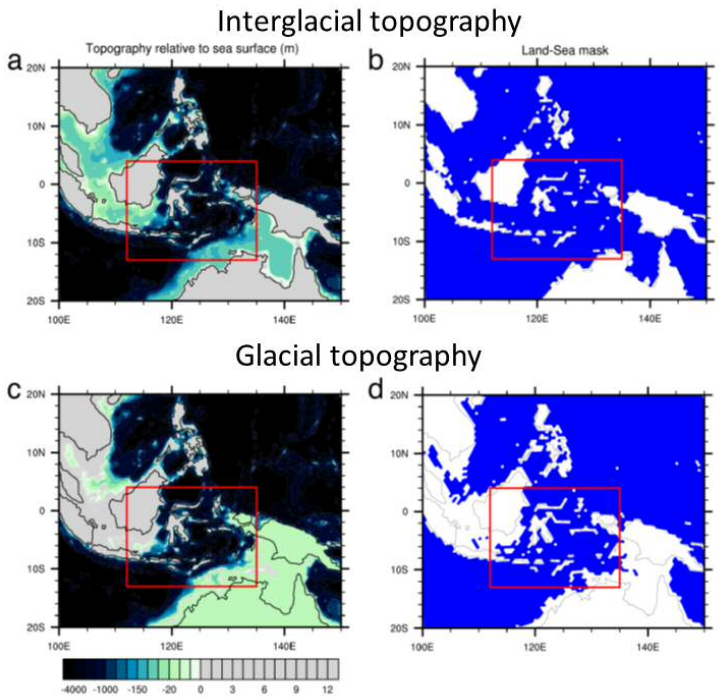


**Figure 7.28** Modelled topography changes (in m) in the Indonesian archipelago between a glacial and interglacial from the ANICE-SELEN coupled sea level-topography model. Note two distinct features: (1) closure of the Java Straits due to land-bridge formation, (2) narrowing of the Timor Straits due to shallowing of the Australian shelf.

Indian surface Ocean. At U1476, I see a saltier glacial signature hinting towards an oceanographic driver overprinting the atmospheric signal.

### 7.5.2 A sporadically very salty Agulhas Leakage

I propose that the reduction and salinification of the ITF drove a transformation in the hydrography of the SEC by reducing the input of cool and fresh thermocline waters from the ITF, while enhancing the recirculation of warm and salty southern Indian Ocean waters. However, if the ITF was the sole driver of salinity in the SEC, one would expect a clearer relationship involving threshold behaviour between the lead times in $\delta^{18}O_{sw}$ and $\delta^{18}O_{benthic}$. I therefore assume a second mechanism to be involved in shaping salinity in the SEC and ultimately the Indian surface ocean.

The Agulhas Leakage effectively controls the release of salty and warm surface waters from the Indian Ocean into the colder, fresher South Atlantic. Evidence suggests that the leakage efficiency increased abruptly at climate terminations with increases in flow volume (Caley et al., 2012; Caley et al., 2014; Peeters et al., 2004), and particularly high salinity spikes (Marino et al., 2013). My data show that salinity in the Mozambique Channel, and effectively in the whole Indian Ocean, are often highest shortly before a volume spike in Agulhas Leakage occurs (Figure 7.29).

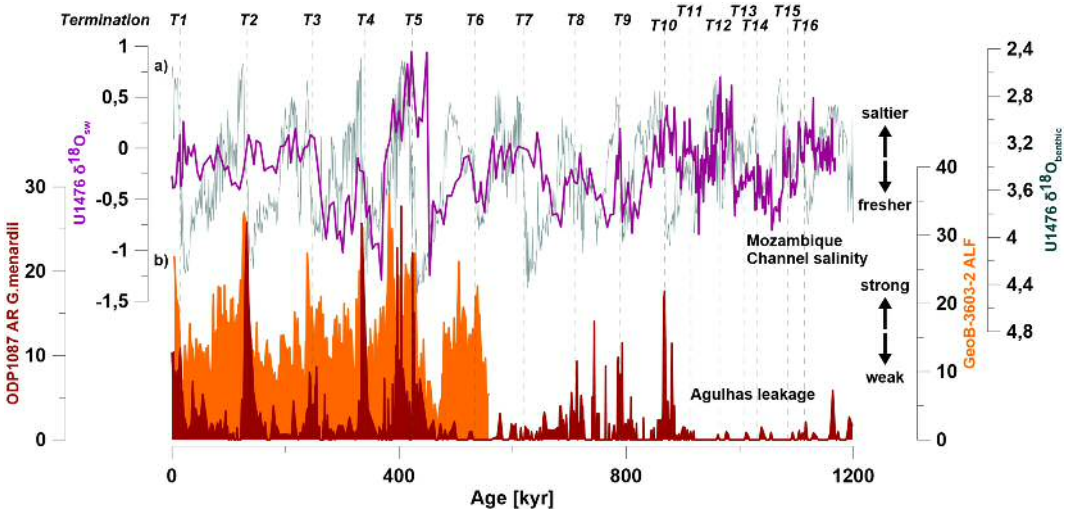


**Figure 7.29** U1476 $\delta^{18}O_{sw}$ (purple) and $\delta^{18}O_{benthic}$ (blue) (a) plotted with Agulhas Leakage proxies (b). Agulhas Leakage fauna (ALF) (orange) (Peeters et al., 2004) and G.*menardii* counts (dark red) (Caley et al., 2012) peak during terminations while U1476 salinity is high.

Considering the timing of salinity changes in relation to Agulhas Leakage, it appears that salinity only reduces after Agulhas Leakage volume peaks. This suggests that the salt stored in the glacial Indian Ocean is exported to the Atlantic Ocean via an active Agulhas Leakage causing glacial and terminal Agulhas Leakage spikes to be particularly salty.

This may have significant implications for rapid climate change and terminations. Across the record, U1476 $\delta^{18}O_{sw}$ increases on average by 0.8‰±0.7 between mid-glacial minima and late glacial maxima. Suggesting from (LeGrande & Schmidt, 2006) that 0.1‰in $\delta^{18}O_{sw}$ represents an equivalent change of 0.625psu in Indian Ocean salinity, the additional 0.8‰ would amount to an increase in 5.1psu±4.1

more salt in the Agulhas Leakage volume spikes. According to modelling results by Jackson & Wood (2018), the Atlantic meridional overturning circulation (AMOC) is highly sensitive to salinity in the North Atlantic, whereby a reduction in 0.3psu in North Atlantic surface salinity due to freshwater input can significantly reduce the AMOC. As such, the Indian Ocean glacial salinity contribution of 5.1psu$\pm$4.1 are likely significant, especially when exported into the Atlantic Ocean during abrupt Agulhas Leakage volume spikes suggested to correlate with abrupt climate change (Dyez et al., 2014). It is possible that millennial variability of the subtropical front south of Africa controls the release of highly salty glacial Indian Ocean surface waters via the Agulhas Leakage. My analyses show that the created spikes can carry up to 5psu more salt than currently transported in the modern. I therefore suggest the Agulhas Leakage as a modulator to the AMOC at times when Indian Ocean salt content is particularly high.

## 7.6 Conclusions

Indian ocean surface circulation represents an important link in the surface limb of the global overturning circulation. The southern exit point, also known as the Agulhas Leakage, has been proposed to influence glacial-interglacial climate by supplying warm and salty water to the South Atlantic surface currents. This can have a direct impact on the potential density of surface waters at deep water formation sites and therefore influence global ocean circulation vigour. Here, I present new sea surface salinity and temperature reconstructions across the last 1.2Ma from the northern Mozambique channel. SSS and SST increase well before glacial maxima and are highest before volume spikes in Agulhas Leakage. This pattern is repeated throughout the glacial Indian Ocean. I show that salinity and temperature anomalies in the Indian Ocean are a direct response to freshwater input from the ITF, and saltwater export through the Agulhas Leakage. During glacial times, these two

gateways were geographically and hydrographically narrowed reducing the flow of freshwater into, and the flow of salty water out of the Indian Ocean. I propose that the isolation of glacial Indian Ocean surface waters led to repeated recirculation with net evaporation causing basin-wide salinification and warming comparable to modern examples of subtropical gyres in the Atlantic and Pacific Oceans. My data show that highest salinity concentrations, on average 5psu higher than minimum concentrations, were reached prior to deglacial spikes in Agulhas Leakage volume flow. This suggests that the Agulhas Leakage volume spikes were transporting particularly salty waters to the Atlantic Ocean which likely had an impact on AMOC and potentially global climate. As such, the glacial Indian Ocean may act as a reservoir for salt which can be released with spikes in Agulhas Leakage activity that may lead to abrupt changes in climate.

# Chapter 8

# DE-COUPLING OF THE ICE VOLUME/$CO_2$ FEEDBACK FROM EXTERNAL FORCING DURING THE EARLY MPT

## 8.1 Abstract

The Mid-Pleistocene transition (MPT) is defined as a major increase in glacial ice volume particularly during the 900kyr event, leading to changes in the shape, periodicity and amplitude of glacial-interglacial climate cycles. In contrast, Late Pleistocene glacial cycles are largely shaped by a feedback combination of ice volume with atmospheric $CO_2$. As such, low glacial $CO_2$ values aid the development of extreme glacial maxima leading to glacial periods sustaining multiple insolation peaks. Yet, little is known about the relationship between $pCO_2$ and ice volume during the MPT. Here, I present 1kyr-resolution $\delta^{11}B$-derived atmospheric $CO_2$ reconstructions from site U1476 across early MPT-glacial MIS30. I find that $pCO_2$ and ice volume diverge in-tandem from external forcing for the first time during

glacials MIS30, and MIS36. I interpret this as the beginning of the 100kyr-cycle evolution. The prolonged low glacial $pCO_2$ values occur in line with saltier Atlantic deep waters enriched in $\delta^{13}C$ which I interpret to be of southern origin. This likely led to increased deep ocean carbon storage and sustained low glacial $pCO_2$. In contrast, global sea surface temperature records show no prolonged cooling during MIS30 and MIS36. I conclude that the early MPT is characterised by a divorce of the $pCO_2$ and ice sheet feedback from external insolation forcing and global temperature. This could have led to an increase in the time-lag between external forcing and ice sheet/$pCO_2$ response, creating a positive cooling feedback when low insolation coincided with low $pCO_2$ and high ice volume causing the 100kyr cycle.

## 8.2 Introduction

According to the Milankovic theory, glacial cycles are characterised by waxing and waning of global ice sheets in response to changes in orbital forcing (Milankovic, 1941). During the early Pleistocene climate cycles, global ice volume does indeed appear to respond to integrated summer insolation, with a periodicity of 41,000 years (41 kyr) (Figure 8.1; Huybers, 2006). In contrast, Late Pleistocene glacial cycles have an extended periodicity of 100kyr, increased glacial amplitude, and end in abrupt glacial terminations (Figure 8.1; Raymo, 1997). They are considered to be paced by external insolation forcing (Hays et al., 1976; Huybers, 2011; Imbrie et al., 1993), but shaped by non-linear climate feedback mechanisms (Figure 8.1; Abe-Ouchi et al., 2013; Tziperman et al., 2006). Coupled atmospheric $CO_2$ and ice sheet dynamics are a likely driver of the extensive glacial maxima (Berger et al., 1998; Ganopolski & Calov, 2011) by supporting the development of large northern hemisphere ice sheets, so that glacials can sustain through multiple peaks in integrated summer insolation (Bintanja & Van De Wal, 2008; Tzedakis et al., 2017). As such, Late Pleistocene

glacial cycles are de-coupled from orbital forcing (Figure 8.1; Huybers and Wunsch, 2005; Ridgwell et al., 1999; Tzedakis et al., 2017).

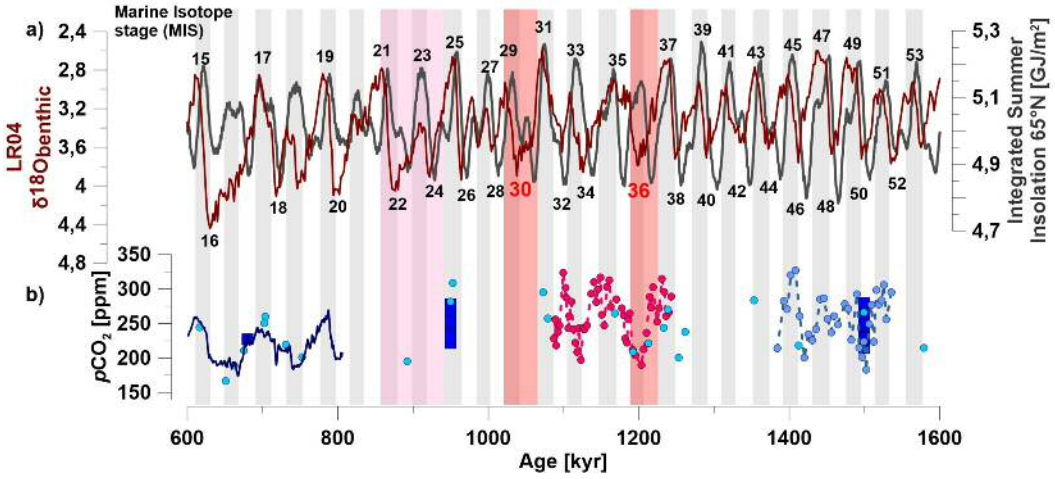


**Figure 8.1** (a) Foraminiferal benthic isotope stack (red) (LR04; Lisiecki and Raymo, 2005) on integrated summer insolation at 65°N (grey) (Huybers, 2006), and (b) available $pCO_2$ data from EPICA Dome C (blue line) (Bereiter et al., 2015), blue ice (blue squares) (Higgins et al., 2015; Yan et al., 2019), and boron isotopes (pink dots; Chalk et al., 2017) (blue dots; Dyez et al., 2018) (ice blue dots; Hönisch et al., 2009). Marine isotope stages (MIS) are labelled in black numbers. Glacials MIS30 and MIS36 are highlighted in red numbers. Shaded vertical pink bars highlight MPT onset glacials MIS30 and MIS36, as well as the 900kyr event (lighter pink). Shaded vertical grey bars highlight times during obliquity maxima.

The transition to the "100kyr world" of the late Pleistocene from the orbitally-paced "40kyr world" of the early Pleistocene is known as the "Mid-Pleistocene Transition" (MPT). The timing and reason of when and why Late Pleistocene climate cycles developed is still widely discussed. Spectral analyses suggest that the first 100kyr climate cycle occurred around 900kyr (Clark et al., 2006; McClymont et al., 2013; Sosdian & Rosenthal, 2009) in line with significant increases in glacial ice volume (Elderfield et al., 2012; Ford & Raymo, 2020), cooling of deep waters (Sosdian & Rosenthal, 2009), disruption in ocean circulation (Pena & Goldstein, 2014), and expansion of carbon storage (Farmer et al., 2019; Lear et al., 2016). Prior to 900kyr, sea surface temperatures (SST) show a long-term decline across the MPT suggesting the MPT as a climate transition rather than an event-like occurrence. Here, I present orbitally resolved stable isotopes and boron isotope-derived $pCO_2$

reconstructions from glacial MIS30 during the early MPT to investigate the evolution of global ice volume and $pCO_2$ with respect to orbital forcing. I combine my data with a compilation of published stable isotope and SST reconstructions to further evaluate the role of temperature and ocean circulation during the early MPT. I provide evidence that ice volume and atmospheric $CO_2$ were already tightly coupled during the early MPT leading to the first glacials during which global ice volume sustained through peaks in orbital forcing.

## 8.3 Methods

### 8.3.1 Core location and age model

New tropical stable isotope records were generated from core site U1476 (2166m depth) located at 15°49.25' S; 41°46.12' E on Davie ridge in the northern Mozambique Channel, with a sedimentation rate of around 2cm/1kyr during the Mid-Pleistocene transition. The age model for U1476 was derived by tuning the high-resolution benthic $\delta^{18}O$ record to LR04 (Barker et al., unpubl.; see also Chapter Materials & Methods 5.4). Preparation and sample analysis follow the methods described elsewhere (Materials and Methods, chapter 5.3). According to Takahashi et al. (2014), modern surface waters above site U1476 are in air-sea $CO_2$ equilibrium with the atmosphere making this a promising site for boron isotope-based palaeo-$pCO_2$ reconstructions (Figure 8.2).

Core locations for published datasets are plotted in Figure 8.3. Age models for published data were not adapted, as all were tuned to either the LR04 benthic $\delta^{18}O$ stack, or to the insolation parameters to which LR04 itself is tuned (Figure 8.4).

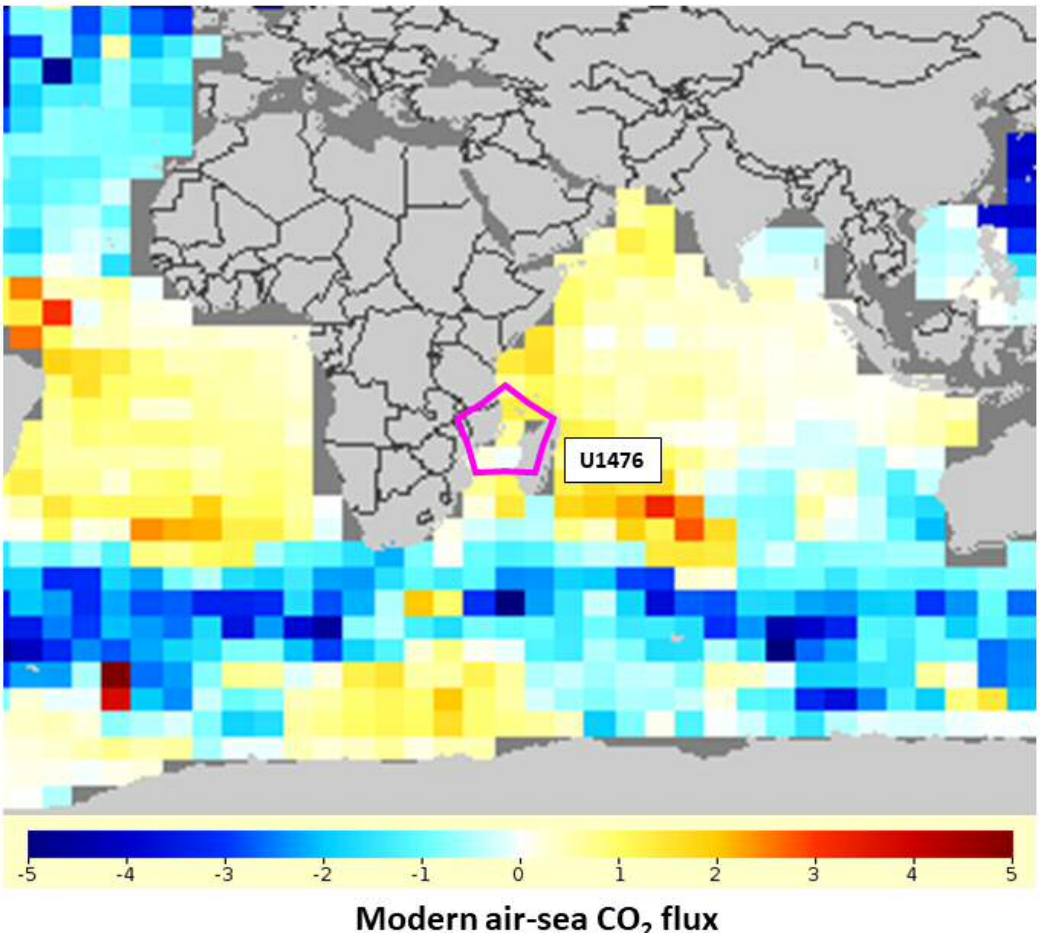


**Figure 8.2** Modern air-sea $CO_2$ flux in the western Indian Ocean (Takahashi et al., 2014). The location of U1476 is indicated with a pink star.

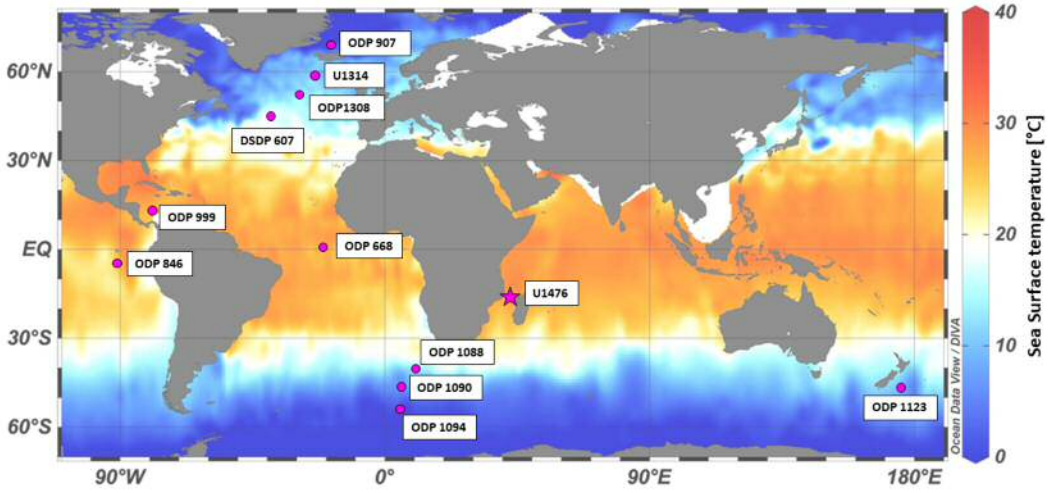


**Figure 8.3** Modern global sea surface temperatures from the GLODAP v2 dataset with core locations used in this study plotted in pink.

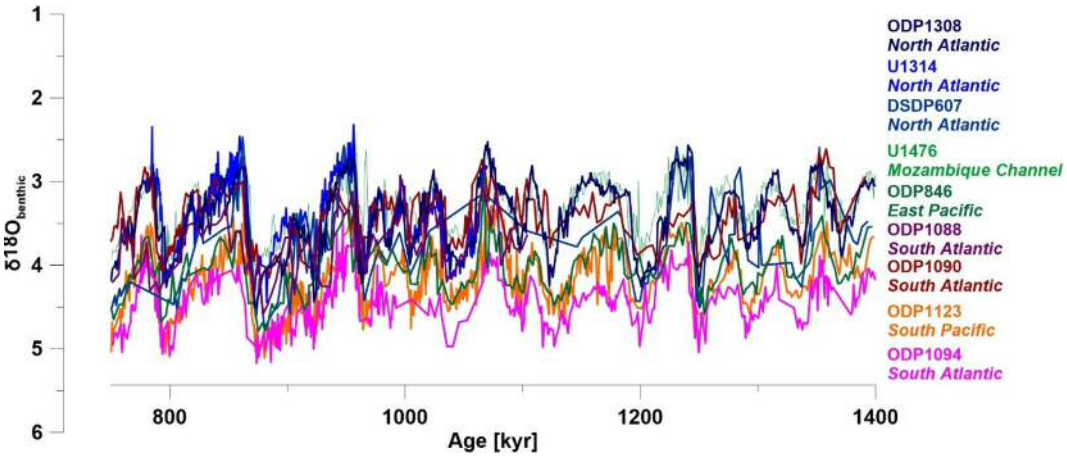


**Figure 8.4** Foraminiferal benthic $\delta^{18}O$ on core-respective published age models across the MPT.

### 8.3.2 Boron isotope analysis

For boron isotope analysis, 55 well preserved *G. ruber* tests were picked from each sample, and crushed, cleaned and dissolved following Barker et al. (2003) (see also Materials & Methods, chapter 5.3). A small aliquot ($\sim 20\mu$L) was used for trace element analysis, to establish B/Ca ratios and boron concentrations, and check for sample cleanliness. Trace elements were analysed on a triple quadrupole mass spectrometer at the STAiG lab in St. Andrews (see also Materials & Methods, chapter 5.3). The remaining sample was used for boron isotope analysis.

Boron was extracted from dissolved foraminiferal calcite MIS30 samples using the Batch Method (Trudgill et al., in prep.). Here, boron is extracted from the matrix in a 1.5mL centrifuge tube filled with 100$\mu$L Amberlite IRA 743 boron-specific resin. Samples were buffered using ammonia-hydroxide acetic-acid buffer with a 1.5:1 buffer:sample ratio, and loaded onto cleaned resin at pH 8.5. Interaction with the resin was created by vortexing each sample for 1 minute, then removing the supernatant from the resin. Samples were washed with 18.2MΩ de-ionized water, and eluted in 500$\mu$L of 0.5M $HNO_3$.

After purification, boron samples were analysed thrice on a Thermo Neptune Plus multi-collector inductively coupled mass spectrometer (MC-ICPMS) at the STAiG

laboratory in St. Andrews following the method described in Rae et al. (2018) (Figure 8.5).

To test the quality of the extraction method, 10$\mu$L splits were taken from each sample to determine the concentration of B, and the matrix elements Na, Ca, and Mg. Samples with high concentration of matrix elements (>100ppb) were interpreted with caution or excluded from the dataset. Before analysis, samples, standards, and 0.5M $HNO_3$ were spiked with 0.3M HF to aid washout and shorten the bracketing time. Each sample was corrected for background by on-peak zeroing with 0.5M $HNO_3$ + 0.3M HF and correct for mass bias by sample-standard bracketing with the NIST 951 boron isotope standard ($\delta^{11}B = 0$). For data quality control, each analytical session contained multiple measurements of the boric acid consistency standards AE121 and boron BIGD, run under the same conditions as samples. Propagated errors for the boron analysis were <0.25‰.

To test the usability of G.*ruber* $\delta^{11}B$ from U1476, an initial low resolution boron isotope record was created at the Foster Laboratories at the National Oceanographic Centre (NOC) in Southampton (Figure 8.5). Here, 250 well preserved *G. ruber* tests were picked from one glacial, and one interglacial sample from 400kyr to 1.6Ma. Samples were crushed, cleaned and dissolved following Barker et al. (2003), and analysed for trace elements on a Thermo Element XR, following the methods described above. Boron was extracted from dissolved foraminiferal calcite samples through column chemistry using PFA micro-columns with 25$\mu$L of Amberlite IRA 743 boron-specific resin. Samples were analysed on a Thermo Neptune MC-ICPMS, with a washout-aid through inlet of gaseous ammonia into the spray chamber (Foster, 2008).

Additionally, to investigate how high resolution $pCO_2$ reconstructions from U1476 compare to ice core data, 55 foraminiferal tests were picked from 21 samples across the last deglaciation (Figure 8.5). Samples were crushed, cleaned and dissolved, and an aliquot was analysed for trace elements as described above. Boron

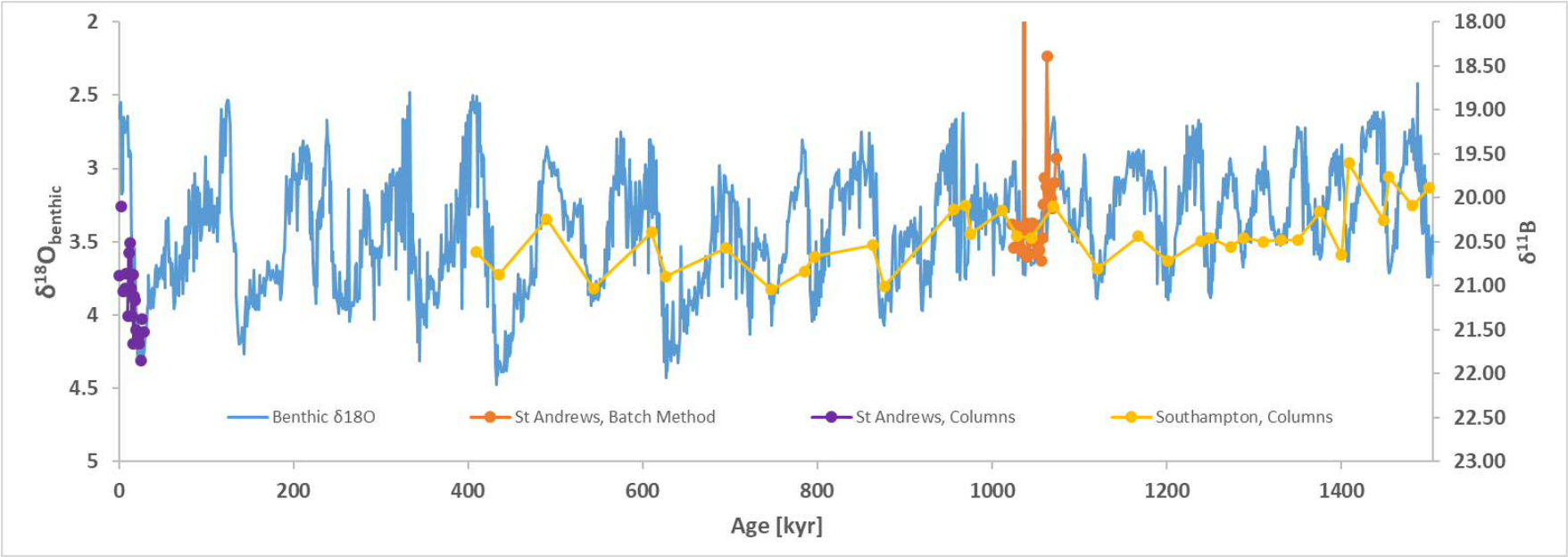


**Figure 8.5** Sampling strategy, laboratory location and method used for all boron isotope data. Purple samples were analysed in the STAiG laboratories of the University of St Andrews using the column boron extraction method. Orange samples were analysed in the STAiG laboratories of the University of St Andrews using the Batch boron extraction method. Yellow samples were analysed in the Foster Laboratories at the National Oceanographic Centre in Southampton using the column boron extraction method.

was extracted using column chemistry at the STAiG laboratories in St. Andrews (Foster, 2008; Rae et al., 2018). After buffering with ammonium hydroxide acetic acid in a 2:1 buffer:sample ratio, samples were loaded onto 25$\mu$L of Amberlite IRA 743 boron-specific resin in PFA micro-columns. Boron was eluted in 600$\mu$L and analysed thrice on a Thermo Neptune Plus, as described above.

To compare the Batch Method with the more widely-used method of column chemistry, three samples were analysed using both methods, including the core top sample, one sample from the middle of the last deglaciation, and one sample from MIS30. The results are listed in table 8.1. Offsets between the different extraction techniques are very small.

**Table 8.1** Comparison of same sub-sample $\delta^{11}B$ using column chemistry and the Batch boron extraction methods

| Age [kyr] | Location | Method | $\delta^{11}B_{G.\ ruber}$ | Reps[a] | 2SD[b] |
|---|---|---|---|---|---|
| 0.000 | St Andrews | Batch | 20.25 | 3 | 0.25 |
| 0.000 | St Andrews | Batch | 20.63 | 3 | 0.09 |
| 0.000 | St Andrews | Batch | 20.65 | 3 | 0.19 |
| 0.000 | St Andrews | Column | 20.67 | 3 | 0.19 |
| 23.132 | St Andrews | Batch | 21.27 | 3 | 0.34 |
| 23.132 | St Andrews | Batch | 21.52 | 3 | 0.33 |
| 23.132 | St Andrews | Batch | 21.53 | 3 | 0.38 |
| 23.132 | St Andrews | Column | 21.44 | 3 | 0.11 |
| 1070.348 | St Andrews | Batch | 20.11 | 3 | 0.26 |
| 1070.348 | Southampton | Column | 20.09 | 2 | 0.10 |

[a] *Reps: number of independent measurements of the same sample during one analytical run*
[b] *2SD: 2x standard deviation*

### 8.3.3 Ocean carbonate calculations

I convert measured $\delta^{11}B_{G.\ ruber}$ to $\delta^{11}B_{borate}$ using the calibration for *G. ruber* from Henehan et al. (2016)

$$\delta^{11}B_{borate} = \frac{\delta^{11}B_{G.\ ruber} - 9.52(\pm 2.02)}{0.6(\pm 0.11)} \tag{8.1}$$

Seawater pH (Figure 8.7) was then calculated using the following equation from Rae (2018)

$$pH = -log\frac{K_B \times {}^{\frac{11}{10}}R_{B(OH)_4^-} - K_B \times {}^{\frac{11}{10}}R_{SW} + \alpha_b \times K_B \times {}^{\frac{11}{10}}R^2_{B(OH)_4^-} - {}^{\frac{11}{10}}R_{SW} + {}^{\frac{11}{10}}R_{SW} \times {}^{\frac{11}{10}}R_{B(OH)_4^-} - \frac{\alpha_b \times K_B \times {}^{\frac{11}{10}}R_{SW} \times {}^{\frac{11}{10}}R_{B(OH)_4^-}}{\alpha_b \times {}^{\frac{11}{10}}R_{B(OH)_4^-} - \alpha_b \times {}^{\frac{11}{10}}R_{B(OH)_4^-}} \tag{8.2}$$

where $K_B$ is the equilibrium constant of the reaction ($K_B \sim 10^{-8.6}$ according to Rae 2018), ${}^{\frac{11}{10}}R$ stands for the ratio between $^{11}B$ and $^{10}B$ of either $B(OH)_4^-$ or seawater (sw), and $\alpha_b$ is the equilibrium fractionation of 27.2‰ (Klochko et al., 2006).

The fractionation factor $\varepsilon$ can be calculated using the equilibrium constant $\alpha_b$

$$\varepsilon = 1000 \times (\alpha_b - 1) \tag{8.3}$$

To solve the carbonate system equations for $pCO_2$, alkalinity was chosen as the second carbonate parameter. I used an estimate for alkalinity of 2300 mol/kg (Fallet et al., 2010) and for salinity of 35psu. This is consistent with the estimates used for alkalinity and salinity in chapter 7. $\alpha_b$ was taken from Klochko et al. (2006), and $\delta^{11}B_{seawater}$ was estimated as

$$\delta^{11}B_{seawater} = (-0.000149) \times age + 39.6 \tag{8.4}$$

as derived in Martinez-Boti et al. (2015), where $\delta^{11}B_{sw}$ is the $\delta^{11}B$ of seawater over time, and age is entered in kyr. Error propagation was conducted through Monte

Carlo analysis with 10,000 repetitions and is plotted as the positive and negative $95^{th}$ quantile.

### 8.3.4 Correcting North Atlantic d$\omega$ for ice sheet $\delta^{18}O_{seawater}$ effects

Oxygen isotopes are known to be influenced by global ice volume, temperature and salinity. To gain a more representative sea level estimate, Sosdian & Rosenthal (2009) corrected their benthic $\delta^{18}O$ data from North Atlantic site DSDP607 for benthic Mg/Ca-derived bottom water temperatures (d$\omega$). Here, I am interested in extracting local $\delta^{18}O_{sw}$ variability from the d$\omega$ data to investigate possible changes in deep water hydrographic stratification. I compare two values for global $\delta^{18}O_{sw}$ to correct d$\omega$ for whole ocean salinity and ice volume changes. The first estimate for $\delta^{18}O_{sw}$-whole ocean is taken from the $\delta^{18}O_{sw}$ stack of Ford & Raymo (2020), while the second estimate is taken from an ice sheet model by de Boer et al. (2014a). The resulting deep water $\delta^{18}O_{sw-ivc}$ is similar for both estimates and yields a robust result for MIS30 (Figure 8.6).

## 8.4 Results

My $\delta^{11}B$ data show a consistent glacial-interglacial difference with high $\delta^{11}B$ during glacials, and low $\delta^{11}B$ during interglacials (Figure 8.7a, b). After converting $\delta^{11}B$ to seawater pH, I find also a clear glacial-interglacial cyclicity with glacial pH values around 8.2–8.3, and interglacial values around 8.1, and 8.0 only during MIS31 (Figure 8.7c).

I then use the reconstructed pH to calculate atmospheric $CO_2$ concentrations. Glacial $pCO_2$ values during the last glacial maximum are around 180ppm which is well in-line with ice core $CO_2$ reconstructions (Figure 8.7d). Late Pleistocene

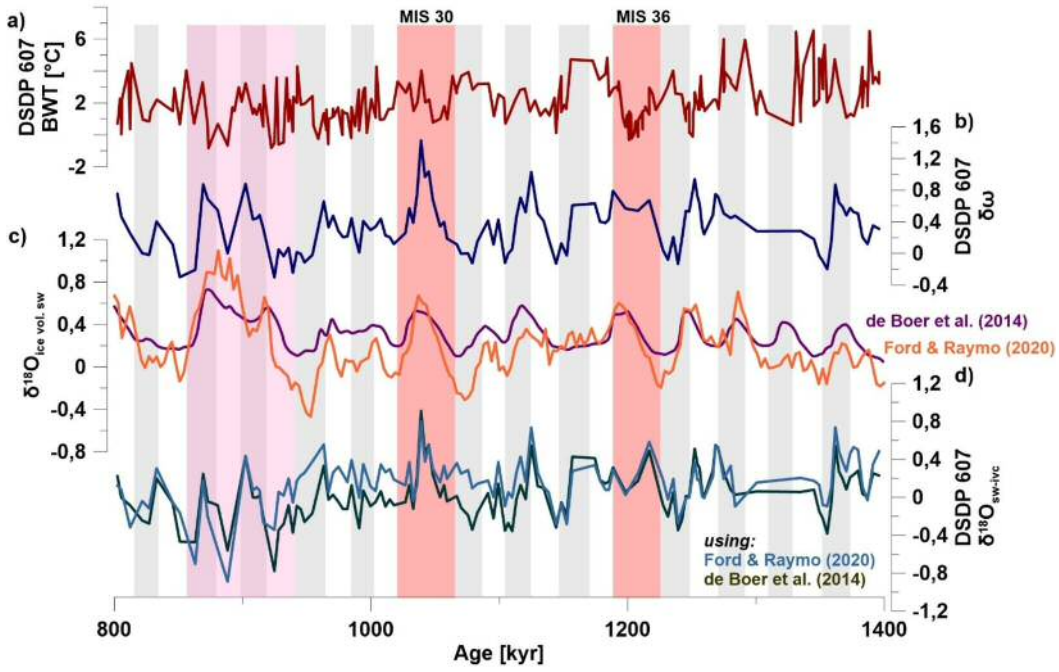


**Figure 8.6** Calculation of the salinity contribution to the DSDP 607 d$\omega$ signal. (a) DSDP 607 bottom water temperatures (BWT) (Ford et al., 2016; Sosdian & Rosenthal, 2009). (b) BWT-corrected $\delta^{18}O_{benthic}$ (Sosdian & Rosenthal, 2009). (c) Estimates of global ice volume $\delta^{18}O_{sw}$ from the MPT $\delta^{18}O_{sw}$ stack (orange; Ford and Raymo, 2020), and relative sea level (dark green; de Boer et al., 2014a). (d) BWT- and ice volume-corrected deep $\delta^{18}O_{sw}$ using either the $\delta^{18}O_{sw}$ stack from Ford & Raymo (2020) (red), or the $\delta^{18}O_{sw}$ from de Boer et al. (2014a) (green) as correction for ice volume. Shaded vertical pink bars highlight MPT onset glacials MIS30 and MIS36, as well as the 900kyr event (lighter pink). Shaded vertical grey bars highlight times during obliquity maxima.

glacial, and interglacial, $CO_2$ values plot around 230ppm, and 330ppm, respectively, presenting a consistent glacial-interglacial difference of 100ppm. My high resolution data from the last deglaciation and MIS31-30 show peaks in high interglacial $pCO_2$ which are likely results of short-term dis-equilibria in the air-sea exchange above U1476 (Shao et al., 2019). From 400kyr to 800kyr, my glacial $pCO_2$ values appear somewhat elevated compared to the last deglaciation and other $\delta^{11}B$ -derived published $pCO_2$ data. This may be due to the use of a consistent alkalinity value throughout the last 1.5Ma. Instead, long-term glacial alkalinity might have changed which could cause differences in glacial $pCO_2$ values over time. Still, given I reconstruct a consistent difference of 100ppm between glacial and interglacial $pCO_2$

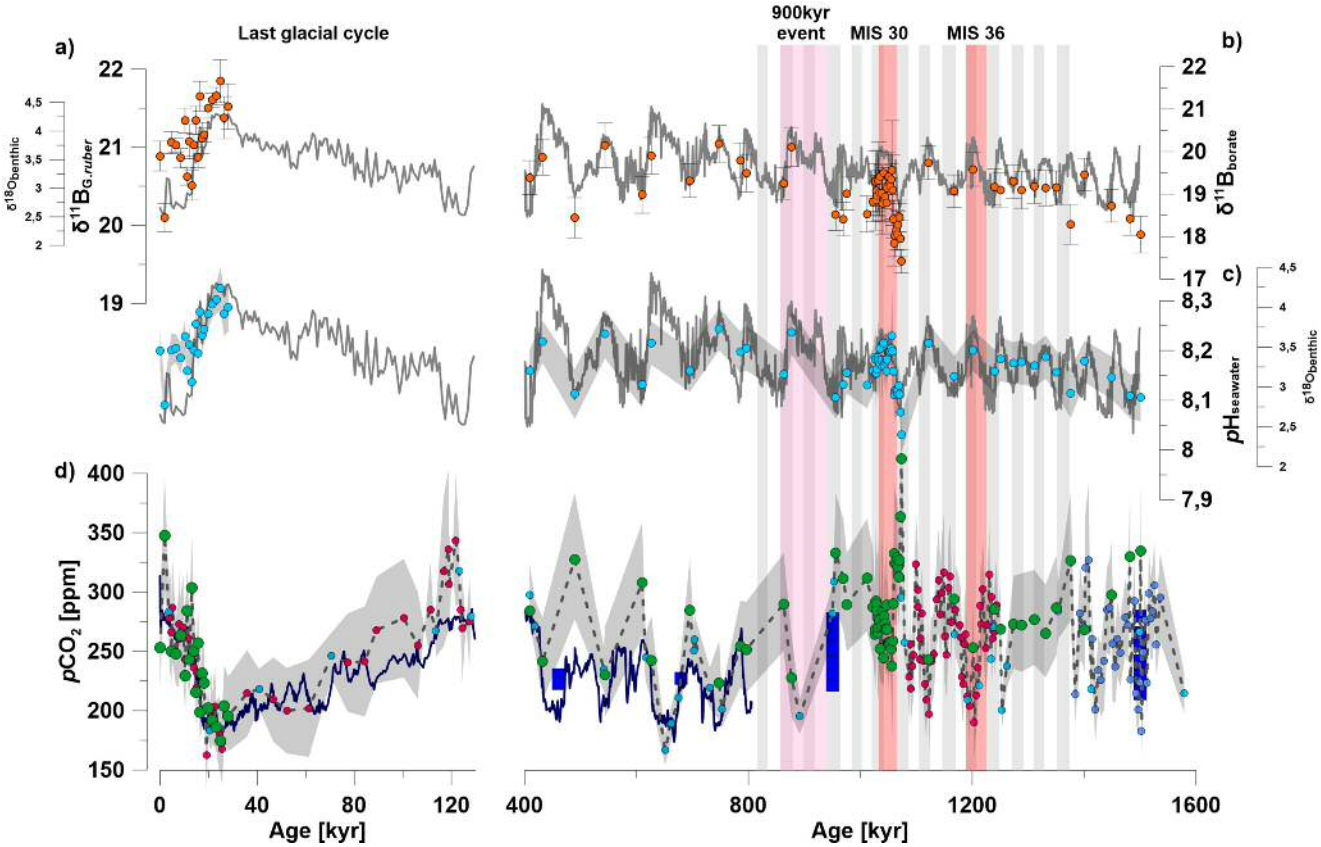


**Figure 8.7** Seawater pH and atmospheric $pCO_2$ calculations for U1476 boron isotope data during the last deglaciation, and the 400-1500kyr time period. (a) $\delta^{11}B$ from foraminifera *G. ruber* (orange) with error bars representing analytical errors as 2xstandard deviation, and (b) calculated $\delta^{11}B_{borate}$ using Henehan et al. (2013) after size correction (green), plotted on U1476 $\delta^{18}O_{benthic}$ (grey). (c) seawater pH (ice blue dots) with grey error envelope representing $95^{th}$ quantiles plotted on U1476 $\delta^{18}O_{benthic}$ (grey). (d) $pCO_2$ (large green dots) with grey error envelope representing $95^{th}$ quantiles. For comparison, ice core $pCO_2$ as dark blue line, blue ice data in light blue squares, and published boron isotope-derived $pCO_2$ in pink, light blue, and bright blue dots. Shaded vertical pink bars highlight MPT onset glacials MIS30 and MIS36, as well as the 900kyr event (lighter pink). Shaded vertical grey bars highlight obliquity maxima during the MPT period.

values across the whole record, I am confident that the $pCO_2$ data displays correct glacial-interglacial variability and allows us to interpret relative changes. From MIS31 to MIS29, I increased the resolution to one data point per 1kyr (Figure 8.8). I find that glacial $pCO_2$ falls abruptly to 230ppm after MIS31, and stays low across glacial MIS30 and early MIS29.

Prior to 1.2Ma, benthic oxygen isotopes ($\delta^{18}O_{benthic}$) show a ~41kyr cyclicity pacing in line with integrated summer insolation (Figure 8.9). However, during MIS30 (~1.1Ma), $\delta^{18}O_{benthic}$ deviates from the external forcing and stays high, while integrated summer insolation increases (Figure 8.8).

The $\delta^{18}O_{benthic}$ data closely correlates with my new high resolution atmospheric $CO_2$ reconstructions from U1476 across MIS30 (Figure 8.8). This occurs despite increases in integrated summer insolation, comparable to $\delta^{18}O_{benthic}$. The glacial $pCO_2$-low is paralleled by light $\delta^{13}C_{benthic}$ in the South Atlantic, and a peak in the $\delta^{18}O_{sw-ivc}$ of North Atlantic deep waters (Figure 8.10). In contrast, I see early increases in high- and low latitude SSTs (Figure 8.10, 8.11), and global benthic $\delta^{13}C$ (Figure 8.10, 8.13), in line with integrated summer insolation. This causes a divergence between $\delta^{18}O_{benthic}/pCO_2$, and insolation/SSTs (Figure 8.10). This pattern is also observed to some degree during glacial MIS36 where low $pCO_2$ and high $\delta^{18}O_{benthic}$ prolong into the insolation peak, while SSTs increase in line with insolation (Figure 8.10).

## 8.5 Discussion

Late Pleistocene glacial cycles are shaped by a close coupling between ice sheet dynamics and changes in atmospheric $CO_2$ (Berger et al., 1998; Ganopolski & Calov, 2011), causing glacial ice masses to be sustained across multiple insolation peaks (Bintanja & Van De Wal, 2008; Tzedakis et al., 2017). Benthic $\delta^{18}O$ can be used to infer global ice volume changes, due to the small influences of bottom water

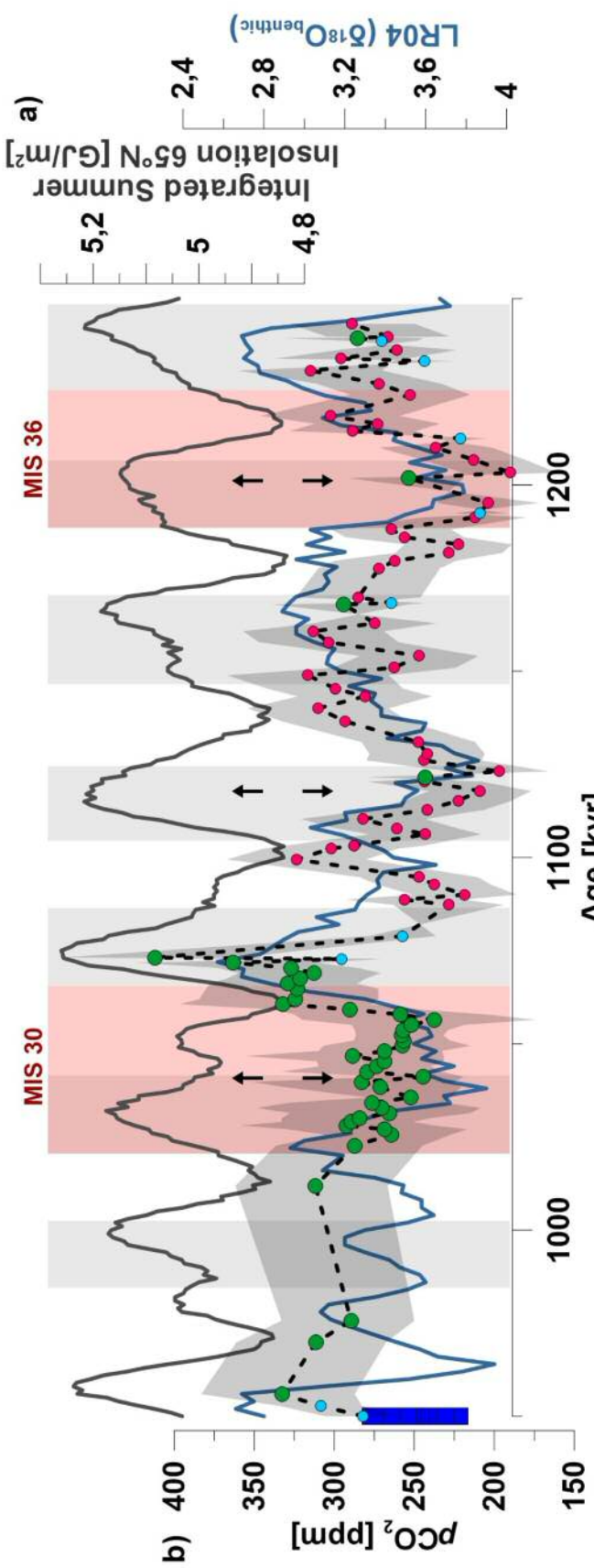


**Figure 8.8** (a) Integrated summer insolation at 65°N (grey) (Huybers, 2006), and (b) atmospheric $CO_2$ data from boron isotopes (green dots; this study) (pink dots; Chalk et al., 2017) (ice blue dots; Hönisch et al., 2009) and blue ice (Higgins et al., 2015) on the LR04 foraminiferal benthic isotope stack (blue) (Lisiecki & Raymo, 2005). Glacial deviations between insolation and LR04/$pCO_2$ are highlighted with black arrows. Shaded vertical pink bars highlight MPT onset glacials MIS30 and MIS36. Shaded vertical grey bars highlight times during obliquity maxima.

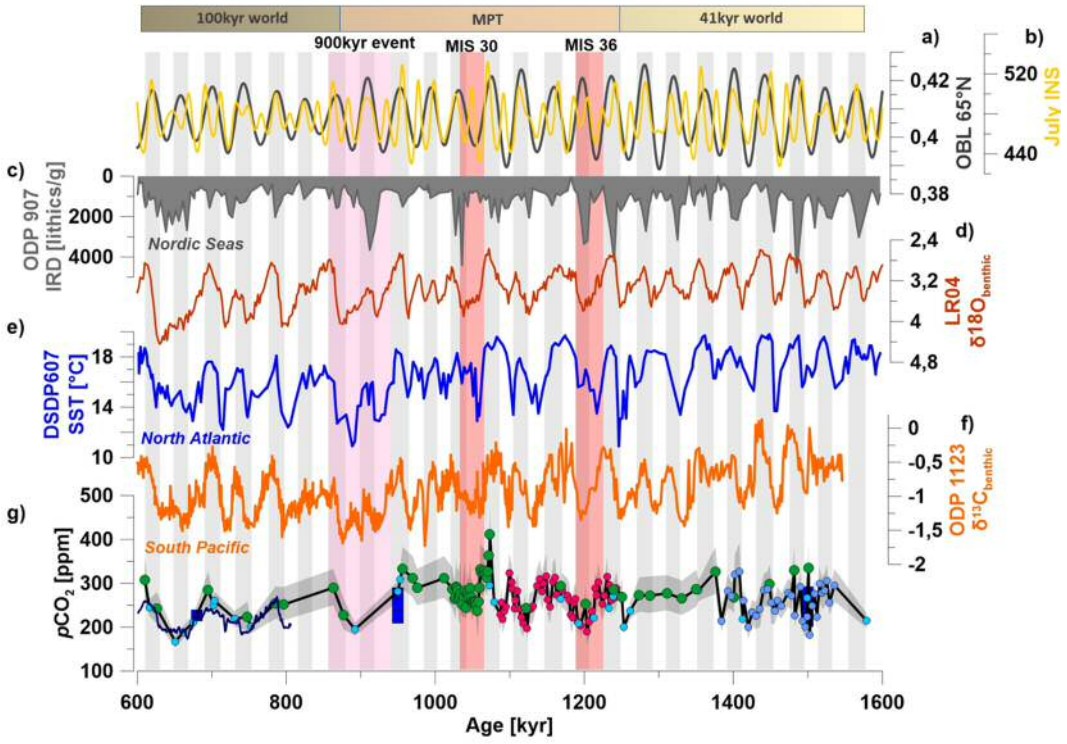


**Figure 8.9** Early to Late Pleistocene climate. (a) Obliquity (dark grey) and 65°N July summer insolation (yellow) (Laskar et al., 2004). (b) Northern hemisphere ice-rafted debris (IRD) (Jansen et al., 2000). (c) Benthic foraminiferal $\delta^{18}O$ stack (LR04) (Lisiecki & Raymo, 2005). (d) North Atlantic sea surface temperatures (SST) (Lawrence et al., 2010). (d) Benthic foraminiferal $\delta^{13}C$ (Elderfield et al., 2012). (e) $p\mathrm{CO}_2$ from ice core (blue line; Bereiter et al., 2015), blue ice (light blue squares; Higgins et al., 2015; Yan et al., 2019, and boron isotopes from this study (green dots), Chalk et al. (2017) (pink dots), Hönisch et al. (2009) (ice blue dots), and Dyez et al. (2018) (light blue dots). Shaded vertical pink bars highlight MPT onset glacials MIS30 and MIS36, as well as the 900kyr event (lighter pink). Shaded vertical grey bars highlight times during obliquity maxima.

temperatures on $\delta^{18}O_{benthic}$ (Shackleton, 1987). My data show that this divorce of the ice sheet/$pCO_2$ feedback from insolation forcing is observed for the first time during the early MPT. During MIS30 (1.1Ma) and MIS36 (1.2Ma), benthic $\delta^{18}O$ stays high, despite increasing integrated summer insolation, and sustains throughout the integrated summer insolation peak (Figure 8.8). This is paralleled by low levels of $pCO_2$ during both glacials (Figure 8.8). I propose that MIS30 and MIS36 present early examples of this divorce between ice sheet/$pCO_2$ and external insolation forcing. Glacial cycles prior to MIS36 do not show this feature. During the 41kyr-world, $\delta^{18}O_{benthic}$-derived ice volume generally follows integrated summer

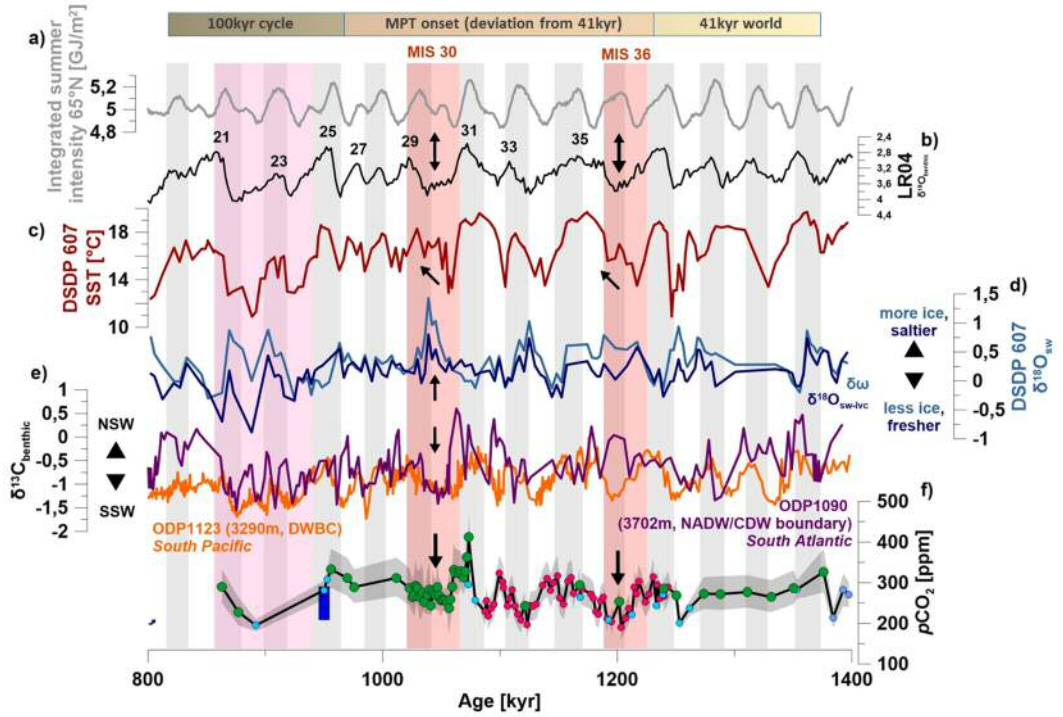


**Figure 8.10** Climate shifts across the MPT. (a) 65°N summer duration insolation as in Huybers (2006) (dark grey) and 65°N July summer insolation (yellow; Laskar et al., 2004). (b) Benthic foraminiferal $\delta^{18}O$ stack (LR04) (Lisiecki & Raymo, 2005). For reference, interglacial MIS are labelled in black. (d) Sea surface temperatures from the North Atlantic (Lawrence et al., 2010). (e) Deep water $\delta^{18}O_{sw}$ from the North Atlantic corrected for BWT only (d$\omega$ in light blue; Sosdian and Rosenthal, 2009), and corrected additionally for global $\delta^{18}O_{sw}$ changes (dark blue, this study). (f) Benthic foraminiferal $\delta^{13}C$ from the deep South Atlantic (purple; Hodell et al., 2003), and the deep South Pacific (orange; Elderfield et al., 2012). (g) $p$CO$_2$ from blue ice (light blue squares; Higgins et al., 2015; Yan et al., 2019), and boron isotopes from this study (green dots), Chalk et al. (2017) (pink dots), Hönisch et al. (2009) (ice blue dots), and Dyez et al. (2018) (light blue dots). Shaded vertical pink bars highlight MPT onset glacials MIS30 and MIS36, as well as the 900kyr event (lighter pink). Shaded vertical grey bars highlight times during obliquity maxima. Note the deviation between LR04-benthic $\delta^{18}$O and SSTs, as well as the spike in d$\omega$ and d18Osw-ivc during MIS30.

insolation (Figure 8.9). This is also the case for $pCO_2$ (Dyez et al., 2018). As such, I suggest that MIS30 and MIS36 present the first glacials, during which high ice volume and low $pCO_2$ prolong across the insolation peak and de-couple from external forcing.

The prolonged $pCO_2$ minima during MIS30 and MIS36 is likely a result of increased deep ocean carbon storage, due to changes in ocean circulation coupled to

a more effective biological pump via iron fertilization (Chalk et al., 2017). Indeed, I note that low $pCO_2$ during MIS30 was paralleled by expansion of salty deep waters with low $\delta^{13}C$ in the Atlantic Ocean (Figure 8.10), similar to the conditions widely thought to drive enhanced carbon storage at depth during the last glacial maximum (e.g. Adkins, 2013). This is also supported by stratification (Hasenfratz et al., 2019) and productivity (Diester-Haass et al., 2018) reconstructions from the Southern Ocean which suggest stronger stratification and increased productivity during MIS30.

I speculate that the expansion of southern-sourced waters in the Atlantic sector of the Southern Ocean could be linked to the formation of brine rejection sites in the Weddell Sea. In the modern, around 30% of Weddell Sea bottom waters are supplied by deep waters created under ice shelf margins (Kerr et al., 2018). However, SST reconstructions coupled with modelling results from the West Antarctic margin suggest that West Antarctic ice sheet (WAIS) marine shelves were diminished during MIS31 (Beltran et al., 2020) probably reducing Weddell Sea bottom water production. Recent modelling results on WAIS thickness show a significant increase in overall ice thickness during MIS30, particularly at Siple Station near the Weddell Sea (Sutter et al., 2019). The authors suggest that this increase is attributable to an expansion in marine-based ice extensions around WAIS. This would have (re-)activated Weddell Sea bottom water production and potentially caused export of salty southern-sourced water masses into the Atlantic Ocean. Regional-wide cooling of surface waters due to ice sheet advance may have also lead to a more effective formation of sea ice (Nicholls et al., 2009) which has been shown to influence storage and outgassing of $pCO_2$ (Rae et al., 2018). As such, the prolonged low in glacial $pCO_2$ may have been initiated by ice margin and sea ice growth in line with ocean stratification.

The divorce between ice sheet/$pCO_2$ dynamics and insolation forcing during early-MPT glacials is not visible in global sea surface temperature (SST) data (Figure 8.11). Prior to MIS36 (1.2Ma), high- and low latitude SSTs vary in line with global

climate which follows integrated summer insolation (Figure 8.11). Then, during MIS30 and MIS36, global SSTs increase in line with external forcing (Figure 8.11), despite a prolonged glacial as defined by $\delta^{18}O_{benthic}$.

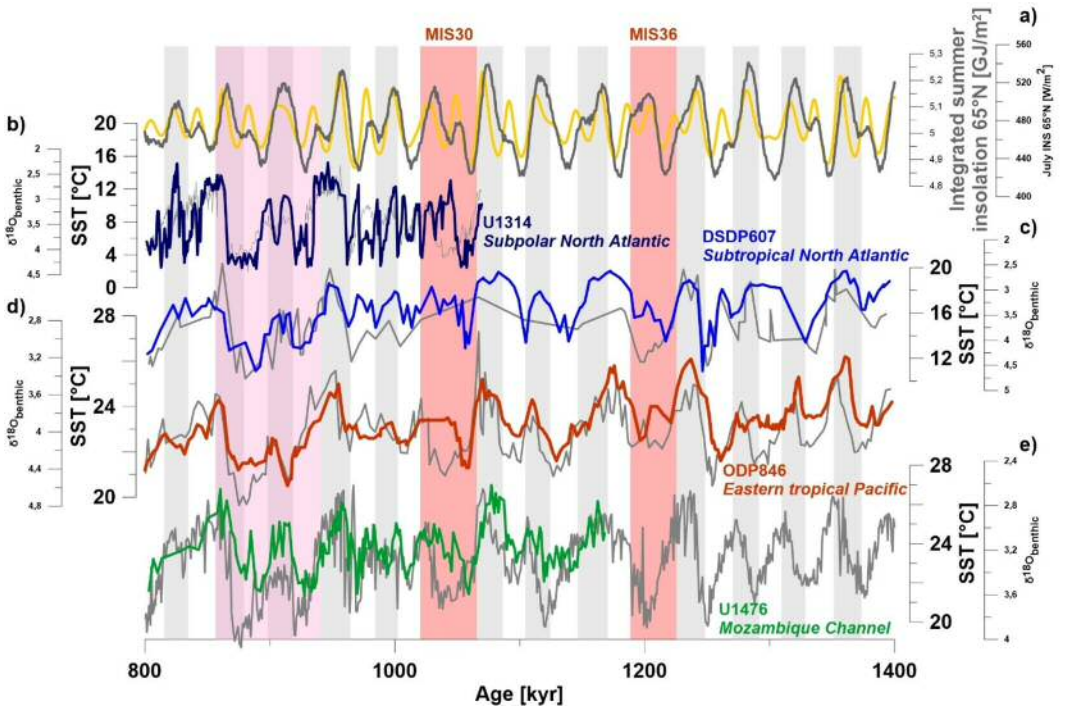


**Figure 8.11** Sea surface temperatures plotted on core respective benthic $\delta^{18}O$ (grey lines). (a) Integrated summer insolation at 65°N (dark grey; Huybers, 2006) and July summer insolation at 65°N (yellow; Laskar et al., 2004). (b) Subpolar North Atlantic (dark blue) (Hernandez-Almeida et al., 2012), (c) subtropical North Atlantic (light blue) (Ford et al., 2016; Lawrence et al., 2010; Sosdian & Rosenthal, 2009), (d) eastern tropical Pacific (red) (Herbert et al., 2010; Mix et al., 1995), and (e) western tropical Indian Ocean (green) (this study). Shaded vertical pink bars highlight MPT onset glacials MIS30 and MIS36, as well as the 900kyr event (lighter pink). Shaded vertical grey bars highlight times during obliquity maxima.

This is also seen in North Atlantic bottom water temperatures (BWT) (Figure 8.12), suggesting a link between global SSTs and North Atlantic BWTs via ventilation of deep waters in the North Atlantic. Warming SSTs may have played a role in the creation of durable ice sheets during MIS30 and MIS36 via increased moisture transport to northern hemisphere ice sheets (i.e. Driscoll and Haug, 1998). This would have led to a change in the ice sheet mass balance and could cause a reduction in ice sheet collapse at the time of insolation increase. Alternatively, global SSTs

may act de-coupled from the ice volume/$pCO_2$ feedback and respond directly to external forcing (Bosmans et al., 2015; Raymo & Nisancioglu, 2003).

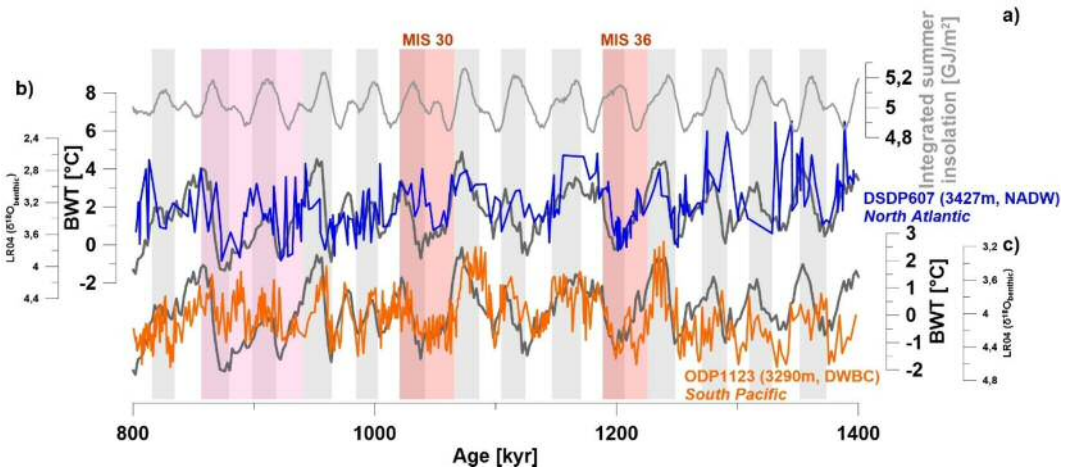


**Figure 8.12** Bottom water temperature records across the MPT. (a) 65°N obliquity (dark grey) and 65°N July summer insolation (yellow) (Laskar et al., 2004). (b) benthic foraminiferal $\delta^{18}O$ stack (LR04, red; Lisiecki and Raymo, 2005). (c) BWT records from the deep subtropical North Atlantic (blue; Ford et al., 2016; Sosdian and Rosenthal, 2009) and the deep South Pacific (orange; Elderfield et al., 2012). Other BWT records are available, but have not been included due to low resolution of data during glacials MIS30, and MIS36. Shaded vertical pink bars highlight MPT onset glacials MIS30 and MIS36, as well as the 900kyr event (lighter pink). Shaded vertical grey bars highlight times during obliquity maxima. Note the deviation in BWT around MIS30.

Global carbon isotopes also follow insolation during MIS30 and MIS36 (Figure 8.13) likely due to SST forcing via air-sea exchange (Lynch-Stieglitz et al., 1995). In contrast, deep South Atlantic carbon isotopes stay light throughout MIS30 which I attribute to the additional drawdown of $CO_2$ via increases in South Atlantic stratification and the efficiency of the biological pump (Figure 8.10).

It has been proposed that ice sheet waxing and waning is characterised by hysteresis (Abe-Ouchi et al., 2013) leading to response-lags of the ice sheet to insolation forcing (Sosdian & Rosenthal, 2009). The development of the 100kyr cycle may therefore be a result of increasing de-coupling between the insolation forcing and the hysteresis-induced response-lag (Sosdian & Rosenthal, 2009). My data suggests that the first increase in this ice sheet-lag occurred during MIS36, and particularly MIS30. However, my $pCO_2$ data strongly underlines that the increase in

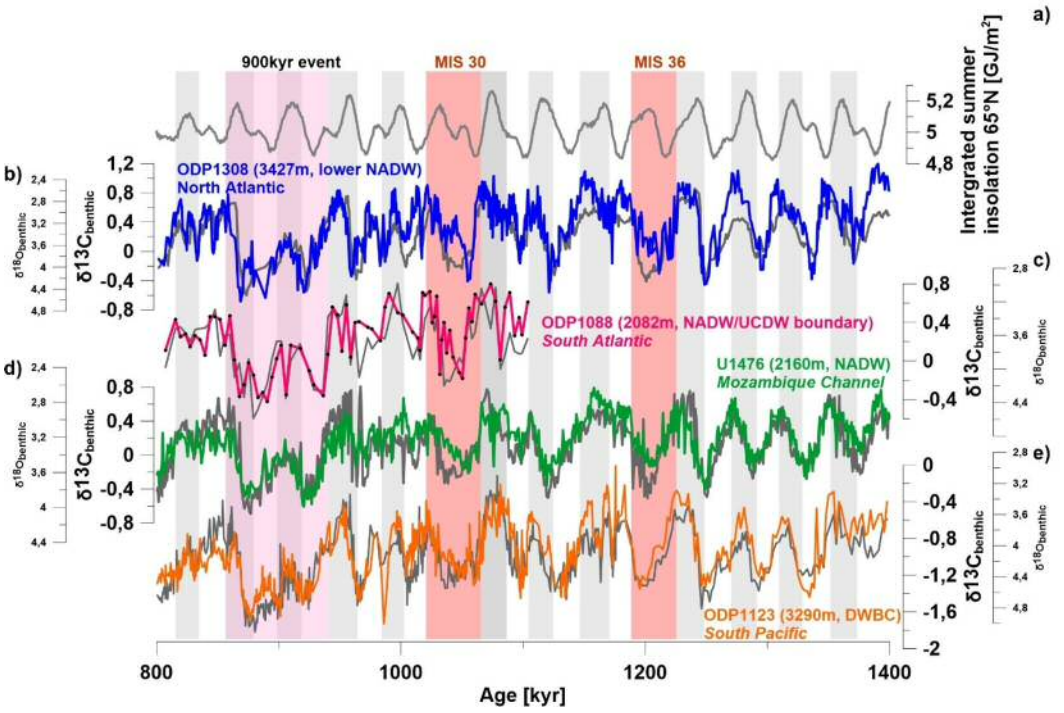


**Figure 8.13** Benthic foraminiferal $\delta^{13}C$ plotted on core respective benthic $\delta^{18}O$ (grey lines). (a) Integrated summer insolation (light grey; Huybers, 2006). (b) Deep subpolar North Atlantic (blue; Hodell et al., 2008), (c) mid-depth subpolar South Atlantic (pink; Hodell et al., 2003), (d) mid-depth western tropical Indian Ocean (green; this study), and (e) deep South Pacific (orange; Elderfield et al., 2012). Shaded vertical pink bars highlight MPT onset glacials MIS30 and MIS36, as well as the 900kyr event (lighter pink). Shaded vertical grey bars highlight times during obliquity maxima.

ice sheet-lag is partnered by changes in $pCO_2$. I suggest that the prolonged glacial $pCO_2$ minima during the MPT after 1.2Ma may have led to an in-phase response when low insolation aligns with high ice volume and low $pCO_2$. This appears particularly significant during 900kyr-event glacials MIS22, and MIS24, which are characterised by particularly low obliquity, significant ice sheet expansion, and likely low $pCO_2$ (Figure 8.9).

## 8.6 Conclusions

I present the first boron isotope-derived high resolution atmospheric $CO_2$ reconstructions for early-MPT glacial MIS30. I find that close coupling between $pCO_2$

and ice volume, which defines the shape and amplitude of Late Pleistocene glacial cycles, already occurred during early-MPT glacials. During glacials MIS30 and MIS36, ice volume sustains across an integrated summer insolation peak for the first time after the 41kyr climate cycles. This occurs in line with prolonged reduced atmospheric $CO_2$. I argue that $CO_2$ stayed reduced during MIS30, despite increases in integrated summer insolation, due to Southern Ocean stratification and isolation of southern-sourced deep water masses. During MIS30 and MIS36, SSTs closely follow insolation forcing leading to increasing SSTs during glacial conditions. This may have supported the creation of durable ice sheets through increased moisture transport to northern hemisphere ice sheets. I hypothesize that the combination of low $pCO_2$ and more durable ice sheets led to the development of ice sheet expansion during times of particularly low external forcing, such as during the 900kyr event. This would have led to a re-organisation of the ice sheet response-lag to insolation forcing and likely shape the 100kyr cycle.

# Chapter 9

# CONCLUSIONS AND FUTURE OUTLOOK

Modern global climate change causes political and socioeconomic concerns on an international level, and is considered one of mankind's greatest challenges today. The increase of anthropogenic atmospheric $CO_2$ has shown to not only increase temperature in the atmosphere, but lead to multiple alterations in other climate parameters. The motivation for the work in this thesis is based upon my long-lasting interest in the scientific functioning of climate feedback systems and their instigation mechanisms.

To investigate the coupling between key climate parameters, such as $pCO_2$, ocean circulation, temperature and ice volume, I chose to direct my research at past climates. This allows for the analysation of climatic behaviour in absence of anthropogenic forcing, and enables the investigation of cause-and-effect analyses during and after periods of climate change. Pleistocene climate change is of particular interest, mainly due to two climatic features. These include (i) abrupt climate change during glacial terminations (0-800kyr), where a pacing in insolation triggers a significant shift in multiple climate feedback mechanisms causing rapid warming, and (ii) the Mid-Pleistocene transition (800-1200kyr; MPT), during which climate cycles changed

from sinusoidal to asymmetrical saw-tooth shape without any measurable changes in insolation. In both cases, the intensity of the climatic change is primarily due to coupled responses from earth internal feedback mechanisms. I therefore provided three research questions in the Indtroduction (chapter 1):

**Research Question 1:** ***What role does the Indian Ocean play in shaping glacial-interglacial climate in the Late Pleistocene (0-1.2 million years)?***

**Research Question 2:** ***What happens to atmospheric $CO_2$ during the Mid-Pleistocene transition (0.8 - 1.2 million years)?***

**Research Question 3:** ***Are established preparation methods and analytical procedures valid for different sized samples with varying initial contamination degrees, and different brands of mass spectrometers?***

To answer the above questions, I used geochemistry in foraminiferal calcite from a recently collected ocean sediment core U1476 to reconstruct various climatic parameters. The new data provide evidence for (a) Indian Ocean circulation dynamics during Late Pleistocene climate cycles (*research question 1*), and (b) an MPT $pCO_2$ and ice volume deviation from external insolation forcing well before the climate disruptive 900kyr event (*research question 2*). As part of the geochemical toolkit, I employ the reconstruction of seawater pH, and atmospheric $CO_2$, via boron isotope analysis. The analytical measurement of boron isotopes is known to be difficult and time consuming. I therefore (c) reviewed the preparational methods and analytical procedures, and applied them to a Nu plasma II inductively coupled mass spectrometer (*research question 3*).

***Answer to research question 1:*** **Indian Ocean salinity dynamics feed a particularly salty deglacial Agulhas Leakage**

After deriving sea surface salinity and sea surface temperature, I find that Indian ocean circulation is of significant importance for Indian Ocean surface salinity distribution during glacials. In chapter 7 "*A Highly Salty Agulhas Leakage linked to Glacial Indian Ocean Salinification*", I show that glacial-interglacial processes in the Indonesian throughflow and the Agulhas Leakage lead to glacial surface salinity increases which cause particularly salty Agulhas leakage rings during the following termination. This may have significant implications for glacial-interglacial climate evolution via strengthening the salinity gradient in Atlantic surface waters on their way to northern deep water formation sites. My work highlights for the first time, that Indian Ocean surface circulation may be involved in shaping global climate.

Chapter 7 includes an initial quantification of the surface salinity increase at peak glacials, but does not provide a quantification of the impact that a highly saline Agulhas Leakage might have on global climate. I therefore initiated a collaboration to test the influence of salt input into the South Atlantic on global circulation and climate. I plan to run a set of general circulation model runs and disturb the ocean circulation through “negative hosing”. This implies simulating the input of surface salt into the South Atlantic, by reducing the freshwater forcing. I believe that the results from this modelling excercise will complement the findings presented in chapter 7, and underline the importance of the surface processes in the Indian Ocean beyond the time of this thesis.

***Answer to research question 2:*** **Early atmospheric $CO_2$ and ice volume deviate from external insolation forcing during the MPT, potentially priming the system for phase change**

The Mid-Pleistocene transition is often assumed synonymous with the 900kyr event, due to the amount of evidence showing disruptions in the earth's climate system at that time. In chapter 8 "*De-coupling of the ice volume/$CO_2$ feedback from external forcing during the early MPT*", I show that glacial low $pCO_2$ and high ice volume sustain an increase in external insolation forcing for the first time during MIS30 ($\sim$1.1Ma), and MIS36 ($\sim$1.2Ma). This effectively presents an early expression of the 100kyr-climate character observed in Late Pleistocene glacial cycles. The prolonged glacial low $pCO_2$ was likely due to expansion of southern-sourced waters, as evident from published Atlantic Ocean stable isotope data, which led to increased stratification and carbon storage potential. I also find that global sea surface temperatures follow insolation during MIS30 and MIS36 which would have caused a divergence between climate feedbacks during the early MPT. I hypothesize that this could have led to in-phase amplification where ice volume increases proportionally more during times of low $pCO_2$ and low insolation forcing, for example during the following 900kyr event. This study presents the first available $pCO_2$ reconstructions from the early-middle MPT and underlines the close coupling between $pCO_2$ and ice volume as major climate feedback mechanisms.

***Answer to research question 3:*** **Large samples can be cleaned with conventional methods, with evidence for contamination potential from ice-rafted debris, but not microscopic black particles. Analytical procedures on a Nu Plasma II (Nu instruments) require methodological adaptation**

Boron isotope analyses from foraminifera often require large foraminiferal samples. In chapter 6 "*A Study of Sample Preparation and Analytical Procedures for*

*Boron Isotopes in Planktonic Foraminifera*", I tested whether conventional cleaning procedures set-up for small samples could be also applied to large samples. My analyses show that large samples of up to 200 foraminiferal tests can be cleaned efficiently in 0.5$\mu$L or 1.5$\mu$L tubes without the necessity of scaling reagents. This provides support for high-quality boron isotope measurements from samples with a high number of tests.

Chapter 6 additionally provides first accuracy and precision measurements for boron isotope standards analysed on a Nu plasma II. I aquired best external reproducibility and accuracy with a PFA cyclonic spray chamber, $10^{11}\Omega$ resistors, and a higher concentrated standard solution. Under optimal conditions, using a 200ppb NIST 951 boron isotope standard solution, accuracy and reproducibility resulted in 0.04($\pm$0.26). Using a less concentrated solution of 50ppb NIST 951, accuracy and precision slightly deteriorated to 0.06($\pm$0.41). This shows that boron isotopes can be successfully measured on a Nu plasma II. To further improve the analytical measurement of boron isotopes on a Nu plasma II instrument in the future, I propose the introduction of a hydrofluoric acid washout aid as a means to reduce the bracketing time by decreasing the washout time. A shorter washout will lead to more efficient blank- and standard bracketing, and allow the bracketing correction to capture short-term mass bias variability. This has the potential of significantly improving the accuracy and precision of a boron isotope standard run.

In this thesis, I have investigated the patterns of earth internal climate parameters, such as atmospheric $CO_2$, and their characteristics as feedback mechanisms using two case studies from the Late Pleistocene and the Mid-Pleistocene transition. My climate reconstructions highlight the importance of Indian Ocean surface salinity circulation (a), and coupled $pCO_2$ - ice sheet dynamics (b) as major climate drivers when coupled with changes in insolation. I also provide evidence that $pCO_2$ can be

reconstructed from boron isotopes measured on a Nu plasma II, albeit needing large samples. I show that cleaning large samples is no hindrance in the method.

The findings outlined above are significant for the analysation of climate in the past and provide baseline knowledge on how climate parameters function for our understanding of climate in the future. As such, the results produced in this thesis are impactful not just for climate science, but for a wider public audience.

# References


Abe-Ouchi, A., Saito, F., Kawamura, K., Raymo, M. E., Okuno, J., Takahashi, K., & Blatter, H. (2013). Insolation-driven 100,000-year glacial cycles and hysteresis of ice-sheet volume. *Nature*, **500**, 190–193.

Adkins, J. F. (2013). The role of deep ocean circulation in setting glacial climates. *Paleoceanography*, **28**, 539–561.

Adkins, J. F., McIntyre, K., & Schrag, D. P. (2002). The salinity, temperature, and $\delta$18O of the glacial deep ocean. *Science*, **298**, 1769–1773.

Agnihotri, R., Bhattacharya, S. K., Sarin, M. M., & Somayajulu, B. L. (2003). Changes in surface productivity and subsurface denitrification during the Holocene: a multiproxy study from the eastern Arabian Sea. *The Holocene*, **13**, 701–713.

Ahn, J., & Brook, E. J. (2008). Atmospheric CO2 and climate on millennial time scales during the last glacial period. *Science*, **322**, 83–85.

Alley, R. B. (2000). The Younger Dryas cold interval as viewed from central Greenland. *Quaternary Science Reviews*, **19**, 213–226.

Anagnostou, E., John, E. H., Edgar, K. M., Foster, G. L., Ridgwell, A., Inglis, G. N., Pancost, R. D., Lunt, D. J., & Pearson, P. N. (2016). Changing atmospheric CO 2 concentration was the primary driver of early Cenozoic climate. *Nature*.

Anand, P., Elderfield, H., & Conte, M. H. (2003). Calibration of Mg/Ca thermometry in planktonic foraminifera from a sediment trap time series. *Paleoceanography*, **18**, n/a–n/a.

Anderson, R. F., Ali, S., Bradtmiller, L. I., Nielsen, S. H., Fleisher, M. Q., Anderson, B. E., & Burckle, L. H. (2009). Wind-driven upwelling in the southern ocean and the deglacial rise in atmospheric CO2. *Science*, **323**, 1443–1448.

Anderson, R. F., Sachs, J. P., Fleisher, M. Q., Allen, K. A., Yu, J., Koutavas, A., & Jaccard, S. L. (2019). Deep-Sea Oxygen Depletion and Ocean Carbon Sequestration During the Last Ice Age. *Global Biogeochemical Cycles*, **33**, 301–317.

Archer, D. (2010). The Global Carbon Cycle (Princeton Primers in Climate). Princeton University Press.

Ashwin, P., & Ditlevsen, P. (2015). The middle Pleistocene transition as a generic bifurcation on a slow manifold. *Climate Dynamics*, **45**, 2683–2695.

Austermann, J., Pollard, D., Mitrovica, J. X., Moucha, R., Forte, A. M., DeConto, R. M., Rowley, D. B., & Raymo, M. E. (2015). The impact of dynamic topography change on antarctic ice sheet stability during the mid-pliocene warm period. *Geology*, **43**, 927–930.

Backeberg, B. C., Penven, P., & Rouault, M. (2012). Impact of intensified Indian Ocean winds on mesoscale variability in the Agulhas system. *Nature Climate Change*, **2**, 608–612.

Bard, E., Hamelin, B., & Delanghe-Sabatier, D. (2010). Deglacial meltwater pulse 1B and younger dryas sea levels revisited with boreholes at tahiti. *Science*, **327**, 1235–1237.

Bard, E., & Rickaby, R. E. (2009). Migration of the subtropical front as a modulator of glacial climate. *Nature*, **460**, 380–383.

Barker, S., Greaves, M., & Elderfield, H. (2003). A study of cleaning procedures used for foraminiferal Mg/Ca paleothermometry. *Geochemistry, Geophysics, Geosystems*, **4**, n/a–n/a.

Barker, S., Cacho, I., Benway, H., & Tachikawa, K. (2005). Planktonic foraminiferal Mg/Ca as a proxy for past oceanic temperatures: a methodological overview and data compilation for the Last Glacial Maximum. *Quaternary Science Reviews*, **24**, 821–834.

Barker, S., Chen, J., Gong, X., Jonkers, L., Knorr, G., & Thornalley, D. (2015). Icebergs not the trigger for North Atlantic cold events. *Nature*, **520**, 333–336.

Barker, S., Diz, P., Vautravers, M. J., Pike, J., Knorr, G., Hall, I. R., & Broecker, W. S. (2009). Interhemispheric Atlantic seesaw response during the last deglaciation. *Nature*, **457**, 1097–1102.

Barker, S., Knorr, G., Edwards, R. L., Parrenin, F., Putnam, A. E., Skinner, L. C., Wolff, E., & Ziegler, M. (2011). 800,000 Years of abrupt climate variability. *Science*, **334**, 347–351.

Barker, S., Knorr, G., Vautravers, M. J., Diz, P., & Skinner, L. C. (2010). Extreme deepening of the Atlantic overturning circulation during deglaciation. *Nature Geoscience*, **3**, 567–571.

Bartoli, G., Sarnthein, M., Weinelt, M., Erlenkeuser, H., Garbe-Schönberg, D., & Lea, D. W. (2005). Final closure of Panama and the onset of northern hemisphere glaciation. *Earth and Planetary Science Letters*, **237**, 33–44.

Bartoli, G., Hönisch, B., & Zeebe, R. E. (2011). Atmospheric CO2 decline during the Pliocene intensification of Northern Hemisphere glaciations. *Paleoceanography*, **26**.

Bassinot, F. C., Beaufort, L., Vincent, E., Labeyrie, L. D., Rostek, F., Müller, P. J., Quidelleur, X., & Lancelot, Y. (1994). Coarse fraction fluctuations in pelagic carbonate sediments from the tropical Indian Ocean: A 1500-kyr record of carbonate dissolution. *Paleoceanography*, **9**, 579–600.

Bè, A. W., & Anderson, R. O. (1976). Gametogenesis in planktonic Foraminifera. *Science*, **192**, 890–892.

Beal, L. M., De Ruijter, W. P., Biastoch, A., Zahn, R., Cronin, M., Hermes, J., Lutjeharms, J., Quartly, G., Tozuka, T., Baker-Yeboah, S., Bornman, T., Cipollini, P., Dijkstra, H., Hall, I., Park, W., Peeters, F., Penven, P., Ridderinkhof, H., & Zinke, J. (2011). On the role of the Agulhas system in ocean circulation and climate.

Beltran, C., Golledge, N. R., Ohneiser, C., Kowalewski, D. E., Sicre, M.-A., Hageman, K. J., Smith, R., Wilson, G. S., & Mainié, F. (2020). Southern Ocean temperature records and ice-sheet models demonstrate rapid Antarctic ice sheet retreat under low atmospheric CO2 during Marine Isotope Stage 31. *Quaternary Science Reviews*, **228**, 106069.

Bemis, B. E., Spero, H. J., Bijma, J., & Lea, D. W. (1998). Reevaluation of the oxygen isotopic composition of planktonic foraminifera: Experimental results and revised paleotemperature equations. *Paleoceanography*, **13**, 150–160.

Bereiter, B., Eggleston, S., Schmitt, J., Nehrbass-Ahles, C., Stocker, T. F., Fischer, H., Kipfstuhl, S., & Chappellaz, J. (2015). Revision of the EPICA Dome C CO 2 record from 800 to 600 kyr before present. *Geophysical Research Letters*, **42**, 542–549.

Berends, C. J., de Boer, B., Dolan, A. M., Hill, D. J., & van de Wal, R. S. W. (2019). Modelling ice sheet evolution and atmospheric CO<sub>2</sub> during the Late Pliocene. *Climate of the Past Discussions*.

Berger, A., Loutre, M. F., & Gallée, H. (1998). Sensitivity of the LLN climate model to the astronomical and CO2 forcings over the last 200 ky. *Climate Dynamics*, **14**, 615–629.

Berger, A., Loutre, M. F., & Laskar, J. (1992). Stability of the astronomical frequencies over the earth's history for paleoclimate studies. *Science*, **255**, 560–566.

Berner, R. A. (2003). The long-term carbon cycle, fossil fuels and atmospheric composition.

Biastoch, A., Böning, C. W., Schwarzkopf, F. U., & Lutjeharms, J. R. (2009). Increase in Agulhas leakage due to poleward shift of Southern Hemisphere westerlies. *Nature*, **462**, 495–498.

Biastoch, A., Durgadoo, J. V., Morrison, A. K., Van Sebille, E., Weijer, W., & Griffies, S. M. (2015). Atlantic multi-decadal oscillation covaries with Agulhas leakage. *Nature Communications*, **6**.

Bintanja, R., & Van De Wal, R. S. (2008). North American ice-sheet dynamics and the onset of 100,000-year glacial cycles. *Nature*, **454**, 869–872.

Bird, M. I., Taylor, D., & Hunt, C. (2005). Palaeoenvironments of insular Southeast Asia during the Last Glacial Period: A savanna corridor in Sundaland? *Quaternary Science Reviews*, **24**, 2228–2242.

Biskaborn, B. K., Smith, S. L., Noetzli, J., Matthes, H., Vieira, G., Streletskiy, D. A., Schoeneich, P., Romanovsky, V. E., Lewkowicz, A. G., Abramov, A., Allard, M., Boike, J., Cable, W. L., Christiansen, H. H., Delaloye, R., Diekmann, B., Drozdov, D., Etzelmüller, B., Grosse, G., … Lantuit, H. (2019). Permafrost is warming at a global scale. *Nature Communications*, **10**.

Bolton, C. T., Chang, L., Clemens, S. C., Kodama, K., Ikehara, M., Medina-Elizalde, M., Paterson, G. A., Roberts, A. P., Rohling, E. J., Yamamoto, Y., & Zhao, X. (2013). A 500,000 year record of Indian summer monsoon dynamics recorded by eastern equatorial Indian Ocean upper water column structure. *Quaternary Science Reviews*, **77**, 167–180.

Bonan, G. B. (2008). Forests and climate change: Forcings, feedbacks, and the climate benefits of forests.

Bond, G. C., & Lotti, R. (1995). Iceberg discharges into the North Atlantic on millennial time scales during the last glaciation. *Science*.

Bony, S., Stevens, B., Frierson, D. M., Jakob, C., Kageyama, M., Pincus, R., Shepherd, T. G., Sherwood, S. C., Siebesma, A. P., Sobel, A. H., Watanabe, M., & Webb, M. J. (2015). Clouds, circulation and climate sensitivity. *Nature Geoscience*, **8**, 261–268.

Bosmans, J. H. C., Hilgen, F. J., Tuenter, E., & Lourens, L. J. (2015). Obliquity forcing of low-latitude climate. *Climate of the Past*, **11**, 1335–1346.

Bouvier-Soumagnac, Y., & Duplessy, J. C. (1985). Carbon and oxygen isotopic composition of planktonic foraminifera from laboratory culture, plankton tows and Recent sediment: implications for the reconstruction of paleoclimatic conditions and of the global carbon-cycle. *Journal of Foraminiferal Research*, **15**, 302–320.

Boyle, E. A., & Keigwin, L. D. (1985). Comparison of Atlantic and Pacific paleochemical records for the last 215,000 years: changes in deep ocean circulation and chemical inventories. *Earth and Planetary Science Letters*, **76**, 135–150.

Boyle, E. A. (1988). Cadmium: Chemical tracer of deepwater paleoceanography. *Paleoceanography*, **3**, 471–489.

Bralower, T., & Bice, D. (n.d.). Feedback Mechanisms | EARTH 103: Earth in the Future.

Brand, W. A., Coplen, T. B., Vogl, J., Rosner, M., & Prohaska, T. (2014). *Assessment of international reference materials for isotope-ratio analysis (IUPAC technical report)* (tech. rep.). IUPAC Secretariat.

Breecker, D. O., Sharp, Z. D., & McFadden, L. D. (2010). Atmospheric CO2 concentrations during ancient greenhouse climates were similar to those predicted for A.D. 2100. *Proceedings of the National Academy of Sciences of the United States of America*, **107**, 576–580.

Broecker, W., & Clark, E. (2001). An evaluation of Lohmann's foraminifera weight dissolution index. *Paleoceanography*, **16**, 531–534.

Broecker, W. S. (1991). THE GREAT OCEAN CONVEYOR. *Oceanography*, **4**, 79–89.

Broecker, W. S. (2006). Was the Younger Dryas triggered by a flood?

Brook, E. J., Sowers, T., & Orchardo, J. (1996). Rapid variations in atmospheric methane concentration during the past 110,000 years. *Science*, **273**, 1087–1091.

Brown, S. J., & Elderfield, H. (1996). Variations in Mg/Ca and Sr/Ca ratios of planktonic foraminifera caused by postdepositional dissolution: Evidence of shallow Mg-dependent dissolution. *Paleoceanography*, **11**, 543–551.

Burke, A., & Robinson, L. F. (2012). The southern ocean's role in carbon exchange during the last deglaciation. *Science*, **335**, 557–561.

Burke, M., Hsiang, S. M., & Miguel, E. (2015). Global non-linear effect of temperature on economic production. *Nature*, **527**, 235–239.

Butos, W. N., & Mcquade, T. J. (2015). Causes and Consequences of the Climate Science Boom. *The Independent Review*, **20**, 1086–1653.

Caillé, A. (2007). *2007 Survey of Energy Resources - Executive Summary* (tech. rep.). World Energy Council.

Caley, T., Kim, J.-H., Malaizé, B., Giraudeau, J., Laepple, T., Caillon, N., Charlier, K., Rebaubier, H., Rossignol, L., Castañeda, I. S., Schouten, S., & Sinninghe Damsté, J. S. (2011). High-latitude obliquity as a dominant forcing in the Agulhas current system. *Climate of the Past*, **7**, 1285–1296.

Caley, T., Giraudeau, J., Malaizé, B., Rossignol, L., & Pierre, C. (2012). Agulhas leakage as a key process in the modes of Quaternary climate changes. *Proceedings of the National Academy of Sciences of the United States of America*, **109**, 6835–6839.

Caley, T., Peeters, F. J. C., Biastoch, A., Rossignol, L., van Sebille, E., Durgadoo, J., Malaizé, B., Giraudeau, J., Arthur, K., & Zahn, R. (2014). Quantitative estimate of the paleo-Agulhas leakage. *Geophysical Research Letters*, **41**, 1238–1246.

Chalk, T. B., Hain, M. P., Foster, G. L., Rohling, E. J., Sexton, P. F., Badger, M. P. S., Cherry, S. G., Hasenfratz, A. P., Haug, G. H., Jaccard, S. L., Martínez-García, A., Pälike, H., Pancost, R. D., & Wilson, P. A. (2017). Causes of ice age intensification across the Mid-Pleistocene Transition. *Proceedings of the National Academy of Sciences of the United States of America*, **114**, 13114–13119.

Charman, D. J. (2002). Peatlands and environmental change. John Wiley & Sons.

Cheng, H., Edwards, R. L., Sinha, A., Spötl, C., Yi, L., Chen, S., Kelly, M., Kathayat, G., Wang, X., Li, X., Kong, X., Wang, Y., Ning, Y., & Zhang, H. (2016a). The Asian monsoon over the past 640,000 years and ice age terminations. *Nature*, **534**, 640–646.

Cheng, H., Edwards, R. L., Sinha, A., Spötl, C., Yi, L., Chen, S., Kelly, M., Kathayat, G., Wang, X., Li, X., Kong, X., Wang, Y., Ning, Y., & Zhang, H. (2016b). The Asian monsoon over the past 640,000 years and ice age terminations. *Nature*, **534**, 640–646.

Chester, R., & Jickells, T. (2012). Marine Geochemistry. John Wiley; Sons.

Clark, I., & Fritz, P. (1997). Environmental Isotopes in Hydrogeology. New York, CRC Press LLC.

Clark, P. U., Alley, R. B., Keigwin, L. D., Licciardi, J. M., Johnsen, S. J., & Wang, H. (1996). Origin of the first global meltwater pulse following the Last Glacial Maximum. *Paleoceanography*, **11**, 563–577.

Clark, P. U., Archer, D., Pollard, D., Blum, J. D., Rial, J. A., Brovkin, V., Mix, A. C., Pisias, N. G., & Roy, M. (2006). The middle Pleistocene transition: characteristics, mechanisms, and implications for long-term changes in atmospheric pCO2. *Quaternary Science Reviews*, **25**, 3150–3184.

Clark, P. U., & Pollard, D. (1998). Origin of the Middle Pleistocene Transition by ice sheet erosion of regolith. *Paleoceanography*, **13**, 1–9.

Clemens, S. C., Prell, W. L., & Sun, Y. (2010). Orbital-scale timing and mechanisms driving Late Pleistocene Indo-Asian summer monsoons: Reinterpreting cave speleothem $\delta$18O. *Paleoceanography*, **25**.

Crutzen, P. J. (2002). Geology of mankind.

Curry, J. A., Schramm, J. L., & Ebert, E. E. (1995). Sea ice-albedo climate feedback mechanism. *Journal of Climate*, **8**, 240–247.

Curry, W. B., & Oppo, D. W. (2005). Glacial water mass geometry and the distribution of $\delta$ 13 C of ΣCO 2 in the western Atlantic Ocean. *Paleoceanography*, **20**, n/a–n/a.

Dansgaard, W., Johnsen, S. J., Clausen, H. B., Dahl-Jensen, D., Gundestrup, N. S., Hammer, C. U., Hvidberg, C. S., Steffensen, J. P., Sveinbjörnsdottir, A. E., Jouzel, J., & Bond, G. (1993). Evidence for general instability of past climate from a 250-kyr ice-core record. *Nature*, **364**, 218–220.

Daruka, I., & Ditlevsen, P. D. (2014). Changing climatic response Changing climatic response: a conceptual model for glacial cycles and the Mid-Pleistocene Transition Changing climatic response Changing climatic response. *Clim. Past Discuss*, **10**, 1101–1127.

Dasgupta, R., & Hirschmann, M. M. (2010). The deep carbon cycle and melting in Earth's interior. *Earth and Planetary Science Letters*, **298**, 1–13.

De Garidel-Thoron, T., Rosenthal, Y., Bassinot, F., & Beaufort, L. (2005). Stable sea surface temperatures in the western Pacific warm pool over the past 1.75 million years. *Nature*, **433**, 294–298.

de Boer, B., Lourens, L. J., & Van De Wal, R. S. (2014a). Persistent 400,000-year variability of antarctic ice volume and the carbon cycle is revealed throughout the plio-pleistocene. *Nature Communications*, **5**.

de Boer, B., Stocchi, P., & van de Wal, R. S. W. (2014b). A fully coupled 3-D ice-sheet–sea-level model: algorithm and applications. *Geoscientific Model Development*, **7**, 2141–2156.

DeConto, R. M., & Pollard, D. (2003). Rapid Cenozoic glaciation of Antarctica induced by declining atmospheric CO2. *Nature*, **421**, 245–249.

Dekens, P. S., Lea, D. W., Pak, D. K., & Spero, H. J. (2002). Core top calibration of Mg/Ca in tropical foraminifera: Refining paleotemperature estimation. *Geochemistry, Geophysics, Geosystems*, **3**, 1–29.

Dekens, P. S., Ravelo, A. C., & McCarthy, M. D. (2007). Warm upwelling regions in the Pliocene warm period. *Paleoceanography*.

Dekker, M. M., Von Der Heydt, A. S., & Dijkstra, H. A. (2018). Cascading transitions in the climate system. *Earth System Dynamics*.

Denman, K., G. Brasseur, A., Chidthaisong, Ciais, P., Cox, P., Dickinson, R., Hauglustaine, D., Heinze, C., Holland, E., Jacob, D., Lohmann, U., Ramachandran, S., Dias, P. d. S., Wofsy, S., & Zhang, X. (2007). *AR4 Climate Change 2007: The Physical Science Basis — IPCC* (tech. rep.).

Denton, G. H., Anderson, R. F., Toggweiler, J. R., Edwards, R. L., Schaefer, J. M., & Putnam, A. E. (2010). The last glacial termination.

Detlef, H., Belt, S. T., Sosdian, S. M., Smik, L., Lear, C. H., Hall, I. R., Cabedo-Sanz, P., Husum, K., & Kender, S. (2018). Sea ice dynamics across the Mid-Pleistocene transition in the Bering Sea. *Nature Communications*, **9**.

Di Nezio, P. N., & Tierney, J. E. (2013). The effect of sea level on glacial Indo-Pacific climate. *Nature Geoscience*, **6**, 485–491.

Di Nezio, P. N., Timmermann, A., Tierney, J. E., Jin, F. F., Otto-Bliesner, B., Rosenbloom, N., Mapes, B., Neale, R., Ivanovic, R. F., & Montenegro, A. (2016). The climate response of the Indo-Pacific warm pool to glacial sea level. *Paleoceanography*, **31**, 866–894.

Dickson, A. G. (1990). Thermodynamics of the dissociation of boric acid in synthetic seawater from 273.15 to 318.15 K. *Deep Sea Research Part A, Oceanographic Research Papers*, **37**, 755–766.

Diekmann, B., & Kuhn, G. (2002). Sedimentary record of the mid-Pleistocene climate transition in the southeastern South Atlantic (ODP Site 1090). *Palaeogeography, Palaeoclimatology, Palaeoecology*, **182**, 241–258.

Diester-Haass, L., Billups, K., & Lear, C. (2018). Productivity changes across the mid-Pleistocene climate transition. Elsevier B.V.

DiNezio, P. N., Tierney, J. E., Otto-Bliesner, B. L., Timmermann, A., Bhattacharya, T., Rosenbloom, N., & Brady, E. (2018). Glacial changes in tropical climate amplified by the Indian Ocean. *Science Advances*, **4**.

Draut, A. E., Raymo, M. E., McManus, J. F., & Oppo, D. W. (2003). Climate stability during the Pliocene warm period. *Paleoceanography*, **18**, n/a–n/a.

Driscoll, N. W., & Haug, G. H. (1998). A short circuit in thermohaline circulation: A cause for Northern Hemisphere glaciation?

Duplessy, J. C., Labeyrie, L., & Waelbroeck, C. (2002). Constraints on the ocean oxygen isotopic enrichment between the last glacial maximum and the holocene: Paleoceanographic implications. *Quaternary Science Reviews*, **21**, 315–330.

Durgadoo, J. V., Loveday, B. R., Reason, C. J., Penven, P., & Biastoch, A. (2013). Agulhas leakage predominantly responds to the southern hemisphere westerlies. *Journal of Physical Oceanography*, **43**, 2113–2131.

Durgadoo, J. V., Rühs, S., Biastoch, A., & Böning, C. W. (2017). Indian Ocean sources of Agulhas leakage. *Journal of Geophysical Research: Oceans*, **122**, 3481–3499.

Dyez, K. A., Hönisch, B., & Schmidt, G. A. (2018). Early Pleistocene Obliquity-Scale pCO2 Variability at around 1.5 Million Years Ago. *Paleoceanography and Paleoclimatology*, **33**, 1270–1291.

Dyez, K. A., Zahn, R., & Hall, I. R. (2014). Multicentennial Agulhas leakage variability and links to North Atlantic climate during the past 80,000 years. *Paleoceanography*, **29**, 1238–1248.

Edgar, K. M., Anagnostou, E., Pearson, P. N., & Foster, G. L. (2015). Assessing the impact of diagenesis on $\delta$11B, $\delta$13C, $\delta$18O, Sr/Ca and B/Ca values in fossil planktic foraminiferal calcite. *Geochimica et Cosmochimica Acta*, **166**, 189–209.

Elderfield, H., Ferretti, P., Greaves, M., Crowhurst, S., McCave, I. N., Hodell, D., & Piotrowski, A. M. (2012). Evolution of Ocean Temperature and Ice Volume Through the Mid-Pleistocene Climate Transition. *Science*, **337**, 704 LP –709.

Erez, J., Almogi-Labin, A., & Avraham, S. (1991). On the Life History of Planktonic Foraminifera: Lunar Reproduction Cycle in Globigerinoides Sacculifer (Brady). *Paleoceanography*, **6**, 295–306.

Ericson, D. B., Ewing, M., Wolling, G., & Heezen, B. C. (1961). Atlantic deep-sea sediment cores. *Geol. Soc. Amer. Bull*, **72**, 93–286.

ESRL. (n.d.). ESRL Global Monitoring Division - Global Greenhouse Gas Reference Network.

Evans, D., Brierley, C., Raymo, M. E., Erez, J., & Müller, W. (2016). Planktic foraminifera shell chemistry response to seawater chemistry: Pliocene-Pleistocene seawater Mg/Ca, temperature and sea level change. *Earth and Planetary Science Letters*, **438**, 139–148.

Fairbanks, R. G. (1989). A 17,000-year glacio-eustatic sea level record: Influence of glacial melting rates on the Younger Dryas event and deep-ocean circulation. *Nature*, **342**, 637–642.

Fallet, U., Brummer, G.-J., Zinke, J., Vogels, S., & Ridderinkhof, H. (2010). Contrasting seasonal fluxes of planktonic foraminifera and impacts on paleother-

mometry in the Mozambique Channel upstream of the Agulhas Current. *Paleoceanography*, **25**, n/a–n/a.

Farmer, J. R., Hönisch, B., Haynes, L. L., Kroon, D., Jung, S., Ford, H. L., Raymo, M. E., Jaume-Seguí, M., Bell, D. B., Goldstein, S. L., Pena, L. D., Yehudai, M., & Kim, J. (2019). Deep Atlantic Ocean carbon storage and the rise of 100,000-year glacial cycles. *Nature Geoscience*, **12**, 355–360.

Farmer, J. R., Hönisch, B., & Uchikawa, J. (2016). Single laboratory comparison of MC-ICP-MS and N-TIMS boron isotope analyses in marine carbonates. *Chemical Geology*, **447**, 173–182.

Ferrari, R., Jansen, M. F., Adkins, J. F., Burke, A., Stewart, A. L., & Thompson, A. F. (2014). Antarctic sea ice control on ocean circulation in present and glacial climates. *Proceedings of the National Academy of Sciences of the United States of America*, **111**, 8753–8758.

Flower, B. P., & Kennett, J. P. (1994). The middle Miocene climatic transition: East Antarctic ice sheet development, deep ocean circulation and global carbon cycling. *Palaeogeography, Palaeoclimatology, Palaeoecology*, **108**, 537–555.

Flude, S., Györe, D., Stuart, F. M., Zurakowska, M., Boyce, A. J., Haszeldine, R. S., Chalaturnyk, R., & Gilfillan, S. M. (2017). The inherent tracer fingerprint of captured CO2. *International Journal of Greenhouse Gas Control*, **65**, 40–54.

Ford, H. L., & Raymo, M. E. (2020). Regional and global signals in seawater $\delta$18O records across the mid-Pleistocene transition. *Geology*, **48**, 113–117.

Ford, H. L., Sosdian, S. M., Rosenthal, Y., & Raymo, M. E. (2016). Gradual and abrupt changes during the Mid-Pleistocene Transition. *Quaternary Science Reviews*, **148**, 222–233.

Foster, G. L., Pogge von Strandmann, P. A. E., & Rae, J. W. B. (2010). Boron and magnesium isotopic composition of seawater. *Geochemistry, Geophysics, Geosystems*, **11**, n/a–n/a.

Foster, G. L., Lear, C. H., & Rae, J. W. (2012). The evolution of pCO 2, ice volume and climate during the middle Miocene. *Earth and Planetary Science Letters*, **341-344**, 243–254.

Foster, G. L., Royer, D. L., & Lunt, D. J. (2017). Future climate forcing potentially without precedent in the last 420 million years. *Nature Communications*, **8**, 1–8.

Foster, G. (2008). Seawater pH, pCO2 and carbonate ion variations in the Caribbean Sea over the last 130 kyr: A boron isotope and B/Ca study of planktic foraminifera. *Earth and Planetary Science Letters*, **271**, 254–266.

Francey, R. J., Allison, C. E., Etheridge, D. M., Trudinger, C. M., Enting, I. G., Leuenberger, M., Langenfels, R. L., Michel, E., & Steele, L. P. (1999). A 1000-year high precision record of delta13C in atmospheric CO2. *Tellus B*, **51**, 170–193.

Franck, S., Bounama, C., & von Bloh, W. (2008). Weathering. In *Encyclopedia of ecology, five-volume set* (pp. 3770–3776). Elsevier Inc.

Franzese, A. M., Hemming, S. R., Goldstein, S. L., & Anderson, R. F. (2006). Reduced Agulhas Leakage during the Last Glacial Maximum inferred from an integrated provenance and flux study. *Earth and Planetary Science Letters*, **250**, 72–88.

Friedlingstein, P., Cox, P., Betts, R., Bopp, L., von Bloh, W., Brovkin, V., Cadule, P., Doney, S., Eby, M., Fung, I., Bala, G., John, J., Jones, C., Joos, F., Kato, T., Kawamiya, M., Knorr, W., Lindsay, K., Matthews, H. D., … Zeng, N. (2006). Climate–Carbon Cycle Feedback Analysis: Results from the C 4 MIP Model Intercomparison. *Journal of Climate*, **19**, 3337–3353.

Galeotti, S., DeConto, R., Naish, T., Stocchi, P., Florindo, F., Pagani, M., Barrett, P., Bohaty, S. M., Lanci, L., Pollard, D., Sandroni, S., Talarico, F. M., & Zachos, J. C. (2016). Antarctic Ice Sheet variability across the Eocene-Oligocene boundary climate transition. *Science*, **352**, 76–80.

Ganopolski, A., & Calov, R. (2011). The role of orbital forcing, carbon dioxide and regolith in 100 kyr glacial cycles. *Climate of the Past*, **7**, 1415–1425.

Garzoli, S. L., Goñi, G. J., Mariano, A. J., & Olson, D. B. (1997). Monitoring the upper southeastern Atlantic transports using altimeter data. *Journal of Marine Research*, **55**, 453–481.

Garzoli, S. L., Gordon, A. L., Kamenkovich, V., Pillsbury, D., & Duncombe-Rae, C. (1996). Variability and sources of the southeastern Atlantic circulation. *Journal of Marine Research*, **54**, 1039–1071.

Geider, R. J., & La Roche, J. (2002). Redfield revisited: Variability of C:N:P in marine microalgae and its biochemical basis.

Gest, L., Parrenin, F., Chowdhry Beeman, J., Raynaud, D., Fudge, T. J., Buizert, C., & Brook, E. J. (2017). Leads and lags between Antarctic temperature and carbon dioxide during the last deglaciation. *Climate of the Past Discussions*, 1–16.

Gillies, J. (2015). California Drought Is Made Worse by Global Warming, Scientists Say - The New York Times.

Goldenberg, S. (2010). 'Hockey stick' graph creator Michael Mann cleared of academic misconduct | Environment | The Guardian.

Goody, R. M. (1995). Principles of atmospheric physics and chemistry. Oxford University Press.

Gordon, A. L. (1986). Interocean exchange of thermocline water. *Journal of Geophysical Research*, **91**, 5037.

Gray, W. R., & Evans, D. (2019). Nonthermal Influences on Mg/Ca in Planktonic Foraminifera: A Review of Culture Studies and Application to the Last Glacial Maximum. *Paleoceanography and Paleoclimatology*, **34**, 306–315.

Gray, W. R., Weldeab, S., Lea, D. W., Rosenthal, Y., Gruber, N., Donner, B., & Fischer, G. (2018). The effects of temperature, salinity, and the carbonate system on Mg/Ca in Globigerinoides ruber (white): A global sediment trap calibration. *Earth and Planetary Science Letters*, **482**, 607–620.

Greenop, R., Sosdian, S. M., Henehan, M. J., Wilson, P. A., Lear, C. H., & Foster, G. L. (2019). Orbital Forcing, Ice Volume, and CO 2 Across the Oligocene-Miocene Transition. *Paleoceanography and Paleoclimatology*, **34**, 316–328.

Grootes, P. M., & Stuiver, M. (1997). Oxygen 18/16 variability in Greenland snow and ice with 10 3 to 10 5 year time resolution. *Journal of Geophysical Research: Oceans*, **102**, 26455–26470.

Guihou, A., Pichat, S., Govin, A., Nave, S., Michel, E., Duplessy, J. C., Telouk, P., & Labeyrie, L. (2011). Enhanced Atlantic Meridional Overturning Circulation supports the Last Glacial Inception. *Quaternary Science Reviews*, **30**, 1576–1582.

Hain, M. P., Sigman, D. M., & Haug, G. H. (2010). Carbon dioxide effects of Antarctic stratification, North Atlantic Intermediate Water formation, and subantarctic nutrient drawdown during the last ice age: Diagnosis and synthesis in a geochemical box model. *Global Biogeochemical Cycles*, **24**, n/a–n/a.

Hall, I. R., Mccave, I. N., Shackleton, N. J., Weedon, G. P., & Harris, S. E. (2001). Intensified deep Pacific inflow and ventilation in Pleistocene glacial times. *Nature*.

Hall, I., Hemming, S., LeVay, L., Barker, S., Berke, M., Brentegani, L., Caley, T., Cartagena-Sierra, A., Charles, C., Coenen, J., Crespin, J., Franzese, A., Gruetzner, J., Han, X., Hines, S., Espejo, F. J., Just, J., Koutsodendris, A., Kubota, K., … Zhang, H. (2017). Site U1476. In *South african climates (agulhas lgm density profile). proceedings of the international ocean discovery program, 361: College station, tx (international ocean discovery*.

Hansen, J., Cacis, A., Rind Russell, D. G., Stone, P., Fung, I., & Ruedy Lerner, R. J. (1984). *CLIMATE SENSITIVITY: ANALYSIS OF FEEDBACK MECHANISMS* (tech. rep.).

Hansen, J., Sato, M., Russell, G., & Kharecha, P. (2013). Climate sensitivity, sea level and atmospheric carbon dioxide. *Philosophical Transactions of the Royal Society A: Mathematical, Physical and Engineering Sciences*, **371**arXiv.

Hasenfratz, A. P., Jaccard, S. L., Martínez-García, A., Sigman, D. M., Hodell, D. A., Vance, D., Bernasconi, S. M., Kleiven, H. F., Haumann, F. A., & Haug, G. H. (2019). The residence time of Southern Ocean surface waters and the 100,000-year ice age cycle. *Science*, **363**, 1080–1084.

Haug, G. H., & Tiedemann, R. (1998). Effect of the formation of the isthmus of panama on atlantic ocean thermohaline circulation. *Nature*, **393**, 673–676.

Hawkins, E., Ortega, P., Suckling, E., Schurer, A., Hegerl, G., Jones, P., Joshi, M., Osborn, T. J., Masson-Delmotte, V., Mignot, J., Thorne, P., & Van Oldenborgh,

G. J. (2017). Estimating changes in global temperature since the preindustrial period. *Bulletin of the American Meteorological Society*, **98**, 1841–1856.

Hays, J. D., Imbrie, J., & Shackleton, N. J. (1976). Variations in the earth's orbit: Pacemaker of the ice ages.

Haywood, A. M., Dowsett, H. J., & Dolan, A. M. (2016). Integrating geological archives and climate models for the mid-Pliocene warm period.

Heinemann, M., Segschneider, J., & Schneider, B. (2019). CO 2 drawdown due to particle ballasting by glacial aeolian dust: an estimate based on the ocean carbon cycle model MPIOM/HAMOCC version 1.6.2p3. *Geoscientific Model Development*, **12**, 1869–1883.

Heinrich, H. (1988). Origin and consequences of cyclic ice rafting in the Northeast Atlantic Ocean during the past 130,000 years. *Quaternary Research*, **29**, 142–152.

Hemleben, C., Spindler, M., & Anderson, O. R. (1989). Modern Planktonic Foraminifera. New York, Springer Verlag.

Hemming, N. G., & Hanson, G. N. (1994). A procedure for the isotopic analysis of boron by negative thermal ionization mass spectrometry. *Chemical Geology*, **114**, 147–156.

Hemming, S. R. (2004). Heinrich events: Massive late Pleistocene detritus layers of the North Atlantic and their global climate imprint. *Reviews of Geophysics*, **42**, RG1005.

Henehan, M. J., Foster, G. L., Bostock, H. C., Greenop, R., Marshall, B. J., & Wilson, P. A. (2016). A new boron isotope-pH calibration for Orbulina universa, with implications for understanding and accounting for 'vital effects'. *Earth and Planetary Science Letters*, **454**, 282–292.

Henehan, M. J., Foster, G. L., Rae, J. W., Prentice, K. C., Erez, J., Bostock, H. C., Marshall, B. J., & Wilson, P. A. (2015). Evaluating the utility of B/Ca ratios in planktic foraminifera as a proxy for the carbonate system: A case study of Globigerinoides ruber. *Geochemistry, Geophysics, Geosystems*, **16**, 1052–1069.

Henehan, M. J., Rae, J. W., Foster, G. L., Erez, J., Prentice, K. C., Kucera, M., Bostock, H. C., Martínez-Botí, M. A., Milton, J. A., Wilson, P. A., Marshall, B. J., & Elliott, T. (2013). Calibration of the boron isotope proxy in the planktonic foraminifera Globigerinoides ruber for use in palaeoCO2 reconstruction. *Earth and Planetary Science Letters*, **364**, 111–122.

Herbert, T. D., Peterson, L. C., Lawrence, K. T., & Liu, Z. (2010). Tropical ocean temperatures over the past 3.5 million years. *Science*, **328**, 1530–1534.

Hernandez-Almeida, I., Sierro, F. J., Cacho, I., & Flores, J. A. (2012). Impact of suborbital climate changes in the North Atlantic on ice sheet dynamics at the Mid-Pleistocene Transition. *Paleoceanography*, **27**.

Heslop, D., Dekkers, M. J., & Langereis, C. G. (2002). Timing and structure of the mid-Pleistocene transition: Records from the loess deposits of northern China. *Palaeogeography, Palaeoclimatology, Palaeoecology*, **185**, 133–143.

Higgins, J. A., Kurbatov, A. V., Spaulding, N. E., Brook, E., Introne, D. S., Chimiak, L. M., Yan, Y., Mayewski, P. A., & Bender, M. L. (2015). Atmospheric composition 1 million years ago from blue ice in the Allan Hills, Antarctica. *Proceedings of the National Academy of Sciences of the United States of America*, **112**, 6887–6891.

Hodell, D., Charles, C., Curtis, J., Mortyn, P., Ninnemann, U., & Venz, K. (2003). Data report: Oxygen isotope stratigraphy of ODP Leg 177 Sites 1088, 1089, 1090, 1093, and 1094. In *Proceedings of the ocean drilling program, 177 scientific results*. Ocean Drilling Program.

Hodell, D. A., Channeil, J. E., Curtis, J. H., Romero, O. E., & Röhl, U. (2008). Onset of "Hudson Strait" Heinrich events in the eastern North Atlantic at the end of the middle Pleistocene transition (around 640 ka)? *Paleoceanography*, **23**.

Hodell, D. A., Minth, E. K., Curtis, J. H., McCave, I. N., Hall, I. R., Channell, J. E., & Xuan, C. (2009). Surface and deep-water hydrography on Gardar Drift (Iceland Basin) during the last interglacial period. *Earth and Planetary Science Letters*, **288**, 10–19.

Holbourn, A., Kuhnt, W., Kochhann, K. G., Andersen, N., & Sebastian Meier, K. J. (2015). Global perturbation of the carbon cycle at the onset of the Miocene Climatic Optimum. *Geology*, **43**, 123–126.

Holbourn, A., Kuhnt, W., & Xu, J. (2011). Indonesian Throughflow variability during the last 140 ka: The timor sea outflow. *Geological Society Special Publication*, **355**, 283–303.

Hönisch, B., Allen, K. A., Russell, A. D., Eggins, S. M., Bijma, J., Spero, H. J., Lea, D. W., & Yu, J. (2011). Planktic foraminifers as recorders of seawater Ba/Ca. *Marine Micropaleontology*, **79**, 52–57.

Hönisch, B., Bijma, J., Russell, A. D., Spero, H. J., Palmer, M. R., Zeebe, R. E., & Eisenhauer, A. (2003). The influence of symbiont photosynthesis on the boron isotopic composition of foraminifera shells. *Marine Micropaleontology*, **49**, 87–96.

Hönisch, B., & Hemming, N. G. (2005). Surface ocean pH response to variations in pCO2 through two full glacial cycles. *Earth and Planetary Science Letters*, **236**, 305–314.

Hönisch, B., Hemming, N. G., Archer, D., Siddall, M., & McManus, J. F. (2009). Atmospheric Carbon Dioxide Concentration Across the Mid-Pleistocene Transition. *Science*, **324**, 1551 LP –1554.

Houghton, R. A. (2007). Balancing the Global Carbon Budget. *Annual Reviews in Earth Planetary Science*, **35**, 313–347.

Huybers, P. (2006). Early pleistocene glacial cycles and the integrated summer insolation forcing. *Science*.

Huybers, P. (2011). Combined obliquity and precession pacing of late Pleistocene deglaciations. *Nature*, **480**, 229–232.

Huybers, P., & Wunsch, C. (2005). Obliquity pacing of the late Pleistocene glacial terminations. *Nature*, **434**, 491–494.

Imbrie, J., Berger, A., Boyle, E. A., Clemens, S. C., Duffy, A., Howard, W. R., Kukla, G., Kutzbach, J., Martinson, D. G., McIntyre, A., Mix, A. C., Molfino, B., Morley, J. J., Peterson, L. C., Pisias, N. G., Prell, W. L., Raymo, M. E., Shackleton, N. J., & Toggweiler, J. R. (1993). On the structure and origin of major glaciation cycles 2. The 100,000-year cycle. *Paleoceanography*, **8**, 699–735.

Imbrie, J., Boyle, E. A., Clemens, S. C., Duffy, A., Howard, W. R., Kukla, G., Kutzbach, J., Martinson, D. G., McIntyre, A., Mix, A. C., Molfino, B., Morley, J. J., Peterson, L. C., Pisias, N. G., Prell, W. L., Raymo, M. E., Shackleton, N. J., & Toggweiler, J. R. (1992). On the Structure and Origin of Major Glaciation Cycles 1. Linear Responses to Milankovitch Forcing. *Paleoceanography*, **7**, 701–738.

IPCC. (2001). IPCC Third Assessment Report: Climate Change 2001. Geneva, IPCC.

IPCC. (2018). *Global Warming of 1.5°C. An IPCC Special Report on the impacts of global warming of 1.5°C above pre-industrial levels and related global greenhouse gas emission pathways, in the context of strengthening the global response to the threat of climate change* (P. Masson-DelmotteV., H.-O. Zhai, D. Pörtner, J. Roberts, P. Skea, A. Shukla, W. Pirani, C. Moufouma-Okia, R. P. Péan, S. Connors, B. Matthews, Y. Chen, X. Zhou, M. Gomis, E. Lonnoy, T. Maycock, M. Tignor, & T. Waterfield, Eds.; tech. rep.). Geneva, World Meteorological Organization.

Jackson, L. C., & Wood, R. A. (2018). Timescales of AMOC decline in response to fresh water forcing. *Climate Dynamics*, **51**, 1333–1350.

Jackson, R. B., Le Quéré, C., Andrew, R. M., Canadell, J. G., Korsbakken, J. I., Liu, Z., Peters, G. P., & Zheng, B. (2018). Global energy growth is outpacing decarbonization. *Environmental Research Letters*, **13**, 120401.

Jansen, E., Raymo, M. E., Blum, P., & leg 162, S. S. P. (1996). *Initial Reports ODP Leg 162* (tech. rep.). Ocean Drilling Program. College Station,TX.

Jansen, E., Fronval, T., Rack, F., & Channell, J. E. T. (2000). Pliocene-Pleistocene ice rafting history and cyclicity in the Nordic Seas during the last 3.5 Myr. *Paleoceanography*, **15**, 709–721.

Johnsen, S. J., Clausen, H. B., Dansgaard, W., Gundestrup, N. S., Hammer, C. U., Andersen, U., Andersen, K. K., Hvidberg, C. S., Dahl-Jensen, D., Steffensen, J. P., Shoji, H., Sveinbjörnsdóttir, Á. E., White, J., Jouzel, J., & Fisher, D. (1997). The $\delta$ 18 O record along the Greenland Ice Core Project deep ice core and the problem of possible Eemian climatic instability. *Journal of Geophysical Research: Oceans*, **102**, 26397–26410.

Jouzel, J., Masson-Delmotte, V., Cattani, O., Dreyfus, G., Falourd, S., Hoffmann, G., Minster, B., Nouet, J., Barnola, J. M., Chappellaz, J., Fischer, H., Gallet, J. C., Johnsen, S., Leuenberger, M., Loulergue, L., Luethi, D., Oerter, H., Parrenin, F., Raisbeck, G., … Wolff, E. W. (2007). Orbital and millennial antarctic climate variability over the past 800,000 years. *Science*, **317**, 793–796.

Karas, C., Nürnberg, D., Bahr, A., Groeneveld, J., Herrle, J. O., Tiedemann, R., & Demenocal, P. B. (2017). Pliocene oceanic seaways and global climate. *Scientific Reports*, **7**.

Kasper, S., Van Der Meer, M. T., Mets, A., Zahn, R., Sinninghe Damsté, J. S., & Schouten, S. (2014). Salinity changes in the Agulhas leakage area recorded by stable hydrogen isotopes of C37 alkenones during Termination i and II. *Climate of the Past*, **10**, 251–260.

Katz, M. E., Miller, K. G., Wright, J. D., Wade, B. S., Browning, J. V., Cramer, B. S., & Rosenthal, Y. (2008). Stepwise transition from the Eocene greenhouse to the Oligocene icehouse. *Nature Geoscience*, **1**, 329–334.

Kellogg, W. W. (1983). Feedback mechanisms in the climate system affecting future levels of carbon dioxide. *Journal of Geophysical Research*, **88**, 1263.

Kemp, A. E., Grigorov, I., Pearce, R. B., & Naveira Garabato, A. C. (2010). Migration of the Antarctic Polar Front through the mid-Pleistocene transition: Evidence and climatic implications. *Quaternary Science Reviews*.

Kender, S., Ravelo, A. C., Worne, S., Swann, G. E., Leng, M. J., Asahi, H., Becker, J., Detlef, H., Aiello, I. W., Andreasen, D., & Hall, I. R. (2018). Closure of the Bering Strait caused Mid-Pleistocene Transition cooling. *Nature Communications*, **9**.

Kennett, J. P. (1977). Cenozoic evolution of Antarctic glaciation, the circum-Antarctic Ocean, and their impact on global paleoceanography. *Journal of Geophysical Research*, **82**, 3843–3860.

Kerr, R., Dotto, T. S., Mata, M. M., & Hellmer, H. H. (2018). Three decades of deep water mass investigation in the Weddell Sea (1984–2014): Temporal variability and changes. *Deep-Sea Research Part II: Topical Studies in Oceanography*, **149**, 70–83.

Kersten, F. (2012). Ocean acidification and the "short term" marine carbon cycle - IEDRO.

Khatiwala, S., Schmittner, A., & Muglia, J. (2019). Air-sea disequilibrium enhances ocean carbon storage during glacial periods. *Science Advances*, **5**.

Kiefer, T., McCave, I. N., & Elderfield, H. (2006). Antarctic control on tropical Indian Ocean sea surface temperature and hydrography. *Geophysical Research Letters*, **33**, L24612.

Klaus, J. S., Meeder, J. F., McNeill, D. F., Woodhead, J. F., & Swart, P. K. (2017). Expanded Florida reef development during the mid-Pliocene warm period. *Global and Planetary Change*.

Klochko, K., Kaufman, A. J., Yao, W., Byrne, R. H., & Tossell, J. A. (2006). Experimental measurement of boron isotope fractionation in seawater. *Earth and Planetary Science Letters*, **248**, 276–285.

Knorr, G., & Lohmann, G. (2003). Southern ocean origin for the resumption of Atlantic thermohaline circulation during deglaciation. *Nature*.

Kochhann, K. G. D., Holbourn, A., Kuhnt, W., Channell, J. E. T., Lyle, M., Shackford, J. K., Wilkens, R. H., & Andersen, N. (2016). Eccentricity pacing of eastern equatorial Pacific carbonate dissolution cycles during the Miocene Climatic Optimum. *Paleoceanography*, **31**, 1176–1192.

Köhler, P., Knorr, G., & Bard, E. (2014). Permafrost thawing as a possible source of abrupt carbon release at the onset of the Bølling/Allerød. *Nature Communications*, **5**.

Komhyr, W. D., Harris, T. B., Waterman, L. S., Chin, J. F. S., & Thoning, K. W. (1989). Atmospheric carbon dioxide at Mauna Loa Observatory: 1. NOAA global monitoring for climatic change measurements with a nondispersive infrared analyzer, 1974-1985. *Journal of Geophysical Research: Atmospheres*, **94**, 8533–8547.

Lambert, F., Delmonte, B., Petit, J. R., Bigler, M., Kaufmann, P. R., Hutterli, M. A., Stocker, T. F., Ruth, U., Steffensen, J. P., & Maggi, V. (2008). Dust - Climate couplings over the past 800,000 years from the EPICA Dome C ice core. *Nature*, **452**, 616–619.

Laskar, J., Joutel, F., & Robutel, P. (1993). Stabilization of the Earth's obliquity by the Moon. *Nature*, **361**, 615–617.

Laskar, J., Robutel, P., Joutel, F., Gastineau, M., Correia, A. C. M., & Levrard, B. (2004). A long-term numerical solution for the insolation quantities of the Earth. *Astronomy & Astrophysics*, **428**, 261–285.

Lawrence, K. T., Sosdian, S., White, H. E., & Rosenthal, Y. (2010). North Atlantic climate evolution through the Plio-Pleistocene climate transitions. *Earth and Planetary Science Letters*, **300**, 329–342.

Lawrence, K. T., Herbert, T. D., Brown, C. M., Raymo, M. E., & Haywood, A. M. (2009). High-amplitude variations in north atlantic sea surface temperature during the early pliocene warm period. *Paleoceanography*, **24**.

LBH. (2019). Weight Conversion Tables.

Le Bars, D., Dijkstra, H. A., & De Ruijter, W. P. M. (2013). Impact of the Indonesian Throughflow on Agulhas leakage. *Ocean Science*, **9**, 773–785.

Lea, D. W., Pak, D. K., & Spero, H. J. (2000). Climate impact of late quaternary equatorial Pacific sea surface temperature variations. *Science*, **289**, 1719–1724.

Lea, D. W., & Spero, H. J. (1992). Experimental determination of barium uptake in shells of the planktonic foraminifera Orbulina universa at 22°C. *Geochimica et Cosmochimica Acta*, **56**, 2673–2680.

Lear, C. H., Elderfield, H., & Wilson, P. A. (2003). A Cenozoic seawater Sr/Ca record from benthic foraminiferal calcite and its application in determining global weathering fluxes. *Earth and Planetary Science Letters*, **208**, 69–84.

Lear, C. H., Billups, K., Rickaby, R. E., Diester-Haass, L., Mawbey, E. M., & Sosdian, S. M. (2016). Breathing more deeply: Deep ocean carbon storage during the mid-Pleistocene climate transition. *Geology*, **44**, 1035–1038.

Lee, K., Tong, L. T., Millero, F. J., Sabine, C. L., Dickson, A. G., Goyet, C., Park, G.-H., Wanninkhof, R., Feely, R. A., & Key, R. M. (2006). Global relationships of total alkalinity with salinity and temperature in surface waters of the world's oceans. *Geophysical Research Letters*, **33**, L19605.

LeGrande, A. N., & Schmidt, G. A. (2006). Global gridded data set of the oxygen isotopic composition in seawater. *Geophysical Research Letters*, **33**, L12604.

Lenton, T. M., Livina, V. N., Dakos, V., Van Nes, E. H., & Scheffer, M. (2012). Early warning of climate tipping points from critical slowing down: Comparing methods to improve robustness. *Philosophical Transactions of the Royal Society A: Mathematical, Physical and Engineering Sciences*.

Lenton, T. M. (2011). Early warning of climate tipping points.

Lenton, T. M., Myerscough, R. J., Marsh, R., Livina, V. N., Price, A. R., & Cox, S. J. (2009). Using GENIE to study a tipping point in the climate system. *Philosophical Transactions of the Royal Society A: Mathematical, Physical and Engineering Sciences*.

Linsley, B. K., Rosenthal, Y., & Oppo, D. W. (2010). Holocene evolution of the Indonesian throughflow and the western Pacific warm pool. *Nature Geoscience*, **3**, 578–583.

Lisiecki, L. E. (2010). Links between eccentricity forcing and the 100,000-year glacial cycle. *Nature Geoscience*, **3**, 349–352.

Lisiecki, L. E., & Raymo, M. E. (2005). A Pliocene-Pleistocene stack of 57 globally distributed benthic $\delta$ 18O records. *Paleoceanography*.

Lisiecki, L. E., & Raymo, M. E. (2007). Plio-Pleistocene climate evolution: trends and transitions in glacial cycle dynamics. *Quaternary Science Reviews*, **26**, 56–69.

Littler, K., Robinson, S. A., Bown, P. R., Nederbragt, A. J., & Pancost, R. D. (2011). High sea-surface temperatures during the Early Cretaceous Epoch. *Nature Geoscience*, **4**, 169–172.

Liu, Z., Otto-Bliesner, B. L., He, F., Brady, E. C., Tomas, R., Clark, P. U., Carlson, A. E., Lynch-Stieglitz, J., Curry, W., Brook, E., Erickson, D., Jacob, R., Kutzbach, J., & Cheng, J. (2009). Transient simulation of last deglaciation with a new mechanism for bolling-allerod warming. *Science*, **325**, 310–314.

Lohmann, G. P. (1995). A model for variation in the chemistry of planktonic foraminifera due to secondary calcification and selective dissolution. *Paleoceanography*, **10**, 445–457.

Longhurst, A. (1995). Seasonal cycles of pelagic production and consumption.

Loveday, B. R., Durgadoo, J. V., Reason, C. J., Biastoch, A., & Penven, P. (2014). Decoupling of the Agulhas leakage from the Agulhas Current. *Journal of Physical Oceanography*, **44**, 1776–1797.

Lüthi, D., Le Floch, M., Bereiter, B., Blunier, T., Barnola, J.-M., Siegenthaler, U., Raynaud, D., Jouzel, J., Fischer, H., Kawamura, K., & Stocker, T. F. (2008). High-resolution carbon dioxide concentration record 650,000–800,000 years before present. *Nature*, **453**, 379.

Lutjeharms, J. R. (2006). Sources of the Agulhas Current. In *The agulhas current* (pp. 53–90). Springer Verlag.

Lynch-Stieglitz, J., Stocker, T. F., Broecker, W. S., & Fairbanks, R. G. (1995). The influence of air-sea exchange on the isotopic composition of oceanic carbon: Observations and modeling. *Global Biogeochemical Cycles*, **9**, 653–665.

MacDonald, G. J. (1990). Role of methane clathrates in past and future climates. *Climatic Change*, **16**, 247–281.

Mackenzie, F., & Mackenzie, J. (1995). Our changing planet. NJ, Prentice-Hall, Upper Saddle River.

Mann, M. E. (2016). The Hockey Stick and the Climate Wars. Columbia University Press.

Mann, M. E., Bradley, R. S., & Hughes, M. K. (1999). Northern hemisphere temperatures during the past millennium: Inferences, uncertainties, and limitations. *Geophysical Research Letters*, **26**, 759–762.

Marcott, S. A., Bauska, T. K., Buizert, C., Steig, E. J., Rosen, J. L., Cuffey, K. M., Fudge, T. J., Severinghaus, J. P., Ahn, J., Kalk, M. L., McConnell, J. R., Sowers, T., Taylor, K. C., White, J. W., & Brook, E. J. (2014). Centennial-scale changes in the global carbon cycle during the last deglaciation. *Nature*, **514**, 616–619.

Marcott, S. A., Shakun, J. D., Clark, P. U., & Mix, A. C. (2013). A reconstruction of regional and global temperature for the past 11,300 years. *Science*, **339**, 1198–1201.

Marino, G., Zahn, R., Ziegler, M., Purcell, C., Knorr, G., Hall, I. R., Ziveri, P., & Elderfield, H. (2013). Agulhas salt-leakage oscillations during abrupt climate changes of the Late Pleistocene. *Paleoceanography*, **28**, 599–606.

Martin, J. B. (2017). Carbonate minerals in the global carbon cycle. *Chemical Geology*, **449**, 58–72.

Martínez-Botí, M. A., Foster, G. L., Chalk, T. B., Rohling, E. J., Sexton, P. F., Lunt, D. J., Pancost, R. D., Badger, M. P., & Schmidt, D. N. (2015). Plio-Pleistocene climate sensitivity evaluated using high-resolution CO2 records. *Nature*.

Martínez-Garcia, A., Rosell-Melé, A., Jaccard, S. L., Geibert, W., Sigman, D. M., & Haug, G. H. (2011). Southern Ocean dust-climate coupling over the past four million years. *Nature*, **476**, 312–315.

Martínez-García, A., Sigman, D. M., Ren, H., Anderson, R. F., Straub, M., Hodell, D. A., Jaccard, S. L., Eglinton, T. I., & Haug, G. H. (2014). Iron fertilization of the subantarctic ocean during the last ice age. *Science*, **343**, 1347–1350.

Martinez-Mendez, G., Zahn, R., Hall, I. R., Peeters, F. J., Pena, L. D., Cacho, I., & Negre, C. (2010). Contrasting multiproxy reconstructions of surface ocean hydrography in the Agulhas Corridor and implications for the Agulhas Leakage during the last 345,000 years. *Paleoceanography*, **25**.

Mason, E., Edmonds, M., & Turchyn, A. V. (2017). Remobilization of crustal carbon may dominate volcanic arc emissions. *Science*, **357**, 290–294.

McCave, I. N., Manighetti, B., & Beveridge, N. A. (1995). Circulation in the glacial North Atlantic inferred from grain-size measurements. *Nature*, **374**, 149–152.

McClymont, E. L., Sosdian, S. M., Rosell-Melé, A., & Rosenthal, Y. (2013). Pleistocene sea-surface temperature evolution: Early cooling, delayed glacial intensification, and implications for the mid-Pleistocene climate transition.

Medina-Elizalde, M., & Lea, D. W. (2005a). The mid-pleistocene transition in the tropical pacific. *Science*, **310**, 1009–1012.

Medina-Elizalde, M., & Lea, D. W. (2005b). The mid-pleistocene transition in the tropical pacific. *Science*, **310**, 1009–1012.

Meyers, S. R., & Hinnov, L. A. (2010). Northern Hemisphere glaciation and the evolution of Plio-Pleistocene climate noise. *Paleoceanography*, **25** doi: 10.1029/2009PA001834.

Milankovic, M. (1930). Mathematische Klimalehre und astronomische Theorie der Klimaschwankungen. Berlin, Gebrüder Borntraeger.

Milankovic, M. (1941). Kanon der Erdbestrahlung und seine Anwendung auf das Eiszeitenproblem. Belgrade, Milhaila Curcica.

Misra, S., Owen, R., Kerr, J., Greaves, M., & Elderfield, H. (2014). Determination of d11B by HR-ICP-MS from mass limited samples: Application to natural carbonates and water samples. *Geochimica et Cosmochimica Acta*, **140**, 531–552.

Mix, A., Le, J., & Shackleton, N. (1995). *43. BENTHIC FORAMINIFERAL STABLE ISOTOPE STRATIGRAPHY OF SITE 846: 0-1.8 MA 1* (tech. rep.).

Monnin, E., Indermühle, A., Dällenbach, A., Flückiger, J., Stauffer, B., Stocker, T. F., Raynaud, D., & Barnola, J. M. (2001). Atmospheric CO2 concentrations over the last glacial termination. *Science*, **291**, 112–114.

Mooney, C. (2013). The Hockey Stick: The Most Controversial Chart in Science, Explained - The Atlantic.

Mukhin, D., Gavrilov, A., Loskutov, E., Kurths, J., & Feigin, A. (2019). Bayesian Data Analysis for Revealing Causes of the Middle Pleistocene Transition. *Scientific Reports*.

Najafpour, M. M., Hou, H. J., & Allakhverdiev, S. I. (2017). Photosynthesis: Natural nanomachines toward energy and food production. In *Photosynthesis: Structures, mechanisms, and applications* (pp. 1–9). Springer International Publishing.

NASA. (n.d.). The GLOBE Program.gov.

NGRIP. (2004). *High-resolution record of Northern Hemisphere climate extending into the last interglacial period North Greenland Ice Core Project members** (tech. rep.).

Nicholls, K. W., Østerhus, S., Makinson, K., Gammelsrød, T., & Fahrbach, E. (2009). Ice-ocean processes over the continental shelf of the Southern Weddell Sea, Antarctica: A review. John Wiley & Sons, Ltd.

Nyman, K. H., & Ditlevsen, P. D. (2019). The middle Pleistocene transition by frequency locking and slow ramping of internal period. *Climate Dynamics*, **53**, 3023–3038.

Obura, D. O., Bandeira, S. O., Bodin, N., Burgener, V., Braulik, G., Chassot, E., Gullström, M., Kochzius, M., Nicoll, M., Osuka, K., Ralison, H. O., Richmond, M., Samoilys, M. A., Scheren, P., & Ternon, J. F. (2019). The Northern mozambique channel. In *World seas: An environmental evaluation volume ii: The indian ocean to the pacific* (pp. 75–99). Elsevier.

O'Dea, A., Lessios, H. A., Coates, A. G., Eytan, R. I., Restrepo-Moreno, S. A., Cione, A. L., Collins, L. S., De Queiroz, A., Farris, D. W., Norris, R. D., Stallard, R. F., Woodburne, M. O., Aguilera, O., Aubry, M. P., Berggren, W. A., Budd, A. F., Cozzuol, M. A., Coppard, S. E., Duque-Caro, H., … Jackson, J. B. (2016). Formation of the Isthmus of Panama. American Association for the Advancement of Science.

Oil&Gas Journal. (2001). Dialogue on Global Warming: Inadequate science leaves climate debate subject to political expediency | Oil & Gas Journal.

Orr, J. C., Fabry, V. J., Aumont, O., Bopp, L., Doney, S. C., Feely, R. A., Gnanadesikan, A., Gruber, N., Ishida, A., Joos, F., Key, R. M., Lindsay, K., Maier-Reimer, E., Matear, R., Monfray, P., Mouchet, A., Najjar, R. G., Plattner, G. K., Rodgers, K. B., … Yool, A. (2005). Anthropogenic ocean acidification over the twenty-first century and its impact on calcifying organisms. *Nature*, **437**, 681–686.

Pagani, M., Huber, M., Liu, Z., Bohaty, S. M., Henderiks, J., Sijp, W., Krishnan, S., & DeConto, R. M. (2011). The role of carbon dioxide during the onset of antarctic glaciation. *Science*, **334**, 1261–1264.

Pagani, M., Zachos, J. C., Freeman, K. H., Tipple, B., & Bohaty, S. (2005). Atmospheric science: Marked decline in atmospheric carbon dioxide concentrations during the Paleogene. *Science*, **309**, 600–603.

Paillard, D. (1998). The timing of Pleistocene glaciations from a simple multiple-state climate model. *Nature*, **391**, 378–381.

Park, R., & Epstein, S. (1961). *Metabolic Fractionation of C 13 &C 12 in Plants* (tech. rep.).

P-co2.org. (n.d.). Data — Palaeo-CO2.

Pearson, P. N. (2012). Oxygen Isotopes in Foraminifera: Overview and Historical Review. *The Paleontological Society Papers*, **18**, 1–38.

Pearson, P. N., & Burgess, C. E. (2008). Foraminifer test preservation and diagenesis: Comparison of high latitude Eocene sites. *Geological Society Special Publication*, **303**, 59–72.

Pearson, P. N., Foster, G. L., & Wade, B. S. (2009). Atmospheric carbon dioxide through the Eocene-Oligocene climate transition. *Nature*, **461**, 1110–1113.

Pedro, J. B., Bostock, H. C., Bitz, C. M., He, F., Vandergoes, M. J., Steig, E. J., Chase, B. M., Krause, C. E., Rasmussen, S. O., Markle, B. R., & Cortese, G. (2016). The spatial extent and dynamics of the Antarctic Cold Reversal. *Nature Geoscience*, **9**, 51–55.

Peeters, F. J., Acheson, R., Brummer, G. J. A., De Ruijter, W. P., Schneider, R. R., Ganssen, G. M., Ufkes, E., & Kroon, D. (2004). Vigorous exchange between the Indian and Atlantic oceans at the end of the past five glacial periods. *Nature*, **430**, 661–665.

Pena, L. D., & Goldstein, S. L. (2014). Thermohaline circulation crisis and impacts during the mid-Pleistocene transition. *Science*, **345**, 318–322.

Petit, J. R., Jouzel, J., Raynaud, D., Barkov, N. I., Barnola, J. M., Basile, I., Bender, M., Chappellaz, J., Davis, M., Delaygue, G., Delmotte, M., Kotiyakov, V. M., Legrand, M., Lipenkov, V. Y., Lorius, C., Pépin, L., Ritz, C., Saltzman, E., & Stievenard, M. (1999). Climate and atmospheric history of the past 420,000 years from the Vostok ice core, Antarctica.

Petrick, B., Martínez-García, A., Auer, G., Reuning, L., Auderset, A., Deik, H., Takayanagi, H., De Vleeschouwer, D., Iryu, Y., & Haug, G. H. (2019). Glacial Indonesian Throughflow weakening across the Mid-Pleistocene Climatic Transition. *Scientific Reports*, **9**.

Petrick, B. F., McClymont, E. L., Marret, F., & van der Meer, M. T. J. (2015). Changing surface water conditions for the last 500 ka in the Southeast Atlantic: Implications for variable influences of Agulhas leakage and Benguela upwelling. *Paleoceanography*, **30**, 1153–1167.

Piotrowski, A. M., Galy, A., Nicholl, J. A. L., Roberts, N., Wilson, D. J., Clegg, J. A., & Yu, J. (2012). Reconstructing deglacial North and South Atlantic deep water sourcing using foraminiferal Nd isotopes. *Earth and Planetary Science Letters*, **357-358**, 289–297.

Plank, T., & Manning, C. E. (2019). Subducting carbon. Nature Publishing Group.

Poirier, R. K., & Billups, K. (2014). The intensification of northern component deepwater formation during the mid-Pleistocene climate transition. *Paleoceanography*, **29**, 1046–1061.

Project Berkeley Earth. (2014). Climate Science & Strategic Anlysis.

Quan, C., Sun, C., Sun, Y., & Sun, G. (2009). High resolution estimates of paleo-CO2 levels through the Campanian (Late Cretaceous) based on Ginkgo cuticles. *Cretaceous Research*, **30**, 424–428.

Quinn, C., Sieber, J., von der Heydt, A. S., & Lenton, T. M. (2018). The Mid-Pleistocene Transition induced by delayed feedback and bistability. *Dynamics and Statistics of the Climate System*, **3**.

Rae, J. W., Burke, A., Robinson, L. F., Adkins, J. F., Chen, T., Cole, C., Greenop, R., Li, T., Littley, E. F., Nita, D. C., Stewart, J. A., & Taylor, B. J. (2018). CO 2 storage and release in the deep Southern Ocean on millennial to centennial timescales. Nature Publishing Group.

Rae, J. W. B. (2018). Boron Isotopes in Foraminifera: Systematics, Biomineralisation, and CO2 Reconstruction. In H. Marschall & G. Foster (Eds.), *Boron isotopes: The fifth element* (pp. 107–143). Cham, Springer International Publishing.

Rae, J. W. B., Sarnthein, M., Foster, G. L., Ridgwell, A., Grootes, P. M., & Elliott, T. (2014). Deep water formation in the North Pacific and deglacial CO 2 rise. *Paleoceanography*, **29**, 645–667.

Rahmstorf, S. (2002). Ocean circulation and climate during the past 120,000 years.

Ravelo, A. C., & Andreasen, D. H. (2000). Enhanced circulation during a warm period. *Geophysical Research Letters*.

Raymo, M. E. (1997). The timing of major climate terminations. *Paleoceanography*, **12**, 577–585.

Raymo, M. E., Oppo, D. W., Flower, B. P., Hodell, D. A., McManus, J. F., Venz, K. A., Kleiven, K. F., & McIntyre, K. (2004). Stability of North Atlantic water masses in face of pronounced climate variability during the Pleistocene. *Paleoceanography*, **19**.

Raymo, M. E., & Nisancioglu, K. H. (2003). The 41 kyr world: Milankovitch's other unsolved mystery. *Paleoceanography*, **18**, n/a–n/a.

Raynaud, D., Barnola, J. M., Souchez, R., Lorrain, R., Petit, J. R., Duval, P., & Lipenkov, V. Y. (2005). Palaeoclimatology: The record for marine isotopic stage 11. *Nature*, **436**, 39–40.

Redfield, A. C. (1934). On the Proportions of Organic Derivatives in Sea Water and Their Relation to the Composition of Plankton. University Press of Liverpool.

Rial, J. A., Oh, J., & Reischmann, E. (2013). Synchronization of the climate system to eccentricity forcing and the 100,000-year problem. *Nature Geoscience*, **6**, 289–293.

Ridgwell, A. J., Watson, A. J., & Raymo, M. E. (1999). Is the spectral signature of the 100 kyr glacial cycle consistent with a Milankovitch origin? *Paleoceanography*, **14**, 437–440.

Ritz, S. P., Stocker, T. F., Grimalt, J. O., Menviel, L., & Timmermann, A. (2013). Estimated strength of the Atlantic overturning circulation during the last deglaciation. *Nature Geoscience*, **6**, 208–212.

Robinson, R. S., Jones, C. A., Kelly, R. P., Rafter, P., Etourneau, J., & Martinez, P. (2019). A Cool, Nutrient-Enriched Eastern Equatorial Pacific During the Mid-Pleistocene Transition. *Geophysical Research Letters*, **46**, 2187–2195.

Robock, A. (1985). An updated climate feedback diagram. *Bulletin - American Meteorological Society*, **66**, 786–787.

Rodgers, K. B., Latif, M., & Legutke, S. (2000). Sensitivity of equatorial Pacific and Indian Ocean watermasses to the position of the Indonesian Throughflow. *Geophysical Research Letters*, **27**, 2941–2944.

Rosenthal, Y., Lohmann, G. P., Lohmann, K. C., & Sherrell, R. M. (2000). Incorporation and preservation of Mg in Globigerinoides sacculifer: implications for reconstructing the temperature and 18 O/ 16 O of seawater. *Paleoceanography*, **15**, 135–145.

Rosenthal, Y., & Boyle, E. A. (1993). Factors controlling the fluoride content of planktonic foraminifera: An evaluation of its paleoceanographic applicability. *Geochimica et Cosmochimica Acta*, **57**, 335–346.

Rosenthal, Y., Boyle, E. A., & Slowey, N. (1997). Temperature control on the incorporation of magnesium, strontium, fluorine, and cadmium into benthic foraminiferal shells from Little Bahama Bank: Prospects for thermocline paleoceanography. *Geochimica et Cosmochimica Acta*, **61**, 3633–3643.

Rostek, F., Bard, E., Beaufort, L., Sonzogni, C., & Ganssen, G. (1997). Sea surface temperature and productivity records for the last 240 kyr on the Arabian Sea. *Deep-Sea Research Part II: Topical Studies in Oceanography*, **44**, 1461–1480.

Rouault, M., Penven, P., & Pohl, B. (2009). Warming in the Agulhas Current system since the 1980's. *Geophysical Research Letters*, **36**, L12602.

Roy, M., Clark, P. U., Raisbeck, G. M., & Yiou, F. (2004). Geochemical constraints on the regolith hypothesis for the middle Pleistocene transition. *Earth and Planetary Science Letters*, **227**, 281–296.

Royer, D. L., Berner, R. A., & Park, J. (2007). Climate sensitivity constrained by CO2 concentrations over the past 420 million years. *Nature*, **446**, 530–532.

Royer, D. L., Berner, Robert, A., Montanez, I. P., Tabor, N. J., & Beerling, D. J. (2004). CO2 as a primary driver of Phanerozoic climate. *GSA today*, **14**, 4–10.

Rutberg, R. L., Hemming, S. R., & Goldstein, S. L. (2000). Reduced North Atlantic Deep Water flux to the glacial Southern Ocean inferred from neodymium isotope ratios. *Nature*, **405**, 935–938.

Sætre, R., & Da Silva, A. (1982). Water masses and circulation of the Mozambique Channel.

Sanyal, A., Hemming, N. G., Broecker, W. S., Lea, D. W., Spero, H. J., & Hanson, G. N. (1996). Oceanic pH control on the boron isotopic composition of foraminifera: Evidence from culture experiments. *Paleoceanography*, **11**, 513–517.

Saraswat, R., Lea, D. W., Nigam, R., Mackensen, A., & Naik, D. K. (2013). Deglaciation in the tropical Indian Ocean driven by interplay between the regional monsoon and global teleconnections. *Earth and Planetary Science Letters*, **375**, 166–175.

Schefuß, E., Sinninghe Damsté, J. S., & Jansen, J. H. (2004). Forcing of tropical Atlantic sea surface temperatures during the mid-Pleistocene transition. *Paleoceanography*, **19**, 1–12.

Schmidt, G., & Ramstorf, S. (2005). Scientists respond to Barton.

Schmidt, M. W., & Lynch-Stieglitz, J. (2011). Florida Straits deglacial temperature and salinity change: Implications for tropical hydrologic cycle variability during the Younger Dryas. *Paleoceanography*, **26**.

Schmitt, J., Schneider, R., Elsig, J., Leuenberger, D., Lourantou, A., Chappellaz, J., Köhler, P., Joos, F., Stocker, T. F., Leuenberger, M., & Fischer, H. (2012). Carbon isotope constraints on the deglacial CO2 rise from ice cores. *Science*, **336**, 711–714.

Schuur, E. A., McGuire, A. D., Schädel, C., Grosse, G., Harden, J. W., Hayes, D. J., Hugelius, G., Koven, C. D., Kuhry, P., Lawrence, D. M., Natali, S. M., Olefeldt, D., Romanovsky, V. E., Schaefer, K., Turetsky, M. R., Treat, C. C., & Vonk, J. E. (2015). Climate change and the permafrost carbon feedback. Nature Publishing Group.

Schuur, E. A. G., Bockheim, J., Canadell, J. G., Euskirchen, E., Field, C. B., Goryachkin, S. V., Hagemann, S., Kuhry, P., Lafleur, P. M., Lee, H., Mazhitova, G., Nelson, F. E., Rinke, A., Romanovsky, V. E., Shiklomanov, N., Tarnocai, C., Venevsky, S., Vogel, J. G., & Zimov, S. A. (2008). Vulnerability of Permafrost Carbon to Climate Change: Implications for the Global Carbon Cycle. *BioScience*, **58**, 701–714.

Seki, O., Foster, G. L., Schmidt, D. N., Mackensen, A., Kawamura, K., & Pancost, R. D. (2010). Alkenone and boron-based Pliocene pCO2 records. *Earth and Planetary Science Letters*, **292**, 201–211.

Sexton, P. F., Wilson, P. A., & Pearson, P. N. (2006). Microstructural and geochemical perspectives on planktic foraminiferal preservation: "Glassy" versus "Frosty". *Geochemistry, Geophysics, Geosystems*, **7**, n/a–n/a.

Shackleton, N. J. (1987). Oxygen isotopes, ice volume and sea level. *Quaternary Science Reviews*, **6**, 183–190.

Shakun, J. D., Clark, P. U., He, F., Marcott, S. A., Mix, A. C., Liu, Z., Otto-Bliesner, B., Schmittner, A., & Bard, E. (2012). Global warming preceded by increasing carbon dioxide concentrations during the last deglaciation. *Nature*, **484**, 49–54.

Shao, J., Stott, L. D., Gray, W. R., Greenop, R., Pecher, I., Neil, H. L., Coffin, R. B., Davy, B., & Rae, J. W. (2019). Atmosphere-Ocean CO2 Exchange Across the Last Deglaciation From the Boron Isotope Proxy. *Paleoceanography and Paleoclimatology*.

Shapley, P. (2010). The Geological Carbon Cycle.

Shepard, D. (2018). Global warming: severe consequences for Africa | Africa Renewal.

Sheppard, K. (2011). Climategate: What Really Happened? – Mother Jones.

Siddall, M., Rohling, E. J., Blunier, T., & Spahni, R. (2010). Patterns of millennial variability over the last 500 ka. *Climate of the Past*, **6**, 295–303.

Siegenthaler, U., Stocker, T. F., Monnin, E., Lüthi, D., Schwander, J., Stauffer, B., Raynaud, D., Barnola, J. M., Fischer, H., Masson-Delmotte, V., & Jouzel, J. (2005). Atmospheric science: Stable carbon cycle-climate relationship during the late pleistocene. *Science*, **310**, 1313–1317.

Sigman, D. M., & Hain, M. P. (2012). The Biological Productivity of the Ocean. *Nature Education Knowledge*, **3**, 21.

Sigman, D. M., & Boyle, E. A. (2000). Glacial/interglacial variations in atmospheric carbon dioxide.

Sigman, D. M., Hain, M. P., & Haug, G. H. (2010). The polar ocean and glacial cycles in atmospheric CO2 concentration.

Simon, M. H., Arthur, K. L., Hall, I. R., Peeters, F. J., Loveday, B. R., Barker, S., Ziegler, M., & Zahn, R. (2013). Millennial-scale Agulhas Current variability and its implications for salt-leakage through the Indian-Atlantic Ocean Gateway. *Earth and Planetary Science Letters*, **383**, 101–112.

Simon, M. H., Gong, X., Hall, I. R., Ziegler, M., Barker, S., Knorr, G., Meer, M. T. J., Kasper, S., & Schouten, S. (2015). Salt exchange in the Indian-Atlantic Ocean Gateway since the Last Glacial Maximum: A compensating effect between Agulhas Current changes and salinity variations? *Paleoceanography*, **30**, 1318–1327.

Skelton, P. W., Spicer, R. A., Kelley, S. P., & Gilmour, I. (2003). The Cretaceous World. Cambridge, Cambridge University Press.

Skinner, L. C., Fallon, S., Waelbroeck, C., Michel, E., & Barker, S. (2010). Ventilation of the deep southern ocean and deglacial CO2 rise. *Science*, **328**, 1147–1151.

Slater, A. G., & Lawrence, D. M. (2013). Diagnosing Present and Future Permafrost from Climate Models. *Journal of Climate*, **26**, 5608–5623.

Smetacek, V., Klaas, C., Strass, V. H., Assmy, P., Montresor, M., Cisewski, B., Savoye, N., Webb, A., D'Ovidio, F., Arrieta, J. M., Bathmann, U., Bellerby, R., Berg, G. M., Croot, P., Gonzalez, S., Henjes, J., Herndl, G. J., Hoffmann, L. J., Leach, H., … Wolf-Gladrow, D. (2012). Deep carbon export from a Southern Ocean iron-fertilized diatom bloom. *Nature*, **487**, 313–319.

Sorby, H. (1879). Structure and origin of limestones. *Proc. Geol. Soc. Lond.*, **35**, 56–95.

Sosdian, S., & Rosenthal, Y. (2009). Deep-sea temperature and ice volume changes across the pliocene-pleistocene climate transitions. *Science*.

Spero, H. J. (1998). Life History and Stable Isotope Geochemistry of Planktonic Foraminifera. *The Paleontological Society Papers*, **4**, 7–36.

Spezzaferri, S., Kucera, M., Pearson, P. N., Wade, B. S., Rappo, S., Poole, C. R., Morard, R., & Stalder, C. (2015). Fossil and Genetic Evidence for the Polyphyletic Nature of the Planktonic Foraminifera Globigerinoides, and Description of the New Genus Trilobatus (S. Abramovich, Ed.). *PLOS ONE*, **10**, e0128108.

Spooner, P. T., Thornalley, D. J. R., & Ellis, P. (2018). Grain Size Constraints on Glacial Circulation in the Southwest Atlantic. *Paleoceanography and Paleoclimatology*, **33**, 21–30.

Sprintall, J., Gordon, A. L., Koch-Larrouy, A., Lee, T., Potemra, J. T., Pujiana, K., & Wijffels, S. E. (2014). The Indonesian seas and their role in the coupled ocean-climate system. *Nature Geoscience*, **7**, 487–492.

Steffen, W., Grinevald, J., Crutzen, P., & Mcneill, J. (2011). The anthropocene: Conceptual and historical perspectives. Royal Society.

Stephens, B. B., & Keeling, R. F. (2000). The influence of antarctic sea ice on glacial-interglacial CO 2 variations. *Nature*, **404**, 171–174.

Stocker, T., Quin, D., Plattner, G. K., Tignor, M. M. B., Allen, S. K., Boschung, J., Nauels, A., Xia, Y., Bex, V., & Midgley, P. M. (2014). Climate change 2013: the physical science basis: Working Group I contribution to the Fifth assessment report of the Intergovernmental Panel on Climate Change. Cambridge University Press.

Stocker, T. F., & Johnsen, S. J. (2003). A minimum thermodynamic model for the bipolar seesaw. *Paleoceanography*, **18**, n/a–n/a.

Stocker, T. F., & Marchal, O. (2000). Abrupt climate change in the computer: Is it real?

Streletskiy, D., Anisimov, O., & Vasiliev, A. (2015). Chapter 10 - Permafrost Degradation. In J. F. Shroder, W. Haeberli, C. B. T. S. Whiteman Risks and Disasters, & I.-R. Hazards (Eds.). Boston, Academic Press.

Stuiver, M., Burk, R. L., & Quay, P. D. (1984). 13 C/ 12 C ratios in tree rings and the transfer of biospheric carbon to the atmosphere. *Journal of Geophysical Research*, **89**, 11731.

Stuiver, M., & Quay, P. (1981). Atmospheric14C changes resulting from fossil fuel CO2 release and cosmic ray flux variability. *Earth and Planetary Science Letters*, **53**, 349–362.

Stuiver, M., & Grootes, P. M. (2000). GISP2 oxygen isotope ratios. *Quaternary Research*, **53**, 277–284.

Sun, Y., Yin, Q., Crucifix, M., Clemens, S. C., Araya-Melo, P., Liu, W., Qiang, X., Liu, Q., Zhao, H., Liang, L., Chen, H., Li, Y., Zhang, L., Dong, G., Li, M., Zhou, W., Berger, A., & An, Z. (2019). Diverse manifestations of the mid-Pleistocene climate transition. *Nature Communications*, **10**.

Sutter, J., Fischer, H., Grosfeld, K., Karlsson, N. B., Kleiner, T., Van Liefferinge, B., & Eisen, O. (2019). Modelling the Antarctic Ice Sheet across the mid-Pleistocene transition – implications for Oldest Ice. *The Cryosphere*, **13**, 2023–2041.

Takahashi, T., Sutherland, S. C., Chipman, D. W., Goddard, J. G., & Ho, C. (2014). Climatological distributions of pH, pCO2, total CO2, alkalinity, and CaCO3 saturation in the global surface ocean, and temporal changes at selected locations. *Marine Chemistry*, **164**, 95–125.

Talley, L. D. (2005). Deep expression of the Indonesian Throughflow: Indonesian Intermediate Water in the South Equatorial Current. *Journal of Geophysical Research*, **110**, C10009.

Tans, P., & Thoning, K. (2008). *NOAA ESRL Global Monitoring Division How we measure background CO 2 levels on Mauna Loa* (tech. rep.).

Tarasov, L., & Peltier, W. R. (2005). Arctic freshwater forcing of the Younger Dryas cold reversal. *Nature*, **435**, 662–665.

Tarduno, J. A., Brinkman, D. B., Renne, P. R., Cottrell, R. D., Scher, H., & Castillo, P. (1998). Evidence for extreme climatic warmth from late cretaceous arctic vertebrates. *Science*, **282**, 2241–2244.

The Open University. (n.d.). Week 7: The Special Ones: 2.2 The greenhouse effect - OpenLearn - Open University - EXO_1.

The Washington Post. (2019). Sea level rise is causing Miami to flood regularly from high tides - The Washington Post.

Thirumalai, K., DiNezio, P. N., Tierney, J. E., Puy, M., & Mohtadi, M. (2019). An El Niño Mode in the Glacial Indian Ocean? *Paleoceanography and Paleoclimatology*, **34**, 1316–1327.

Thoning, K. W., Tans, P. P., & Komhyr, W. D. (1989). Atmospheric carbon dioxide at Mauna Loa Observatory: 2. Analysis of the NOAA GMCC data, 1974-1985. *Journal of Geophysical Research: Atmospheres*, **94**, 8549–8565.

Thornalley, D. J., Bauch, H. A., Gebbie, G., Guo, W., Ziegler, M., Bernasconi, S. M., Barker, S., Skinner, L. C., & Yu, J. (2015). A warm and poorly ventilated deep Arctic Mediterranean during the last glacial period. *Science*, **349**, 706–710.

Thornalley, D. J. R., McCave, I. N., & Elderfield, H. (2010). Freshwater input and abrupt deglacial climate change in the North Atlantic. *Paleoceanography*, **25**.

Thornalley, D. J., Barker, S., Broecker, W. S., Elderfield, H., & McCave, I. N. (2011). The deglacial evolution of north atlantic deep convection. *Science*, **331**, 202–205.

Tierney, J. E., Haywood, A. M., Feng, R., Bhattacharya, T., & Otto-Bliesner, B. L. (2019). Pliocene Warmth Consistent With Greenhouse Gas Forcing. *Geophysical Research Letters*, **46**, 9136–9144.

Toggweiler, J. R. (1999). Variation of atmospheric CO 2 by ventilation of the ocean's deepest water. *Paleoceanography*, **14**, 571–588.

Toggweiler, J. R., Russell, J. L., & Carson, S. R. (2006). Midlatitude westerlies, atmospheric CO 2 , and climate change during the ice ages. *Paleoceanography*, **21**, n/a–n/a.

Trumbore, S. E., & Druffel, E. R. M. (1995). Carbon isotopes for characterizing sources and turnover of nonliving organic matter. In R. G. Zepp & C. ( Sonntag (Eds.), *The role of nonliving organic matter in the earth's carbon cycle : Report of the dahlem workshop on the role of nonliving organic matter in the earth's carbon cycle, berlin 1993, september 12-17* (pp. 7–22). J. Wiley.

Turetsky, M. R., Donahue, W. F., & Benscoter, B. W. (2011). Experimental drying intensifies burning and carbon losses in a northern peatland. *Nature Communications*, **2**.

Turnbull, J. C., Graven, H., & Krakauer, N. Y. (2016). Radiocarbon in the Atmosphere. In *Radiocarbon and climate change* (pp. 83–137). Cham, Springer International Publishing.

Turnbull, J., Rayner, P., Miller, J., Naegler, T., Ciais, P., & Cozic, A. (2009). On the use of 14 CO 2 as a tracer for fossil fuel CO 2 : Quantifying uncertainties using an atmospheric transport model. *Journal of Geophysical Research*, **114**, D22302.

Turnbull, J. C., Lehman, S. J., Miller, J. B., Sparks, R. J., Southon, J. R., & Tans, P. P. (2007). A new high precision 14 CO 2 time series for North American continental air. *Journal of Geophysical Research*, **112**, D11310.

Tzedakis, P. C., Crucifix, M., Mitsui, T., & Wolff, E. W. (2017). A simple rule to determine which insolation cycles lead to interglacials. *Nature*, **542**, 427–432.

Tziperman, E., Raymo, M. E., Huybers, P., & Wunsch, C. (2006). Consequences of pacing the Pleistocene 100 kyr ice ages by nonlinear phase locking to Milankovitch forcing. *Paleoceanography*, **21**.

Uemura, R., Motoyama, H., Masson-Delmotte, V., Jouzel, J., Kawamura, K., Goto-Azuma, K., Fujita, S., Kuramoto, T., Hirabayashi, M., Miyake, T., Ohno, H., Fujita, K., Abe-Ouchi, A., Iizuka, Y., Horikawa, S., Igarashi, M., Suzuki, K., Suzuki, T., & Fujii, Y. (2018). Asynchrony between Antarctic temperature and CO 2 associated with obliquity over the past 720,000 years. *Nature Communications*, **9**.

Ullgren, J. E., van Aken, H. M., Ridderinkhof, H., & de Ruijter, W. P. (2012). The hydrography of the Mozambique Channel from six years of continuous temperature, salinity, and velocity observations. *Deep-Sea Research Part I: Oceanographic Research Papers*, **69**, 36–50.

US Department of Commerce, NOAA, E. S. R. L. (n.d.-a). ESRL Global Monitoring Division - Global Greenhouse Gas Reference Network.

US Department of Commerce, NOAA, E. S. R. L. (n.d.-b). ESRL Global Monitoring Division - Global Greenhouse Gas Reference Network.

van de Wal, R. S. W., de Boer, B., Lourens, L. J., Köhler, P., & Bintanja, R. (2011). Reconstruction of a continuous high-resolution CO 2 record over the past 20 million years. *Climate of the Past*, **7**, 1459–1469.

Van Sebille, E., Barron, C. N., Biastoch, A., Van Leeuwen, P. J., Vossepoel, F. C., & De Ruijter, W. P. (2009a). Relating Agulhas leakage to the Agulhas Current retroflection location. *Ocean Science*, **5**, 511–521.

Van Sebille, E., Biastoch, A., Van Leeuwen, P. J., & De Ruijter, W. P. (2009b). A weaker Agulhas current leads to more Agulhas leakage. *Geophysical Research Letters*, **36**.

Veizer, J., Ala, D., Azmy, K., Bruckschen, P., Buhl, D., Bruhn, F., Garden, G. A., Diener, A., Ebneth, S., Godderis, Y., Jasper, T., Korte, C., Pawellek, F., Podlaha, O. G., & Strauss, H. (1999). 87 Sr/ 86 Sr, $\delta$ 13 C and $\delta$ 18 O evolution of Phanerozoic seawater. *Chemical Geology*, **161**, 59–88.

Visconti, G. (2016). Fundamentals: Thermodynamics of the Atmosphere. In *Fundamentals of physics and chemistry of the atmosphere* (pp. 1–35). Cham, Springer International Publishing.

WAIS. (2015). Precise interpolar phasing of abrupt climate change during the last ice age. *Nature*, **520**, 661–665
Buizert, Christo Adrian, Betty Ahn, Jinho Albert, Mary Alley, Richard B. Baggenstos, Daniel Bauska, Thomas K. Bay, Ryan C. Bencivengo, Brian B. Bentley, Charles R. Brook, Edward J. Chellman, Nathan J. Clow, Gary D. Cole-Dai, Jihong Conway, Howard Cravens, Eric Cuffey, Kurt M. Dunbar, Nelia W. Edwards, Jon S. Fegyveresi, John M. Ferris, Dave G. Fitzpatrick, Joan J. Fudge, T. J. Gibson, Chris J. Gkinis, Vasileios Goetz, Joshua J. Gregory, Stephanie Hargreaves, Geoffrey M. Iverson, Nels Johnson, Jay A. Jones, Tyler R. Kalk, Michael L. Kippenhan, Matthew J. Koffman, Bess G. Kreutz, Karl Kuhl, Tanner W. Lebar, Donald A. Lee, James E. Marcott, Shaun A. Markle, Bradley R. Maselli, Olivia J. McConnell, Joseph R. McGwire, Ken-

neth C. Mitchell, Logan E. Mortensen, Nicolai B. Neff, Peter D. Nishiizumi, Kunihiko Nunn, Richard M. Orsi, Anais J. Pasteris, Daniel R. Pedro, Joel B. Pettit, Erin C. Price, P. Buford Priscu, John C. Rhodes, Rachael H. Rosen, Julia L. Schauer, Andrew J. Schoenemann, Spruce W. Sendelbach, Paul J. Severinghaus, Jeffrey P. Shturmakov, Alexander J. Sigl, Michael Slawny, Kristina R. Souney, Joseph M. Sowers, Todd A. Spencer, Matthew K. Steig, Eric J. Taylor, Kendrick C. Twickler, Mark S. Vaughn, Bruce H. Voigt, Donald E. Waddington, Edwin D. Welten, Kees C. Wendricks, Anthony W. White, James W.C. Winstrup, Mai Wong, Gifford J. Woodruff, Thomas E.

Wang, Y., Cheng, H., Edwards, R. L., Kong, X., Shao, X., Chen, S., Wu, J., Jiang, X., Wang, X., & An, Z. (2008). Millennial- and orbital-scale changes in the East Asian monsoon over the past 224,000 years. *Nature*, **451**, 1090–1093.

Watson, A. J., Bakker, D. C., Ridgwell, A. J., Boyd, P. W., & Law, C. S. (2000). Effect of iron supply on Southern Ocean CO2 uptake and implications for glacial atmospheric CO2. *Nature*, **407**, 730–733.

Weldeab, S., Menke, V., & Schmiedl, G. (2014). The pace of East African monsoon evolution during the Holocene. *Geophysical Research Letters*, **41**, 1724–1732.

Weston, M. J. (2017). INFOGRAPHIC: How Climate Change Will Impact Taiwan - The News Lens International Edition.

Willeit, M., Ganopolski, A., Calov, R., & Brovkin, V. (2019). Mid-Pleistocene transition in glacial cycles explained by declining CO2 and regolith removal. *Science Advances*, **5**.

Willeit, M., Ganopolski, A., Calov, R., Robinson, A., & Maslin, M. (2015). The role of CO2 decline for the onset of Northern Hemisphere glaciation. *Quaternary Science Reviews*, **119**, 22–34.

Wilson, J. D., Barker, S., Edwards, N. R., Holden, P. B., & Ridgwell, A. (2019). Sensitivity of atmospheric CO 2 to regional variability in particulate organic matter remineralization depths. *Biogeosciences*, **16**, 2923–2936.

Www1. (n.d.). Global Carbon Cycle | The carbon cycle refers to the continu... | Flickr.

Xu, J., Holbourn, A., Kuhnt, W., Jian, Z., & Kawamura, H. (2008). Changes in the thermocline structure of the Indonesian outflow during Terminations I and II. *Earth and Planetary Science Letters*, **273**, 152–162.

Xu, J., Kuhnt, W., Holbourn, A., Andersen, N., & Bartoli, G. (2006). Changes in the vertical profile of the Indonesian Throughflow during Termination II: Evidence from the Timor Sea. *Paleoceanography*, **21**.

Yan, Q., Wei, T., Korty, R. L., Kossin, J. P., Zhang, Z., & Wang, H. (2016). Enhanced intensity of global tropical cyclones during the mid-Pliocene warm period. *Proceedings of the National Academy of Sciences*.

Yan, Y., Bender, M. L., Brook, E. J., Clifford, H. M., Kemeny, P. C., Kurbatov, A. V., Mackay, S., Mayewski, P. A., Ng, J., Severinghaus, J. P., & Higgins, J. A.

(2019). Two-million-year-old snapshots of atmospheric gases from Antarctic ice. *Nature*, **574**, 663–666.

Yu, J., Elderfield, H., & Hönisch, B. (2007). B/Ca in planktonic foraminifera as a proxy for surface seawater pH. *Paleoceanography*, **22**.

Zachos, J., Pagani, H., Sloan, L., Thomas, E., & Billups, K. (2001). Trends, rhythms, and aberrations in global climate 65 Ma to present.

Zachos, J. C., Dickens, G. R., & Zeebe, R. E. (2008). An early Cenozoic perspective on greenhouse warming and carbon-cycle dynamics. Nature Publishing Group.

Zalasiewicz, J., Waters, C., Williams, M., Summerhayes, C., Head, M., Leinfelder, R., Grinevald, J., McNeill, J., Oreskes, N., Steffen, W., Wing, S., Gibbard, P., Vidas, D., Hancock, T., Barnosky, A., Hazen, B., Smith, A., & McNeill, J. R. (2019). Anthropocene geological time unit guide scientific evidence and current debate | Sedimentology and stratigraphy | Cambridge University Press.

Zeebe, R., & Wolf-Gladrow, D. (2001). CO2 in Seawater: Equilibrium, Kinetics, Isotopes, Volume 65 1st Edition. Elsevier Science.

Zhang, X., Knorr, G., Lohmann, G., & Barker, S. (2017). Abrupt North Atlantic circulation changes in response to gradual CO 2 forcing in a glacial climate state. *Nature Geoscience*, **10**, 518–523.

Zhang, X., Lohmann, G., Knorr, G., & Purcell, C. (2014). Abrupt glacial climate shifts controlled by ice sheet changes. *Nature*, **512**, 290–294.

Zhang, Y. G., Pagani, M., Liu, Z., Bohaty, S. M., & Deconto, R. (2013). A 40-million-year history of atmospheric CO2. *Philosophical Transactions of the Royal Society A: Mathematical, Physical and Engineering Sciences*, **371**.

Zhao, C. L., & Tans, P. P. (2006). Estimating uncertainty of the WMO mole fraction scale for carbon dioxide in air. *Journal of Geophysical Research*, **111**, D08S09.

Zuraida, R., Holbourn, A., Nürnberg, D., Kuhnt, W., Dürkop, A., & Erichsen, A. (2009). Evidence for Indonesian Throughflow slowdown during Heinrich events 3 to 5. *Paleoceanography*, **24**, n/a–n/a.

# Appendix A

# Atmospheric $CO_2$ and its relevance in modern climate change

## A.1 $CO_2$ - an Atmospheric Greenhouse Gas

Carbon dioxide (chemical formula $CO_2$) is an invisible odourless gas which contains one carbon and two oxygen atoms connected via double bonds. It is the fourth most important gas in the atmosphere, after nitrogen, oxygen and argon, making up 0.04% of dry air volume (Mackenzie & Mackenzie, 1995). $CO_2$ has two important features which make it irreplaceable for life on earth.

First, it is a greenhouse gas (Goody, 1995). Atmospheric greenhouse gases have the ability to absorb short wave radiation, internalise it, and emit it as longwave radiation, also known as heat (Figure A.1). Additionally, they can re-emit longwave radiation from the earth's surface back towards the earth. As such, greenhouse gases store heat in the atmosphere which would otherwise emit into space. Without greenhouse gases, earth's average temperature lay around -18°C (Goody, 1995). Instead, it rose to 15°C enabling liquid water to exist and providing all necessities for the development of life (Goody, 1995). The energy trapped in form of heat in the atmosphere by the greenhouse effect, expresses itself through climate and weather

(Visconti, 2016). By definition, climate is the mean state of the atmosphere over the duration of 30 years, while weather is the mean state of the atmosphere in a certain location over a period of days or weeks (Visconti, 2016). Weather is driven by climate, but includes an internal stochastic element where extreme events abnormal to the overall climate appear with a certain likelihood (Visconti, 2016).

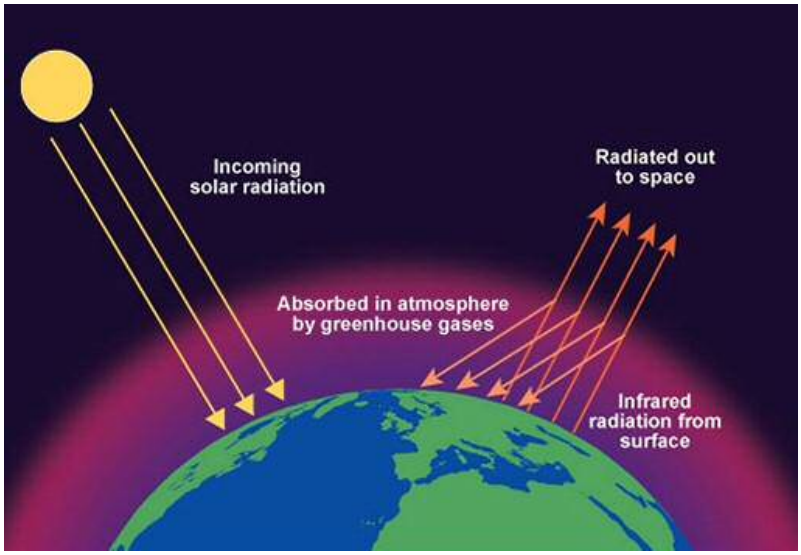


**Figure A.1** The Greenhouse Effect (The Open University, n.d.).

Second, it contains carbon. This makes it particularly interesting as an energy source for our carbon-based life. Plants, or autotrophs, take up $CO_2$ and turn it into living biomass via photosynthesis (Figure A.2) (Najafpour et al., 2017). When the plant material is eaten by heterotrophs, the $CO_2$ is released back into the atmosphere during respiration (Najafpour et al., 2017). This is essentially known as the carbon cycle. Due to the longevity of different carbon molecules, multiple carbon cycles exist on several timescales (Archer, 2010). These include the biological/biomass carbon cycle, the marine carbon cycle, and the weathering cycle (Archer, 2010).

Throughout the biological carbon cycle, biomass is produced via photosynthesis and then processed either during consumption of fresh plant material or during remineralisation of dead biomass. In the former, the carbon cycle can be fulfilled within days, while the latter can take years. Under specific (geologic) circumstances,

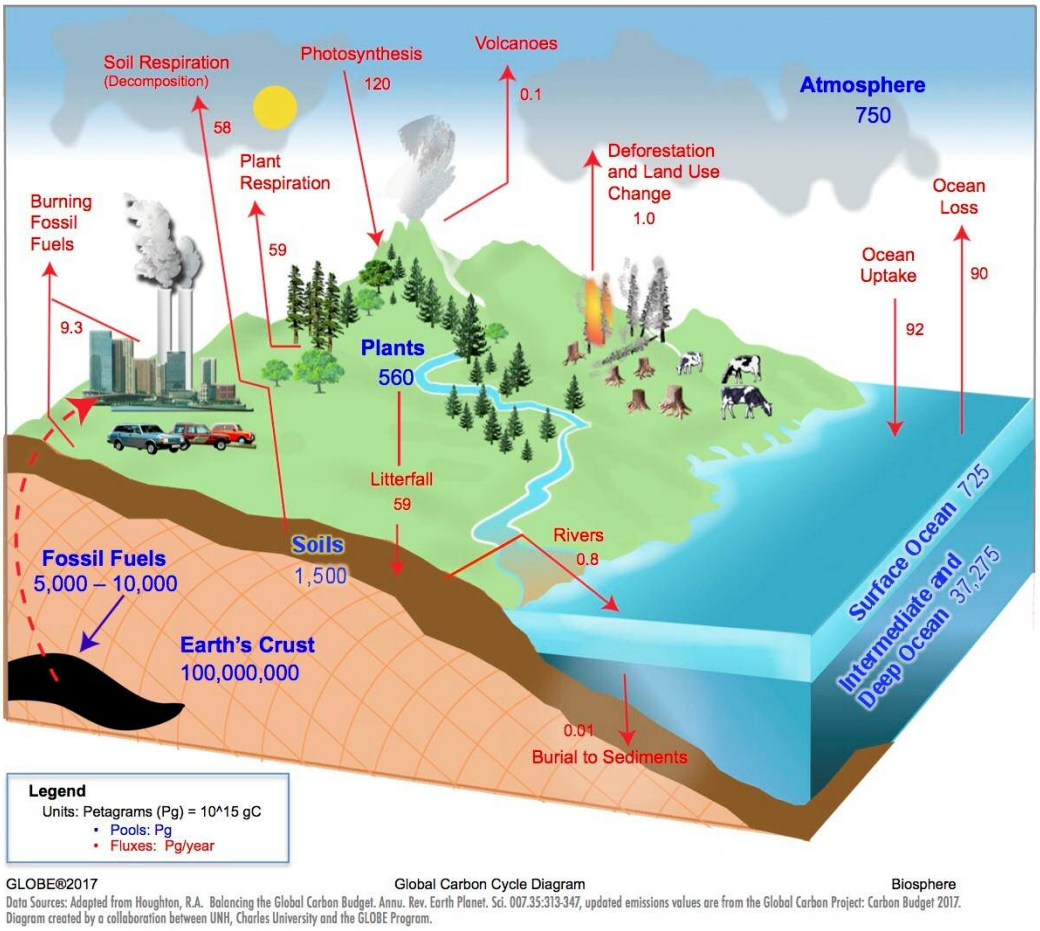


**Figure A.2** Modern carbon cycle. Blue labels show major carbon pools and their carbon content in Pg/yr. Red arrows indicate carbon fluxes in Pg/yr. Figure from (Www1, n.d.), with credit to (NASA, n.d.) and (Houghton, 2007).

biomass is turned into geologically stable forms such as peat, coal, oil and gas. In this case, carbon has been effectively removed from the biological cycle as it cannot be remineralised on daily, monthly or yearly timescales anymore.

The marine carbon cycle (Figure A.3) is active on hundreds to thousands of years (Sigman & Hain, 2012). The ocean is in constant pursuit of $CO_2$-concentration equilibrium with the atmosphere (Takahashi et al., 2014). This causes atmospheric $CO_2$ to dissolve in ocean water, providing carbon to the marine part of the biological carbon cycle (Sigman & Hain, 2012). In the ocean, dead biomass sinks and is remineralised on the way (Sigman & Hain, 2012). This causes the respiratory $CO_2$ to be released into a deeper water mass than the ocean surface leading to an enrichment

of dissolved $CO_2$ in the deep ocean (Sigman & Hain, 2012). If ocean circulation changes and limits these water masses from rising and exchanging gases with the atmosphere, $CO_2$ is effectively stored until the circulative regime is broken. This can happen on centennial to millennial timescales. The downward transport of carbon via biomass is called the biological pump (Sigman & Hain, 2012). In summary, the marine carbon cycle is driven by ocean circulation dynamics in combination with a short-term biological carbon cycle.

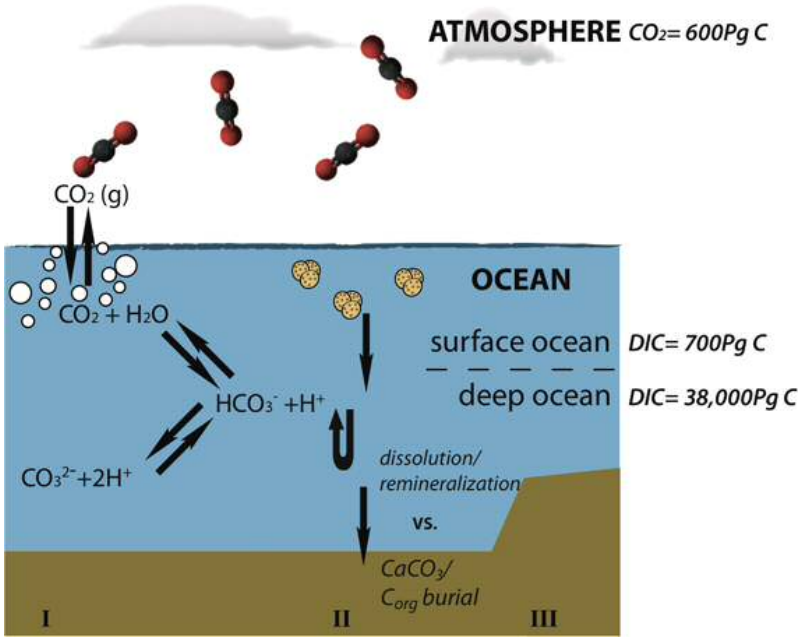


**Figure A.3** Schematic of the marine carbon cycle (Kersten, 2012).

The weathering cycle (Figure A.4) explains atmospheric $CO_2$ changes over millions of years (Berner, 2003; Franck et al., 2008). Geological carbon contains 90% of all carbon on Earth in the core, mantle and crust (Dasgupta & Hirschmann, 2010). Crust carbon exists mostly in form of carbonic rocks, such as calcite and aragonite rock blocks, and fossil fuels (Berner, 2003). Rain water can dissolve carbonate rocks and transport it to the oceans on thousand- to million-year timescales (Franck et al., 2008), as evident in karst systems. The weathered geological material ends up on the ocean floor through the marine carbon cycle, where it becomes part of subduction complexes (Berner, 2003; Franck et al., 2008; Plank & Manning, 2019).

After subduction and re-melt, the carbon is fully removed from the earth's surface and re-enters the atmosphere through volcanic and tectonic outgassing (e.g. Mason et al., 2017).

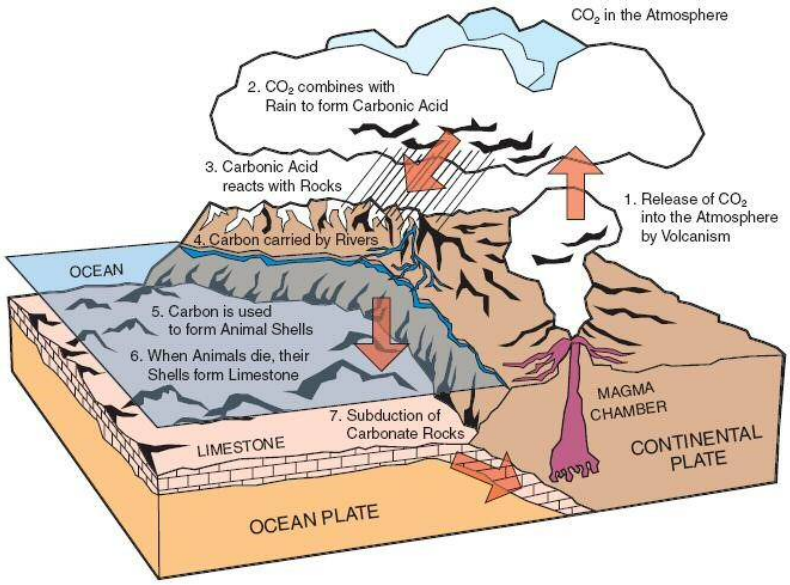


**Figure A.4** The geological weathering cycle (Shapley, 2010).

### A.1.1 $CO_2$ as a feedback mechanism

Greenhouse gases, such as $CO_2$, possess physical and chemical properties that lead to a globally warmer climate than otherwise natural for a comparable planet without the greenhouse effect. As such, changes in greenhouse gas concentrations, for example in $CO_2$, can act as a climate feedback mechanism. A climate feedback mechanism may influence climate and amplify or diminish a change in the energy input (Hansen et al., 1984). Feedback mechanisms often act in loops (Kellogg, 1983; Robock, 1985). A positive feedback loop will lead to amplification of the initial signal and promotes a change in the mean climate state, whereas a negative feedback mechanism will attenuate change and stabilize the prevailing climate mode (Figure A.5). For example, the ice-albedo feedback acts as a positive loop whereby more ice induces greater energy loss, because a greater area is covered with highly reflective

white snow. As a result, air temperatures will cool leading to greater ice cover (e.g. Curry et al., 1995). For some, such as cloud-climate feedbacks, the direction of the loop is more difficult to assess (Bony et al., 2015). Warming climates promote water evaporation and cloud formation. Increasing cloud cover shields the earth from incoming solar radiation due to their high reflectivity, while increasing concentrations of water vapour strengthen the greenhouse effect (Bony et al., 2015). As such, clouds can act either as positive or negative loops. This shows how intrinsically connected all feedback mechanisms are. Well known examples of feedback mechanisms are changes in ice-albedo (Curry et al., 1995), greenhouse gases (Kellogg, 1983), cloud cover (Bony et al., 2015), vegetation (Bonan, 2008), ocean circulation (Broecker, 1991), carbon cycle dynamics (Friedlingstein et al., 2006), monsoon systems (Cheng et al., 2016b), methane clathrate release (MacDonald, 1990) and permafrost melting (Schuur et al., 2015). If one equilibrium is disturbed, it can be projected through the different climate components via cascading effects and lead to the development of a new systemic equilibrium (Dekker et al., 2018). In some cases, the disturbance may be large enough to push the feedback over a tipping point. Tipping points are bifurcation points in the system after which a small change in the leading variable will cause a large non-linear response in the internal dynamics of the depending system (Lenton, 2011). Examples include rainforest die-back, irreversible ice sheet collapse, and significant ocean deep water convection disruption (Lenton, 2011). Lenton et al. (2012; 2009) argue that tipping points may be statistically predictable if long enough time series exist. They see an increase in variability shortly before tipping points were reached in the earths climatic past. However, they note that their methods do not pick out every tipping event making prediction only moderately possible (Lenton et al., 2012).

The bifurcation in the system often appears as a hysteresis loop, whereby two possible climate states exist for the same variable setting (Rahmstorf, 2002; Stocker & Marchal, 2000). This means that passing a bifurcation point or tipping point can

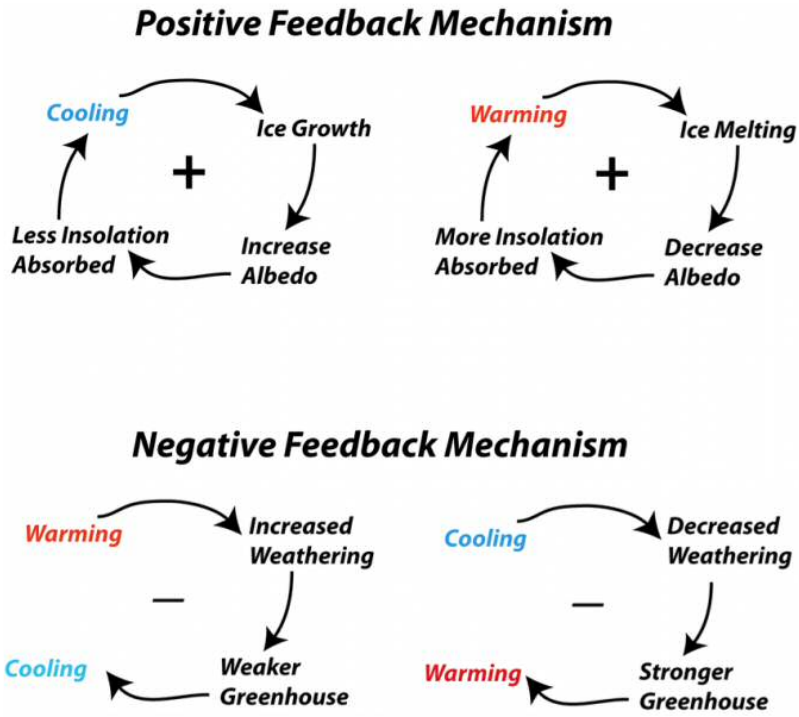


**Figure A.5** Examples of positive and negative climate feedback loops. A positive loop causes an acceleration of the climatic change, while a negative loop diminishes the change and acts as a stabilizer (Figure from Bralower and Bice, n.d.)

cause irreversible changes, since the status quo is only one of two return options (Figure A.6). Knorr & Lohmann (2003) modelled the bifurcation response of North Atlantic deep water production to density disturbance from freshwater input and found that the character of the hysteresis loop may change depending on the background climate (figure 15). This suggests that correct prediction of tipping point behaviour using paleoclimate data might be more difficult than assumed. This further shows that hysteresis loops have potential path directions whereby the recovery of the previous climate is unable to be reached when the starting point lies past a certain tipping point. In other words, the location of the status quo on the hysteresis loop will define the direction of change and essentially the next stable climate (Figure A.6).

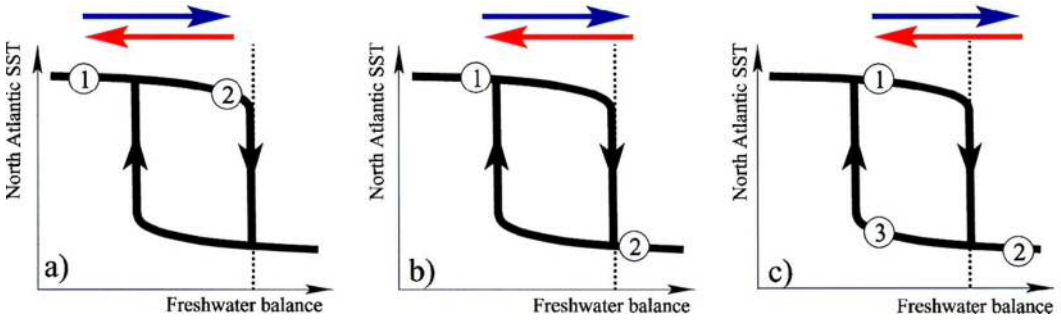


**Figure A.6** Schematic example of a hysteresis loop in the Atlantic meridional overturning circulation (Stocker & Marchal, 2000). Increases in the north Atlantic freshwater flux can lead to reductions in North Atlantic sea surface temperatures (SST). The system has limited buffer capacity with respect to changes in SST. As such, the freshwater forcing may vary without significantly influencing SST (a). If the freshwater forcing increases beyond a certain bifurcation point, little further changes in freshwater forcing will cause large changes in SST (b). When a bifurcation point is passed, it is unclear whether a return to initial freshwater forcing values will cause a subsequent change in SST or not. If two stable equilibria exist for the system, the freshwater balance will have to increase further than the initial starting balance to induce a change in SSTs (c) (Stocker & Marchal, 2000).

## A.1.2 Atmospheric $CO_2$ data and reconstructions

Carbon dioxide is the fourth most important greenhouse gas in the atmosphere (Mackenzie & Mackenzie, 1995). As such, changes in atmospheric concentrations can have direct effects on global average temperatures and evolving climate (see chapter 2.3). Research on atmospheric $CO_2$ variability goes hand in hand with the scientific methods development that enabled the measurement or reconstruction of atmospheric $CO_2$ concentrations. In the following chapter, I will present the most important $CO_2$ records which led to a significant leap in the scientific understanding of $pCO_2$ dynamics and their drivers.

### Mauna Loa record

The Mauna Loa Earth Observatory in Hawaii, USA is located near the top of Mauna Loa volcano surrounded by bare lava fields. The lack of nearby vegetation, human settlements and industry make this location especially suited for the in-situ measurement of “background air” or “baseline air” (Tans & Thoning, 2008).

Background air describes air masses whose gas concentrations are well mixed and representative of a hemispherical or global-wide average (Tans & Thoning, 2008). $CO_2$ concentrations are measured in mole fraction. This describes the amount of $CO_2$ molecules in a given number of dry air molecules, from which any water vapour was removed (Zhao & Tans, 2006). The unit is described as "parts per million" or ppm. The Mauna Loa $CO_2$ record is the longest continuous record so far. At Mauna Loa, measurements are taken continuously since 1959, using an infrared absorption technique (Komhyr et al., 1989). To ensure high quality data collection, the sensors are calibrated hourly by sending in "calibration air" from store bottles (Tans & Thoning, 2008). Every 25h, the system measures a standard "target gas" which is treated as an unknown (Tans & Thoning, 2008). Additionally, measurements are regularly compared with $CO_2$ measurements taken at Scripps Institution of Oceanography in California (Tans & Thoning, 2008). With this calibration strategy, $CO_2$ measurements can be made with an accuracy of better than 0.2ppm (Tans & Thoning, 2008). To create the final multi-decadal record, measurements are averaged hourly, then daily and monthly. Before averaging, the data is "cleaned" of any data points that might not represent true baseline air (Thoning et al., 1989). This includes $CO_2$ transported by diurnal wind cycles from Mauna Loa volcano crater, or high short-term variability which is indicative of locally sourced $CO_2$ (Thoning et al., 1989).

The final Mauna Loa record depicts an averaged measurement per month (Tans & Thoning, 2008; Thoning et al., 1989) (Figure A.7). Annual cycles are clearly visible (Figure A.7). The cycles are a product of strong photosynthetic activity in the northern hemisphere during summer months and reduced activity in winter. On multi-decadal timescales, the record shows a continuous increase in atmospheric $CO_2$ since 1959 (Figure A.7).

In the mid-20th century, $pCO_2$ was measured at 315ppm, while in May 2019 it had risen to 412ppm (Figure A.7). This is an increase of around 100ppm in

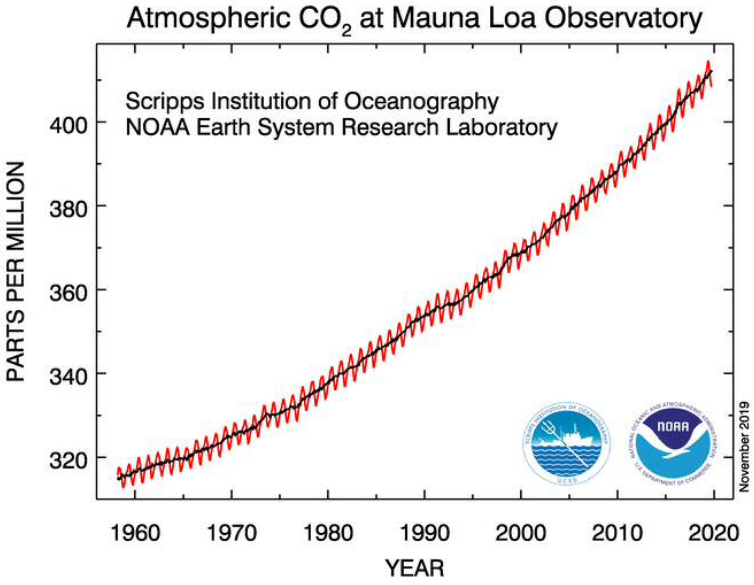


**Figure A.7** Monthly mean (red) and yearly average (black) global atmospheric $CO_2$ concentration in ppm since 1957 measured at the Mauna Loa Earth Observatory and validated with measurements from Scrippts Institution of Oceanography (US Department of Commerce, NOAA, n.d.-a).

less than 60 years. Using the raw $CO_2$ data, annual growth rates can be calculated and averaged over 10 years for robustness. Since 1960, growth rates have been consistently increasing with one exception during the 60s and two during the 90s when growth rates reduced (Figure A.8). This suggests that the current increase in atmospheric $CO_2$ will likely extend further without significant changes in policy and economic energy use (IPCC, 2018).

### The "Hockey Stick" curve

In 1999, Michael Mann and colleagues published a scientific study which became internationally known as "the hockey stick curve" (Mann et al., 1999). The study consists of a stacked dataset using mostly Mauna Loa and tree ring data to reconstruct $pCO_2$ and global mean temperature across the last 1000 years. The term arose from the shape of the graph printed in the paper (Figure A.9). The graph depicts a long horizontal trend followed by a sharp increase. This looks similar to a hockey stick

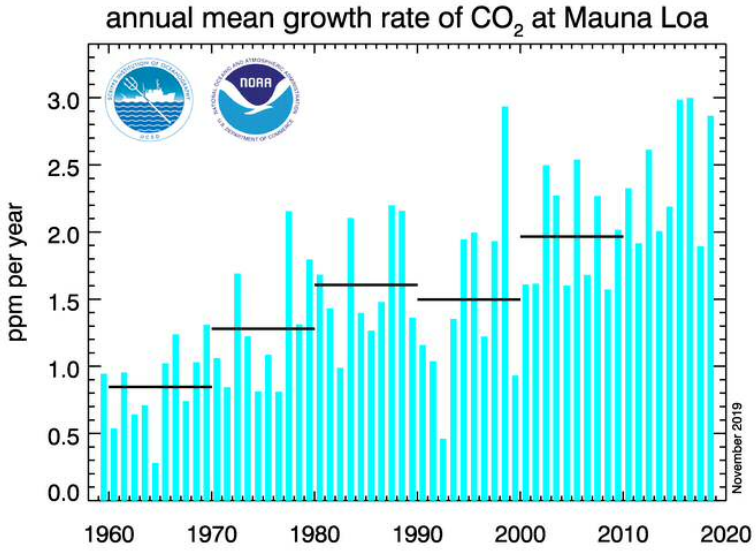


**Figure A.8** Annual mean growth rates of global atmospheric $CO_2$ concentrations in ppm/year since 1959 (US Department of Commerce, NOAA, n.d.-b).

lying on its back. The data suggests that until around 1790, variability could be averaged out to a background level. However, since 1790, $pCO_2$ clearly increased well above the millennial average (Figure A.9b). This was a significant find as it suggests the industrial revolution with the start of significant fossil fuel burning as a potential source for the increasing $CO_2$ (IPCC, 2018; Steffen et al., 2011) already seen in the Mauna Loa record. Additionally, and more importantly, it implied that the recent $CO_2$ increase deviated off the Holocene mean (Mann et al., 1999) and could potentially lead to changes in the global mean climate state (IPCC, 2018). This interpretation was especially supported by the temperature stack published in the same paper (Figure A.9a). Temperature co-varied closely with $CO_2$ creating the same "hockey stick" shaped curve. However, the rise began later than the $CO_2$ rise with statistical significance in the latter half of the $20^{th}$ century (Mann et al., 1999). This strongly suggests that modern $pCO_2$ and global mean atmospheric temperature are tightly coupled.

The publication of both graphs resulted in a significant political and media turmoil (e.g. Butos and Mcquade, 2015; Goldenberg, 2010; Mann, 2016; Mooney,

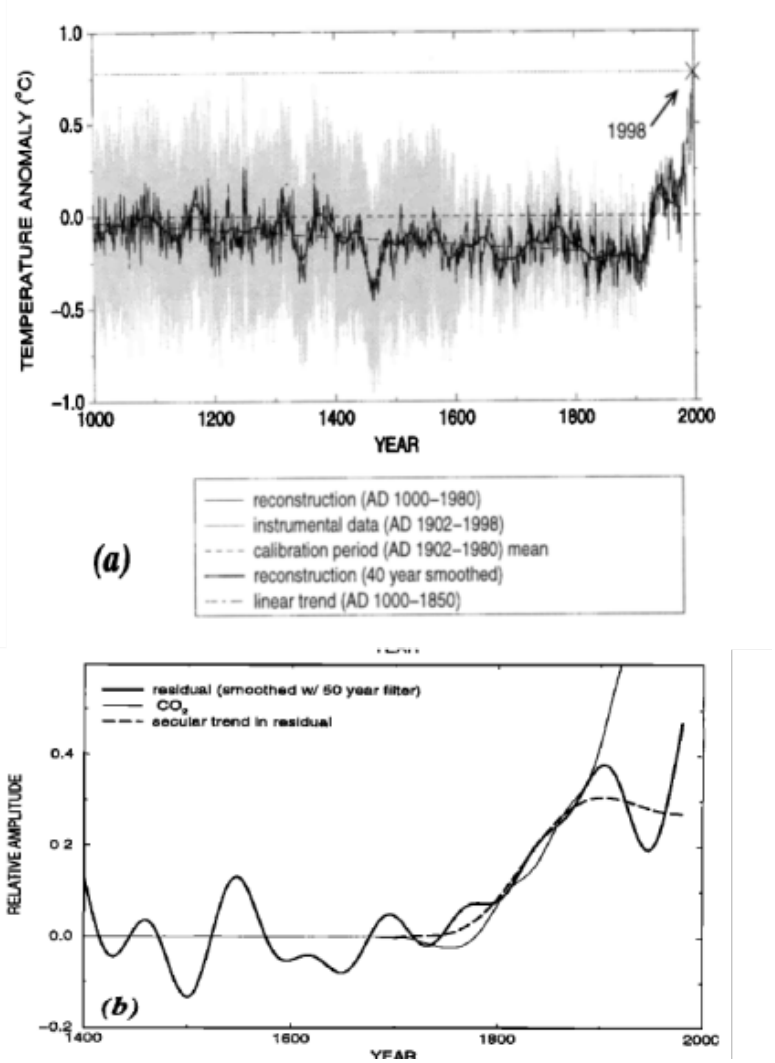


**Figure A.9** Reconstructed temperature anomaly between 1000 and 2000 A.D. (a), and atmospheric $CO_2$ (b) between 400 and 2000 A.D. from Mann et al (1999). Both curves show a "hockey stick"-shaped increase after 1800.

2013; Schmidt and Ramstorf, 2005; Sheppard, 2011.) The statistical measures used by Mann et al. (1999) that highlighted significantly warmer late 20th century were widely attacked (e.g. Oil&Gas Journal, 2001; for discussion see also Butos and Mcquade, 2015; Mann, 2016; Sheppard, 2011). Given that the "Hockey Stick curve" featured centrally in the following IPCC report (IPCC, 2001), it questioned the integrity of the IPCC community and science itself (Goldenberg, 2010; Schmidt & Ramstorf, 2005; Sheppard, 2011). Since then, further scientific studies have validated the significant temperature increase (e.g. Hawkins et al., 2017; Marcott

et al., 2013) as well as the link between $CO_2$-rise and fossil fuel release (see chapter A.2). The most recent human-induced global changes, including climatic shifts, plastic pollution, species extinctions, and appearance of non-natural elements in the geological record have reached an extent that led to the suggestion of a new geological time period: The Anthropocene (Crutzen, 2002). So far, the Anthropocene is not officially recognised. However, in 2016, the Anthropocene working group of the International Commission on Stratigraphy voted to begin a formal proposal for the golden spike that shall mark the begin of the Anthropocene in the geological record (Zalasiewicz et al., 2019).

### Ice core record

Ice cores drilled in Arctic or Antarctic ice sheets can provide information on the last 800kyr of atmospheric characteristics (Jouzel et al., 2007). In ice sheet accumulation zones, annual snowfall presses down on older snow and turns it into ice under its own weight-induced pressure. Most snow accumulation happens during the winter season, while melting occurs during the summer. This creates seasonal banding in the ice which provide a useful tool for dating. During the reorganisation, air bubbles are trapped in the ice and frozen. Using a specific melting technique, air bubbles can be extracted and their gaseous contents measured (Lüthi et al., 2008). This allows for the reconstruction of atmospheric $CO_2$ in centennial to millennial resolution across multiple glacial-interglacial cycles (Bereiter et al., 2015; Lüthi et al., 2008; Marcott et al., 2014). Ice sheets are dynamic systems. Their weight causes basal ice to melt and form a wet slippery layer between the ice sheet and the rock. As a result, the ice sheet slides and deforms. Hence, finding suitable ice core locations is not trivial. So far, several cores have been taken in Greenland (NGRIP, 2004) and Antarctica (Lüthi et al., 2008; Monnin et al., 2001; Petit et al., 1999; Raynaud et al., 2005; Siegenthaler et al., 2005). Many climate variables can be reconstructed from ice core

material. Carbon dioxide concentrations are mostly reconstructed using Antarctic ice (Figure A.10). Besides $pCO_2$, atmospheric temperature was reconstructed using hydrogen isotopes (Jouzel et al., 2007) (Figure A.10).

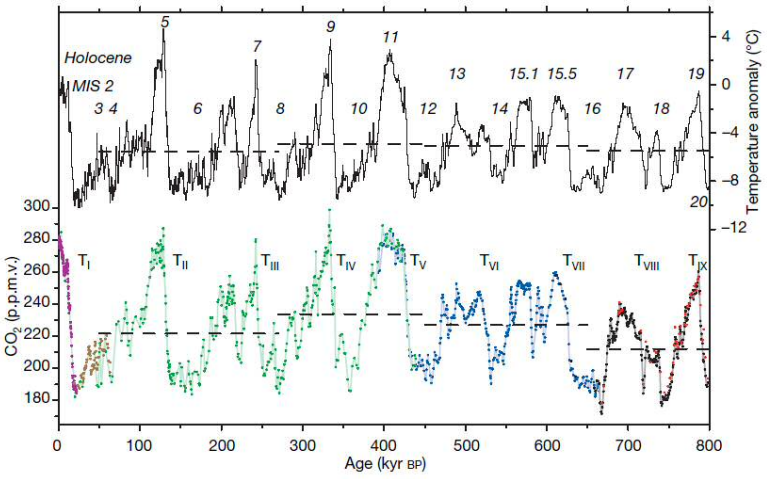


**Figure A.10** Atmospheric temperature anomaly (black) and $CO_2$ concentrations from Dome C (purple, blue, black, red), Taylor Dome (brown) and Vostok (green) from Luethi et al. (2008).

Additionally, records of atmospheric methane and wind-blown dust were also published (Lüthi et al., 2008). In Antarctica, most sites recover until around 400kyr ago (Petit et al., 1999). Site EPICA Dome C is an exception with recovery back to 800kyr (Lüthi et al., 2008). This is the longest continuous ice core record taken. Multiple ice cores during the last 400kyr and single EPICA Dome C measurements from 400 to 800kyr were compiled to a final $pCO_2$ record (Figure A.10) (Bereiter et al., 2015; Lüthi et al., 2008) which characterises changes in global $CO_2$ concentrations for the Late Pleistocene. The record shows that $pCO_2$ varied between 180ppm and 280ppm across the last 800kyr incorporating 8 glacial-interglacial cycles. Each interglacial is coherent with $CO_2$ highstands around 280-300ppm, while glacials appear during low $pCO_2$ at 180ppm. $CO_2$ decrease is highly variable and follows a 90,000-year trajectory until minimum values are reached. $CO_2$ increases across terminations occur abrupt with 100ppm released in only 10,000 years. When looking at the original data by Lüthi et al. (2008), it appears that the last five interglacials,

including the current Holocene, reach higher $pCO_2$ levels (up to 300ppm) than the previous four at 250ppm. Bereiter et al. (2015) revisited the data and corrected for previously unidentified gas diffusion in the near bottom old ice. The new record depicts interglacial $CO_2$ for the last 3 cycles around 270ppm (Figure A.11) (Bereiter et al., 2015). Therefore, it appears that $CO_2$ maxima may have increased around 540kyr ago. Still, it is worth noting that the oldest 400kyr rely on the EPICA Dome C ice core only, whereas a multitude of cores from different locations exists for more recent cycles.

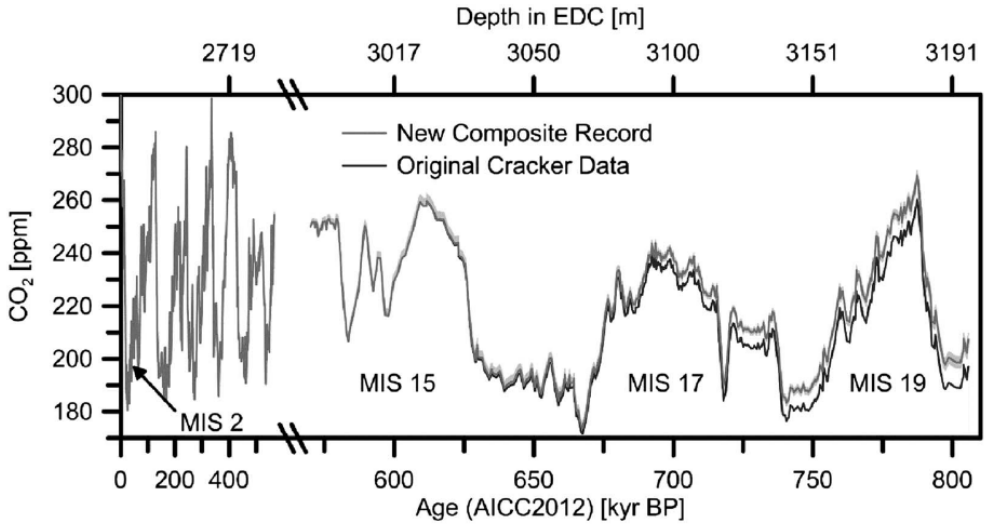


**Figure A.11** Atmospheric $CO_2$ reconstructions before (black) and after (grey) the new diffusion correction from Bereiter et al. (2015).

Recently, discontinuous samples of older ice were presented (Higgins et al., 2015; Yan et al., 2019). This ice is also known as blue ice and allows the discontinuous recovery of air bubbles older than 800kyr (Higgins et al., 2015). The oldest samples presented were 2.7Ma old (Yan et al., 2019). The breakthrough was mostly connected to a new dating method, by which the ice can be dated using argon and potassium (Yan et al., 2019). Other samples reached around 1Ma (Higgins et al., 2015).

In ice-core data, temperature correlates closely with $pCO_2$. In fact, the two records match so well that a simple interpretation of lead-lag relationships is difficult.

Shakun et al. (2012) claim that changes in $pCO_2$ lead changes in temperature after analysing EPICA Dome C records from the last deglaciation. Gest et al. (2017) confirm these finds using a new centennial-resolution ice core $pCO_2$ record (Marcott et al., 2014). They find a lag of 165 $\pm$116yrs at the end of the Antarctic cold reversal period in the middle of the last glacial cycle which widens to 406 $\pm$200yrs at the onset of the Holocene. Contrary, Uemura et al. (2018) call for caution as their results suggest that lead-lag relationships from ice cores might be amplified by signals carried in the moisture source. This highlights that $pCO_2$-temperature relationships might be more complicated on millennial timescales than previously thought.

**Deep-time record**

Beyond the Plio-Pleistocene, atmospheric $CO_2$ reconstructions decrease significantly in their temporal resolution (Figure A.12). Most of our understanding is based upon a few estimates spanning from 50Ma to 16Ma (Anagnostou et al., 2016; Pagani et al., 2011; Pagani et al., 2005). The record shows a long-term decrease from $pCO_2$ values around 800-1400ppm at 50Ma to 200ppm at 16Ma (Anagnostou et al., 2016; Pagani et al., 2011; Pagani et al., 2005). Similar values have been found by a few boron isotope measurements around 35Ma (Pearson et al., 2009). During the Oligocene, alkenone-$CO_2$ estimates appear to de-couple from benthic $\delta^{18}O$, a proxy for global ice volume. Beyond 40Ma, a few data points (n=8) characterise the Eocene epoch as a high $CO_2$ world with averages of 1000ppm (Anagnostou et al., 2016; Pagani et al., 2005). However, measurement error bars and dataset spread are large. A few higher resolution reconstructions exist around 15Ma. This time is known as the Middle Miocene Climate Optimum (MMCO) and depicts a time where atmospheric $CO_2$ might have undergone significant variability. It appears that $pCO_2$ increased from background values around 200-300ppm to 500-600ppm (Foster et al., 2012; Greenop et al., 2019). This was paralleled by major climate and ocean carbon cycle

disturbances (Flower & Kennett, 1994; Holbourn et al., 2015; Kochhann et al., 2016), including a drop in ocean pH from 8.2 to around 7.6 (Greenop et al., 2019). Given the importance of $pCO_2$ for the climate system and the potential threat for future climates, more reconstructions are needed to understand the geological history of atmospheric $pCO_2$.

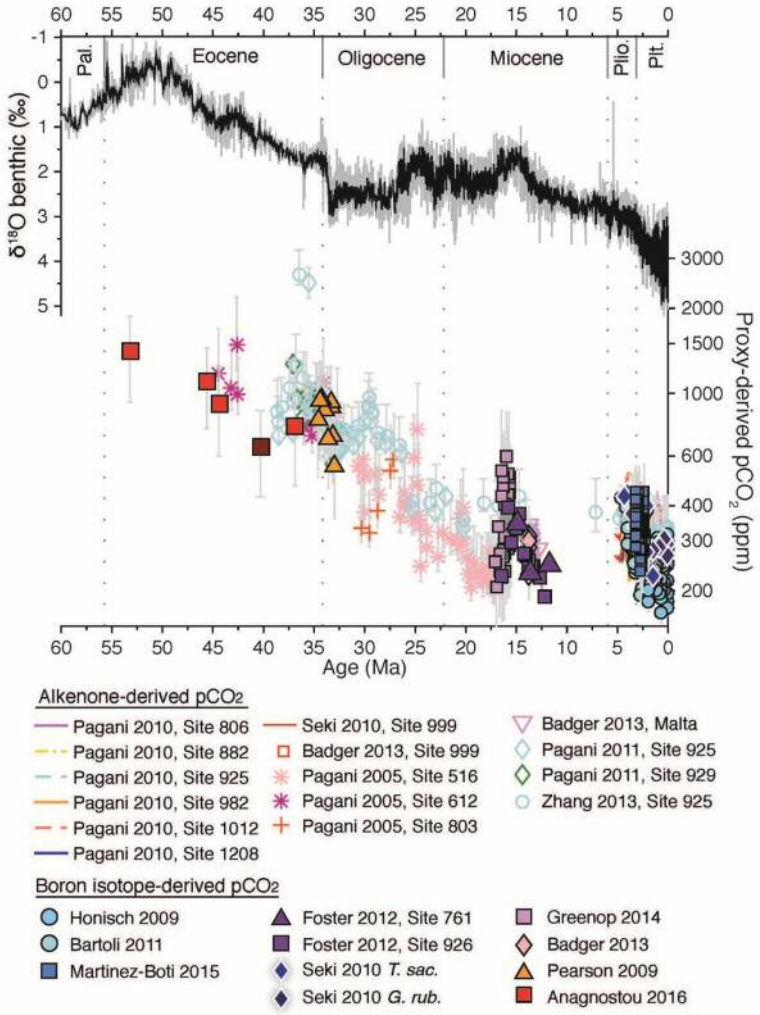


**Figure A.12** Atmospheric $CO_2$ reconstructions from boron isotopes and alkenones for the last 60Ma (P-co2.org, n.d., see also Foster et al., 2017)

## A.2 Anthropogenic $CO_2$ release – scientific evidence for fossil fuel-induced $CO_2$ increase

Reconstructing past atmospheric $CO_2$ concentrations provides historical background against which the modern Mauna Loa $CO_2$ increase can be observed. It is evident that the currently measured increase in $pCO_2$ is unprecedented in the last 800,000 years (Figure 3.10), and likely unprecedented until the middle Miocene (Figure A.12). When comparing the Mauna Loa increase to the Late Pleistocene glacial-interglacial cycle $pCO_2$ variability, both show increases of around 100ppm. The difference lies in the absolute values and the rate. Previous interglacial maximum recorded $pCO_2$ never exceeded 300ppm, while glacial $pCO_2$ was around 190-200ppm. The release of around 80ppm deglacial $CO_2$ took 11,100 years (Marcott et al., 2014) presenting an average degassing rate of 7.2ppm/1000 years or 0.0072ppm/year. This stands in contrast to roughly 93ppm that entered the atmosphere over the duration of approximately 60 years with a rate of 1.55ppm/year (Figure A.7; ESRL, n.d.). That is about 216 times more $CO_2$ released in the Mauna Loa record compared to average rates in the last 800,000 years. Marcott et al. (2014) report three deglacial $CO_2$ venting events with higher release rates of 10-15ppm in less than 200 years. This is equivalent to average rates of 0.072ppm/yr which is 10 times higher than the average deglacial degassing rate, but still 22 times lower than modern rates.

This strongly suggests that the current excess $CO_2$ degasses from sources that were inactive across the last 2 million years. Fossil fuels are a good candidate for excess $CO_2$ release. Other stable carbon storages include carbonate rocks, moors and peatlands, permafrost soils, dead biomass, and volcanism. Carbonate rocks are unsuitable for quick carbon release as their weathering takes hundreds to thousands of years (Martin, 2017). Moors and peatlands are ecosystems in which waterlogged plant material resists decomposition due to anoxic conditions, and forms

dark carbon-rich peat (Charman, 2002). Peat is fairly stable, but when dry will burn easily releasing $CO_2$ in the process (e.g. Turetsky et al., 2011). Permafrost soils are similar in that they preserve large amounts of frozen uncomposed biomass in cold landscapes (Streletskiy et al., 2015). After thaw, re-mineralisation happens quickly, as the frozen biomass did not undergo peating process (Biskaborn et al., 2019; Streletskiy et al., 2015). Yet, neither of those storage systems are able to explain the most recent $CO_2$ increase. Jackson et al. (2018) calculated that 36.2Gt $CO_2$ were released in 2018 alone. If peat burning was responsible, 37.31 trillion m3 of peat need to be burned each year, assuming a peat wet weight at 0.96t/$m^3$ (LBH, 2019), a calorific value of 9.76GJ/t, and a $CO_2$ emissions potential of 106g$CO_2$/MJ (Stocker et al., 2014). In comparison, the global amount of peat in 2007 was only 3.5 to 4.0 trillion $m^3$ according to the world energy council (Caillé, 2007). Accounting for the excess carbon through permafrost outgassing is similarly unlikely. Permafrost melting sensitivity is reported at 0.8 – 2.3 million $km^2$ melting/1°C (Streletskiy et al., 2015). Given that currently 4-25 million $km^2$ of permafrost globally (Slater & Lawrence, 2013) hold around 750Gt carbon in the upper 3m (Schuur et al., 2008), this means that 1$m^3$ permafrost soil incorporates around 1tC/$m^3$ – 6.25tC/$m^3$ of permafrost soil. Using the robust estimate of 6.25tC/$m^3$, and assuming a linear release of $CO_2$, this calculates around 193,000 $km^2$ permafrost that need melting each year. With a robust sensitivity of 0.8 million $km^2$/1°C, we would have needed a warming of 0.024°C/year which accounts to 1,44°C in 60 years. This warming needed to happen prior to the $CO_2$ release if permafrost melting is to account for the initial $CO_2$ increase. However, that is not recorded in the data. In 2013, Burton et al. published new estimates on volcanic greenhouse gas emission rates. They account for various sources including active and inactive surface volcanoes, as well as flanks, submarine volcanoes, hydrothermal vents and to a certain extent mid ocean ridges. According to the results, Holocene volcanic activity accounts for 0.54 Gt/yr. This is around 60 times lower than the yearly emissions release from fossil fuels making

volcanism an unlikely sole source. Therefore, it is likely that the burning of fossil fuels has caused the increase in $pCO_2$.

To further test this hypothesis, isotope systems can be used as gas-source tracers in the atmosphere (Stuiver et al., 1984). Carbon has two stable $^{12}C$ and $^{13}C$ and one radioactive isotope $^{14}C$. During biochemical metabolic interactions, isotopic fractionation occurs creating distinct isotopic signatures (Park & Epstein, 1961). For example, during photosynthesis plants exert a strong preference to the uptake of $^{12}C$ over $^{13}C$ (Park & Epstein, 1961). As such, different carbon isotope signatures exist for animals, plants and dead biomass (Figure A.13) (Trumbore & Druffel, 1995) which includes fossil fuels (Flude et al., 2017). At the same time, smaller amounts of $^{14}C$ are additionally incorporated (Turnbull et al., 2016). $^{14}C$ is radioactive and will therefore decay. Older biomass will have less $^{14}C$ than younger biomass, due to the radioactive mass loss. Both isotopic signatures together form a specific carbon footprint that can be measured in the atmosphere (Turnbull et al., 2016). Fossil fuels, such as coal, oil and gas, have a distinct light stable carbon isotope signature due to significant isotopic fractionation during the process of biomass petrification (Flude et al., 2017) in addition to near zero radiocarbon, because of age (Turnbull et al., 2009). This makes $CO_2$ sourced from fossil fuels easily distinguishable from $CO_2$ released from natural carbon sources (Stuiver et al., 1984).

The stable carbon isotopic signature is published as the ratio between the two stable isotopes in comparison to a standard ($\delta^{13}C$). $\delta^{13}C$ measurements from air samples show a continuous reduction in value since 1860 (Figure A.14) (Francey et al., 1999). This is consistent with addition of $CO_2$ molecules that carry a lighter isotopic signature, such as fossil fuels (Francey et al., 1999). More compelling evidence comes from the signature left by decaying $^{14}C$. The “age signature” created by the age of decayed $^{14}C$ of atmospheric $CO_2$ has decreased significantly between 2003 and 2006 from 70‰/yr to 55‰/yr (Turnbull et al., 2007). Using a simple back-of-the-envelope mixing model calculation, the results show that a source with a

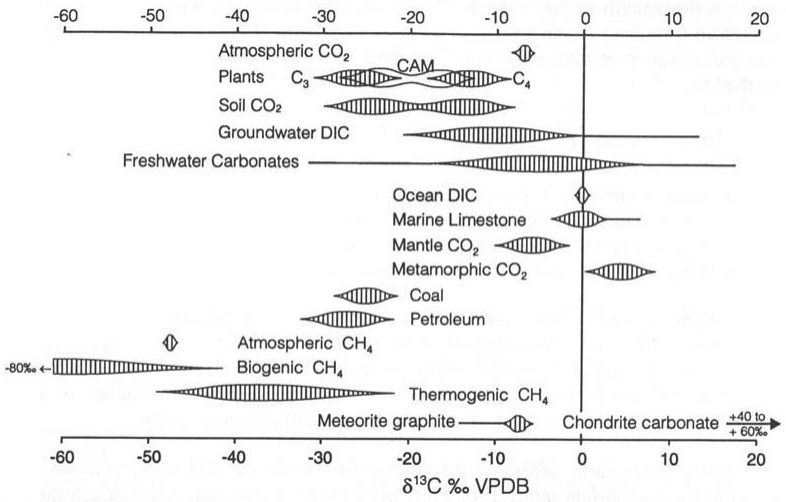


**Figure A.13** Stable carbon isotope signatures for different carbon pools from Clark & Fritz (1997), with data from Trumbore & Druffel (1995).

negative signature (-18.6) is needed to shift from a signature of 70‰/yr to 55‰/yr. Stuiver & Quay (1981) model the distribution and development of $^{14}C$ over time and conclude that the lighter signature can only be achieved through the addition of lightest carbon from fossil fuels.

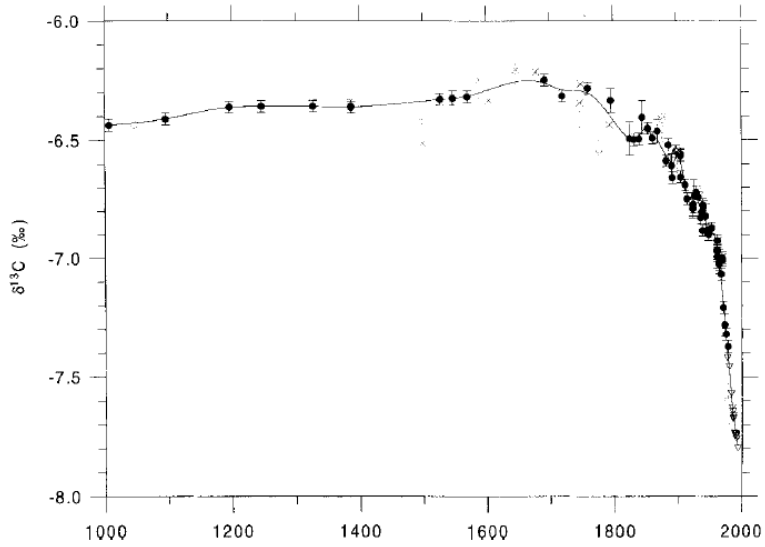


**Figure A.14** Stable carbon isotopes across the last 1000 years from firn tree ring and ice core samples from Francey et al. (1999).

It can therefore be concluded that the recent increase in atmospheric $CO_2$ concentrations is highly likely due to the release of anthropogenic fossil fuels, rathr than $CO_2$ release from natural processes.